Modelling of Mono and Bimetallic Amides for C–H Metalation

A thesis submitted in partial fulfilment of the requirements for the degree of

Doctor in Philosophy

at the

University of Dublin, Trinity College

by

Manting Mu

2025

Under the supervision of Prof. Max García-Melchor

and Prof. Graeme Watson

June 2025

Trinity College Dublin

Declaration of Authorship

I declare that this thesis has not been submitted as an exercise for a degree at this or any other university and it is entirely my own work.

I agree to deposit this thesis in the University's open access institutional repository or allow the Library to do so on my behalf, subject to Irish copyright legislation and Trinity College Library conditions for use and acknowledgement.

I consent to the examiner retaining a copy of the thesis beyond the examining period, should they so wish (EU GDPR May 2018)

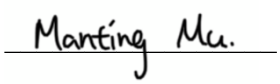

Manting Mu
26th June 2025

Trinity College, The University of Dublin

Summary

One of the central challenges in modern synthetic chemistry is the selective activation of unreactive C–H bonds, which underpin many key transformations in fine chemical synthesis and pharmaceutical development. Despite significant advances in transition metal catalysis, activity and selectivity prediction models for selective C–H activation remain limited, particularly for systems based on earth-abundant elements. This thesis addresses this challenge by integrating detailed computational modelling with experimental observations to investigate mono- and bimetallic amide complexes, systems that exhibit cooperative effects between alkali and transition metals. It provides mechanistic insight into how ligand design, solvent environment, and metal cooperativity influence C–H metalation, which offers the principles to guide the rational design of future C–H activation reagents and catalysts.

The thesis begins by establishing a conceptual framework based on the NaCo bimetallic amide system, highlighting the cooperativity between NaHMDS and $Co(HMDS)_2$ (HMDS = bis(trimethylsilyl)amide) in C–H activation reactions. A "seesaw effect" is identified for substrates bearing halide substituents in the ortho positions of the activated aryl, whereby the balance between mono- and tetra-aryl metalation pathways is modulated by the strength of Na···X interactions (X = F, Cl, Br, H). These interactions influence the thermodynamic stability of the resulting metalated species and determines whether a monoaryl product or a tetra-aryl square-planar Co(II) complex is formed. Density functional theory calculations and microkinetic modelling reveal that even subtle variations in halide substitution can lead to significant changes in product selectivity. These findings not only rationalise previous experimental results but also provide design principles for tuning C–H activation reactivity through strategic selection of alkali metal combinations.

Building on this bimetallic framework, the thesis examines KCo systems, which exhibit a striking dependence on the sequence of reagent addition. In contrast to Na-based systems, where thermodynamic and kinetic control can operate in concert, the reactivity of KCo systems is predominantly governed by kinetic factors. When K(HMDS) is introduced to toluene before the cobalt source, a transient potassium amide dimer forms. This reactive species engages $Co(HMDS)_2$ via a cooperative S_N2-like transition state to selectively cleave the benzylic C–H bond of toluene. The resulting benzyl-Co complex was isolated as a linear coordination

polymer. Conversely, when potassium and cobalt precursors are added simultaneously, the system generates a stable yet unreactive potassium cobaltate complex, $KCo(HMDS)_3$, which inhibits C–H activation. These findings highlight the critical role of sequence-dependent speciation and coordination dynamics. DFT simulations support this observed reactivity switch, indicating that the formation energies of intermediates and solvent-mediated equilibria are key determinants of whether the system proceeds via a productive or an inert pathway.

The focus then shifts to monometallic systems, specifically low-coordinate Fe and Co amides supported by sterically rigid TMP ligands. These complexes provide a valuable opportunity to investigate C–H activation through ligand modification in the absence of alkali metal cooperativity, as the Fe and $Co(HMDS)_2$ complexes are non-reactive. Despite their structural similarity, $Fe(TMP)_2$ and $Co(TMP)_2$ (TMP = 2,2,6,6-tetramethylpiperidide) exhibit markedly different reactivity profiles. $Fe(TMP)_2$ is capable of dual activation of pentafluorobenzene, yielding a bis-aryl product via two sequential C–H metalation events. In contrast, $Co(TMP)_2$ activates only a single arene molecule and forms a stable dimeric complex $\{Co(TMP)(C_6F_5)\}_2$ that acts as a thermodynamic sink. This divergence is explored through a suite of computational techniques, including natural bond orbital analysis, independent gradient model and quantum theory of atom in molecules. The results indicate that $Fe(TMP)_2$ benefits from stronger donor-acceptor interactions between Fe and O atom, greater geometric flexibility, and therefore more favourable THF coordination, all of which facilitate the formation of reactive intermediates. The Co complex, by contrast, displays more rigid coordination and a stronger tendency to dimerise, thereby hindering further activation. To accurately capture the role of THF coordination and solvent effects, a hybrid solvation model was devised. By integrating explicit THF molecules in calculation and continuum solvation approaches, the model successfully reproduces the experimentally observed binding strengths and speciation equilibria. Microkinetic simulations further refine the mechanistic understanding, revealing the time-concentration plots for product distributions. These simulations accurately replicate experimental concentration profiles and explain the observed divergence. Fe systems progress to the bis-aryl product, whereas Co systems stops at the mono-activated dimer complex.

Overall, this thesis demonstrates that subtle electronic and structural features, ranging from alkali metal coordination preferences and ligand geometry to solvent dynamics and reagent addition sequence, play a decisive role in determining whether C–H activation occurs. The combination of computational mechanistic understanding and insights provide a coherent

mechanistic framework that not only rationalises known outcomes but also guides future synthetic efforts. By identifying and quantifying key species and transition states, the work paves the way toward more predictive models for cooperative and monometallic systems alike. This research ultimately advances our understanding of how earth-abundant metals can be used in C–H activation reactions and provides foundational principles for tuning reactivity through metal-ligand-solvent interactions. These findings are expected to inform future developments in sustainable catalysis, particularly in the design of alkali-free or mixed-metal complexes for site-selective arene functionalisation.

Abstract

Understanding the origins of reactivity and selectivity in metal amide-mediated C–H metalation remains a central challenge in organometallic chemistry. This thesis investigates the fundamental factors controlling selective C–H activation through computational mechanistic study of alkali metal and transition metal amide complexes. Focusing on both bimetallic systems (NaCo and KCo) and monometallic Fe and Co complexes supported by sterically rigid TMP ligands, this thesis applies DFT, energy decomposition analysis, non-covalent interaction and independent gradient model analyses, as well as microkinetic model to understand divergent reactivity profiles. For the reactivity with the NaCo system, a "seesaw effect" was uncovered, whereby the strength of Na···X interactions (X = F, Cl, Br, H) tunes the balance between mono-aryl and tetra-aryl Co(II) square planar complex formation pathways. It rationalises the experimentally observed selectivity trends and provides design rules for modulating reactivity. For the KCo system we reveal a striking sequence-dependent reactivity, whereby the stepwise addition of K(HMDS) and $Co(HMDS)_2$ enables formation of reactive potassium amide dimers that undergo S_N2-type methyl C–H activation of toluene. In contrast, simultaneous reagent mixing yields a thermodynamically stable but catalytically inert $KCo(HMDS)_3$ cobaltate, precluding further activation. Monometallic studies contrast the behaviour of $Fe(TMP)_2$ and $Co(TMP)_2$ in the metalation of pentafluoroarene; while both exhibit low-coordinate geometries, only $Fe(TMP)_2$ shows polybasicity, effecting polybasic behaviour. $Co(TMP)_2$ performs a single activation before stabilising as a dimeric complex. This divergence is traced to stronger Fe–N bonding and favourable THF exchange equilibria, as shown by the activation strain, natural bond orbital and independent gradient model analyses. Hybrid solvation models are employed to accurately reproduce solvent effects and microkinetic simulations validated against experimental rates, which capture the interplay of reaction barriers and product speciation. Together, these studies illuminate how subtle variations in the choice of metal, ligand, and solvent govern the energy landscape of C–H metalation and product formation. The results lay the groundwork for predictive design of cooperative, earth-abundant metal-based C–H activation systems.

Acknowledgements

Firstly I would like to thank my supervisor, Professor Max García-Melchor, for all his help and encouragement throughout the PhD research, I am so very grateful for his inspiration for me to carry out this research project and for pursuing a PhD working in research.

I would like to thank our collaborators, especially Professor Eva Hevia and her research group, for their invaluable support and collaboration throughout the course of my PhD. I am particularly thankful for their outstanding experimental contributions, which have greatly enriched this work. It has been a genuine pleasure to engage in discussions on the fascinating field of bimetallic chemistry with them.

I would also like to thank Professor Graeme Watson for the detailed discussion on the theory behind the applied methods which boosted my understanding. Also Dr. Marconi Peñas-Defrutos for discussions on the organometallic chemistry, experimental techniques and spectra interpretations.

I'm very grateful for the Irish Research Council which funded all the work of this PhD.

Thank you to all the current and past CCEM group members from whom I learnt from each of them, Marconi, Michael, Eric, Arantxa, Pepe, Kevin, Anna, Cian, Ale, Conor, Ana and Timo.

Thank you to the TCHPC and ICHEC staff for maintaining compute clusters and hardware, also for their technical support on the HPCs.

At last I would like to thank my friends and family, without whom I would not have been able to complete this journey.

Publications

Publications related to the contents of this thesis.

1. A. Logallo, M. Mu, M. García-Melchor, E. Hevia. Building Square Planar Cobalt (II) Complexes via Sodium Mediated Cobaltation of Fluoroarenes, *Angew. Chem. Int. Ed.* **2022**, *61*, e202213246.
2. M. Mu, A. Logallo, E. Hevia, M. García-Melchor. Interaction and Energy Decomposition Analyses to Predict Stability of Tetraaryl Square Planar Cobalt Complexes, *ChemCatChem*, **2023**, *15*, e202300769.
3. A. Logallo, L. C. H. Maddock, M. Mu, L. Gravogl, N. Jin, M. N. Peñas-Defrutos, K. Meyer, M. García-Melchor, E. Hevia. Unlocking the Metalation Applications of TMP-powered Fe and Co(II) bis(amides): Synthesis, Structure and Mechanistic Insights, *Angew. Chem. Int. Ed.* **2024**, *64*, e202402907.
4. M. Mu; M. N. Peñas-Defrutos, M. García-Melchor. Chapter: Challenges in the Computational Modelling of Bimetallic C–H Activation Processes, *Advances in Organometallic Chemistry*, Vol 81, **2024**, pp. 329-348.

Other publications

5. L. C. H. Maddock, M. Mu, A. R. Kennedy, M. García-Melchor, E. Hevia. Facilitating the Ferration of Aromatic Substrates through Intramolecular Sodium Mediation, *Angew. Chem. Int. Ed.* **2021**, *60*, 15296.
6. A. Tortajada, L. J. Bole, M. Mu, M. Stanford, M. N. Peñas-Defrutos, M. García-Melchor, E. Hevia. Sodium Mediated Deprotonative Borylation of Arenes using Sterically Demanding $B(CH_2SiMe_3)_3$: Unlocking Polybasic Behaviour and Competing Lateral Borane Sodiation, *Chem. Sci.* **2023**, *14*, 6538.
7. C. Casadevall, A. Lage, M. Mu, H. F. Greer, D. Antón-García, J. N. Butt, L. J. C. Jeuken, G. W. Watson, M. García-Melchor, E. Reisner. Size-dependent Activity of Carbon Dots for Photocatalytic H_2 Generation in Combination with a Molecular Ni Cocatalyst, *Nanoscale*, **2023**, *15*, 15775.

8. M. Mu, K. L. Walker, G. Sánchez-Sanz, R. Waymouth, C. Trujillo, M. Muldoon, M. Garcia-Melchor. Insights into the Palladium(II)-Catalyzed Wacker-Type Oxidation of Styrene with Hydrogen Peroxide and *tert*-Butyl Hydroperoxide, *ACS Catal.* **2024**, *14*, 1567.
9. A. Tortajada, G. L. Righetti, A. McGinley, M. Mu; M. García-Melchor; E. Hevia. Alkene Isomerisation Catalysed by a Superbasic Sodium Amide, *Angew. Chem. Int. Ed*. **2024**, *61*, e202407262.
10. J. Moore, T. J. Miller, M. Mu, M. N. Peñas-Defrutos, K. L. Gullett, L. S. Elford, S. Quintero, M. García-Melchor, A. Fout. Selective Stepwise Reduction of Nitrate and Nitrite to Dinitrogen or Ammonia, *J. Am. Chem. Soc.* **2025**, *147*, 8444.

Abbreviations

AMLA ambiphilic metal-ligand assistance
ASA activation strain analysis
BCP bond critical point
CC coupled-cluster
CCPs cage critical points
CDC cross-dehydrogenative couplings
CMD concerted metalation-deprotonation
CP critical points
CPCM conductor-like polarizable continuum model
CT charge transfer
DFT density functional theory
DG directing group
ED electron density
GGA generalised gradient approximation
GsES Gibbs solvation energy surface
HF Hartree-Fock
HMDS bis(trimethylsilyl)amide
LDA diisopropylamide
LDA local density approximation
MKM microkinetic modelling
MO molecular orbital
NBOs natural bond orbitals
NCPs nuclear critical points
NCI non-Covalent Interaction
NEDA natural energy decomposition analysis
NAO natural atomic orbitals
NON bis(amido)xanthene ligand
PDP pyridine diimine ligand
PES potential energy surface
PMDETA N,N,N′,N″,N″-pentamethyldiethylenetriamine
POL polarisation
QTAIM quantum theory of atoms in molecules
RCPs ring critical points
RDG reduced density gradient
SCRF self-consistent reaction field
SMD solvation model based on density
TDGs transient directing groups
TMP 2,4,6-trimethylpyridine
TS transition state
XRD X-ray diffraction

Table of Contents

Chapter 1
General introduction

Protons give an atom its identity, electrons its personality.
– Bill Bryson

1.1 Organometallic chemistry

Organometallic chemistry is a dynamic branch of chemistry that investigates compounds featuring "*bonds between one or more metal atoms and one or more carbon atoms of an organyl group*".[1] These organometallic compounds serve as a critical link between organic and inorganic chemistry, showcasing their unique ability to integrate aspects of both disciplines. This inherently interdisciplinary field combines principles and methodologies from organic chemistry and inorganic chemistry.[2] On the one hand, organometallic species involve metal centres, often studied through the lens of coordination chemistry and electronic structure theory. On the other, they incorporate organic fragments whose reactivity and transformations draw from classic organic chemistry. This dual character enables organometallic chemistry to serve as a versatile platform for a wide range of applications, ranging from catalysis development[3-5] to advancements in mimicking biological systems.[6,7]

At its core, organometallic chemistry explores the synthesis, structure, reactivity, and applications of M–C bonds. These bonds frequently involve transition metals, which offer a distinctive combination of *d*-orbital availability and variable oxidation states. This unique set of properties facilitates reactivity that is often unattainable with purely organic molecules. Organometallic compounds play a crucial role in advancing our understanding of fundamental processes, such as metal-ligand interactions,[2] electron transfer,[8] and the activation of small molecules.[9]

1.1.1 History and fundamental concepts

The origins of organometallic chemistry can be dated back to the 18th and 19th centuries. In 1760, Cadet prepared "*Cadet's fuming liquid*", an ill-smelling red-brown oil during his work with inks, now recognised as the first synthetic organometallic compound, involving metalloid–carbon bonds, known as kakodyl oxide.[10] Nearly a century later, in 1827, W.C. Zeise had isolated Zeise's salt ($K[PtCl_3(C_2H_4)]\cdot H_2O$), the first transition-metal olefin complex, demonstrating that ethylene could coordinate to a metal through its π-bond.[11] Shortly thereafter, in 1849, Frankland prepared the first zinc alkyl (pyrophoric diethylzinc) while attempting to make "ethyl radicals," thus inaugurating the study of main-group metal–carbon σ-bonds.[12] The rapid expansion continued into the late 19th century: in 1890 Ludwig Mond discovered nickel tetracarbonyl $Ni(CO)_4$, the first homoleptic metal carbonyl complex, which showcased how CO ligands could stabilise a metal in zero oxidation state.[13] Each of these early breakthroughs not only revealed new bond types but also expanded the known reactivity of metals and carbon. For example, Grignard's 1900 discovery of organomagnesium reagents (RMgX) provided powerful carbon nucleophiles for forming C–C bonds in synthesis.[14] This was soon followed by the development of organolithium reagents (e.g., RLi by Schlenk in 1917), which offered even more reactive and strongly basic carbanions.[15] Such organometallic reagents rapidly became cornerstones of organic synthesis, ushering in the golden era of organometallic chemistry.

These historical advances unveiled the remarkable structural diversity possible for metal–carbon bonds, from simple σ-bonded alkyls to multiple bonds and extensive π-coordination frameworks as shown in Figure 1.1. Metals can form single, double, or triple bonds to carbon: for instance, Fischer and Schrock showed that stable metal–carbene complexes ($M{=}CR_2$)[16] and metal–carbyne complexes ($M{\equiv}CR$)[17] are attainable, expanding the

concept of multiple bonding in organometallics. Moreover, metals can bind to organic ligands in a variety of hapticities (η^n coordination modes). Early examples like Zeise's ethylene (η^2) and later the discovery of ferrocene in 1951 (an η^5–cyclopentadienyl sandwich complex) demonstrated that carbon frameworks could coordinate through multi-centered bonds.[18] Metals were soon also observed coordinating to six-carbon aromatic rings (η^6, as in arene–chromium complexes),[19] among other motifs, covering a continuous range from η^2 up to η^6 (Figure 1.1) and more.[20,21] Each bonding mode confers distinct chemical properties: strongly polarised metal–alkyl σ-bonds (as in Grignard and organolithium reagents) impart high reactivity (e.g. toward electrophiles or protic sources) but tend to be kinetically labile, whereas π-bound ligands (such as aromatic η^6 or cyclopentadienyl η^5 systems) often lend exceptional stability by satisfying the 18-electron rule and delocalising charge. This breadth of structures and bond types has been instrumental in tuning organometallic reactivity and stability, allowing chemists to design complexes that undergo diverse transformations (from insertions and eliminations to catalytic cycles) while remaining sufficiently robust.[22]

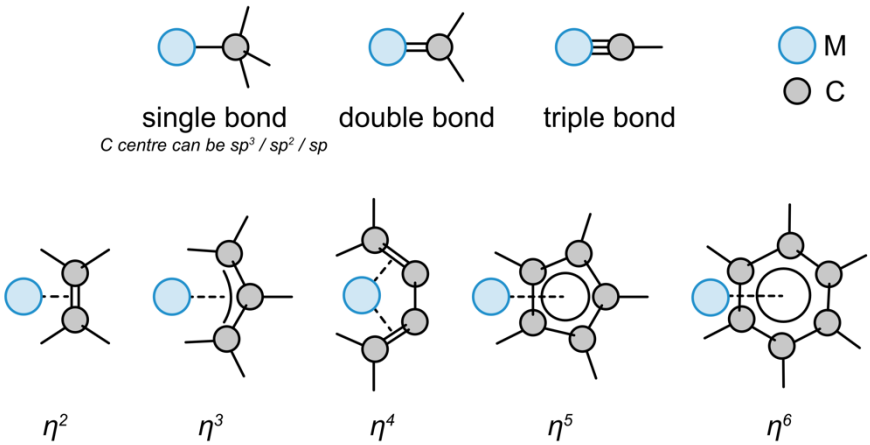

Figure 1.1. Representation of various types of M–C bonds. The top row illustrates single, double, and triple M–C bonds, where the carbon atom adopts sp^3, sp^2, or sp hybridisation, respectively. The bottom row depicts different hapticities, η^n, of M–C interactions with π systems, where n is the number of carbon atoms coordinated to the metal centre. These bonding modes play crucial roles in organometallic chemistry and catalysis, influencing reactivity and stability.

Despite the advances in bonding concepts above, many classic organometallic reactions (e.g., cross-couplings) long relied on *prefunctionalised* reagents.[8] In typical 20th-century cross-coupling, both coupling partners require activating groups (such as halides, organometallics, etc.), which adds synthetic steps and waste.[23] This limitation spurred interest in direct C–H bond functionalisation methods that bypass the need for preactivated substrates. In recent years, transition-metal-catalysed C–H activation has emerged as a powerful strategy in both organometallic and synthetic organic chemistry.[24] The ability to transform ubiquitous but inert C–H bonds directly into C–C, C–O, C–N and other bonds is often more step-economical and atom-efficient than traditional routes.[25] Indeed, the past few decades have witnessed an explosion of C–H activation reactions, many proceeding under mild conditions with high selectivity.[26] Such methodologies greatly expand the scope of organometallic chemistry, enabling new catalytic processes and more efficient syntheses that were previously impractical with prefunctionalised approaches.

1.2 C–H activation reactions

The activation of C–H bonds, which are abundant in organic compounds, represents a highly efficient strategy for synthesising organometallic complexes containing M–C bonds. This process is a pivotal step in the manufacturing of complex molecules used in pharmaceuticals,[27] agrochemicals,[28] polymers,[29] and various other everyday chemicals.[24] By eliminating the need for additional synthetic steps, C–H metalation reactions significantly enhance atom economy, a cornerstone of green chemistry.

1.2.1 Characterisation of C–H bonds

Based on the bonding exhibited by the carbon atom and its neighbouring groups, C–H bonds can be classified into four major types, with their general order of acidity being: C(*sp*)–H > C(sp^2)–H > C(*aromatic*)–H > C(sp^3)–H, with the pK_a values shown in Figure 1.2a. The orientation of these bonds in the transition state must be carefully considered, as their antibonding orbitals differ in shape and positioning. Additionally, the presence of π-orbitals can assist cleavage by stabilising the resulting metal-bound carbanion.

Neighbouring functional groups, either through electronic or steric effects, can also influence the acidity of C–H bonds.[30] Electron donating groups decrease acidity, while electron

withdrawing groups increase it, with the extent of the effect depending on the strength of the substituents. Through space interactions, such as hydrogen bond donors interacting with the hydrogen atom, or lone pairs from certain metals, can also impact acidity. Furthermore, the d-orbitals of transition metals can interact with the C–H bonding orbital to form agostic or anagostic interactions.[31] Agostic interactions involve significant orbital overlap, characterized by forward σ-donation from the C–H bond to the metal and potential back-donation from the metal into the σ* orbital, whereas anagostic interactions are predominantly electrostatic in nature, with minimal orbital contribution. These interactions can weaken the C–H bond and enhance its acidity, as illustrated in Figure 1.2.

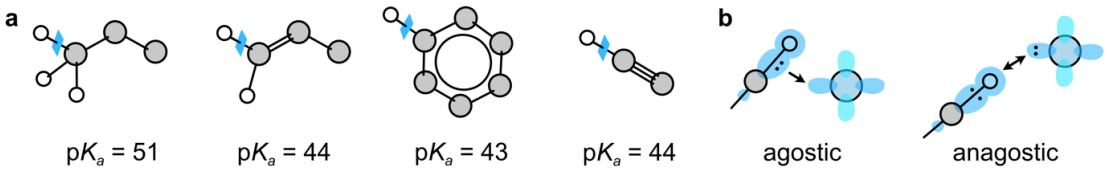

Figure 1.2. a) pK_a values of common C–H bonds in organic molecules. b) Metal and C–H bond interactions.

1.2.2 Reaction mechanisms

C–H activation plays a vital role in modern catalytic chemistry, particularly in the selective transformation of otherwise unreactive hydrocarbons. The mechanisms by which C–H bonds are cleaved can vary significantly depending on the catalyst and its surrounding environment. This section outlines four well-established heterolytic mechanisms, distinguished by the origin of bond cleavage and classified according to whether activation is initiated by the metal centre, the ligand, or through metal–ligand cooperation, each case is illustrated with representative examples in (Figure 1.3).

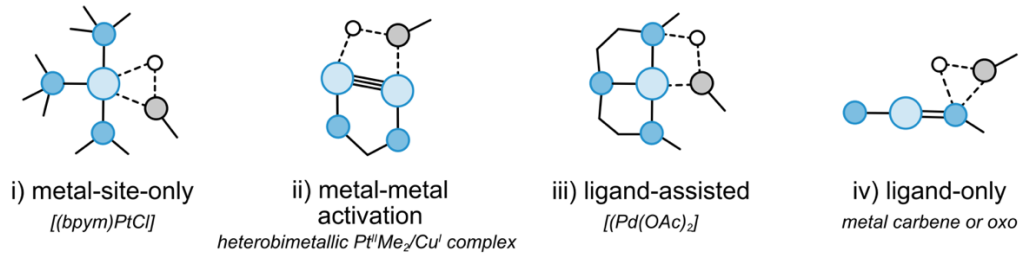

Figure 1.3. Overview of C–H activation mechanisms, categorised by whether the metal, the ligand, or both serve as the active species initiating C–H bond cleavage, with an example of chemical system shown below.

Metal-site-only mechanism.

In certain systems, C–H bond cleavage occurs directly at the metal centre, without any significant assistance from the ligand framework. The quintessential metal-site-only mechanism is oxidative addition of a C–H bond, that yields a metal–carbon bond and a metal–hydride. In a formal oxidative addition, the C–H σ-bond breaks with both fragments attaching to the metal, increasing the metal's oxidation state and coordination number by two.[32] For example, a low-valent transition metal M^n (often electron-rich and in a low formal oxidation state) will oxidise to M^{n+2} upon inserting into a C–H bond, forming an organometallic hydride (M–H) and a metal–carbon (M–C) bond. This process requires a metal centre with available electron density and vacant coordination sites, which is why oxidative addition is typically observed with electron-rich, late transition metal complexes in low oxidation states.[32]

A classic illustration is the C–H oxidative addition at an iridium centre. Vaska's complex ($Ir(CO)(PPh_3)_2Cl$) and related 16-electron Ir(I) complexes readily undergo oxidative addition of H–H and other σ-bonds; under the right conditions, they can also insert into C–H bonds to form Ir(III) hydride-alkyl species.[3] In 1982, Bergman and Graham independently reported the first examples of intermolecular alkane C–H bond oxidative additions: an Ir(I) half-sandwich complex [$Cp^*Ir(PMe_3)$] was shown to cleave the C–H bonds of simple alkanes, yielding stable iridium(III) alkyl hydride complexes.[35] This landmark result demonstrated that even inert C(sp^3)–H bonds (e.g. in neopentane) could be activated by a suitably designed low-valent metal complex. Similarly, zero-valent palladium and platinum complexes can undergo oxidative addition with aromatic C–H bonds. For instance, a Pd(0) or Pt(0) centre supported by strong donor ligands can insert into a benzene C–H bond to produce a hydrido-aryl metal(II) complex.[36] Such reactions, while often requiring specific conditions (e.g. strain or directing effects), confirm the general principle: electron-rich d^8/d^{10} metals in low oxidation states (Pt(0), Pd(0), Ir(I), Rh(I), etc.) are capable of cleaving C–H bonds via oxidative addition. The metal's ability to accept electron density (to form M–C) and donate into antibonding orbitals (to form M–H) is crucial, which is why strongly donating spectator ligands (L-type ligands like phosphines, N-heterocyclic carbenes, etc.) are often used to support such low-valent metals.[33] These ligands elevate the electron density at the metal and stabilise the higher oxidation state formed after addition. Overall, oxidative addition represents a direct cleavage of the C–H bond at the metal site, the defining feature of the metal-centre-only mechanism. Other pathways

could involve homolytic cleavage are beyond the scope of this thesis and will not be discussed in detail.

Metal-metal activation.

In multinuclear molecular systems, cooperative interactions between two or more metal centres can significantly enhance C–H bond activation through complementary functions.[37] In such systems, one metal typically acts as the primary site for substrate coordination or bond cleavage, while the second facilitates electron transfer, modulates electronic density, or stabilises reactive intermediates. This cooperative effect, often described as bimetallic synergy (discussed in detail in Chapter 4.1), broadens the range of accessible reactivity profiles, enabling transformations that are difficult or inaccessible with monometallic complexes alone. (Monometallic in the context of this thesis refers to complexes containing only one metal type, but could be of monomeric, dimeric, trimeric or other oligomeric forms, hence bimetallic refers to complexes containing two metal types.)

One prototypical example is the Pd–Ag bimetallic system, in which silver salts facilitate C–H bond cleavage via a transmetalation-like pathway. In these systems, Pd(II) forms the C–H activation product, but Ag(I) plays a crucial role in abstracting halides and tuning the electrophilicity of the palladium centre, ultimately enabling efficient C–H bond scission under mild conditions.[38] Similarly, Rh–Cu and Ir–Sn bimetallic complexes have been shown to exhibit ambiphilic metal–metal cooperativity, wherein one metal acts as a Lewis acid and the other as a redox-active or nucleophilic centre. For example, Brookhart and co-workers demonstrated that Rh–Cu complexes could engage in synergistic activation of aryl C–H bonds, with Cu(I) assisting in π-complexation of the arene and Rh mediating bond cleavage.[39] In another class of systems, metal–metal complexes enable C–H activation via cooperative redox pathways. In Pt–Ir and Ru–Ru dinuclear compounds, electron density is shuttled between the two metals during the activation event, stabilising high-energy oxidation states or metal–hydride intermediates that facilitate challenging transformations.[40,41] Overall, metal–metal cooperation in molecular complexes enables novel reactivity through electronic, steric, and orbital complementarity. This approach not only improves reactivity and selectivity but also unlocks new catalytic pathways by combining the individual capabilities of different metals in a single scaffold.

Ligand-assisted mechanism.

In a ligand-assisted C–H activation mechanism, a coordinated ligand plays an active role in the bond-cleavage step rather than serving as a passive spectator.[42] In this pathway, often termed ambiphilic metal–ligand assistance (AMLA) or concerted metalation–deprotonation (CMD), the ligand (typically a basic anion like carboxylate) abstracts the proton from the C–H bond at the same time as the metal inserts into the C–H bond,[43] in which the carbon is stabilised by coordination to the metal centre. A prototypical example is the use of Pd(II) catalysts bearing acetate (OAc) ligands: the Pd–OAc unit engages the substrate's C–H, and the acetate ligand deprotonates it to produce acetic acid as byproduct.[44] This example resulted in a cyclopalladated species (a Pd–C bond) and HOAc, illustrating how the ligand acts as an base to facilitate intramolecular C–H cleavage.

Notably, such ligand-assisted pathways are crucial even under unconventional conditions, for instance, in electrocatalytic C–H functionalisations where external chemical oxidants or bases are absent, the bound acetate can fulfil the dual role of directing and deprotonating the C–H bond. Depending on the spatial arrangement, this mechanism can proceed intramolecularly (when a directing group or chelating ligand holds the C–H close to the metal centre for internal deprotonation) or intermolecularly (if an external ligand or base mediates the deprotonation in solution).[43] Each scenario underscores that the ligand is an active participant in lowering the barrier for C–H bond activation, extending the catalyst's reach beyond mere structural support and enabling efficient C–H to metal bond transmetalation.

Ligand-only activation.

In some cases, the ligand itself is responsible for activating the C–H bond, with little to no involvement from the metal centre. Such mechanisms are frequently observed in systems featuring carbene or hydroperoxyl (–OOH) groups. Carbenes, for example, exhibit nucleophilic or electrophilic reactivity that can promote C–H bond cleavage. A recent study demonstrates that silver-bound trifluoromethyl carbenes can insert into methane and other alkane C–H bonds via a pathway with no enthalpic barrier, where the carbene carbon directly cleaves the C–H bond without initial metal participation, highlighting a purely ligand-controlled activation mode.[45] Similarly, OOH-based ligands can generate reactive species that enable hydrogen abstraction or C–H bond activation. For instance, a non-heme iron complex

ligated with an N-heterocyclic carbene ligand was shown to oxidise methane in water with high selectivity and efficiency.[46] The oxidation proceeds through an Fe-based oxo species, but the surrounding ligand cavity is crucial in selectively capturing the C–H bond of methane and modulating its reactivity by local confinement, reinforcing a ligand-dominated mechanism of activation.

Each of the mechanisms illustrated in Figure 1.3 illustrates the versatility and complexity of C–H activation. This fundamental knowledge shaped the discovery of many state-of-the-art catalysts as detailed in the next section.

1.2.3 Precious metal catalysts

Monometallic catalysts based on precious metals (e.g., Pd, Pt, Rh, Ir, Ru) have dominated C–H activation since the field's inception. For the past 10 years, researchers achieved significant advances in reactivity and selectivity using these noble-metal catalysts. Key strategies that were utilised include *i) directed C–H activation*, where a coordinating directing group (DG) binds the metal to position it for C–H cleavage and *ii) undirected C–H activation*, which relies on inherent substrate bias or transient interactions. These strategies are succinctly discussed below.

Directed C–H activation.

Directed C–H functionalisation have been achieved with Pd(II), Rh(III), and Ru(II) complexes. These have been widely applied to ortho-C–H bond arylation, alkylation, and coupling with unsaturated partners. For example, Pd(II) catalysts performing the classical C–C coupling reaction had been improved to directly perform C–H activation to obtain the Pd–C bond using DG for selectivities.[47] On the other hand, Kakiuchi and co-workers extended the Murai reaction (Ru(0)-catalysed ortho-alkylation of aromatics). Kakiuchi's improved catalytic systems involving transition metals (Rh, Ru) for alkylation of arenes under milder reaction conditions.[48] The Rh(III)-Cp* class of catalysts enabled versatile ring formation reactions through C–H activation of benzamide which then reacts with alkynes to give isoquinolones. Despite these successes, a persistent challenge has been the reliance on installing and later removing DGs, increasing synthetic complexity. The reactions described in these sections presents some of typical examples of utilising ortho DG groups to directly form the M–DG interaction to control

selectivity; however, due to DGs driving force for ortho positioned C–H bond activation, the other meta and para positioned C–H bonds could not be activated directly by this approach.

A breakthrough in this period was the development of template-directed and weak-interaction-guided remote C–H activation to go beyond ortho positions. In 2016, Li *et al.* introduced a nitrile-containing U-shaped template DG that directs Pd(II) to activate the meta-C–H bonds of benzoic acid derivatives.[49] This nitrile template coordinates to an added Ag(I) salt, which in turn positions the Pd catalyst at the meta position, enabling meta-selective olefination of benzoic acids under. Such removable DG templates overcame electronic effects which favoured ortho positions, and these enabled functionalisation of electron-poor arenes that were previously intractable. Similarly, other researchers leveraged non-covalent interactions (NCIs): for instance, electrostatic and π-stacking interactions have been explored to direct metals to distal C–H sites. Non-covalent methods with stronger interactions, such as ion-pair and H-bonding strategies, proved to be more effective. In 2022, Chen and co-workers employed a pair of opposite charges (a cationic ligand and anionic substrate) to guide Pd(II) to meta sites, achieving olefinations on aromatics without a covalent DG (a concept dubbed "charge-assisted directed C–H activation").[50] Overall, through this improved DG template approach and NCIs, meta- and even para-selective C–H functionalisation become feasible. These examples hint at selectivity modulation through the design of DGs on the substrate and through the ligand structure.

The design of specialised ligands was another pillar of progress. Jin-Quan Yu's group demonstrated that carefully crafted monodentate ligands can accelerate C–H insertion and even impart enantioselectivity.[51] In a landmark study, they reported chiral aminoethyl quinoline ligands that enable Pd(II)-catalysed enantioselective β-methylene C(sp^3)–H arylations. Such ligand-accelerated catalysis addresses the problem of non-asymmetric C–H activation by establishing an electrostatic interaction between ligand carbonyl and the C–H bond to be cleaved, thus increasing both the rate and selectivity of C–H cleavage.

Transient directed C–H activation.

Additionally, transient directing groups (TDGs) were developed: these are catalytic auxiliaries that form *in situ* (e.g., imines from aldehydes or reversible imine/aniline conjugates) to guide a metal to a C–H bond and then dissociate. These provide a method to enable directed C–H

functionalisation *without* needing a pre-installed DG, since the directing moiety is formed and removed in the same pot. For example, transient imine formation has allowed Pd-catalysed γ-C–H arylation of amines and amino acids, greatly streamlining such transformations.[52,53] While these produce less waste and are highly selective, TDG systems often require careful tuning of conditions to favour DG formation and avoid side-reactions.

Other than improving selectivity of C–H activations using direct DG, researchers also focused on increasing the reactivity. Iridium catalysis had long been known to activate C–H bonds, which has revolutionised undirected C–H functionalisation, expanding to the less activated alkyl C–H bonds. A notable advance was Hartwig's report of an Ir(I) complex to borylate unactivated alkyl C–H bonds,[54] which the selectivity was ensured through the use of hydrosilane functionality as a transient directing group. The Si–H group coordinates to Ir, or undergoes σ-bond metathesis, to direct borylation to the carbon at *β* position to silicon, yielding alkyl boronates from alkanes with high site-selectivity. This "hydrosilyl-directed" strategy effectively brings undirected sp^3 C–H bonds into reach, complementing the well-established Ir-catalysed borylation of arenes and heteroarenes, which generally occurs at positions dictated by sterics or electronics. Additionally, new ligands (e.g. bipyridines with large substituents) were developed to alter Ir-borylation regioselectivity on aromatics, enabling, for instance, borylation at less-hindered positions that were previously inaccessible through neither a DG or a TDG on the substrate but ligand effects.[55] Undirected C–H borylation has become a workhorse method to install versatile B–X functional handles on complex molecules with minimal prefunctionalisation.[56,57]

Undirected C–H activation.

Another group of catalysts that is known to promote C–H activation is metal carbenes and nitrenes. Precious metal carbenes and nitrenes continued to find applications in C–H functionalisation via insertion mechanisms. Dirhodium(II) paddlewheel catalysts (Rh_2L_4) are classic for carbene insertion into C–H bonds, and recent years saw improved chiral Rh_2 catalysts that insert carbenes into diazo compounds, benzylic, and even unactivated C–H bonds with high enantioselectivity, which are useful in cyclopropanation and C–H amination chemistry.[58-59] Similarly, Ir(III) imine carbene complexes have enabled intermolecular C–H alkylation via concerted insertion.[60] Though these insertion reactions are formally C–H activations, they typically do not rely on directing groups to bind the substrate to the catalyst

metal centre and proceed via radical-like or concerted pathways distinct from the CMD mechanism, thus broadening the toolkit of C–H functionalisation beyond the traditional DG paradigm.

Despite these advances, precious metal catalysts face limitations of cost and sustainability. Doyle and co-workers also noted that traditional Pd(II) and Ru(0) methods for C(sp^3)–H arylation needed harsh conditions and often were not amenable to asymmetric catalysis.[61] Additionally, controlling site-selectivity without DGs remains difficult, even with new strategies, achieving reactivity at a specific C–H bond in a complex molecule. Thus, a major ongoing goal is to improve catalyst efficiency and selectivity so that C–H functionalisation can occur at ambient conditions on complex substrates with simple, commercially available ligands, while reducing reliance on precious metals by finding earth-abundant alternative materials. Nevertheless, the past 10 years firmly established that monometallic Pd, Rh, Ir, Ru, and Pt catalysts can unlock reactions once deemed impossible, from distal arene functionalisation to enantioselective C–H bond formation, marking a golden age of C–H activation chemistry.[49]

1.2.4. First-row transition metal catalysts

Driven by cost and sustainability targets, recent years saw a surge in C–H activation catalysed by first-row transition metals, notably Co, Mn, Fe, Ni, and Cu, with Fe being a cheap alternative to the others. These metals are often orders of magnitude cheaper and more abundant than Pd or Rh, and offer attractive alternatives, but this comes with challenges such as limited oxidative stability and sometimes lower reactivity or selectivity due to side reactions. Nonetheless, significant progress had been made in expanding the scope of base-metal-catalysed C–H functionalisation.[62] Researchers drew inspiration from precious metal chemistry (e.g., designing base-metal analogues of Pd(II) or Rh(III) catalysts), while leveraging unique reactivity of first-row metals, like one-electron redox and radical pathways.

Cobalt-based catalysts.

A standout development was the introduction of pentamethylcyclopentadienyl cobalt(III) ([CpCo]$^{2+}$) complexes as catalysts for directed C–H activation. CpCo(III) complexes provide similar chemistry to Cp*Rh(III), achieving ortho-C–H activation of substrates bearing DGs uch as *N*-heterocycles, amides, or oximes.[63] For example, cobalt(III) acetates enabled the

coupling of benzamides with alkynes to form isoquinolones (previously a Rh-catalysed reaction) with comparable efficiency.[48] Similarly, Co(III) has been used for C–H amidation and alkylation.[64] Although Co(III) is less electrophilic than Rh(III), the use of strong oxidants (e.g. persulfate)[65] can drive these reactions. An appealing aspect is cost: cobalt ($0.03 per gram) is far cheaper than rhodium ($194.15 per gram),[66,67] making such methods attractive for scale-up uses. The enantioselective C–H functionalisations using chiral cyclopentadienyl cobalt catalysts were also demonstrated despite remaining less developed than Rh asymmetric catalysis.[69] One limitation is that cobalt(III) often requires an external oxidant to generate or regenerate the active species, which can limit functional group compatibility.[63]

Cobalt's ability to access multiple oxidation states enabled entirely different C–H functionalisation manifolds as well. Cobalt(II) salts (like simple $Co(OAc)_2$) under oxidising conditions can catalyse cross-dehydrogenative couplings (CDC). For instance, coupling of an C(sp^2)–H with an C(sp^3)–H via radical pathways.[69,70] Cobalt(II) porphyrins and phthalocyanines have also achieved intramolecular C–H amination (nitrene insertion) to form aziridines or lactams, analogous to Rh_2 catalysts but at lower cost.[71-73] While such methods often suffer from competing oxidation or low selectivity, they demonstrate cobalt's distinct radical chemistry compared to typical Pd(II)-type mechanisms.

Manganese-based catalysts.

Another earth-abundant metal, made strides especially in C–H alkenylation and allylation reactions. Organometallic Mn(I) complexes, with a d^6 electronic configuration, exists typically as piano-stool complexes with carbonyl ligands, can undergo oxidative addition with C–H bonds that are reminiscent of Co(I) or Rh(I). Ackermann's group has extensively explored Mn(I)–alkyl complexes for directed C–H activation; for example, in 2015, they reported Mn(I)-catalysed C–H olefination of aromatics using acrylates. Under redox-neutral conditions the Mn(I) undergoes a two electron oxidative addition to Mn(III) in C–H activation, then reductive elimination and Mn(I) regeneration via protonation.[74,75] Manganese catalysis often requires the assistance of coordinating auxiliaries (e.g. pyridyl or imine DGs) to bind to the metal and direct it to access the C–H bond. Compared to 4*d*/5*d* metals, Mn reactions suffer from sensitivity towards air and moisture requiring specific reaction conditions. However, at the same time, it offers unique opportunities, such as high endo/exo selectivity in C–H annulations that differ from Rh catalysis.[76-79]

Iron-based catalysts.

Iron catalysis in C–H activation is prominently represented in C–H oxygenation reactions. Fe-based complexes, which are often inspired by enzymes like the cytochrome P450, have been used with peroxides to selectively oxidise C–H bonds to alcohols or ketones. A notable system is the Fe(PDP) catalyst (PDP = Pyridine diimine ligand) developed by White and coworkers, which in presence of H_2O_2, hydroxylates allylic and tertiary C–H bonds in complex molecules with high selectivity (e.g. late-stage functionalisation of natural products).[80,81] While these are technically C–H activations (forming C–O bonds), they differ from the traditional cross-coupling reactions. White's group and others introduced iterative improvements to Fe-based C–H oxidation, such as more chemoselective catalysts that can distinguish subtle differences in C–H bond strength and stereoelectronics in molecules.[82-84] For C–C bond formation, iron is less ubiquitous, but not absent, as Fe(II) has been reported to catalysed oxidative coupling of benzene with heteroarenes using persulfate as oxidant, essentially a direct aryl–aryl coupling via two C–H activations (one by Fe, one by a radical process).[85,86] Nonetheless, iron catalysts often struggle with controlling radical pathways, Fe can easily switch between one-electron and two-electron chemistry, sometimes leading to over-oxidation or side reactions. Furthermore, achieving asymmetric C–H functionalisation with iron is an ongoing challenge, unlike with Co or Ni, which have more developed chiral ligands. Nonetheless, iron's biorelevance and abundance make it a prime target for future catalyst development.

Nickel-based catalysts.

Nickel, being in the same group as Pd, has invited attempts to duplicate Pd(II)-type chemistry. In these five years, several groups showed Ni(II) can indeed accomplish directed C–H functionalisation. For example, Daugulis and colleagues used $Ni(OAc)_2$ with bidentate 8-aminoquinoline auxiliaries to activate C(sp^2)–H bonds in benzamides, effecting arylations and alkylations (Ni was proposed to go through a Ni(II)/Ni(IV) cycle analogously to Pd(II)/Pd(IV)).[87] Nickel's advantage is its ability to also catalyse substrate-unbound pathways, as Ni(0)/Ni(II) cycles can also perform oxidative additions and reductive couplings. However, Ni(0) typically does not insert into a C–H bond without assistance of the ligand progressing through a CMD mechanism.[88]

Nickel catalysts proved especially powerful when combined with external oxidants or catalysts. A prominent example is Ni/photoredox dual catalysis, as despite involving two catalysts, Ni is the organometallic workhorse that forms the new bond. Nickel's ability to undergo single-electron steps is crucial. Ni can capture radicals and form C–C bonds that Pd(II) would not as easily. For instance, in the α-amino C–H arylation, Ni(0) oxidative addition into an aryl bromide followed by radical capture and reductive elimination was the key cycle.[60] There has also been success in Ni-catalysed enantioselective C–H annulations. For example, a Ni(II)/Salox (salicyl-oxazoline) catalyst was shown to asymmetrically cyclise benzamides with bicyclic alkenes to form chiral isoindolinones.[89] Such advances illustrate that Ni, once thought too "reactive" for controlled C–H activation, can be tamed by ligand design to perform highly selective chemistry. There are however still challenges to be faced; in the previous examples, nickel catalysts can undergo competing pathways (e.g., β-hydride elimination, over-reduction) that precious metals typically avoid, which could lead to side products. Achieving high oxidation states in Ni (needed for two-electron C–H cleavage akin to Pd(IV)) often requires harsh oxidants, limiting functional group tolerance and substrate scope.

Copper-based catalysts.

Copper has a long history in oxidative couplings, also known as Ullmann reactions.[90] Cu(II) salts have been used to couple arenes with heteroatom nucleophiles, which was later achieved with C–H activation steps instead of halogen-carbon bond cleavage. One prototypical reaction is the Chan–Lam coupling, where a Cu(II) species mediates the coupling of an arylboronic acid with an NH- or OH-containing substrate, through the C–H activation of one of the coupling partners. It is often proposed to then involve Cu(III)–aryl and Cu(III)–nucleophile intermediates.[91] However, extending this to C–H activate both coupling partners is challenging because Cu(II) readily undergoes one-electron processes.

In summary, many earth-abundant catalysts for C–H activation face several challenges, including the need for harsher conditions that reduce functional group tolerance, poor selectivity due to uncontrolled radical pathways (e.g., with Fe and Cu), and limited catalyst longevity from ligand oxidation or formation of inactive complexes (as with Ni or Co). Although new ligand frameworks, such as pincer and macrocyclic designs, have improved stability and reactivity, many systems still suffer from limited substrate scopes and downstream functionalisation. To address these issues, this thesis turned to a class of simpler, commercially

available metal complexes that are often overlooked: metal amides. Typically used as precursors for more elaborate catalysts, these species offer a general and accessible platform for C–H activation reaction, with potential to bypass side reactions such as β-hydride elimination and over-reduction through the introduction of bimetallic and monometallic amide complexes, as discussed in the following sections.

1.3 Metal amides in C–H metalation reactions

Among various approaches, metal amido complexes (M–NR_2) are particularly notable due to their high reactivity and adaptability, providing an alternative strategy for addressing the persistent hurdles in C–H activation. These complexes, which contain an amido ligand (NR_2^-) bound to a metal,[20] exhibit unique properties such as pronounced basicity and nucleophilicity. These characteristics are critical to ensure chemical reactivity of these complexes.

1.3.1 Basicity and nucleophilicity

Basicity, in the context of the Brønsted base, the ability of a compound to accept a proton (H^+), is one of the defining features of metal amido complexes and underpins their reactivity towards C–H activation. The formation of M–C bonds instead of N–C bonds is influenced by the nucleophilicity of the nitrogen atom. This behaviour is partially governed by the nature of the metal and the atom coordinated to the pre-activated carbon. For instance, if the carbon is bound to a partially positively charged hydrogen atom, C–H activation is preferred. This is because metal hydrides are generally less stable than N–H bonds. Conversely, when the carbon is bound to a fluorine atom, and the metal is an alkali metal such as sodium, the Na–F bond forms as a salt, leading to the subsequent formation of a C–N bond. This process promotes the nucleophilicity of the NR_2^- ligand.

In these complexes, the nitrogen atom in the amido ligand possesses a lone pair of electrons, making it a strong Brønsted base. The proton affinity of these complexes is influenced by the electronic properties of the metal centre and the electronic and steric characteristics of the ligand framework. Metals with low electronegativity and low oxidation states, such as sodium in Na(HMDS) (HMDS = bis(trimethylsilyl)amide), tend to increase the electron density on the nitrogen atom, thereby enhancing its basicity. Conversely, metals with higher electronegativity and higher oxidation states reduce the basicity of the nitrogen atom but enhance the metal's

electrophilicity, stabilising the carbon anion after deprotonation, as seen in $Fe(HMDS)_2$. The deprotonation power could also be affected by the electronic properties of the ligand framework, the substituents on the amido group can tune the electron density of the N atom, thus affect its basicity. In HMDS, the nitrogen atom is bound to two silicon atoms, which are more electronegative than carbon atoms. Replacing silicon with carbon, as in LDA (LDA = diisopropylamide), increases the basicity of the ligand when bound to the same metal. For instance, Li(LDA) is more basic than Li(HMDS).

The steric environment of the ligand also plays a crucial role, albeit in a nuanced manner. Bulkier ligands can weaken ligand binding to the metal centre, while also strengthen the ligand binding to the hydrogen atom post-deprotonation, driving the reaction forward. For example, HMDS(H) is highly stable, promoting efficient deprotonation. On the other hand, excessively bulky ligands can shield the lone pair on the nitrogen, hindering the interaction of the ligand with the substrate and thus deprotonation.

Overall, the high basicity of $M(NR_2)$ complexes makes them excellent candidates for deprotonation reactions. These complexes are frequently employed as strong bases in organic synthesis, where they abstract protons from weak acids to form new reactive species. For instance, metal amido complexes are commonly utilised in catalytic cycles involving N–H bond formation and activation.[92,93] These complexes $X(HMDS)_1$ or $X(HMDS)_2$ are also readily synthesised with HMDS ligands[94-106] with metal elements across the periodic table, as shown in Figure 1.4, with their full potential not yet been explored, as detailed in the next chapters.

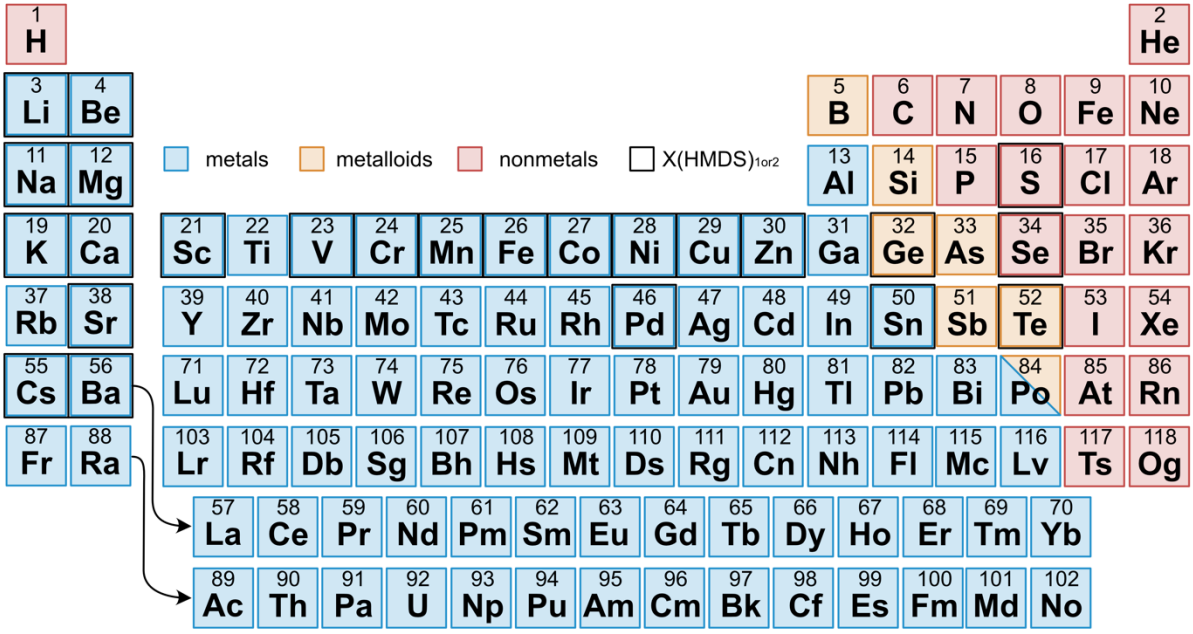

Figure 1.4. The periodic table of chemical elements with metals, metalloids, and nonmetals highlighted in different colours, and the element (X) with that forms $X(HMDS)_1$ or $X(HMDS)_2$ are depicted with a black outline.

1.3.2 Speciation of mono- and bimetallic amides

Monometallic amides often exist in various oligomeric forms due to the unique bonding capabilities of the nitrogen atom in the amido ligand.[107] This nitrogen atom carries a negative charge and possesses an additional lone pair, enabling two bonding modes. As such, it can act as i) terminal ligand bound to a single metal centre, or ii) form a three-centre two-electron bond, bridging two metal centres. These binding modes allow for the formation of dimeric, trimeric, tetrameric, as well as other oligomeric structures, as illustrated in Figure 1.5.

Oligomeric forms are particularly prevalent among alkali metals owing to their valence *s* orbitals, which are spherical and highly adaptable to various coordinating modes. Multiple oligomeric species may coexist in solution, necessitating a thorough speciation study to characterise them accurately. For transition metals, the situation is distinct due to the symmetry of the *d* orbitals, depending on the oxidation state of the metal (+1, +2, or +3). Transition metals in the +2 oxidation state are predominantly found in monomeric forms, though dimeric forms are also observed occasionally.[108] This thesis primarily focuses on transition metals in a M^{2+} oxidation state, along with main group metals in the same oxidation state.

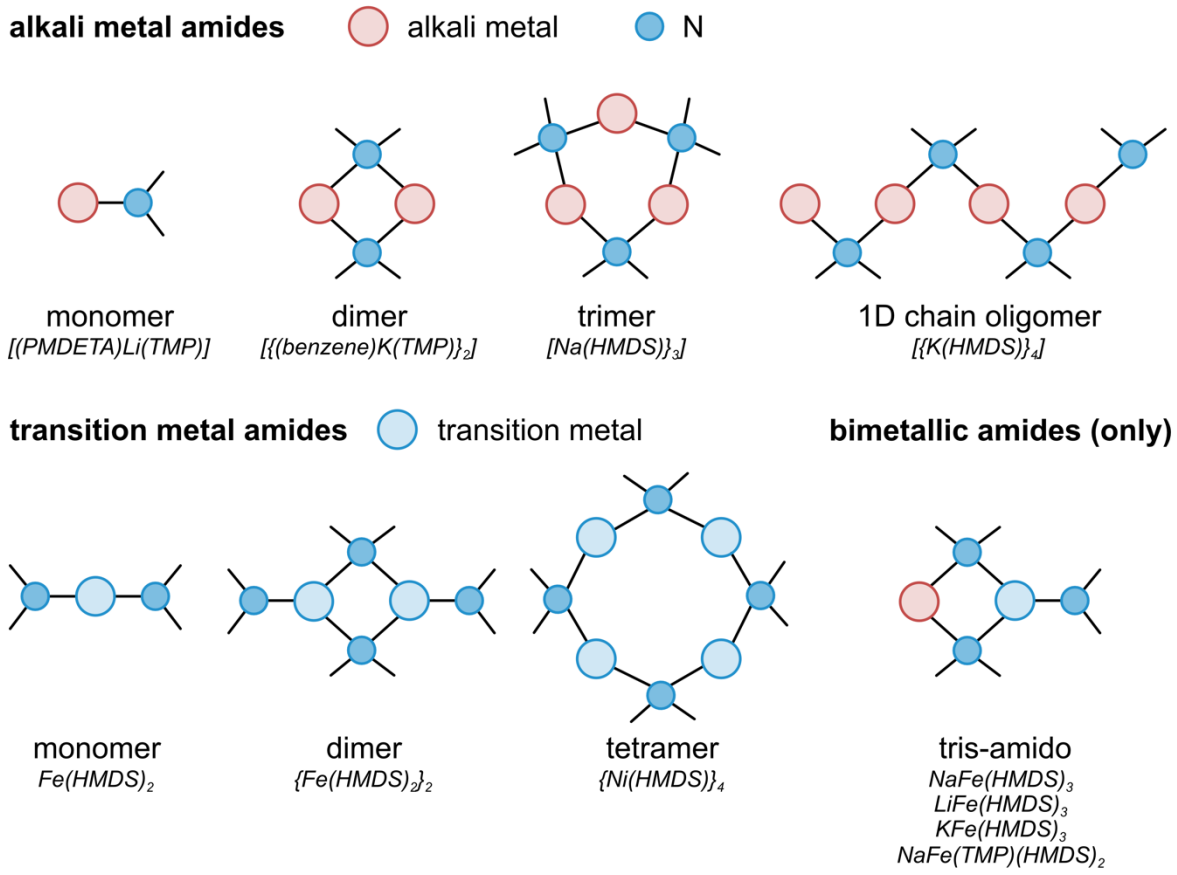

Figure 1.5. Common structures of metal amides, depicting alkali metal, transition metal, and bimetallic amides. The diagram highlights representative monomeric, dimeric, trimeric, tetrameric, and 1D oligomeric arrangements, as well as tris-amido bimetallic complexes, with examples provided for each structure. These variations emphasise the influence of the metal type and coordination environment on aggregation and reactivity.[107,109] (PMDETA = N,N,N′,N″,N″-pentamethyldiethylenetriamine, TMP = 2,4,6-trimethylpyridine)

When two monometallic amides are present together in solution, they can either exist as isolated monometallic species or form bimetallic complexes. These bimetallic reagents often adopt a tris-amido structure (Figure 1.5), although upon reacting with organic substrates, they may convert into other type of structures. The resulting configurations depend on both the size of the alkali metal and the preferred coordination geometry of the transition metal, which will be discussed for cobalt in Chapter 4 as an example.

1.3.3 Cooperativities in bimetallic systems

The importance of speciation lies in the different types of cooperativities observed in bimetallic processes, which can be classified into three main categories: i) bimetallic reagents, bimetallic active species. ii) monometallic reagents, bimetallic active species. iii) monometallic reagents, monometallic active species followed by transmetalation/co-complexation (Figure 1.6).

In the first case, the reagents are present as bimetallic species, either through bridging ligands, M–M bonds, or both. If a highly reactive M–M bond is present, it often reacts with a substrate (A–B) to cleave the bond and forms two M_1–A and M_2–B bonds[110] via oxidative addition. Alternatively, if the bimetallic complex is held together by bridging ligands, the reactivity depends on factors such as the proximity of the metal centres and the steric bulk of the ligands, which may affect the substrate's ability to approach the metal centres. In these cases, activation can occur via M–M bonds or through metal-ligand bonds.[111]

In the second case, monometallic reagents do not favour the formation of bimetallic complexes and instead exist as separate, independent species. This behaviour often arises from steric or coordination incompatibilities rather than solely from the bulkiness of the ligands.[112,113] When a substrate is introduced, the two monometallic reagents interact with the substrate at non neighbouring positions, with one playing an activation role and the other a stabilisation role to cleave the desired bond. However, this type of cooperativity incurs a higher entropy cost compared to the other types and is therefore rare. It often requires carefully planned experimental procedures, such as employing stepwise versus one-pot additions of the reagents and also controlling the order of reagent addition.

In the third type, the reagents prefer to remain as separate monometallic species. Here, one reagent cleaves the A–B bond of the substrate but cannot stabilise the resulting product, leading to reversion to the reactants or an equilibrium state. The second monometallic reagent does not assist in the activation process but acts as a spectating reagent. Once the A–B bond is cleaved, stabilisation of the product occurs through transmetalation or co-complexation with the spectating reagent.

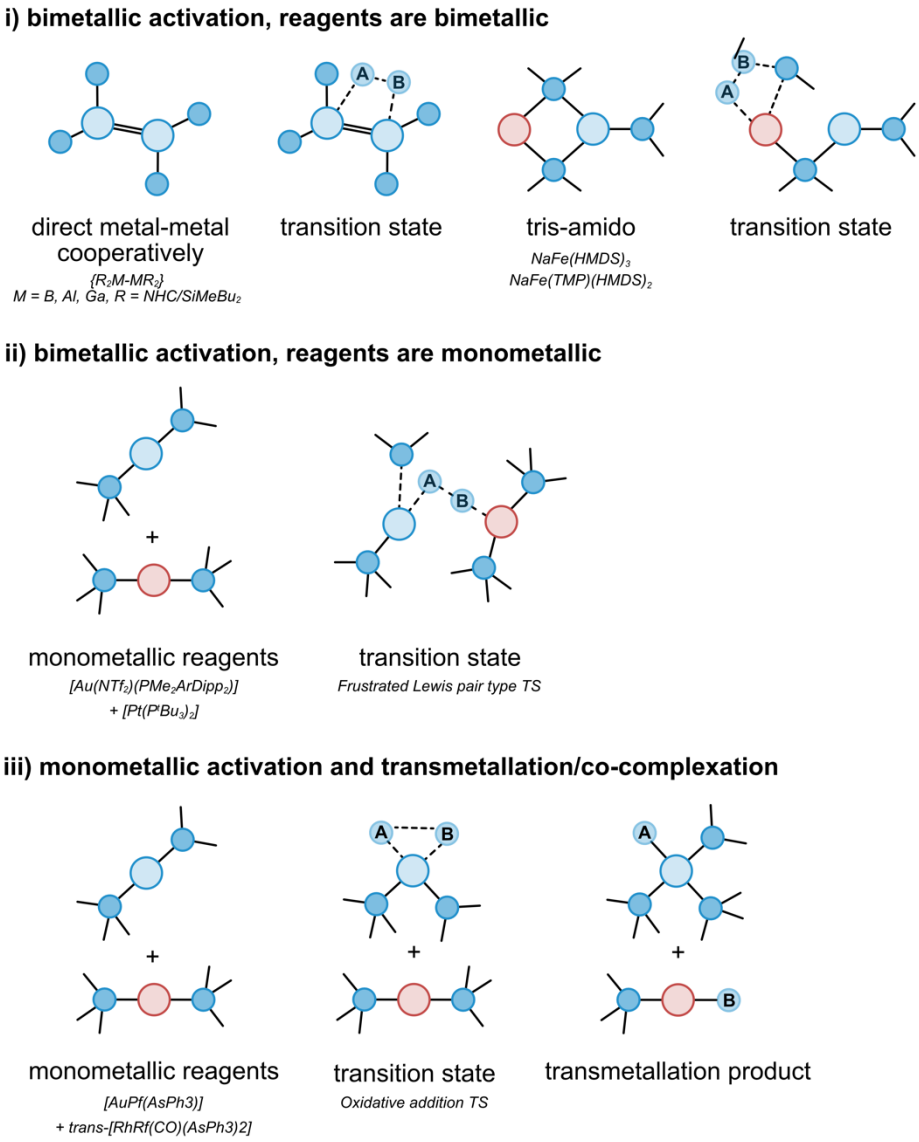

Figure 1.6. Mechanisms of bimetallic cooperativity with examples from the literature provided at the bottom for each type.

Lastly, it is important to note that the formation of co-complexation complexes does not always result in cooperativity, especially in monometallic oligomers. If the resulting dimeric or oligomeric complex diminishes the active features of the monometallic reagents without introducing new, more active structural characteristics, the reagents may exhibit no reactivity and hence the reaction may not occur. In such scenarios, the formation of unreactive dimers should be avoided, as discussed in Chapter 6.

1.3.4 Metal amide systems for C–H activation

Bimetallic C–H activation systems pair an alkali metal amide with a second metal (from the *d*-block or *p*-block) to create "ate" complexes or mixed-metal reagents. These reagents harness synergistic effects: the highly polar alkali metal can activate and polarise C–H bonds; while the second, less electropositive metal stabilises the resulting carbanion or directs product formation and further functionalisation reactivity. Such combinations, often formulated as $[M^1M^2(NR_2)_n]$, was proposed to operate via the CMD mechanism; however, the exact bimetallic coupling mechanism is case specific as discussed in the results chapters. Nonetheless, these systems have been shown to become more prominent for tackling substrates which were challenging for monometallic bases.[114]

Li/Mg- and Na/Mg-based amides exemplify how cooperative effects can be leveraged to enhance C–H metalation. The Knochel-Hauser base TMPMgCl·LiCl, though formally containing two metals, behaves like a monometallic magnesium amide augmented by LiCl,[115] whereas $[KMg(TMP)_2Bu]$ is a better representation of a truly heterobimetallic magnesiate. Mulvey and coworkers reported that this potassium magnesiate can deprotonate naphthalene, an unactivated aromatic, under mild conditions.[116] Remarkably, the product is an "inverse crown" cluster containing six [{$KMg(TMP)_2$(naphthalene)}] units, where each naphthalene has been selectively magnesiated at its C2 position.[117] The cooperation between K^+ and $Mg(TMP)_2^-$ is crucial. A comparable sodium magnesiate $[NaMg(TMP)_2Bu]$ displays different reactivity, executing a two-fold deprotonation of naphthalene to give a di-magnesiated aromatic dianion.[117] This striking divergence underscores how replacing the alkali metal can modulate both the extent and regioselectivity of metalation. From a synthetic perspective, alkali magnesiates enable metalations of sensitive aromatics that would otherwise require cryogenic lithiation. Mongin and others have exploited $Li/Mg(TMP)_2$ bases for regioselective deprotonation of azines and other heterocycles under much milder conditions than traditional bases.[118] A practical benefit of these mixed amides is their kinetic activation: the presence of two different cations often disrupts aggregation, increasing the effective basicity and solubility in hydrocarbon solvents. However, challenges remain. The reactivity of magnesiate bases can be too high, leading to polydeprotonation (as seen with NaMg on naphthalene) or difficulty in controlling stoichiometry.[119]

Organometallic bases containing Zn and an alkali metal, also known as “zincates”, have surged in popularity due to their unique blend of high basicity and mild nucleophilicity.[120,121] In a pioneering work, Mosrin and Knochel introduced TMPZnCl·LiCl as a selective base for direct C–H to Zn exchange on sensitive (hetero)arenes.[122] This lithium zincate cleanly deprotonates a wide range of polyfunctional aromatics at room temperature, tolerating groups like NO_2 or CHO that would be destroyed by alkyllithium reagents. The resulting aryl zinc intermediates can be subsequently converted to functionalised products via trapping with electrophiles or cross-coupling. The same authors also showed that aldehyde- and nitro-substituted aromatics could be metalated without incident using (TMP)Zn(Cl)·Li(Cl), expanding the scope of direct C–H metalation.[122] Building on this, Balkenhohl and Knochel developed a predictive model for site-selective deprotonation using (TMP)Zn(Cl)·Li(Cl), correlating calculated C–H acidities (pK_a) with observed metalation sites on fused heterocycles.[123] They demonstrated that subtle changes in substrate structure or base composition (e.g., mixing with $(TMP)_2Zn{\cdot}2Li(Cl)$ vs (TMP)Zn(Cl)·Li(Cl)) allow to target different C–H bonds in polyfunctional molecules with high selectivity.

Beyond being just stoichiometric reagents, alkali–zinc amides have also shown promise in catalytic regimes. A striking example is the tris(hexamethyldisilazide) potassium zincate, $[KZn(HMDS)_3]$. Mulvey et al. found that this heteroleptic K/Zn amide can directly metalate toluene at room temperature, abstracting a benzylic proton to form the zincate complex $[KZn(HMDS)_2(CH_2Ph)]$.[124] Neither KHMDS (a strong base) nor $Zn(HMDS)_2$ (a weaker base) could deprotonate toluene by itself, highlighting the synergistic effect of combining K and Zn. The resulting benzyl zincate catalyses the addition of benzylic C–H bonds to unsaturated molecules to allow C–C bond formation. In a newly developed reaction, this catalyst also serves as a catalyst for the addition of diarylmethane C–H bonds across styrenes and conjugated dienes, achieving intermolecular benzylic alkylation without any transition-metal catalyst.[125,126] The proposed mechanism involves the zincate deprotonating diphenylmethane to generate a diphenylmethyl zincate, which then adds to the styrene; the resulting new carbanion is protonated by another molecule of diphenylmethane, regenerating the active zincate. This cycle, essentially a base-catalysed coupling of a C(sp^3)–H bond with an alkene, is an unusual feat, enabled by the robust yet selective basicity of the K/Zn amide. Notably, no external oxidants or transition metals are needed, and the reactions proceed under mild conditions with good yields.

A very recent advance in zincates is the design of hybrid ligands to stabilise reactive intermediates. Hevia and co-workers reported a novel potassium–zinc amide incorporating both a bulky silyl-bis(amido) ligand and a sterically unhindered TMP ligand.[127] This "mixed-ligand" K/Zn zincate was engineered specifically for the regioselective metalation of fluoroarenes, a notoriously challenging substrate class due to the ease of side reactions (e.g. formation of aryllithium species that eliminates fluoride or rearranges).[128] The new base cleanly deprotonates fluoroarenes at positions ortho to fluorine, and crucially, the presence of the bulky silyl amide allows the intermediate fluoroaryl–Zn species to be trapped and characterised at low temperature.[127] This work provided the first direct structural evidence of an intermediate in Zn–H exchange on a fluoroarene. The ability to observe these intermediates shed light into the deprotonative mechanism and how the heteroleptic ligand framework avoids common decomposition pathways (e.g., benzyne formation). From an application standpoint, this K/Zn base enabled the regioselective functionalisation of a range of fluoroarenes under relatively mild conditions, showcasing how fine-tuning bimetallic amide structure translates to better selectivity in complex molecule synthesis. The direct generation of fluoroaryl zinc intermediates, which can be subsequently coupled to form products valuable in pharmaceutical chemistry. The broader lesson from zincates is that combining an alkali metal with zinc strikes an effective balance: the alkali component enhances the base's brute force, while the zinc tames the carbanion's reactivity and opens pathways (like transition-metal coupling or one-pot multi-step sequences) that simple alkali amides alone would not allow.

Bimetallic combinations of alkali metals with *p*-block metals in low oxidation states can exhibit unusual reactivity, especially for C–H activation. A breakthrough in this area was the discovery of nucleophilic Al(I) complexes stabilised by potassium, so-called "aluminyl" reagents. Aldridge and co-workers reported a crystalline potassium aluminyl complex, $K_2[Al(NON)]_2$ (NON = bis(amido)xanthene ligand), which behaves as a nucleophilic Al^- species.[129] This K–Al(I) reagent directly adds across the C–H bond of benzene as a formal oxidative addition pathway, forming a potassium phenyl aluminate in which aluminum is oxidised to Al(III). In a related system, Harder and co-workers synthesised a K-stabilised aluminyl that can doubly insert into benzene, breaking two C–H bonds to yield a 1,4-dimetalated product.[130] If potassium is masked, this reagent only performs a single C–H activation, underscoring potassium's role in enabling more extensive activation by coordinating to the aromatic ring and providing stabilisation. While the applications of these K–Al systems are still at an early stage, they hint at new opportunities in C–H activation.[116]

Gallium, being a congener of aluminium, has similarly been used in "trans-metal-trapping" strategies. A combination of LiTMP with $Ga(CH_2SiMe_3)_3$ cleanly metalates challenging azines, with gallium coordinating and stabilising the anionic intermediates that would otherwise decompose if left as organolithiums.[131] These Li/Ga tandem systems achieve the functional equivalent of a bimetallic base. The LiTMP deprotonates the substrate and the organogallium then catches the anion, preventing side reactions. Such advances illustrate how *p*-block metals like Al or Ga can partner with alkali amides to broaden the scope of C–H deprotonation to substrates previously considered "unlithiable." The current limitations of these systems include the need for specialised bulky ligands (to stabilise low-valent Al or Ga) and sometimes non-trivial synthesis of the reagents. Moreover, their reactivity can be extreme, the benzene C–C bond cleavage by K–aluminyl, for instance, while fascinating, underscores the challenge of controlling these potent reagents.

Mixed alkali/transition-metal bases have become the focus in more recent times, as well as the centre of the work outlined in this thesis. Pairings of alkali metals with *d*-block metals in amide ligands have enabled new C–H activation modes, often termed "ferration" when involving iron. A representative example is an intramolecularly sodium-mediated iron amide reported by Maddock et al. in 2021.[132] This heterobimetallic complex contained an Fe(II) centre and a pendant Na^+ linked via an amido ligand. The Na–Fe cooperation facilitated the deprotonation of an aromatic ring bound to iron, effectively, sodium "assisted" iron in abstracting a C–H to form a sodiated intermediate, followed by sequential transmetalation to yield a new Fe–C bond.[133] The presence of sodium was crucial to achieve this C–H activation; without it, the iron amide complex alone could not sufficiently polarise the C–H bond. Such Na/Fe amido systems represent a bridge between traditional base-induced metalation and transition-metal C–H activation, as have been improved to perform catalytic C–C coupling reactions, however with the Na fragment being a sacrificial reagent.[134] Similarly, alkali–cobalt or alkali–manganese amide reagents have been explored: a lithium–cobalt TMP base was shown to metalate specific aromatic frameworks that neither lithium nor cobalt alone could effectively deprotonate. These early studies hint at a wide unexplored territory of bimetallic bases involving non-innocent transition metals.

Bimetallic amide reagents significantly expand C–H deprotonation methods, enabling selective metalation of otherwise difficult substrates. They often offer higher functional group tolerance, regioselectivity, and even catalytic turnover compared to monometallic bases. However,

challenges such as stability and handling still persist. Selectivity control is another challenge, as the synergy of two metals can lead to unintended reactions like poly-metalation or β-hydride elimination. In some cases, external ligands or fine-tuning (such as introduction of donor ligands) are needed to prevent side reactions and multi-functionalisation. Functional group tolerance remains a concern, as powerful bases can deprotonate unintended acidic sites, requiring protection. Catalytic applications also face challenges in turnover and compatibility with other reagents, with certain systems being sensitive to deactivating substituents. Despite these limitations, during the period of this thesis work there has been significant progress from both experimental and computational efforts with some contribution from the published work in this thesis. The optimisation of monometallic amides led to the establishment of donor induced reactive monomers and bimetallic amides, which unlock new reactivity for C–H metalation and catalytic transformations.

Advancements in this topic are currently focusing on improving reagent stability and usability, such as developing one-pot catalytic cycles or well-defined bimetallic complexes to prevent mixing issues. We hope the mechanistic studies reported in this thesis, as well as other experimental and computational works, will continue to help in understanding the cooperativity between two metals and amide ligands and guide the future design of more efficient systems. The field of cooperative bimetallic C–H activation, once a niche, is now expanding, offering a promising future of strong-base chemistry under mild conditions.

References

1. IUPAC Compendium of Chemical Terminology, 5th ed.; International Union of Pure and Applied Chemistry: 2025. Online version 5.0.0, 2025. https://doi.org/10.1351/goldbook.O04328.
2. R. Hoffmann, *Angew. Chem. Int. Ed.* **1982**, *21*, 711–724.
3. N. Miyaura, A. Suzuki, *Chem. Rev.* **1995**, *95*, 2457–2483.
4. V. Farina, *Org. Process Res. Dev.* **2023**, *27*, 831–846.
5. S. Gutiérrez, M. Tomás-Gamasa, J. L. Mascareñas, *Chem. Sci.* **2022**, *13*, 6478–6495.
6. J. van Brussel, L. Que, Jr., *Acc. Chem. Res.* **2018**, *51*, 2115–2124.
7. P. Gotico, Z. Halime, W. Leibl, A. Aukauloo, *ChemPlusChem* **2023**, *88*, e202300222.
8. N. G. Connelly, W. E. Geiger, *Chem. Rev.* **1996**, *96*, 877–910.
9. G. J. Kubas, *Chem. Rev.* **2007**, *107*, 4152–4205.
10. T. Graham, B. Graham, A. Bunsen, *A History of Chemistry*; Palgrave: London, 1964; Chapter IX.
11. L. B. Hunt, *Platin. Met. Rev.* **1984**, *28*, 76.
12. a) P. Morris, *Endeavour* **1989**, *13* (1), 34–40; b) E. Abel, *J. Organomet. Chem.* **1990**, *383* (1–3), 11–20; c) W. A. Herrmann, *J. Organomet. Chem.* **1990**, *383* (1–3), 21–44.
13. P. W. Jolly, G. Wilke, *The Organic Chemistry of Nickel: Organonickel Complexes*; Academic Press: New York, 1974; Chapter I.
14. S. S. Rossander, C. S. Marvel, *J. Am. Chem. Soc.* **1928**, *50*, 1491.
15. C. S. Marvel, F. D. Hager, D. D. Coffman, *J. Am. Chem. Soc.* **1927**, *49*, 2323.
16. D. J. Cardin, B. Cetinkaya, M. F. Lappert, *Chem. Rev.* **1972**, *72*, 545–574.
17. F. R. Kreißl, *Transition Metal Carbyne Complexes*; Springer Science & Business Media: 1993; pp. 1–268.
18. H. Werner, *Angew. Chem. Int. Ed.* **2012**, *51*, 6052–6058.
19. M. F. Semmelhack, G. R. Clark, J. L. Garcia, J. J. Harrison, Y. Thebtaranonth, W. Wulff, A. Yamashita, *Tetrahedron* **1981**, *37*, 3957–3965.
20. H. Wang, Q. Du, Y. Xie, R. B. King, H. F. Schaefer III, *J. Organomet. Chem.* **2010**, *695*, 215–225.
21. C. C. Romão, L. F. Veiros, *Organometallics* **2007**, *26*, 1777–1781.
22. F. R. Hartley, S. Patai, *The Chemistry of the Metal Carbon Bond*, Vol. 2: The Nature and Cleavage of Metal-Carbon Bonds; Wiley: 1985; Chapters 1 and 10.
23. K. M. Korch, D. A. Watson, *Chem. Rev.* **2019**, *119*, 8192–8228.
24. S. K. Sinha, P. Ghosh, S. Jain, S. Maiti, S. A. Al-Thabati, A. A. Alshehri, M. Mokhtar, D. Maiti, *Chem. Soc. Rev.* **2023**, *52*, 7461–7503.
25. J. H. Docherty, T. M. Lister, G. McArthur, M. T. Findlay, P. Domingo-Legarda, J. Kenyon, S. Choudhary, I. Larrosa, *Chem. Rev.* **2023**, *123*, 7692–7760.
26. N. Kuhl, M. N. Hopkinson, J. Wencel-Delord, F. Glorius, *Angew. Chem. Int. Ed.* **2012**, *51*, 10236–10254.
27. D. J. C. Constable, P. J. Dunn, J. D. Hayler, G. R. Humphrey, J. L. Leazer, Jr., R. J. Linderman, K. Lorenz, J. Manley, B. A. Pearlman, A. Wells, A. Zaksh, T. Y. Zhang, *Green Chem.* **2007**, *9*, 411–420.
28. K. Chojnacka, *Curr. Opin. Green Sustainable Chem.* **2024**, *46*, 100898.
29. J. T. Blaskovits, M. Leclerc, *Macromol. Rapid Commun.* **2019**, *40*, 1800512.
30. Chemistry Steps database: https://www.chemistrysteps.com/pka-acid-strength-organic-chemistry/ (accessed Jan 2025).
31. W. He, D. D. Beattie, H. Zhou, E. G. Bowes, L. L. Schafer, J. A. Love, P. Kennepohl, *Chem. Sci.* **2021**, *12*, 15298.
32. K. M. Altus, J. A. Love, *Commun. Chem.* **2021**, *4*, 173.

33. L. Vaska, *Science* **1963**, *140* (3568), 809–810.
34. a) A. H. Janowicz, R. G. Bergman, *J. Am. Chem. Soc.* **1982**, *104*, 352. b)
35. J. K. Hoyano, W. A. G. Graham, *J. Am. Chem. Soc.* **1982**, *104*, 3723.
36. R. L. Carvalho, G. G. Dias, C. L. M. Pereira, P. Ghosh, D. Maiti, E. N. da Silva Júnior, *J. Braz. Chem. Soc.* **2021**, *32* (5), 917–952.
37. S. Deolka, O. Rivada-Wheelaghan, S. L. Aristizábal, R. R. Fayzullin, S. Pal, K. Nozaki, E. Khaskin, J. R. Khusnutdinova, *Chem. Sci.* **2020**, *11*, 5494.
38. T. Bhattacharya, S. Dutta, D. Maiti, *ACS Catal.* **2021**, *11* (15), 9702–9714.
39. D. Lapointe, K. Fagnou, *Chem. Lett.* **2010**, *39* (11), 1118–1126.
40. V. Ritleng, C. Sirlin, M. Pfeffer, *Chem. Rev.* **2002**, *102* (5), 1731–1770.
41. R. J. Burford, A. Yeo, M. D. Fryzuk, *Coord. Chem. Rev.* **2017**, *334*, 84–99.
42. T. W. Lyons, M. S. Sanford, *Chem. Rev.* **2010**, *110*, 1147.
43. D. L. Davies, S. A. Macgregor, C. L. McMullin, *Chem. Rev.* **2017**, *117* (13), 8649–8709.
44. Y. Park, Y. Kim, S. Chang, *Chem. Rev.* **2017**, *117* (13), 9247–9301.
45. J. Martínez-Laguna, J. Altarejos, M. Á. Fuentes, G. Sciortino, F. Maseras, J. Carreras, A. Caballero, P. J. Pérez, *J. Am. Chem. Soc.* **2024**, *146*, 34014.
46. H. Fujisaki, T. Ishizuka, H. Kotani, Y. Shiota, K. Yoshizawa, T. Kojima, *Nature* **2023**, *616*, 476.
47. X. Chen, K. M. Engle, D. H. Wang, J. Q. Yu, *Angew. Chem. Int. Ed.* **2009**, *48* (2), 5094–5115.
48. S. Chen, Y. Yang, C. Chen, C. Wang, *Chinese J. Org. Chem.* **2023**, *43* (1), 1–16.
49. S. Li, L. Cai, H. Ji, et al., *Nat. Commun.* **2016**, *7*, 10443.
50. A. Mondal, M. Díaz-Ruiz, F. Deufel, F. Maseras, M. van Gemmeren, *Chem* **2023**, *9* (4), 1004–1016.
51. G. Chen, W. Gong, Z. Zhuang, M. S. Andrä, Y.-Q. Chen, X. Hong, Y.-F. Yang, T. Liu, K. N. Houk, J.-Q. Yu, *Science* **2016**, *353* (6303), 1023–1027.
52. M. Wasa, K. M. Engle, D. W. Lin, E. J. Yoo, J.-Q. Yu, *J. Am. Chem. Soc.* **2011**, *133* (49), 19598–19601.
53. J. Joy, T. D. Demina, A. K. Durgi, A. Vijayan, *RSC Adv.* **2025**, *15*, 11065–11084.
54. M. A. Larsen, S. H. Cho, J. Hartwig, *J. Am. Chem. Soc.* **2016**, *138* (3), 762–765.
55. R. Oeschger, B. Su, I. Yu, C. Ehinger, E. Romero, S. He, J. F. Hartwig, *Science* **2020**, *368* (6492), 736–741.
56. R. J. Oeschger, M. A. Larsen, A. Bismuto, J. F. Hartwig, *J. Am. Chem. Soc.* **2019**, *141* (41), 16479–16485.
57. M. A. Larsen, R. J. Oeschger, J. F. Hartwig, *ACS Catal.* **2020**, *10*, 3415–3424.
58. O. Inoue, Y. Sato, Y. Nagashima, K. Tanaka, *ACS Catal.* **2025**, *15*, 4061–4068.
59. F. J. Lombard, M. J. Coster, *Org. Biomol. Chem.* **2015**, *13*, 6419–6431.
60. D. J. Timmons, M. P. Doyle, Chiral Dirhodium(II) Catalysts and Their Applications. In: F. A. Cotton, C. A. Murillo, R. A. Walton, *Multiple Bonds Between Metal Atoms*; Springer: Boston, MA, 2005; pp. 185–201.
61. D. T. Ahneman, A. G. Doyle, *Chem. Sci.* **2016**, *7*, 7002–7006.
62. Y. Hu, C. Wang, *Acta Physico-Chim. Sin.* **2019**, *35* (9), 913–922.
63. T. Yoshino, S. Matsunaga, *Adv. Synth. Catal.* **2017**, *359* (8), 1245–1262.
64. S. S. Bera, M. S. Maji, *Org. Lett.* **2020**, *22* (7), 2615–2620.
65. J. Lee, U. von Gunten, J.-H. Kim, *Environ. Sci. Technol.* **2020**, *54* (6), 3064–3081.
66. G. Williams, Cobalt Market Update: Q1 2025 in Review. *Investing News Network*, Apr 9, 2025. https://investingnews.com/daily/resource-investing/battery-metals-investing/cobalt-investing/cobalt-forecast/.

67. P. Devitt, Rhodium prices to outperform platinum and palladium in 2025, *Kitco News*, May 19, 2025. https://www.kitco.com/news/off-the-wire/2025-05-19/rhodium-prices-outperform-platinum-and-palladium-2025-metals-focus.
68. K. Ozols, Y.-S. Jang, N. Cramer, *J. Am. Chem. Soc.* **2019**, *141* (14), 5675–5680.
69. C.-J. Wu, J.-J. Zhong, Q.-Y. Meng, T. Lei, X.-W. Gao, C.-H. Tung, L.-Z. Wu, *Org. Lett.* **2015**, *17* (4), 884–887.
70. Q. Li, W. Hu, R. Hu, H. Lu, G. Li, *Org. Lett.* **2017**, *19* (17), 4676–4679.
71. H. Lu, V. Subbarayan, J. Tao, X. P. Zhang, *Organometallics* **2010**, *29* (2), 389–393.
72. V. Lyaskovskyy, A. I. Olivos Suarez, H. Lu, H. Jiang, X. P. Zhang, B. de Bruin, *J. Am. Chem. Soc.* **2011**, *133* (31), 12264–12273.
73. R. Singh, A. Mukherjee, *ACS Catal.* **2019**, *9* (4), 3604–3617.
74. P. Knochel, D. Ziegler, *Synfacts* **2018**, *14* (10), 1074.
75. W. Liu, L. Ackermann, *ACS Catal.* **2016**, *6* (6), 3743–3752.
76. R. Cano, K. Mackey, G. P. McGlacken, *Catal. Sci. Technol.* **2018**, *8*, 1251–1266.
77. Y. Hu, B. Zhou, C. Wang, *Acc. Chem. Res.* **2018**, *51* (3), 816–827.
78. J. M. Pérez, R. Postolache, M. Castiñeira Reis, E. G. Sinnema, D. Vargová, F. de Vries, E. Otten, L. Ge, S. R. Harutyunyan, *J. Am. Chem. Soc.* **2021**, *143* (48), 20071–20076.
79. M. Milan, M. Bietti, M. Costas, *ACS Cent. Sci.* **2017**, *3* (3), 196–204.
80. A. M. Zima, D. E. Babushkin, O. Y. Lyakin, K. P. Bryliakov, E. P. Talsi, *ChemCatChem* **2022**, *14* (2), e202101430.
81. A. M. Zima, O. Y. Lyakin, A. A. Bryliakova, D. E. Babushkin, K. P. Bryliakov, E. P. Talsi, *The Chem. Rec.* **2022**, *22* (5), e202100334.
82. N. Holmberg-Douglas, D. A. Nicewicz, *Chem. Rev.* **2021**, *122* (2), 1925–2016.
83. A. M. Zima, O. Y. Lyakin, R. V. Ottenbacher, K. P. Bryliakov, E. P. Talsi, *ACS Catal.* **2016**, *6* (8), 5399–5404.
84. M. A. Bigi, P. Liu, L. Zou, K. N. Houk, M. C. White, *Synlett* **2012**, *23* (19), 2768–2772.
85. C.-L. Sun, B.-J. Li, Z.-J. Shi, *Chem. Rev.* **2011**, *111* (3), 1293–1314.
86. W. Du, L. Tian, J. Lai, X. Huo, X. Xie, X. She, S. Tang, *Org. Lett.* **2014**, *16* (9), 2470–2473.
87. A. Lachguar, A. V. Pichugov, T. Neumann, Z. Dubrawski, C. Camp, *Dalton Trans.* **2024**, *53*, 1393–1409.
88. S. Tang, O. Eisenstein, Y. Nakao, S. Sakaki, *Organometallics* **2017**, *36* (15), 2761–2771.
89. J.-H. Chen, Q.-J. Yao, M.-Y. Zhong, T.-Y. Jiang, F.-R. Huang, X. Li, B.-F. Shi, *ACS Cent. Sci.* **2025**, *11* (1), 127–135.
90. H. Lin, D. Sun, *New J. Org. Synth.* **2013**, *45* (5), 342.
91. J.-Q. Chen, J.-H. Li, Z.-B. Dong, *Adv. Synth. Catal.* **2020**, *362* (16), 3311–3331.
92. K. M. Byrne, S. D. Robertson, R. E. Mulvey, T. Krämer, *ChemCatChem* **2024**, *16* (19), e202400655.
93. P. A. Macdonald, A. R. Kennedy, C. E. Weetman, et al., *Commun. Chem.* **2024**, *7*, 94.
94. D. H. Woen, G. P. Chen, J. W. Ziller, T. J. Boyle, F. Furche, W. J. Evans, *Angew. Chem. Int. Ed.* **2017**, *56*, 2050.
95. Y.-F. Deng, T. Han, Z. Wang, Z. Ouyang, B. Yin, Z. Zheng, J. Krzysteke, Y.-Z. Zheng, *Chem. Commun.* **2015**, *51*, 17688.
96. D. C. Bradley, M. B. Hursthouse, A. A. Ibrahim, K. M. Abdul Malik, M. Motevalli, R. Möseler, H. Powell, J. D. Runnacles, A. C. Sullivan, *Polyhedron* **1990**, *9*, 2959.
97. M. Faust, A. M. Bryan, A. Mansikkamäki, P. Vasko, M. M. Olmstead, H. M. Tuononen, F. Grandjean, G. J. Long, P. P. Power, *Angew. Chem. Int. Ed.* **2015**, *54*, 12914.
98. J. P. Coyle, E. R. Sirianni, I. Korobkov, G. P. A. Yap, G. Dey, S. T. Barry, *Organometallics* **2017**, *36*, 2800.

99. D. Naglav, A. Neumann, D. Bläser, C. Wölper, R. Haack, G. Jansena, S. Schulz, *Chem. Commun.* **2015**, *51*, 3889.
100. H. Phull, D. Alberti, I. Korobkov, S. Gambarotta, P. H. M. Budzelaar, *Angew. Chem. Int. Ed.* **2006**, *45*, 5331.
101. L. T. Wendell, J. Bender, X. He, B. C. Noll, K. W. Henderson, *Organometallics* **2006**, *25*, 4953.
102. B. A. Vaartstra, J. C. Huffman, W. E. Streib, K. G. Caulton, *Inorg. Chem.* **1991**, *30*, 121.
103. T. Fjeldberg, H. Hope, M. F. Lappert, P. P. Power, A. J. Thorne, *J. Chem. Soc., Chem. Commun.* **1983**, *11*, 639.
104. R. W. Chorley, P. B. Hitchcock, M. F. Lappert, W.-P. Leung, P. P. Power, M. M. Olmstead, *Inorganica Chim. Acta* **1992**, *198*, 203.
105. G. Wolmershauser, C. R. Brulet, G. B. Street, *Inorg. Chem.* **1978**, *17*, 3586.
106. J. Bresien, C. Hering-Junghans, P. Kumm, A. Schulz, M. Thomas, A. Villinger, *Eur. J. Inorg. Chem.* **2018**, *2018*, 647.
107. M. Lappert, A. Protchenko, P. P. Power, A. Seeber, *Metal Amide Chemistry*; Wiley: UK, 2014; Chapters 2 and 6.
108. H. E. Bryndza, W. Tam, *Chem. Rev.* **1988**, *88*, 1163–1188.
109. A. Logallo, E. Hevia, *Chimia* **2022**, *76*, 336.
110. C. C. Carter, T. R. Cundari, *Polyhedron* **2022**, *219*, 115797.
111. T. Miyazawa, T. Suzuki, Y. Kumagai, K. Takizawa, T. Kikuchi, S. Kato, A. Onoda, T. Hayashi, Y. Kamei, F. Kamiyama, M. Anada, M. Kojima, T. Yoshino, S. Matsunaga, *Nat. Catal.* **2020**, *3*, 851.
112. A. Lachguar, A. V. Pichugov, T. Neumann, Z. Dubrawski, C. Camp, *Dalton Trans.* **2024**, *53*, 1393.
113. J. Campos, *J. Am. Chem. Soc.* **2017**, *139*, 2944.
114. a) M. Uchiyama, T. Miyoshi, Y. Kajihara, T. Sakamoto, Y. Otani, T. Ohwada, Y. Kondo, *J. Am. Chem. Soc.* **2002**, *124*, 8514.; b) S. Wunderlich, P. Knochel, *Angew. Chem., Int. Ed.* **2007**, *46*, 7685.; c) M. Mosrin, P. Knochel, *Org. Lett.* **2009**, *11*, 1837.
115. M. Baenziger, S. Eswaran, Y. Jiang, G. Kasinathan, *Synthesis* **2019**, *51* (7), 1649–1654.
116. J. M. Gil-Negrete, E. Hevia, *Chem. Sci.* **2021**, *12*, 1982–1992.
117. A. J. Martínez-Martínez, D. R. Armstrong, B. Conway, B. J. Fleming, J. Klett, A. R. Kennedy, R. E. Mulvey, S. D. Robertson, C. T. O'Hara, *Chem. Sci.* **2014**, *5*, 771–781.
118. a) M. Mosrin, P. Knochel, *Org. Lett.* **2009**, *11*, 1837–1840; b) K. Groll, S. M. Manolikakes, X. M. du Jourdin, M. Jaric, A. Bredihhin, K. Karaghiosoff, T. Carell, P. Knochel, *Angew. Chem. Int. Ed.* **2013**, *52*, 6776–6780; *Angew. Chem.* **2013**, *125*, 6909–6913; c) Z. Dong, G. C. Clososki, S. H. Wunderlich, A. Unsinn, J. Li, P. Knochel, *Chem. Eur. J.* **2009**, *15*, 457–468.
119. D. R. Armstrong, A. R. Kennedy, R. E. Mulvey, J. A. Parkinson, S. D. Robertson, *Chem. Sci.* **2012**, *3*, 2700–2707.
120. P. Mastropierro, Z. Livingstone, S. D. Robertson, A. R. Kennedy, E. Hevia, *Organometallics* **2020**, *39* (23), 4273–4281.
121. Y.-F. Liu, D.-D. Zhai, X.-Y. Zhang, B.-T. Guan, *Angew. Chem. Int. Ed.* **2018**, *57* (27), 8245–8249.
122. M. Mosrin, P. Knochel, *Org. Lett.* **2009**, *11* (8), 1837–1840.
123. V. Dhayalan, V. S. Dodke, M. P. Kumar, H. S. Korkmaz, A. Hoffmann-Röder, P. Amaladass, R. Dandela, R. Dhanusuraman, P. Knochel, *Chem. Soc. Rev.* **2024**, *53*, 11045–11099.
124. W. Clegg, G. C. Forbes, A. R. Kennedy, R. E. Mulvey, S. T. Liddle, *Chem. Commun.* **2003**, 406–407.

125. L. Davin, A. Hernán-Gómez, C. McLaughlin, A. R. Kennedy, R. McLellan, E. Hevia, *Dalton Trans.* **2019**, *48*, 8122–8130.
126. C. C. Bao, Y. L. Luo, H. Z. Du, et al., *Sci. China Chem.* **2021**, *64*, 1349–1354.
127. P. Mastropierro, A. R. Kennedy, E. Hevia, *Chem. Commun. (Camb.)* **2022**, *58* (34), 5292–5295.
128. L. Gupta, A. C. Hoepker, K. J. Singh, D. B. Collum, *J. Org. Chem.* **2009**, *74*, 2231.
129. a) J. Hicks, P. Vasko, J. M. Goicoechea, S. Aldridge, *Nature* **2018**, *557*, 92; b) J. Hicks, P. Vasko, J. M. Goicoechea, S. Aldridge, *J. Am. Chem. Soc.* **2019**, *141*, 1100.
130. S. Grams, J. Eyselein, J. Langer, C. Färber, S. Harder, *Angew. Chem. Int. Ed.* **2020**, *59*, 15982.
131. M. Uzelac, A. R. Kennedy, E. Hevia, R. E. Mulvey, *Angew. Chem. Int. Ed.* **2016**, *55*, 1–5.
132. L. C. H. Maddock, T. Cadenbach, A. R. Kennedy, I. Borilovic, G. Aromí, E. Hevia, *Inorg. Chem.* **2015**, *54* (18), 9201–9210.
133. L. C. H. Maddock, M. Mu, A. R. Kennedy, M. García-Melchor, E. Hevia, *Angew. Chem. Int. Ed.* **2021**, *133* (28), 15424–15429.
134. I. Takahashi, A. Tortajada, D. E. Anderson, et al., Iron-catalysed direct coupling of organosodium compounds, *Nat. Synth.* **2025**, https://doi.org/10.1038/s44160-025-00771-1.

Chapter 2
Computational theory

The electron is a theory we use; it is so useful in understanding the way nature works that we can almost call it real.
– Richard P. Feynman

2.1 Fundamentals of quantum chemistry

Theoretical chemistry focuses on developing methods to describe molecules, atoms, and electrons in ways that enable the prediction of chemical behaviour and reactivity of complexes.

The field has evolved significantly, from simple, intuitive models to sophisticated quantum mechanical descriptions of matter. The simplest representation is the Lewis structure, which treats electrons as discrete particles, existing either in pairs or alone, and shared or transferred between atoms to form covalent or ionic bonds. Atoms act as hubs where valence electrons in the outermost shell interact, striving for stable configurations, such as achieving an octet. Molecules are depicted as 2D arrangements of atoms connected by bonds, an oversimplified yet powerful model for predicting structure and reactivity, which remains widely used today.

Building on this foundation, molecular orbital (MO) theory provides a more nuanced perspective. In this approach, electrons are delocalised and occupy molecular orbitals formed from the overlap of atomic orbitals in the outermost shell. MO theory explains phenomena such as bond order, paramagnetism, and delocalisation in aromatic systems. It treats molecules as quantum systems with molecular orbitals that exhibit discrete energy levels, rather than merely as collections of atoms.

2.1.1 Descriptions of molecule, atom, and electron

The advent of quantum mechanics revolutionised our understanding of electrons, revealing their wave-particle duality: electrons exhibit properties of both waves and particles. Electrons are now described as quantum entities governed by the Schrödinger equation (Section 2.1.2), with wavefunctions (Ψ) characterising their probabilistic behaviour. MOs are solutions to the Schrödinger equation for molecules, and these solutions correspond to discrete energy levels. However, the exact location of electrons cannot be precisely determined. Instead of following fixed paths, the square of the wavefunction ($|\Psi|^2$) represents the probability density of finding an electron in a given region of space. Molecules are represented by molecular wavefunctions that describe the distribution and energy of electrons.

Electron density has since emerged as a unifying concept in modern computational chemistry. As a measurable, experimentally observable quantity, electron density bridges classical and quantum perspectives, visualising electrons as overlapping probability clouds that influence molecular properties such as reactivity and intermolecular forces. Density Functional Theory (DFT), a cornerstone method in quantum chemistry, refines this understanding by analysing electron density and MOs. This complex view can then be simplified into more interpretable representations, such as Lewis structures or other reactivity descriptors. DFT provides a comprehensive framework for exploring the behaviour of atoms, electrons, and molecules.

2.1.2 The Schrödinger equation

The earliest method to predict the behaviour of particles in a quantum system was introduced in 1926 when Schrödinger proposed that "*all the information about a quantum system is contained in the system's wavefunction (Ψ)*".[1] To determine the energy of the system,

Schrödinger developed an equation based on the classical Hamiltonian, adapting it to quantum mechanics by replacing classical variables with quantum operators. This approach also incorporated the wave-like nature of electrons through wavefunctions, reflecting de Broglie's concept of wave-particle duality. The equation satisfied key criteria: it conserved energy, explained the quantised energy levels observed in atomic spectra, and aligned with Heisenberg's matrix mechanics. Furthermore, it was linear, time-reversible, and provided a foundation for understanding atomic orbitals and complex quantum systems.

This is translated into the Equation 2.1 shown below,[2] which describes the total energy (E) of a chemical system of j electrons and l nucleus with atomic numbers (Z_l).

$$\left(-\sum_i \frac{\hbar^2}{2m_e}\nabla_i^2 - \sum_k \frac{\hbar^2}{2m_N}\nabla_k^2 - \sum_i \sum_k \frac{e^2 Z_k}{r_{ik}} + \sum_{i<j} \frac{e^2}{r_{ij}} + \sum_{k<l} \frac{e^2 Z_k Z_l}{r_{kl}}\right)\Psi = E\Psi \qquad (2.1)$$

Here, $\hbar$ is Planck's constant divided by 2π, m_e represents the mass of an electron, ∇^2 is the Laplacian operator, e denotes the charge of an electron, and r is the distance between electrons and/or nuclei. However, solving Schrödinger's equation for multielectron systems is both computationally challenging and time consuming due to the well-known *three body (or many body) problem*. This difficulty motivated the development of alternative theories and methods that simplify solving Schrödinger's equation through assumptions and approximations.

The variation principle states that for any trial wavefunction (Ψ_{trial}), the expectation value of the Hamiltonian (E_{trial}), serves as an upper bound for the true ground-state energy (E_0). By minimising E_{trial}, one can iteratively approach E_0. This principle emerges because the trial wavefunction can be expressed as a linear combination of the system's eigenfunctions, and the ground state contributes the minimum energy. The variation principle ensures that the calculated energy cannot be lower than the true ground-state energy, and it simplifies the complex problem of finding exact solutions into a minimisation problem.

2.1.3 The Born-Oppenheimer approximation

Another key approximation that significantly accelerates calculations is the Born-Oppenheimer approximation. This approximation leverages the fact that nuclei move much more slowly

compared to electrons due to their significantly greater mass. As a result, when considering the movement of electrons, the nuclei can be approximated as stationary, with fixed positions. This simplification allows the focus to remain on the behaviour of electrons, which primarily govern chemical reactivity, while treating the properties associated with nuclei as constant potentials.[3] Beyond its physical interpretation, the Born-Oppenheimer approximation also showcases the advantages of describing electrons using wavefunctions. Specifically, it enables the wavefunction to be factorised, simplifying the Schrödinger equation into two separate terms: one for the electronic wavefunction (Ψ_{ele}) at fixed nuclear positions and the other for the nuclear wavefunction (Ψ_{nuc}). In this framework, the energy of the electronic wavefunction acts as a potential energy term for the nuclear wavefunction.

$$\Psi_{tot}(R,r) = \Psi_{ele}(R,r)\Psi_{nuc}(R,r) \tag{2.2}$$

When the Hamiltonian (Equation 2.3) is applied to both wavefunction terms, the electronic and nuclear Schrödinger equations are obtained. In this framework, T_{el} and T_{nuc} represent the kinetic energy of electrons and nuclei, respectively. V_{ne} denotes the Coulombic attraction between electrons and nuclei, while V_{ee} and V_{nn} describe the Coulombic repulsion between electrons and between nuclei, respectively.

$$H_{tot} = T_{tot} + V_{tot} = (T_{el} + T_{nuc}) + (V_{ne} + V_{ee} + V_{nn}) \tag{2.3}$$

Solving the electronic Schrödinger equation provides the electronic wavefunction (Equation 2.4) and an adiabatic potential energy (U_n), which is the sum of the electronic energy and the potential energy of the nuclei. This energy depends on the positions of the nuclei.

$$(T_{el} + V)\Psi_{ele}(R,r) = U_n(R)\Psi_{ele}(R,r) \tag{2.4}$$

Thus, a different electronic wavefunction is obtained for each nuclear position. This adiabatic potential energy can then be used to solve the Schrödinger equation by applying the full Hamiltonian to the nuclear wavefunction (Equation 2.5).

$$(T_{nuc} + T_{el} + V)\Psi_{nuc}(R) = (T_{nuc} + U_n(R))\Psi_{nuc}(R) = E_{tot}\Psi_{nuc}(R) \tag{2.5}$$

This gives rise to the nuclear vibrational energy levels, which can be used to calculate molecular vibrations and the thermochemistry of the system, such as Gibbs energy. These calculations contribute to determining the relative energies of different nuclear positions, which in turn dictate whether a reaction is likely to occur and predict reactivity. Nevertheless, the primary energy contribution to the relative energies of systems is the potential energy. Therefore, methods have been developed to approximate the potential energy accurately. This is the central simplification offered by the Born-Oppenheimer approximation, which underpins methods for solving the electronic Schrödinger equation, commonly referred to as electronic structure calculations. These calculations are essential for determining molecular properties and understanding reaction mechanisms.

2.2 *Ab initio* quantum chemistry methods

Significant efforts have been made to develop computational methods that balance efficiency and accuracy in solving electronic structures. The earliest approaches involved solving wavefunctions to determine the energy and properties of quantum systems, most notably the Hartree-Fock (HF) method. In this framework, the N electron wavefunction is approximated by a single Slater determinant, which is an antisymmetric product of one-electron orbitals that automatically enforcing the Pauli principle, capturing exchange while neglecting dynamic correlation, and serving as the foundation of the mean-field approximation. While this captures exchange effects, it neglects dynamical correlation, i.e., the instantaneous interactions between electrons. Practical implementation of Hartree-Fock requires expanding molecular orbitals in a finite set of basis functions (often atom-centered Gaussian functions), which converts the HF integro-differential equations into a matrix eigenvalue problem, making the problem computationally tractable but introducing a basis set approximation. Enlarging the basis set systematically improves the description of the electronic structure and approaches the Hartree-Fock limit. To address the remaining limitation, the neglect of electron correlation, post-Hartree-Fock methods were developed to recover electron correlation, but these come at a much higher computational cost.

To reduce computational demands, methods based on electron density were introduced, eventually leading to hybrid approaches that incorporate wavefunctions, electron density, and higher-order derivatives of electron density with respect to spatial coordinates. This chapter outlines the evolution from early electron density-based methods to modern hybrid density

functionals, like Jacob's ladder with each new functional provide more accuracy than the previous ones. With the power of high-performance computing, modern DFT can now efficiently handle systems with hundreds of atoms at reasonable level of theory with satisfactory accuracy, making it the method of choice in this thesis.

2.2.1 Density Functional Theory

One year after the establishment of the Schrödinger equation, Thomas and Fermi independently proposed a new approach to quantum predictions. By treating electrons as a "*gas of electrons surrounding the nucleus [...] in a completely degenerate condition*," their computation relied solely on electron densities as fundamental variables, eliminating the need for explicit wavefunctions.[4,5] This approach, known as the Thomas-Fermi theory, laid the foundation for modern DFT, where the total energy is expressed as a functional of the electron density.

DFT simplifies the many-electron problem by using electron density as the primary variable. Traditional wavefunction-based methods require solving a function dependent on 3N spatial coordinates plus *N* spin variables, where *N* is the total number of electrons. In contrast, DFT reduces this complexity to a function dependent only on three spatial coordinates, which define the electron density distribution. The electron density, $\rho(\vec{r_1})$, represents the probability of finding any of the *N* electrons with arbitrary spin within a given volume. This can be further interpreted as *N* times the probability of a single electron being at that position. Mathematically, the electron density is expressed as the squared modulus of the wavefunction, integrated over the spin variables (s_i) of all electrons and over all but one of the spatial coordinates (x_i). This expression assumes that the electrons are non-interacting, indistinguishable particles, as shown in Equation 2.6.[6]

$$\rho(\vec{r}_1) = N \int \cdots \int |\Psi(\vec{x}_1, \vec{x}_2, \ldots, \vec{x}_N)|^2 ds_1 d\vec{x}_2 \ldots d\vec{x}_N \qquad (2.6)$$

2.2.1.1 Hohenberg-Kohn theorems

The idea of DFT was completed and formally established in 1964 by Hohenberg and Kohn[7] when they stated two major theorems that set the basis of modern DFT methods. The first theorem states: "*The external potential* $V_{ext}(\vec{r})$ *is [within a constant] a unique functional of* $\rho(\vec{r})$*; since, in turn,* $V_{ext}(\vec{r})$ *fixes* $\hat{H}$ *we see that the full many-particle ground state is a unique*

functional of $\rho(\vec{r})$".[7] The expectation value (or energy of the system $E[\rho]$) can then be expressed as a functional of the electron density according to Equation 2.7 by summing the kinetic energy of the electrons and nuclei, $T[\rho]$, the electron-electron repulsion, $V_{ee}[\rho]$, and the nuclei-electron attractive potential, $V_{ne}[\rho]$.

$$E[\rho] = T[\rho] + V_{ee}[\rho] + V_{ne}[\rho] \tag{2.7}$$

By grouping the terms independent of the external potential, the so-called universal functional, $F_{HK}[\rho]$, can be written as shown in Equation 2.8. This allows the total electronic energy and other properties of the system to be expressed in terms of the electron density.

$$F_{HK}[\rho] \equiv T[\rho] + V_{ee}[\rho] \tag{2.8}$$

To assess whether the calculated density is the ground state density, Hohenberg and Kohn's second theorem states: "The functional $F_{HK}[\rho]$, which provides the ground state energy of the system provides the lowest energy if and only if the input density is truly the ground state density."[7] Thus, the minimum total electronic energy is provided by $F_{HK}[\rho]$ for the exact electron density. This implies the validity of applying the variational principle (established for wavefunction methods) to the expectation values in terms of the electron density:

$$E_0 \leq E[\tilde{\rho}] + V_{ee}[\tilde{\rho}] + V_{ne}[\tilde{\rho}] \tag{2.9}$$

Unfortunately, the exact expression of $F_{HK}[\rho]$ is not known, and therefore, approximations must be made to calculate the electronic energy.

2.2.1.2 Kohn-Sham density functional theory

The earliest universal functional approximation, $E_{TFD}[\rho]$, known as the Thomas-Fermi-Dirac (TFD) method [68], partitions the $V_{ee}[\rho]$ term into the classical Coulombic electron-electron repulsion ($J[\rho]$) and the exchange energy ($K[\rho]$), as shown in Equation 2.10.[8–10] The kinetic energy ($T_{TF}[\rho]$) is treated as in the Thomas-Fermi theory, assuming non-interacting electrons.

$$E_{TFD}[\rho] = T_{TF}[\rho] + J[\rho] + K[\rho] + V_{ne}[\rho] \tag{2.10}$$

Nonetheless, However, the neglect of electron correlation in this method results in unsatisfactory accuracy. This limitation was addressed by Kohn and Sham, who developed a more accurate approach for describing the total electronic energy of a system by splitting the kinetic energy into two components. The first component, which includes the major contributions, is calculated accurately using wavefunctions (as in the Hartree-Fock method) for a system of non-interacting electrons ($T_S[\rho]$), as shown in Equation 2.11. The second component accounts for the correlation contributions to the kinetic energy ($T[\rho] - T_S[\rho]$), representing the difference between a real system of interacting electrons and a fictitious non-interacting system. This second term, along with other unknown contributions, is grouped into the so-called exchange-correlation functional, $E_{XC}[\rho]$, as defined in Equation 2.12:[11]

$$E[\rho] = T_S[\rho] + J[\rho] + E_{XC}[\rho] \quad ; \quad T_S = -\frac{1}{2}\sum_i^N \langle\varphi_i|\nabla^2|\varphi_i\rangle \tag{2.11}$$

$$E_{XC}[\rho] \equiv (T[\rho] - T_S[\rho]) + (V_{ee}[\rho] - J[\rho]) \tag{2.12}$$

The first two terms in the above equation correct the difference between the true and the approximate kinetic energies, $T_S[\rho]$, while the last two account for the difference between the classical electron-electron interaction $J[\rho]$ and the real one.

2.2.1.3 Exchange correlation functionals

Modern Kohn-Sham DFT focuses on improving the exchange-correlation functional ($E_{XC}[\rho]$). Certain fundamental properties of the exchange-correlation functional can be empirically drived, with two key principles: 1) "*The coordinate scaling of the exchange energy should be linear, that is multiplying the electron coordinates with a constant factor should resulting a similar linear scaling of the exchange energy*" and 2) "*No direct scaling law applies for the correlation energy*." These two properties strongly support the separation of exchange and correlation functionals, allowing them to be developed independently and combined in various ways in earlier DFT formulations. However, modern approaches increasingly construct these components in an integrated manner. The exchange and correlation energies can be expressed in terms of energy per electron density, ε_x and ε_c, respectively.

$$E_{XC}[\rho] = E_X[\rho] + E_C[\rho] = \int \rho(r)\varepsilon_x[\rho(r)]dr + \int \rho(r)\varepsilon_c[\rho(r)]dr \quad (2.13)$$

One of the earliest formulations of the exchange functional is the local density approximation (LDA), which treats the local density as a uniform electron gas under the assumption that the density is a slowly varying function. Thus, the exchange energy in LDA is expressed using the Dirac formula. In the open shell case, where the α and β spin densities are not equal, a spin-polarisation function is added to account for the normalised differences between the two densities.

$$\varepsilon_x^{LDA} = -C_x\rho^{1/3} \quad (2.14)$$

$$\varepsilon_x^{LDA} = -C_x f_1(\xi)\rho^{1/3}, \qquad f_1(\xi) = 1/2[(1+\xi)^{4/3} + (1-\xi)^{4/3}] \quad (2.15)$$

Alongside the development of the LDA exchange functional, the correlation functionals were formulated, demonstrating a more complex relationship with electron density. While analytical expression can be derived for high- and low- density limits, intermediate density regions require Monte Carlo methods. These computationally derived values were fitted into analytical expressions, leading to well-known functionals such as the, Vosko-Wilk-Nusair, VWN correlation functional, and Perdew-Wang, PW, correlation functionals. However, their highly parameterised nature means they lack direct physical interpretation.

Despite the conceptual simplicity and computational efficiency of LDA, its fundamental approximation of a uniform electron gas is not entirely valid, especially for molecular systems, leading to an underestimation of energy by ca. 10%, which is larger than the total correlation energy. Nonetheless, for metallic systems, where the electron density varies more smoothly, LDA is more applicable. Efforts to improve LDA have led to the development of more refined approximations that better capture variations in electron density. A significant improvement over LDA was achieved by incorporating the gradient of the electron density, $\nabla\rho$, as an additional parameter. This refinement, known as the Generalised Gradient Approximation (GGA), improves the accuracy of exchange functionals by accounting for local density variations. Personally, I believe that the success of GGA lies in the fact that the gradient is a local variable yet effectively captures non-local properties of the surrounding electron density. One of the most widely used GGA exchange functionals is the Becke 88 (B88) functional, developed by A.D. Becke.

$$\varepsilon_x^{B88} = \varepsilon_x^{LDA} + \Delta\varepsilon_x^{B88} \tag{2.16}$$

$$\Delta\varepsilon_x^{B88} = -\beta\rho^{1/3}\frac{x^2}{1+6\beta x sinh^{-1}x}, \quad x = \frac{|\nabla\rho|}{\rho^{4/3}} \tag{2.17}$$

The parameter β was optimised by fitting to rare gas atoms, and x represents a dimensionless gradient variable. GGA functionals was then shown to "*reduce the error in the exchange energy by almost two orders of magnitude compared to previous functionals like LDA*". Another example of GGA functional would be the LYP that is done through introducing the electron gradient also into the improvement of the correlation functional, developed by Becke and Lee, Yang, and Parr.[12,13] The combination of B88 exchange and LYP correlation, commonly referred to as the 'magical combination', has been remarkably successful in predicting molecular properties. However, the effectiveness of a given functional depends on the system under study, and careful benchmarking and validation are necessary, either against experimental data or high-level coupled-cluster (CC) calculations.

The logical progression from GGA functionals is the inclusion of the second derivative of the electron density, known as the Laplacian ($\nabla^2\rho$), or alternatively, the orbital kinetic energy density τ. Functionals incorporating these terms fall into the Meta-GGA category, as they rely on additional orbital information, which offer incremental improvements over GGA.

$$\tau(r) = 1/2\sum_{i}^{occ}|\nabla\phi_i(r)|^2 \tag{2.18}$$

The next explosion of functional development come as the establishment of hybrid methods, which incorporate a certain percentage of exact exchange from Hartree-Fock (HF) theory. The proportion of HF exchange is controlled by an additional parameter, *a* and *c*. An example of such a hybrid functional is B3LYP, which is composed of B88 exchange and LYP correlation functionals with some proportion of HF.[14]

$$E_{xc}^{B3LYP} = (1-a)E_x^{LSDA} + aE_x^{HF} + b\Delta E_x^{B88} + (1-c)E_c^{LSDA} + cE_c^{LYP} \tag{2.19}$$

The logical extension of hybrid methods is double-hybrid functionals, that instead of only include the occupied orbitals the virtual orbitals are also included. Including the full

information of the KS orbital allows the calculation of a MP2-like energy but using the DFT orbitals and orbital energies in the calculation. This resulting MP2-like energy term is included with an empirical parameter (bE_c^{MP2}) and can be generally expressed as following. This could be expended to multi-hybrid functionals, but the computational costs increase similarly to the MP methods due to the calculations of the MP-like energy terms.

$$E_{xc}^{DHDFT} = (1-a)E_x^{DFT} + aE_x^{HF} + (1-b)E_c^{DFT} + bE_c^{MP2} \tag{2.20}$$

However, hybrid functionals face issues due to the incorrect long-range behaviour of the self-exchange-correlation potential. This potential fails to fully cancel out the self-coulomb potential for all one-electron densities, as it does in Hartree-Fock theory, resulting in self-interaction errors. In other words, the electron erroneously "interacts" with itself, leaving a residual energy error. This issue has been addressed using range-separated methods, which partitions the electron-electron Coulomb operator for the exchange energy into short and long ranges parts and uses different exchange functionals for the short- and long-range parts.[15] Typically, Hartree-Fock (exact) exchange is used for the long-range component. For example, ωB97X is a range-separated version of the B97 functional.

Additionally, Grimme dispersion corrections (D2)[16] are often applied to improve the modelling of van der Waals-type interactions, leading to functionals like ωB97XD. The ωB97XD functional has demonstrated promising results in numerous computational studies of homogeneously catalysed reactions [17–22] and was therefore selected for this thesis. Other standard DFT methods fail to describe dispersion forces; at long-range distances, the functionals fail to exhibit the correct R^{-6} long-range distance behaviour. Thus, Grimme proposed including this missing dispersion through additive empirical terms. These terms are similar to the van der Waals energy from force field methods, which have the physical meaning that the dispersion energy between A and B is inversely proportional to the sixth power of the interatomic distance R between atoms A and B. The general expression for Grimme's dispersion correction is as follows.

$$\Delta E_{disp} = -\sum_{n=6(8,10)} s_n \sum_{AB}^{atoms} \frac{C_n^{AB}}{R_{AB}^n} f_{damp}(R_{AB}) \tag{2.21}$$

Commonly the method includes R^{-6} energy terms, but as progression continues, other higher-order terms such as $R^{-8}$and R^{-10}have also been included. These terms are attractive energy terms and could diverge at short interatomic distances. A damping function was applied to eliminate this. The other parameter s_n is a scaling factor arising from parameterisation of different exchange-correlation functionals.

The remarkable performance of modern, state-of-the-art DFT stems from the development of advanced density-dependent methods for solving the Schrödinger equation, combined with the integration of key elements from other computational approaches. These include kinetic energy computation from wavefunction-based methods, the incorporation of HF exchange, and insights from force field methods to account for R^{-6} dependent dispersion energy corrections.

2.3 Modelling chemical reactivity

Chemical reactivity describes whether a reaction, such as bond breaking and formation, is likely to occur. This can be predicted by determining the relative stabilities of key critical nuclear positions: reactants, transition states, intermediates, and products. The potential energies (U_n) of these nuclear positions, as well as other possible configurations, can be calculated using the electronic structure methods described earlier. These energies can then be used to construct a multidimensional surface plotting U_n against nuclear positions (also referred to as atomic coordinates). This multidimensional representation, known as the potential energy surface (PES), provides a framework for rationalising the reactivity of a chemical system.

2.3.1 Exploration of the potential energy surface

The PES serves as a central framework for understanding molecular behaviour, enabling the identification of stationary points such as minima and saddle points, which correspond to stable structures and transition states. The search for these stationary points led to the development of the Hessian matrix (Equation 2.22),[23] which contains the second derivatives of the potential energy with respect to atomic coordinates and is pivotal for analysing the PES.

$$HESS_{ij} = \frac{\partial^2 U_n}{\partial x_i \partial x_j} \tag{2.22}$$

The Hessian provides insight into the curvature of the PES at any given point and is used to characterise stationary points. These points are defined by the gradient of the potential energy (∇U_n), which is zero at stationary points. Physically, this means that the forces acting on the nuclei vanish at these points. Thus, critical points are also referred to as stationary points. The type of stationary point can be determined by the eigenvalues of the Hessian matrix. Positive eigenvalues correspond to directions of positive curvature and identify minima on the PES. Negative eigenvalues indicate directions of negative curvature and are associated with saddle points when there is only one negative eigenvalue. The eigenvectors, on the other hand, define the principal directions of curvature and correspond to the normal modes of vibration in molecular systems. Together, the eigenvalues and eigenvectors enable the characterisation of molecular stability, transition states, and vibrational behaviour.

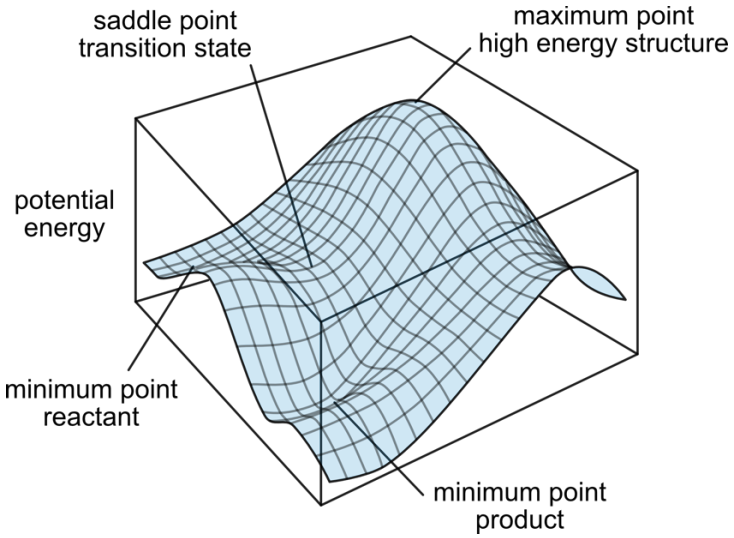

Figure 2.1. Simplified 3D-PES representation, showing the minimum and saddle points corresponding to reactant/product and transition state, respectively.

2.3.2 Introducing solvation effects

Experimentally, chemical reactions are typically carried out in solvents, and therefore solvent effects must be accounted for in computational calculations. Solvent effects can play a critical role in chemical reactivity. Two major methods are used to model solvent effects: explicit and implicit solvation models, each with its advantages and limitations.

Explicit solvation models include solvent molecules discretely in the calculations, increasing the degrees of freedom and computational cost. Additionally, determining the number and positions of explicit solvent molecules is non-trivial, as is accurately describing their entropic contributions, such as the energy cost of bringing a solvent molecule from a distant position to proximity. Due to these limitations, this thesis employs an implicit solvation model, specifically the self-consistent reaction field (SCRF) method.[24] In this approach, the solvent is modelled as a continuous, uniform polarizable medium characterised by its dielectric constant (ε). The solute is placed in a *cavity* within this medium, incurring an energy cost (ΔE_{cav}) associated with the creation of the solvent cavity. The charge distributions of the solvent medium and the solute interact iteratively, maximising attractive dispersion (ΔE_{disp}) and minimising repulsion (ΔE_{rep}) and electrostatic interactions (ΔE_{elec}) until self-consistency is achieved.[25] The total solvation energy is then calculated as:

$$\Delta E_{solvation} = \Delta E_{cav} + \Delta E_{disp} + \Delta E_{rep} + \Delta E_{elec} \quad (2.23)$$

In this project, the implicit solvation model used is the Solvent Model Based on Density (SMD),[25] which defines the solute as the union of interlocking spheres centred on the atoms. However, this model captures only the electrostatic interactions between the solvent medium and the solute. It does not account for entropic effects when the solvent molecule participates in the reaction instead of acting as a spectator. Such effects can only be included via explicit solvation models.

To address the limitations of explicit solvation models while minimising computational costs, a hybrid solvation approach was introduced. In this method, a set of rules defines the placement of the minimum number of explicit solvent molecules. For instance, if a solvent molecule interacts with the reactant, transition state, or product, it is included in the calculation. Solvent molecules are positioned based on their involvement: when they bind to the active site, they are placed; accordingly, if they do not participate directly in the step but were involved in a previous step, they are positioned away from the active site while maximising weak NCIs with the solute. This approach is applied selectively, such as for strongly binding solvents like THF coordinating with sodium via oxygen donor atoms. However, it is unnecessary for weaker interactions, such as THF with Pd or Pt. On the other hand, when the solvent has both hydrogen

bond donor and acceptor properties, forming solvent networks is better modelled using cluster models or COSMO.

In addition to solvation effects, converting units from the gas to the solvated phase requires standard state corrections. Gibbs solvation energies (ΔG_{solv}) are computed under standard conditions of 1 bar and 298.15 K. However, experimental reactions in solution typically use molar concentrations, leading to differences in standard state units (1 bar vs 1 M). This discrepancy becomes significant when the number of product and reactant molecules differs. To address this, when a molecule associates or dissociates during a step, the Gibbs energy is corrected according to Equation 2.24:[26]

$$G^{o}_{gas}(X) = G^{0\,(1bar)}_{gas} - RTln(V^{-1}) \tag{2.24}$$

Where R is the universal gas constant, T the absolute temperature (in Kelvin) and V the volume of 1 mol of an ideal gas, i.e., 22.4 dm^3. If T is taken as the room temperature, 298.15 K, the correction term $-RTln(V^{-1})$ is equal to +1.90 kcal/mol per molecules associated.

2.3.3 Micro-kinetic modelling

The rate is dictated by the chemical barrier on the PES, or more accurately said in terms of realistic chemical modelling, instead of the potential energy surface we are now considering the Gibbs solvation Energy Surface (GsES). From the DFT calculations we could establish fragments of the GsES in specific direction of the reaction, this creates the 2D reaction profile that is commonly seen in literature computational studies. This provides us information of the energy of the transition state. Considering a simple bimolecular reaction with transition state species ($AB^{‡}$).

$$A + B \rightleftharpoons AB^{‡} \rightarrow C \tag{2.25}$$

One could consider the transition state structure as a pseudo short lived intermediate that as soon as it is formed it will proceed to led to product. The rate of the reaction could then be equated to the number of the activated complexes decomposing to form products. The rate can be expressed as the concentration of the transition state multiplied by the frequency of its

surmounting the barrier. The concentration of the transition state could be written in terms of the concentration of $[A]$ and $[B]$ times the equilibrium constant. Through manipulation we arrived to the relationship for the forward rate constant (k) as the frequency times the transition state equilibrium constant ($vK^{\ddagger}$).

$$rate = v[AB^{\ddagger}] = v[A][B]K^{\ddagger} \tag{2.26}$$

$$k[A][B] = v[A][B]K^{\ddagger} \tag{2.27}$$

$$k = vK^{\ddagger} \tag{2.28}$$

The frequency of vibration could be written in terms of Boltzmann's constant (k_B), absolute temperature (T) and the Planck's constant (h) which arrives to a new expression for the forward rate constant only dependent on the $K^{\ddagger}$.

$$k = \frac{k_B T}{h} K^{\ddagger} \tag{2.29}$$

Introducing the relationship between the equilibrium constant and Gibbs solvation energy we could express k in terms of Gibbs solvation energy of the transition state referenced to the reactants.

$$\Delta G^{\ddagger} = -RTlnK^{\ddagger} \tag{2.30}$$

$$k = \kappa \frac{k_B T}{h} e^{-\frac{\Delta G^{\ddagger}}{RT}} \tag{2.31}$$

The DFT calculated Gibbs reaction energies presented in this thesis were used to compute equilibrium constants (K) and rate constants (k) using the Arrhenius (2.30) and Eyring equations (2.31), respectively. The transmission coefficient (κ), shown in Equation 2.28, was assumed to be 1, implying that every oscillation along the reaction coordinate takes the complex through the transition state.[30]

$$\Delta G^{o} = -RTlnK \tag{2.32}$$

Applying the previously described methods for modelling chemical systems enables the accurate determination of reaction energies and transition state energies, including solvation effects. Taking the overall reaction barrier, from the lowest energy intermediate to the highest transition state, often provides a good estimate of the activation energy. However, this approach fails in certain cases,[27] particularly when the concentration of reagents plays a significant role in the reaction equilibrium. To address this limitation, microkinetic modelling (MKM) can be used. This approach accounts for concentration effects using a kinetic model based on the lowest-energy reaction pathways calculated via DFT and the mass action reversible rate law, as implemented in the software COPASI.[28]

For this thesis, we assumed that all elementary steps involving the association or dissociation of a ligand have an associated energy barrier of +5.0 kcal mol^{-1}. This value is based on a previous report suggesting that such processes are often diffusion-limited, with an estimated barrier of +5.0 kcal mol^{-1}.[29]

From the modelling of the kinetic steps, we could determine the rate determining step as well as the step for the selectivity, which depends not only on the kinetic barrier but also on the kinetic effective concentration of the prior species to the transition states, these could be captured by MKM proving it as a powerful method.

2.4 Electronic structure and bonding analyses

Once we have identified the rate limiting step or the selective step, we can further investigate the key intermediates and transition states with various analyses to identify the electronic and structural factors that govern reactivity and selectivity. Gaining such insights enables the development of improved systems through either rational design or computational screening. The analysis is commonly performed by dissecting molecular interactions and their electronic contributions, which help establish structure-property relationships. This approach typically falls into two main categories: i) Decomposing the interaction energy between two molecular fragments into individual energy contributions. This provides a quantitative understanding of the strength and nature of the key interactions. ii) Examining individual interactions between two or three atoms, focusing on the properties of the atoms and their surrounding environments, as well as the nature of the specific atomic contacts, in a semi-quantitative manner.

2.4.1 Energy decomposition analyses

2.4.1.1 Activation strain analysis

One way to understand the chemical properties and the structure-function relationships in chemical systems is by performing the so-called activation strain analysis (ASA), developed by Bickelhaupt and Houk.[31] It consists in breaking down the relative energy of a transition state or intermediate structure, $\Delta E_{binding}$), into the distortion energy (ΔE_{dist}) and interaction energy contributions (ΔE_{int}) between two or more fragments in the system:

$$\Delta E_{binding} = \Delta E_{dist} + \Delta E_{int} \quad (2.33)$$

The term ΔE_{dist} accounts for the energy required to distort each of the fragments in their non-interacting relaxed geometries to the interacting optimised geometries, and hence, they provide insight on the steric contributions and is always a positive value. On the other hand, ΔE_{int} corresponds to the stabilisation energy resulting from the interaction between the two fragments and is always negative.

2.4.1.2 Natural energy decomposition analysis

In contrast to ASA, which provides a surface-level understanding of total interaction energies, natural energy decomposition analysis (NEDA) offers a deeper insight into the individual contributions to the total ΔE_{int} , as shown in Equation 2.34.[32–33] NEDA, performed using NBO 7.0,[34] relies on overlap free domains of natural atomic orbitals, detailed in Section 2.4.2.

$$\Delta E_{int} = E_{CT} + E_{POL} + E_{ES} + E_{EX} + E_{DEF} \quad (2.34)$$

Here, E_{CT} is the charge transfer energy contribution, representing interactions between filled orbitals of one subunit and unfilled orbitals of the other. E_{POL}, E_{ES}, E_{EX} denote the polarisation, electrostatic, and exchange contributions, respectively. DEF refers to the *deformation* energy, representing the energy cost of forming perturbed localised wavefunctions (Ψ_A^{DEF}) from the initial fragment wavefunctions (Ψ_A). This deformation accounts for the combined effects of the electric field and quantum mechanical interactions experienced by each fragment within the

complex. In this thesis, we focus on the ratio between the charge transfer (CT) and polarisation (POL) components to analyse the extent of orbital and non-orbital contributions involved in specific NCIs. While NEDA provides quantitative information on the contributions to overall interactions, the next section introduces a method that offers semiquantitative insights.

2.4.2 Bonding and interaction analyses

2.4.2.1 Quantum theory of atoms in molecules analysis

To understand the nature of interactions between atoms, one approach is to examine the electron density and its spatial variation, a method known as topological analysis under the Quantum Theory of Atoms in Molecules (QTAIM).[35,36] This approach relies on the quantum observable electron density distribution to precisely define atoms and bonds within a molecule. The distribution of electron density in the 3D space of a chemical system can be likened to the distribution of U_n in the multidimensional space of nuclear coordinates, as described in Section 2.3.1. A critical point (CP), where the gradient of the electron density is zero, serves as a key feature in the electron density distribution and is used to determine the positions of atoms, bonds, and sometimes repulsions. To characterise the nature of these CPs, a Hessian matrix can be constructed for each position in the 3D space of the chemical system (Equation 2.35):

$$HESS_\rho = \begin{bmatrix} \frac{\partial^2\rho}{\partial x^2} & \frac{\partial^2\rho}{\partial x\partial y} & \frac{\partial^2\rho}{\partial x\partial z} \\ \frac{\partial^2\rho}{\partial y\partial x} & \frac{\partial^2\rho}{\partial y^2} & \frac{\partial^2\rho}{\partial y\partial z} \\ \frac{\partial^2\rho}{\partial z\partial x} & \frac{\partial^2\rho}{\partial z\partial y} & \frac{\partial^2\rho}{\partial z^2} \end{bmatrix} \tag{2.35}$$

The eigenvectors of this Hessian matrix are position-dependent and sample the curvature of electron density in various directions within the 3D space of the CP. The direction with the highest curvature (λ_1) is chosen as the primary axis, denoted as $\vec{v}_1$, and its corresponding eigenvalue is λ_1. Two additional vectors, $\vec{v}_2$ and $\vec{v}_3$, are constructed perpendicular to $\vec{v}_1$. For convention, $\vec{v}_3$ is chosen as the direction with the lowest curvature (λ_3), while $\vec{v}_2$ corresponds to the intermediate curvature (λ_2). These eigenvalues are ranked such that $\lambda_1 > \lambda_2 > \lambda_3$. The Laplacian of the electron density ($\nabla^2\rho$) is the sum of the three eigenvalues and serves as a

scalar measure of the total curvature at the CP of interest. This quantity helps determine whether a CP is covalent or non-covalent in nature. If the CP corresponds to a bond critical point (BCP), this will be discussed further in Section 2.4.2.2.

There are four key types of CPs. Nuclear critical points (NCPs) are characterised by three negative curvatures and denote the positions of atomic nuclei. BCPs are identified by two negative curvatures, which indicate the presence of a bond. This is logical because electron density is most concentrated around atomic nuclei and is redistributed to form bonding regions between atoms. This redistribution results in one positive curvature (λ_3) where electrons are depleted from the atoms and two negative curvatures (λ_1 and λ_2) where electron density accumulates. Ring critical points (RCPs) are characterised by two positive curvatures and represent steric repulsion at the centre of a ring. Cage critical points (CCPs), on the other hand, exhibit three positive curvatures and denote regions enclosed by multiple atomic arrangements.[63] The electron density at BCPs is equivalent to the disks used in NCI analysis, allowing for a consistent representation of interactions between the same atoms.

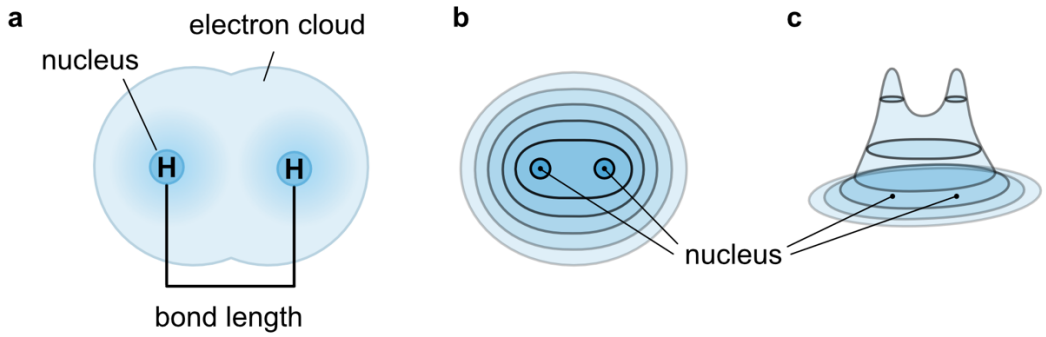

Figure 2.2. Visualisation of the chemical bond in a diatomic hydrogen molecule, as an example. a) Schematic representation showing the electron cloud shared between two hydrogen nuclei (H), defining the bond length. b) Contour map illustrating the electron density distribution around the nuclei. The electron density is concentrated between the nuclei, forming a covalent bond. c) Three-dimensional representation of the electron density distribution, highlighting the bond as a region of high electron density between the two nuclei.

2.4.2.2 Non-covalent interaction analysis

NCI analysis provides qualitative insights into weak electrostatic and van der Waals interactions. This section briefly outlines the theory behind the analysis.[37] NCI analysis is based on the correlation between the reduced density gradient (*RDG*) and the electron density (ρ). The RDG can be used to estimate the strengths of NCIs present in a chemical system. It characterises the regions of electron density where the reduced density matrix approaches zero. In these regions, the *RDG* also approaches zero, indicating the presence of an inflection point between two density maxima. While the Laplacian ($\nabla^2\rho$) measures the abruptness of electron density changes, the *RDG* provides a more refined alternative for assessing these variations in 3D space. The *RDG* is expressed as a function of the gradient of ρ:

$$s(\boldsymbol{r}) = \frac{1}{2(3\pi^2)^{\frac{1}{3}}} \frac{|\nabla\rho(\boldsymbol{r})|}{\rho(\boldsymbol{r})^{\frac{4}{3}}} \tag{2.36}$$

The strength of NCIs is proportional to the electron density at these points, while the attractive or repulsive nature of the interaction can be assessed by analysing the curvature of the electron density (λ). This curvature is primarily influenced by attractive electron-core interactions, making the λ_2 of the Hessian matrix of the electron density a useful indicator. If λ_2 is negative/positive, the interaction is attractive/repulsive, respectively. For instance, in a hydrogen bonding interaction (H–O···H), the pathway following the maximum electron depletion from the nuclei corresponds to the largest eigenvalue (λ_1), while λ_2 and λ_3 are both negative, indicating the attractive nature of the bond. In contrast, weak repulsive interactions result in a positive λ_2 with λ_3 remaining negative. This pattern is observed at the centres of ring systems (RCPs), where λ_3 is not indicative of the interaction's nature.

A 2D plot of the *RDG* (y-axis) against sign(λ_2)ρ (x-axis) helps identify NCIs as peaks of electron density where the *RDG* is zero. This plot also provides information about the nature of the interaction, distinguishing between hydrogen bonding, electrostatic, or van der Waals regions. A cut-off value of 0.05 a.u. is typically applied to the *RDG*, with values below this threshold corresponding to weak NCIs, where the electron density distribution changes are less abrupt compared to covalent regions. The electron density, along with the sign of λ_2, can then

be visualised in 3D space to highlight regions of attraction or repulsion, with colour coding to indicate the interaction strength and type.

It is worth noting that, in practice, regions of repulsion often accompany regions of attraction in 3D space when the electron density (ρ) approaches zero.[38] This characteristic is typical of van der Waals interactions, which are associated with the atoms in these regions. Despite the presence of repulsive contributions, such interactions are, by definition, weakly attractive overall.

2.4.2.3 Independent gradient model

This is an overall introduction of the theory behind independent gradient model (IGM) analysis, which defers from the NCI analysis by the way covalent and NCI are separated. This analysis is performed with the IGMPlot software. For a more detailed description, see the original work by Hénon et al.[39,40] The IGM-δg approach relies on the new definition of a non-interacting system in term of ρ contragradience (i.e., "ρ overlap" between two atomic centres). More precisely, the new descriptor, δg, represents locally the difference between a virtual upper limit of the ρ gradient (∇_ρ^{IGM}) representing a non-interacting system and the true ρ gradient (∇_ρ). It can be expressed as:

$$\delta g = |\nabla \rho^{IGM}| - |\nabla \rho| \tag{2.37}$$

Here in IGM analysis the δg provides information on the strength and nature of the interactions and it is plotted against a function (sign(λ_2)ρ) of the ρ. Whereas the sign of the second eigenvalue of the ED hessian matrix serves to differentiate repulsive (λ_2>0) from attractive (λ_2<0) interactions.

2.4.2.4 Natural bond orbital analysis

In addition to NCIs, covalent interactions can be analysed using Natural Bond Orbitals (NBOs), which are localised orbitals derived from molecular wavefunctions. NBOs provide an intuitive representation of chemical bonding, closely aligning with the concepts of Lewis structures to facilitate the understanding of key covalent interactions.

Natural bond orbitals, like molecular orbitals, are constructed from natural atomic orbitals (NAOs). NAOs are the localised, one-centre equivalents of atomic orbitals, representing the natural orbitals of an atom in its molecular environment. Unlike atomic orbitals, NAOs are not predetermined; instead, they are derived from the molecular wavefunction to optimise the description of the atomic electron density within a molecule. To identify the NBOs, the NBO 7.0 program searches across all possible bonding patterns, including bonds and lone pairs, to find the variationally optimal bonding arrangement that best represents the Lewis structure of the molecule.[41] NBOs are localised one-centre or two-centre orbitals (and occasionally more) that describe the Lewis-like bonding pattern of electron pairs in a compact and intuitive form. More specifically, NBOs are an orthonormal set of localised "maximum occupancy" orbitals whose leading *N/2* members provide the most accurate Lewis-like description of the total N electron density.[42]

This structured approach simplifies the interpretation of molecular bonding, making NBOs particularly useful for analysing resonance structures, donor-acceptor interactions, and hybridisation patterns. Unlike MOs, which are delocalised across the entire molecule and constrained by molecular symmetry, NBOs reflect the local bonding environment. They can break molecular symmetry when necessary, providing a more physically meaningful and chemically intuitive description of the bonding.

References

1. E. Schrödinger, *Phys. Rev.* **1926**, *28*, 1049.
2. C. F. Matta, R. J. Boyd, in *The Quantum Theory of Atoms in Molecules*, John Wiley & Sons, Ltd, **2007**, Chapter 1.
3. M. Born, R. Oppenheimer, *Ann. Phys.*, **1927**, *389*, 457. (translation in English is provided on the website: https://www.studocu.com/en-gb/document/birkbeck-university-of-london/quantum-mechanics/born-oppenheimer-original-paper-1927-translated/87655668)
4. E.Fermi, *Accad. Naz. dei Lincei Cl.* **1927**, *6*, 602.
5. L. H. Thomas, *Math. Proc. Camb. Philos.* **1927**, *23*, 542.
6. M. G. Melchor, *A Theoretical Study of Pd-Catalyzed C-C Cross-Coupling Reactions*, Springer International Publishing, **2013**.
7. P. Hohenberg, W. Kohn, *Phys. Rev.* **1964**, *136*, B864.
8. P. a. M. Dirac, *Math. Proc. Camb. Philos. Soc.* **1930**, *26*, 376.
9. E. H. Lieb, B. Simon, *Adv. Math.* **1977**, *23*, 22.
10. L. H. Thomas, *Math. Proc. Camb. Philos. Soc.* **1927**, *23*, 542.
11. W. Kohn, L. J. Sham, *Phys. Rev.* **1965**, *140*, A1133.
12. A. D. Becke, *Phys. Rev. A.* **1988**, *38*, 3098; b) C. T. Lee, W. T. Yang, R. G. Parr, *Phys. Rev. Appl.* **1988**, *37*, 785.
13. A. D. Becke, *J. Chem. Phys.* **1993**, *98*, 5648; b) P. J. Stephens, F. J. Devlin, C. F. Chabalowski, M. J. Frisch, *J. Chem. Phys.***1994**, *98*, 11623.
14. E. F. Grossman, D. A. Daramola, G. G. Botte, *ChemistryOpen*. **2021**, *10*, 316.
15. J.-D. Chaia, M. Head-Gordon, *Phys. Chem. Chem. Phys.* **2008**, *10*, 6615.
16. S. Grimme, *J. Comput. Chem.* **2006**, *27*, 1787.
17. M. N. Peñas-Defrutos, C. Bartolomé, M. García-Melchor, P. Espinet, *Angew Chem. Int. Ed.* **2019**, *58*, 3501.
18. G. Marcos-Ayuso, M. N. Peñas-Defrutos, A. M. Gallego, M. García-Melchor, J. M. Martínez-Ilarduya, P. Espinet, *J. Am. Chem. Soc*. **2023**, *145*, 527.
19. D. C. Najera, M. N. Peñas-Defrutos, M. García-Melchor, A. R. Fout, *Chem. Commun.* **2022**, *58*, 9626.
20. Y. J. Park, M. N. Peñas-Defrutos, M. J. Drummond, Z. Gordon, O. R. Kelly, I. J. Garvey, K. L. Gullett, M. García-Melchor, A. R. Fout, *Inorg. Chem*. **2022**, *61*, 8182.
21. J. W. Nugent, M. García-Melchor, A. R. Fout, *Organometallics*. **2020**, *39*, 2917.
22. M. N. Peñas-Defrutos, C. Bartolomé, M. García-Melchor, P. Espinet, *Chem. Commun*. **2018**, *54*, 984.
23. J. B. Hiriart-Urruty, J. J. Strodiot, V. H. Nguyen, *Appl Math Optim*, 1984, *11*, 43.
24. J. Tomasi, M. Persico, *Chem. Rev.* **1994**, *94*, 2027.
25. A. V. Marenich, C. J. Cramer, D. G. Truhlar, *J. Phys. Chem. B.* **2009**, *113*, 6378.
26. J. H. Jensen, *Phys. Chem. Chem. Phys.* **2015**, *17*, 12441.
27. M. Mu, M. N. Peñas-Defrutos, M. García-Melchor, *Adv. Organomet. Chem*., **2024**, *81*, 329.
28. M. Besora, F. Maseras, *Wiley Interdiscip. Rev. Comput. Mol. Sci.* **2018**, *8*, 1.
29. a) C. L. McMullin, J. Jover, J. N. Harvey, N. Fey, *Dalt. Trans.* **2010**, *39*, 10833; b) C. L. McMullin, N. Fey, J. N. Harvey, *Dalt. Trans.* **2014**, *43*, 13545.

30. P. Atkins, J. Paula, J. Keeler, *Atkin's Physical Chemistry 11th ed*, OUP, Oxford, **2018**, p. 793.
31. F. M. Bickelhaupt, K. N. Houk, *Angew. Chem. Int.Ed.* **2017**, *56*, 10070.
32. E. D. Glendening, *J. Am. Chem. Soc.* **1996**, *118*, 2473.
33. G. K. Schenter, E. D. Glendening, *J. Phys. Chem.* **1996**, *100*, 17152.
34. E. D. Glendening, C. R. Landis, F. Weinhold, *J. Comput. Chem.* **2013**, *34*, 1429.
35. J. Avery, *The Quantum Theory of Atoms, Molecules and Photons*: McGraw-Hill, **1972**.
36. C. F. Matta, R. J. Boyd, *The Quantum Theory of Atoms in Molecules: From Solid State to DNA and Drug Design*: WILEY-VCH Verlag GmbH & Co.KGaA, Weinheim, **2007**, Chapter 1.
37. J. Contreras-García, E. R. Johnson, S. Keinan, R. Chaudret, J.-P. Piquemal, D. N. Beratan, W. Yang, *J Chem Theory Comput.* **2011**, *7*, 625.
38. a) D. Kehoe, E. Mates-Torres, P. Samokhvalov, M. García-Melchor, Y. K. Gun'ko, *J. Phys. Chem. C.* **2021**, *126*, 434; b) C. Sahm, E. Mates-Torres, N. Eliasson, K. Sokolowski, A. Wagner, K. Dalle, Z. Huang, O. Scherman, L. Hammarström, M. García-Melchor, E. Reisner, *Chem. Sci.* **2021**, *12*, 9078; c) C. D. Sahm, A. Ciotti, E. Mates-Torres, V. Badiani, K. Sokołowski, G. Neri, A. J. Cowan, M. García-Melchor, E. Reisner, *Chem. Sci.* **2022**, *13*, 5988; d) D. C. Najera, M. N. Peñas-Defrutos, M. García-Melchor, A. R. Fout, *Chem. Commun*. **2022**, *58*, 9626.
39. C. Lefebvre, G. Rubez, H. Khartabil, J. C. Boisson, J. Contreras-García, E. Hénon, *Phys Chem Chem Phys.* **2017**, *19*, 17928.
40. M. Ponce-Vargas, C. Lefebvre, J. C. Boisson, E. Hénon, *J. Chem. Inf. Model.* **2020**, *60*, 268.
41. E. D. Glendening, C. R. Landis, and F. Weinhold, *J. Comput. Chem.* **2019**, *40*, 2234.
42. F. Weinhold, C. R. Landis, *Chem. Educ. Res. Pract.* **2001**, *2*, 91.

Chapter 3 Objectives

The goal of this thesis is to unravel the reaction mechanism and key factors that dictate reactivity, selectivity, and speciation in alkali metal and transition metal amide-mediated C–H activation, with particular focus on bimetallic cooperativity and monometallic divergence. Each of the following objectives corresponds to a core results chapter and outlines the rationale and specific scientific questions addressed.

3.1 Bimetallic Na/Co amides in C–H metalation

NaCo cooperative systems offer a tuneable platform for selective arene metalation, particularly for electron-deficient substrates like fluoroarenes. However, the interplay between alkali metal coordination, substrate electronics, and pathway selectivity remains poorly defined. This chapter addresses the following objectives:

- Elucidate the mechanistic origin of ortho-fluoride selective C–H activation in Na/Co amide systems, distinguishing between mono- and bimetallic reaction pathways.
- Explain the role of Na···X (X = F, Cl, Br, H) interactions in product selectively and how they contribute to stabilisation of distinct square planar Co(II) products.
- Utilising microkinetic simulations, with DFT energies as input, to quantify the most accessible energy pathways, and reproduce the experimental observed reactivities across substituted fluoroarenes.
- Provide a transferable framework for understanding and tuning reactivity in other sodium-mediated systems based on energy and electronic structure analyses.

3.2 Bimetallic K/Co amides in C–H metalation

KCo amides display striking sequence-dependent reactivity, with product formation highly sensitive to the order of reagent addition. This reactivity switch remains underexplored and poorly rationalised. This chapter sets out to:

- Characterise the structural and electronic features of potassium amide aggregates that engage in cooperative C–H activation with $Co(HMDS)_2$.

- Compare stepwise and one-pot addition protocols, identifying how formation of potassium cobaltate or transient potassium dimers channels the reaction into inactive or active pathways, respectively.
- Investigate the S_N2-like transition state for methyl C–H activation in toluene and rationalise why analogous reactivity fails in benzene.
- Use DFT, NBO, and NCI analyses to define how solvent coordination, ion-pairing, and π-stacking interactions stabilise reactive assemblies and control accessibility of transition states.

3.3 Monometallic Fe/Co amides in C–H metalation

Despite their apparent structural similarity, $Fe(TMP)_2$ and $Co(TMP)_2$ exhibit divergent reactivity in arene C–H activation. Understanding the mechanistic basis for this divergence provides insights into metal-specific effects in low-coordinate amide systems. This chapter aims to:

- Determine why $Fe(TMP)_2$ undergoes sequential dual C–H metalation of pentafluorobenzene, while $Co(TMP)_2$ promotes single metalation before forming an unreactive dimer.
- Quantify metal-ligand, donor-acceptor interactions, and steric constraints using NBO, IGM, and QTAIM tools, and correlate these with observed reactivity trends.
- Investigate solvent effects on monomer/dimer equilibria and THF association/dissociation by comparing implicit and hybrid solvation models, clarifying how coordination environment influences access to reactive species.
- Simulate kinetic profiles via MKM to compare predicted reactivity trends with experimental product distributions, capture solvent-dependent speciation, and explain divergent thermodynamic sinks.

Chapter 4
Bimetallic Na/Co amides in C–H metalation

Happiness is a conscious choice, not an automatic response.
–Mildred Barthel

4.1 Introduction

The use of earth-abundant and cost-effective 3*d* transition metals for regioselective C–H bond activation of aromatic substrates has garnered significant interest as a strategy for developing more sustainable synthetic methods.[1] Among these metals, cobalt (Co)-mediated C–H activation has emerged as a promising approach for functionalising organic molecules, particularly in the context of fluoroarene functionalisation.[2] Low-valent cobalt complexes, such as $[Co(PMe_3)_4]$, have shown remarkable selectivity for C–F bond activation in hexafluorobenzene and pentafluoropyridine, while C–H activation predominates with pentafluorobenzene.[3] In addition, Co(I) complexes supported by sterically demanding b-diketiminate ligands can cleave C–F bonds in fluoroarenes, such as fluorobenzene,[4] and

bis(phosphino)pyridine Co catalysts mediate C–H borylation, selectively activating C–H bonds in fluoroarenes at the ortho position relative to the fluorine atom.[5] These findings demonstrate cobalt's versatility in the functionalisation of fluoroaromatic compounds, where bond activation often leads to a change in the cobalt oxidation state.

Despite these advances, cobalt's role in regioselective C–H activation of fluoroarenes had not been fully explored. Building on our previous work with sodium amides paired with Fe(II) bis(amide) complexes such as $Fe(HMDS)_2$, which promote regioselective C–H activation via cooperative bimetallic behaviour, we sought to investigate whether cobalt could exhibit similar reactivity in C–H activation of fluoroarenes. In the Fe system, sodium triggers the initial metalation, and both sodium and iron stabilise the resulting aryl anion, leading to regioselective activation.[6] Building on our previous work, we explored the reactivity of cobalt in C–H activation, specifically focusing on $Co(HMDS)_2$, synergistically enhanced by sodium amide Na(HMDS). This system enabled the regioselective cobaltation of fluoroarenes, leading to the formation of novel homoleptic square planar complexes, such as $[\{(benzene)Na\}_2Co(C_6F_5)_4]$. When the reaction was conducted at lower temperatures at 0 °C in benzene, a monoaryl complex, $[NaCo(HMDS)_2(C_6F_5)]$, was isolated and characterised by X-ray diffraction (XRD), analogous to the NaFe product (Scheme 4.1.).

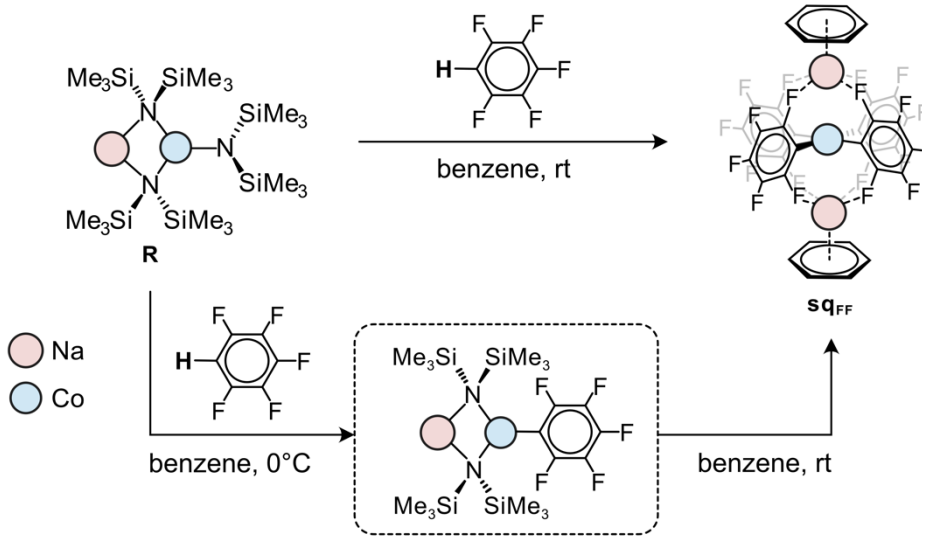

Scheme 4.1. Reaction scheme illustrating the reaction between $NaCo(HMDS)_3$ (**R**) and pentafluoroarene for the formation of square planar complex (**sq$_{FF}$**) at room temperature. At 0 °C, a different intermediate product $[NaCo(HMDS)_2(C_6F_5)]$ is observed, which proceed to form **sq$_{FF}$** upon warming to room temperature.

However, at room temperature, the tetra-aryl complex [{(benzene)Na}$_2$Co(C_6F_5)$_4$] was formed, which undergoes oxidation with I_2 or IC_6F_5, leading to C–C coupling reactions. Notably, this geometry was only achieved with substrates containing two ortho-fluorine atoms. For substrates with mono-ortho fluorine or other ortho-substituents like bromine or chlorine, only the monoaryl product was observed.

C–C coupling processes typically involve reductive elimination of organic substrates from square planar metal complexes, with many such reactions featuring precious metals like Pd.[7–9] The formation of such complexes based on earth-abundant elements, however, remains a major challenge in moving toward greener and cost-effective catalysis. This underscores the importance of designing cobalt-based systems capable of achieving square planar geometry, as they may facilitate the installation of monodentate carbanion ligands, which are potential coupling substrates. Cobalt complexes have recently drawn increased attention due to their high abundance, low cost, and special reactivity.[9] However, the Co(II) oxidation state, with a d^7 electronic configuration, is not ideal for achieving the desired d^8 configuration required for square planar geometry.[10] Despite this, a few examples of square planar Co(II) systems have been reported, often involving ligand chelation to stabilise the structure.[11,12] Notably, a Co(II) complex featuring two bridging oxygens has been reported by Doerrer et al., as well as a Co(II) species with monodentate carbene ligands capable of undergoing C–C bond formation.[13–15] The reported tetra-aryl complex [{Na(C_6H_6)$_2$}$_2$Co(C_6F_5)$_4$] (sq_{FF}), formed via Co–H exchange with an optimal 2:1:4 ratio of Na:Co:C_6F_5H observed in experiments (Scheme 4.1), shares similarities with these earlier cobalt systems, particularly in the presence of K···O and Na···F interactions, which contribute to its stability.[15,16]

In contrast to previously reported non-ion-contacted pairs, such as {[NBu_4]$^+$}$_2$[Co(C_6F_5)$_4$]$^{2-}$, which were synthesised via salt metathesis with LiC_6F_5, the formation of sq_{FF} does not require the use of highly sensitive lithium intermediates, making it a more practical and scalable method.[17,18] Experimental results from our collaborators revealed that the formation of the square planar complex can also occur with other doubly ortho-substituted arenes, such as 1,3-difluorobenzene, 1,3,5-trifluorobenzene and 1,3,4,5-tetrafluorobenzene. However, when non-doubly fluorine-substituted arenes in the ortho positions were used, including 1,2,3,4-tetrafluorobenzene (**Ar$_{FH}$**), 1,3,5-trichlorobenzene (**Ar$_{Cl}$**), and 1,4-dibromo-2,5-difluorobenzene (**Ar$_{Br}$**), metalation resulted in the formation of the relevant [NaCo(HMDS)$_2$(Ar)] intermediates, but no square planar complex was observed (shown in

Figure 4.1). To gain a deeper understanding of the Na and Co HMDS complexes in the C–H activation of fluoroarenes and to predict the formation of bimetallic NaCo(II) square planar complexes.

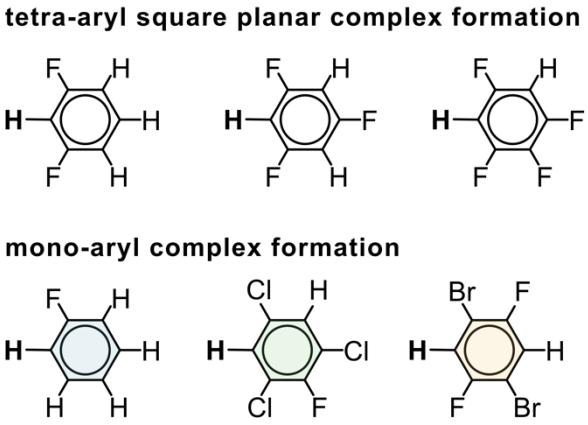

Figure 4.1. Substrate scope for the formation of square planar complex [{Na(C_6H_6)$_2$}$_2$Co(Ar)$_4$] and mono-aryl complex [NaCo(HMDS)$_2$(Ar)] formation.

4.2 Computational details

The mechanisms for the C–H metalation of C_6F_5H were elucidated using DFT calculations, employing the dispersion-corrected hybrid exchange-correlation functional ωb97xd,[19] as implemented in the Gaussian09 software package.[20] The lanl2dz effective core potential and its associated double-zeta basis set, along with an *f*- and *d*-polarisation functions (exponents = 2.780 and 0.428, respectively) were used to describe the Co and Br atoms, respectively.[21] The Na, Si, C, and H atoms were modelled with the double-zeta 6-31g(d,p) basis set, while the more electronegative N, O, F, and Cl atoms were described using the 6-31+g(d) basis set, which includes diffuse *d*-functions.

Geometry optimisations were carried out in vacuum without imposing symmetry constraints and using unrestricted method for open-shell systems. Co(II) complexes with a square planar geometry were modelled as low-spin doublets ($S = 1/2$) based on experimental magnetic data.[22] In all other cases, Co atoms were modelled as high-spin Co(II), consistent with reported experimental magnetic data.[23] The nature of the stationary points was confirmed by vibrational frequency analysis, wherein energy minima were confirmed to display only real frequencies, and transition states exhibited a single imaginary frequency corresponding to the desired reaction coordinate. The optimised transition states structures were also relaxed in both

directions along the reaction coordinate to confirm that they connect the expected energy minima. The effect of the solvent employed in experiments (benzene, ε = 2.2706) was included via single-point calculations at the optimised structures in vacuum using the SMD continuum solvation model.[24] Standard state corrections were applied by adding (subtracting) 1.90 kcal/mol to the computed reaction Gibbs energies for every additional molecule with respect to the products (reactants).[25]

Gibbs energies reported in this work were calculated in benzene at the experimental temperature and pressure of 298 K and 1 atm, and are provided in units of kcal mol^{-1}. The NCI analysis and corresponding plots were obtained using the Critic2 software.[26,27] The electron density at the critical points was calculated by the QTAIM[28] using the Multiwfn software.[29] NEDA was computed using the converged wavefunctions and structures through the NBO 7.0 software.[30]

4.3 Speciation of Na/Co amide complexes

To initiate the mechanistic investigation, we first examined the speciation of monometallic Na(HMDS) due to its well-known tendency to oligomerise. Additionally, we explored the bimetallic NaCo structures to identify the most stable species present in solution as a reference point. This analysis also provided insights into whether the active species in the reaction could be monometallic, bimetallic, or a combination of both.

4.3.1 Monometallic Na(HMDS) species

According to XRD data, the solid-state form of Na(HMDS) exists as a trimeric structure, [{Na(HMDS)}$_3$]. However, when dissolved in solution, its speciation depends on the presence of potential donor species, allowing it to adopt monomeric, dimeric, or ionic forms. In our case, the solvent used in experiments, benzene, can act as a π-coordinating donor. NMR studies, specifically measuring the Si–N coupling parameters,[31] was used to determine the local environment of the nitrogen atoms in the HMDS ligands. These results provided evidence for a dimeric structure in solution, as depicted in Figure 4.2. Hence, we explored the formation of Na(HMDS) with two benzene molecules to saturate the coordination sphere of Na. This leads to the favourable formation of the dimer [{(benzene)Na(HMDS)}$_2$], with a stabilisation energy of –7.3 kcal mol^{-1}. In contrast, our previous study[6] also examined the formation of monomeric

Na(HMDS) structures, which were found to be significantly higher in energy and therefore less favourable.

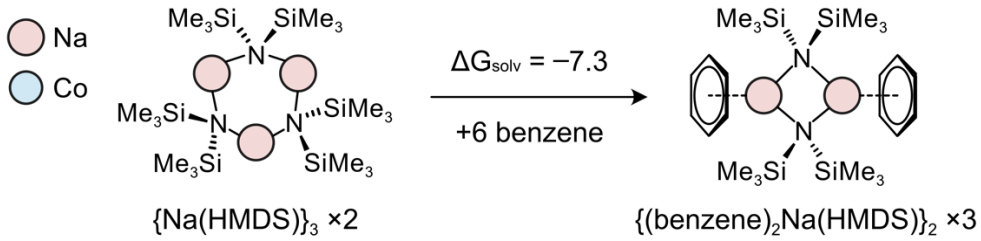

Figure 4.2. Speciation of Na(HMDS). The calculated Gibbs energy (in kcal mol^{-1}) in benzene agrees with experimental solution studies which show that the di-solvated dimer [{(benzene)Na(HMDS)}$_2$] is the most stable species as confirmed by experiment.[31]

4.3.2 Bimetallic NaCo(HMDS)$_3$ species

We then considered the potential co-complexation to form bimetallic species. Since the reaction was conducted with either a 1:1 or 2:1 Na:Co ratio, both yielding the same product, we examined the co-complexation of Na and Co amides in a 1:1 ratio to form an "ate" species analogous to the previously reported NaFe complex.[6] Additionally, we investigated the possibility of Na and Co amides co-complexing in a 2:1 ratio to form a tetrahedrally coordinated Co centre with four bridging HMDS ligands and two sodium atoms coordinated via two HMDS ligands at either terminal position, as illustrated in Figure 4.3.

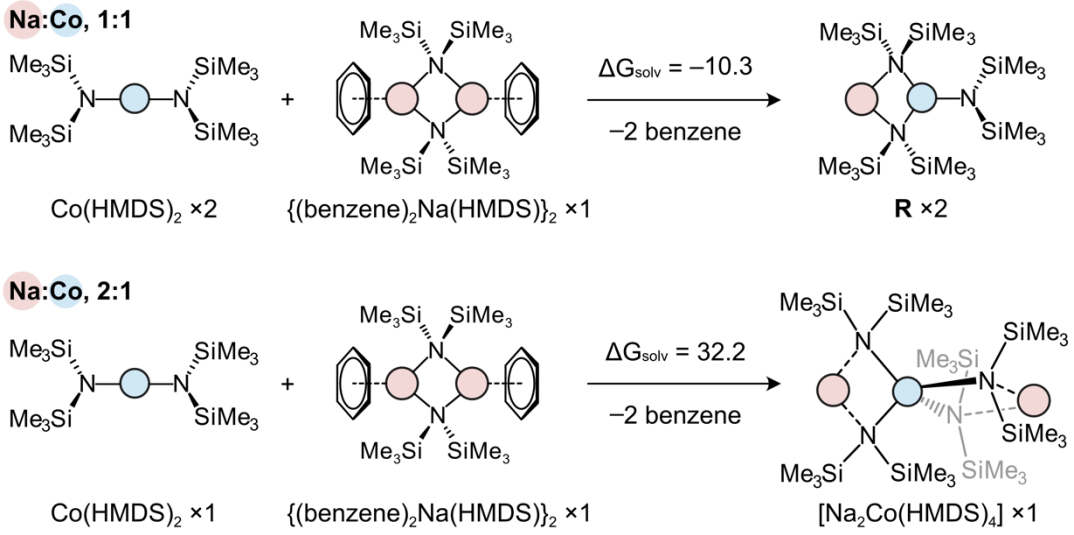

Figure 4.3. Speciation with Na(HMDS):Co(HMDS)$_2$ in 1:1 (top) and 2:1 (bottom ratios). Gibbs energies calculated at the experimental conditions (benzene, 298.15 K, 1 atm) are reported in kcal mol^{-1}.

The Gibbs formation energy calculations revealed that the formation of [NaCo(HMDS)$_3$] is energetically favourable (–10.3 kcal mol^{-1}), whereas the formation of the [Na$_2$Co(HMDS)$_4$] structure is highly endergonic (+32.2 kcal mol^{-1}), making it unfavourable. We also considered potential dissociation pathways for the energetically favoured [NaCo(HMDS)$_3$] complex to yield monometallic Co(HMDS)$_2$ and monomeric Na(HMDS) species. This analysis was conducted because directly comparing the relative energies of monomeric and dimeric Na(HMDS) species would not reflect the dissociation pathways of the bimetallic complex due to the differing numbers of Na(HMDS) monomers produced.

For monomeric Na(HMDS), we considered two extreme cases: one with no benzene molecules coordinated to the Na atom and another with two benzene molecules. Both dissociation pathways were found to be highly endergonic, with energy changes of +24.0 kcal mol^{-1} and +14.5 kcal mol^{-1}, respectively, making dissociation highly unfavourable (Figure 4.4). These speciation results suggest that the [NaCo(HMDS)$_3$] complex is very stable. Therefore, in the next section, we consider this complex as a potential active species, along with the most stable monometallic dimeric form, [{(benzene)Na(HMDS)}$_2$].

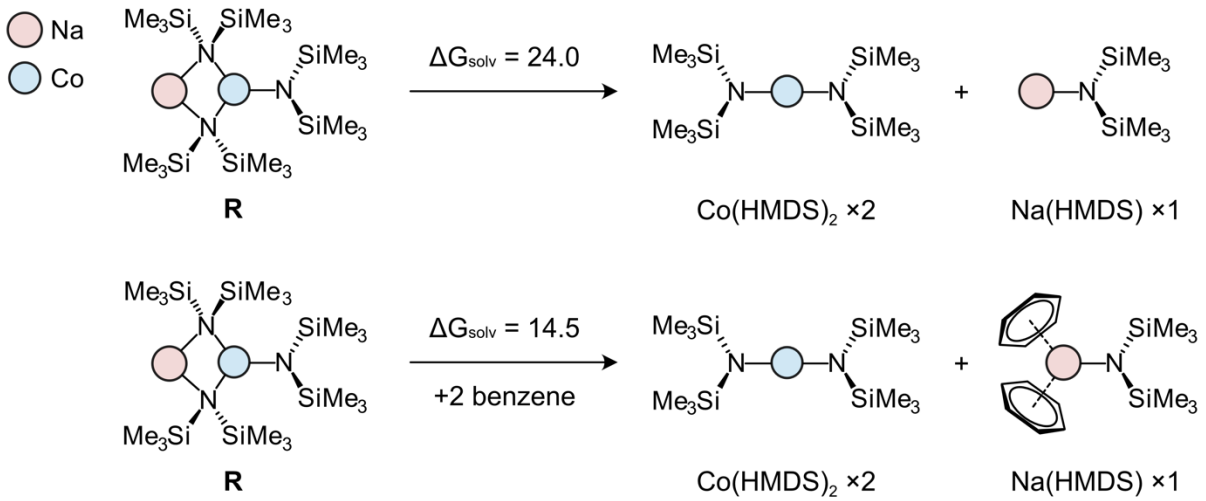

Figure 4.4. Calculated Gibbs reaction energies for the dissociation of the sodium cobaltate [NaCo(HMDS)$_3$] into monometallic cobalt and sodium monometallic complexes. Gibbs energies are reported at the experimental conditions (benzene, 298.15 K, 1 atm) and in kcal mol^{-1}.

4.4 C–H activation mechanisms

Two experimental reaction conditions were attempted for the C–H activation of fluorobenzene, involving the addition of Na and Co amides in either a 1:1 or 2:1 ratio. In the former case, a bimetallic pathway was envisioned, where Na and Co co-complex to form the ate species. In the latter case, a monometallic pathway was hypothesised, wherein one equivalent of Na(HMDS) co-complexes with $Co(HMDS)_2$, while the additional equivalent of Na(HMDS) acts as a potential reactive species. These two cases will be discussed in the following subsections.

4.4.1 Monometallic Na(HMDS) pathways

We first investigated the monometallic Na(HMDS) pathways under conditions where the reagents were added in a 2:1 ratio of Na(HMDS):$Co(HMDS)_2$. Monometallic species tend to co-complex whenever possible to stabilise the system. Consequently, we consider that one equivalent of Na(HMDS) can co-complex with one equivalent of $Co(HMDS)_2$ to form [$NaCo(HMDS)_3$], while the other equivalent of Na(HMDS) remains in solution as a monometallic species. The remaining Na(HMDS) then dimerises with benzene coordination, forming [{(benzene)Na(HMDS)}$_2$]. Based on this, we considered this sodium dimer as a potential active species (Figure 4.5). This conclusion was supported by ^{1}H NMR monitoring studies, which showed the presence of sodium cobaltate in similar amounts to the unreacted sodium amide prior to the addition of C_6F_5H.

The proposed mechanism is analogous to the NaFe pathway we reported previously,[6] requiring the initial dissociation of benzene to allow pentafluorobenzene to approach and form I1'. In this intermediate, fluorobenzene interacts with Na via a Na···F interaction (2.431 Å), while the H atom targeted for deprotonation points towards the N atom of the bridging HMDS ligand. This ligand partially dissociates from Na at the rear end in the transition state (TS). Notably, this new monometallic **TS1'** exhibits a significantly lower energy barrier of +16.1 kcal mol^{-1} compared to the NaFe analogue (+24.1 kcal mol^{-1}). Relaxing the **TS1'** along the reaction coordinate leads to the formation of **I2'**. The subsequent rapid dissociation of HMDS(H) yields the sodiated intermediate **I3'**, where the deprotonated fluoroarene bridges the two Na atoms via the anionic carbon and interactions with the two ortho F atoms (2.734 and 2.715 Å). Unlike the intramolecular mechanism observed for NaFe, **I3'** undergoes intermolecular

transmetalation with sodium cobaltate, yielding the monoaryl product and regenerating the dimeric sodium complex [{(benzene)Na(HMDS)}$_2$], as shown in Figure 4.5. Although the exact mechanism of this transmetalation is unclear, we propose it to be kinetically feasible, as similar ligand exchanges between [(toluene)NaFe(μ-benzyl)(μ-TMP)(TMP)] and [(toluene)NaFe(HMDS)$_3$] are known to occur rapidly.[6] Attempts to experimentally mimic such intermolecular transmetalation were made by our collaborator, who reacted Na(C_6F_5) with the sodium cobaltate complex. However, this attempt was unsuccessful due to the fragility of the fluoroaryl sodium species at room temperature. In contrast, when the reaction was performed using Na(C_6H_5), the formation of free Na(HMDS) was observed in C_6D_6 solutions, along with the appearance of a new set of signals attributed to [NaCo(HMDS)$_2$(C_6H_5)].

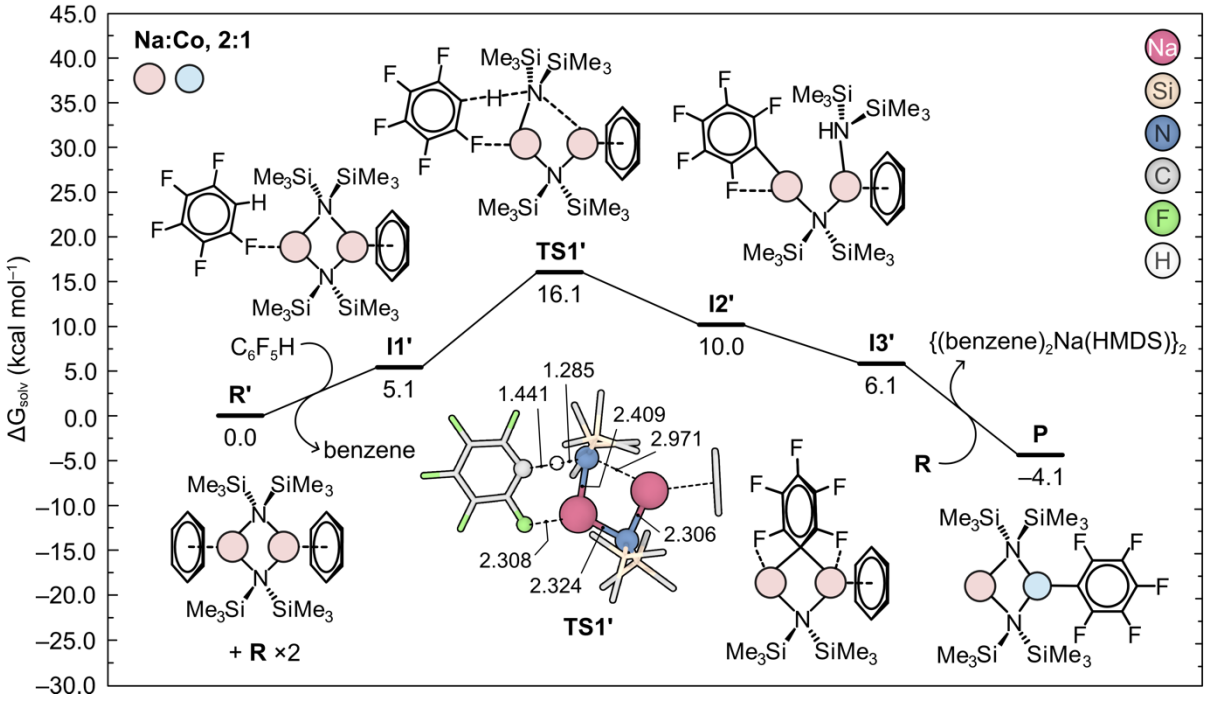

Figure 4.5. Gibbs energy diagram calculated at the experimental conditions (benzene solution, 298 K and 1 atm) for the C–H metalation of C_6F_5H with Na(HMDS) and Co(HMDS)$_2$ in 2:1 ratio by taking [{(benzene)Na(HMDS)}$_2$] as reactive species. Inset: optimised structures of **TS1'** with relevant bond distances shown in Å.

4.4.2 Bimetallic NaCo(HMDS)$_3$ pathways

For the reaction where Na(HMDS) and Co(HMDS)$_2$ were added in a 1:1 ratio, sodium cobaltate [NaCo(HMDS)$_3$] was isolated via XRD and further supported by DFT calculations shown in

Figure 4.3 and 4.4. Given its greater stability in equimolar mixtures of Na(HMDS) and $Co(HMDS)_2$, the presence of monometallic species was ruled out, as later confirmed by MKM studies described in the next chapter. Taking sodium cobaltate as the reference point and active species, the reaction mechanism closely mirrors that of the NaFe analogue, beginning with the coordination of pentafluorobenzene to sodium via two Na···F dative interactions to yield intermediate **I1** (Figure 4.6). From this species, a coordination shift occurs, where a bridging HMDS ligand adopts a pseudo-terminal position on Na, leading to **I2**. This rearranged amide group is ideally positioned to facilitate the metalation of C_6F_5H, yielding **I3** in an exergonic process (–3.9 kcal mol^{-1}) with an overall energy barrier of +21.8 kcal mol^{-1} (**TS1**).

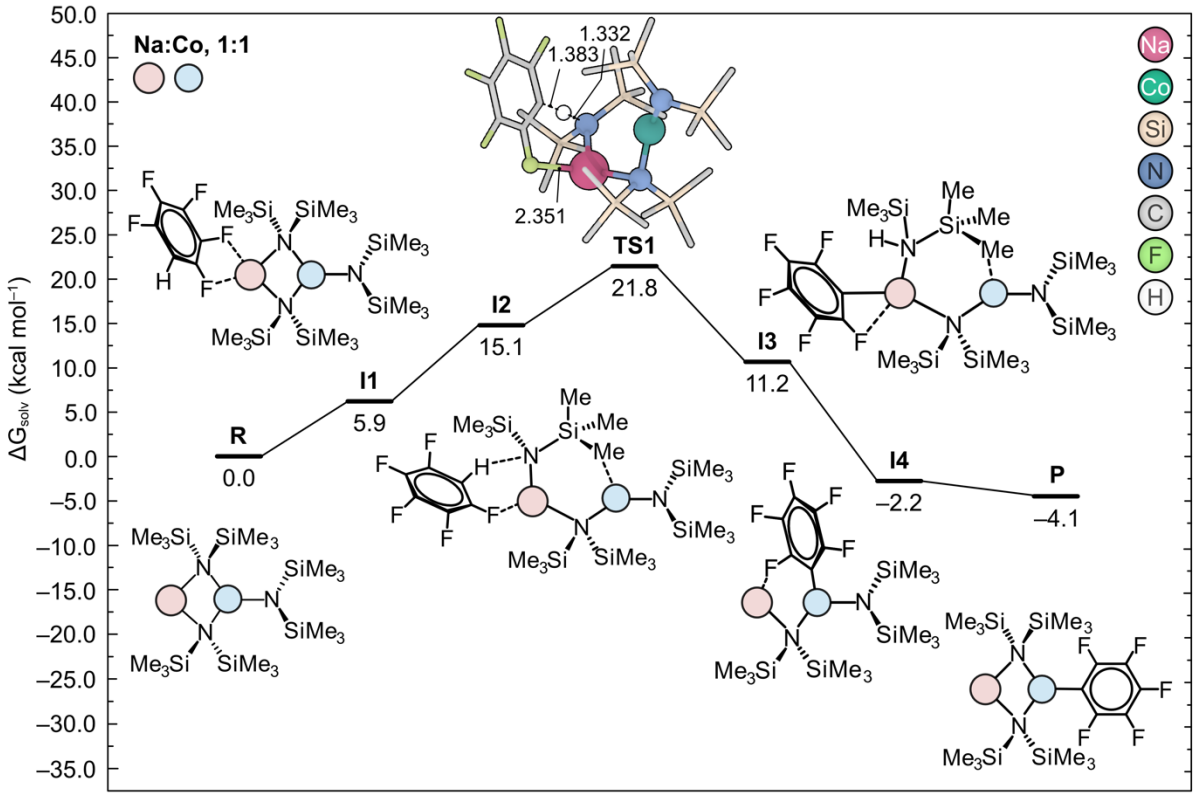

Figure 4.6. Gibbs energy diagram calculated at the experimental conditions (benzene solution, 298 K and 1 atm) for the C–H metalation of C_6F_5H with Na(HMDS) and $Co(HMDS)_2$ in 1:1 ratio by taking [$NaCo(HMDS)_3$] as reactive species. Inset: optimised structures of **TS1** with the relevant bond distance shown in Å.

Due to the structural similarities between sodium cobaltate and sodium ferrate, this pathway was modelled assuming the same lowest-energy pathway previously identified for the sodium ferrate complex. However, to confirm whether the transition metal alters the reaction

mechanism, alternative transition states were also considered (Figure 4.7). One such pathway involved the transition metal contributing directly to the deprotonation step, where the bridging ligand partially dissociates from sodium to form a pseudo terminally bound HMDS ligand to Co, ultimately leading to a sodiation intermediate. Another alternative mechanism involves the pseudo-Na terminally bound HMDS ligand performing the deprotonation, but instead of generating a sodiation intermediate, it directly facilitates cobaltation. Despite these considerations, the alternative TSs were found to be higher in energy, with Gibbs energy barriers of +24.5 and +23.8 kcal mol^{-1}, respectively. These findings once again underscore the critical role of the Na amide in the initial C–H activation step.

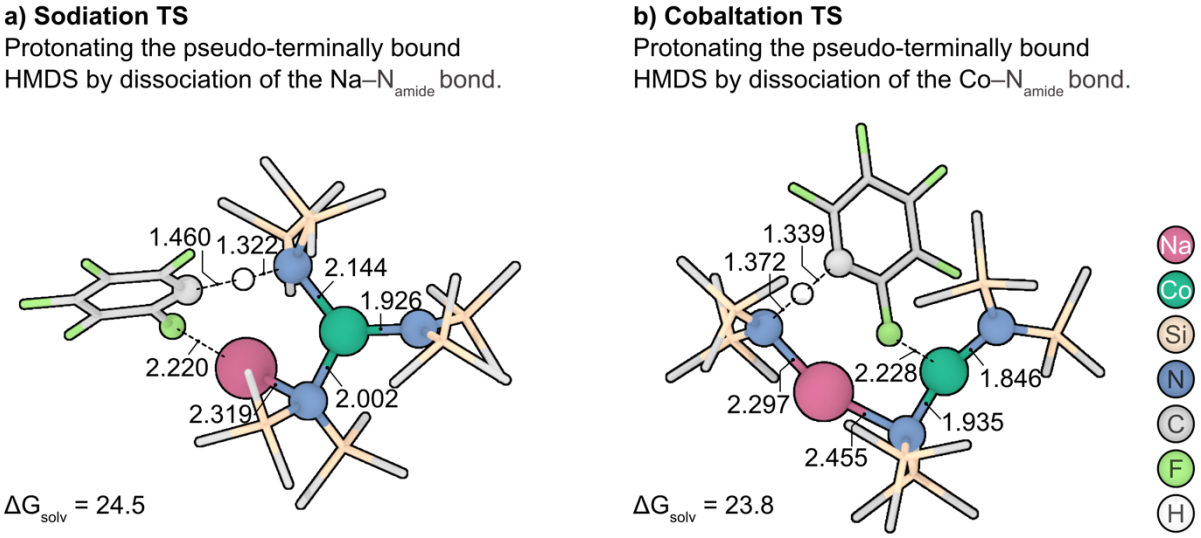

Figure 4.7. Alternative bimetallic C–H metalation transition states for the reaction of $[NaCo(HMDS)_3]$ with C_6F_5H (Na:Co in a 1:1 ratio). These transition states have higher activation barriers than the TS1 reported in Figure 4.6. Gibbs energies at the experimental conditions (benzene, 298.15 K, 1 atm) are referenced to the lowest possible intermediate $[NaCo(HMDS)_3]$. Relevant bond distances (in Å) are also provided.

From this point, the intramolecular transmetalation of the fluoroaryl group by Co was observed as a negligible-barrier process during the geometry optimisation of **I3** following the removal of the protonated HMDS(H). This resulted in the formation of **I4**, where the pentafluoroaryl anion is stabilised through the formation of a more covalent Co–C bond compared to the Na–C bond, alongside a dative Na···F interaction (2.248 Å). Subsequent rearrangement of I4 yielded the final metalation product **P**, wherein the pentafluoroaryl is coordinated terminally to Co. Overall, DFT calculations predict the Co–H exchange to be thermodynamically

favourable by –4.1 kcal mol^{-1}, consistent with the experimental observation of the mono-aryl product via XRD.

Notably, this reaction mechanism mirrors the one we previously reported for the ferration of C_6F_5H using [NaFe(HMDS)$_3$], demonstrating its general applicability for screening the effects of alkali metals, transition metals, and other main group elements in the M^{2+} oxidation state. These findings underscore the cooperative role of the two metal centres, describing the metalation reaction as a sodium-mediated cobaltation, where Na acts as the primary agent in initiating C–H metalation, while Co stabilises the newly formed pentafluorophenyl anion via intramolecular transmetalation.[18] Furthermore, these results explain the lack of reactivity of sodium cobaltate with C_6F_5H in the presence of 15-crown-5. Under these conditions, the formation of [{Na(15-crown-5)$_2$}$^+${Co(HMDS)$_3$}$^-$] coordinatively saturates sodium, thereby preventing substrate coordination and the terminal bonding of HMDS, as illustrated in **I2**.

4.4.3 Catalytic effect of excess Na(HMDS)

The differences in the initial species present in the solution for the 1:1 and 2:1 Na:Co ratios led to the diverge of the reaction mechanisms. In the 2:1 case, it is relatively straightforward to identify the most favourable mechanism, as the active species [{(benzene)Na(HMDS)}$_2$] and [(benzene)NaCo(HMDS)$_3$] for the inter and intramolecular pathways both co-exist in solution with a 0.0 kcal/mol formation energy. The intermolecular pathway has a lower energy barrier (16.1 kcal mol^{-1}) compared to the intramolecular pathway (21.8 kcal mol^{-1}). Consequently, the reaction proceeds via the intermolecular route. In contrast, for the 1:1 ratio, the distinction is less apparent because the formation of the monometallic sodium dimer [{(benzene)Na(HMDS)}$_2$] incurs an energy cost of 10.3 kcal mol^{-1}. The overall kinetic barrier for this pathway can be estimated but does not correspond precisely to the sum of the transition state barrier and the formation energy of the active species. To more accurately ascertain whether the lowest energy pathway is the intermolecular or intramolecular transmetalation route, we performed MKM. In this MKM simulation, each elementary step, as shown in Scheme 4.2, was accounted for by inputting the DFT-computed energies for the kinetic barriers and reaction energies of each step. For ligand association/dissociation steps, a diffusion-controlled barrier of 5.0 kcal mol^{-1} was adopted, based on estimates from previous experimental studies.[31]

One advantage of MKM is the ability to label the products of the two pathways, which is not achievable experimentally for the reaction under investigation. The simulated concentration profiles shown in Figure 4.8 distinctly illustrate the evolution of the products for the intra- (light blue) and intermolecular (grey) transmetalation pathways, respectively, differentiated solely by the labels we intentionally applied. As a side note, the formation of **I4** (the bridging isomer of **P**) was observed in negligible amounts, explaining why this species could not be detected by ^{1}H NMR. These results confirm that the intramolecular pathway via the bimetallic sodium cobaltate is the dominant mechanism operating under the 1:1 Na:Co ratio.

Scheme 4.2. Summary of the complete microkinetic model considered for the C–H metalation of C_6F_5H with $Co(HMDS)_2$ and Na(HMDS) in a 1:1:1 ratio. The intermolecular sodiation pathway (red) and the intramolecular bimetallic pathway (blue) are displayed.

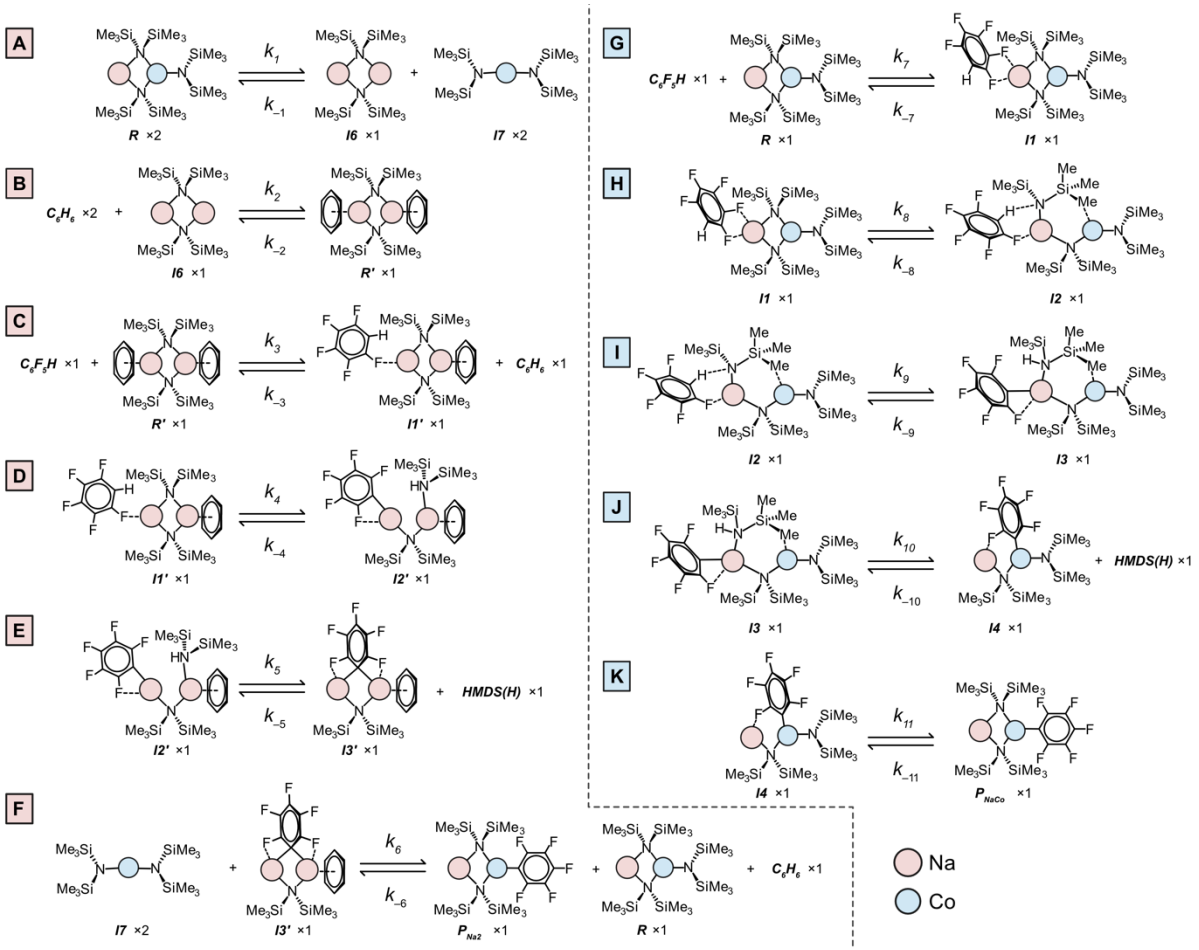

Table 4.1. Calculated rate constants from DFT energies from Scheme 4.2 for the forward (k_i) and backward (k_{-i}) reactions at the experimental reaction conditions: $[NaCo(HMDS)_3]^0 = 0.1$ M, $[C_6F_5H]^0 = 0.1$ M, $[C_6H_6] = 10.0$ M (excess). Rate constants for 1st and 2nd order reactions are given in units of s^{-1} or L mol^{-1} s^{-1}, respectively.

	Rate constants
k_1	1.69×10^{-4}
k_{-1}	$1.34 \times 10^{+9}$
k_2	$1.34 \times 10^{+9}$
k_{-2}	$5.98 \times 10^{+3}$
k_3	$2.45 \times 10^{+5}$
k_{-3}	$1.34 \times 10^{+9}$
k_4	$5.37 \times 10^{+4}$
k_{-4}	$2.10 \times 10^{+8}$
k_5	$1.34 \times 10^{+9}$
k_{-5}	$1.86 \times 10^{+6}$
k_6	$1.34 \times 10^{+9}$
k_{-6}	1.26×10^{-6}

	Rate constants
k_7	$6.36 \times 10^{+4}$
k_{-7}	$1.34 \times 10^{+9}$
k_8	$3.83 \times 10^{+4}$
k_{-8}	$1.34 \times 10^{+9}$
k_9	$7.62 \times 10^{+7}$
k_{-9}	$1.05 \times 10^{+5}$
k_{10}	$1.34 \times 10^{+9}$
k_{-10}	$0.20 \times 10^{+0}$
k_{11}	$1.34 \times 10^{+9}$
k_{-11}	$5.44 \times 10^{+7}$
-	-
-	-

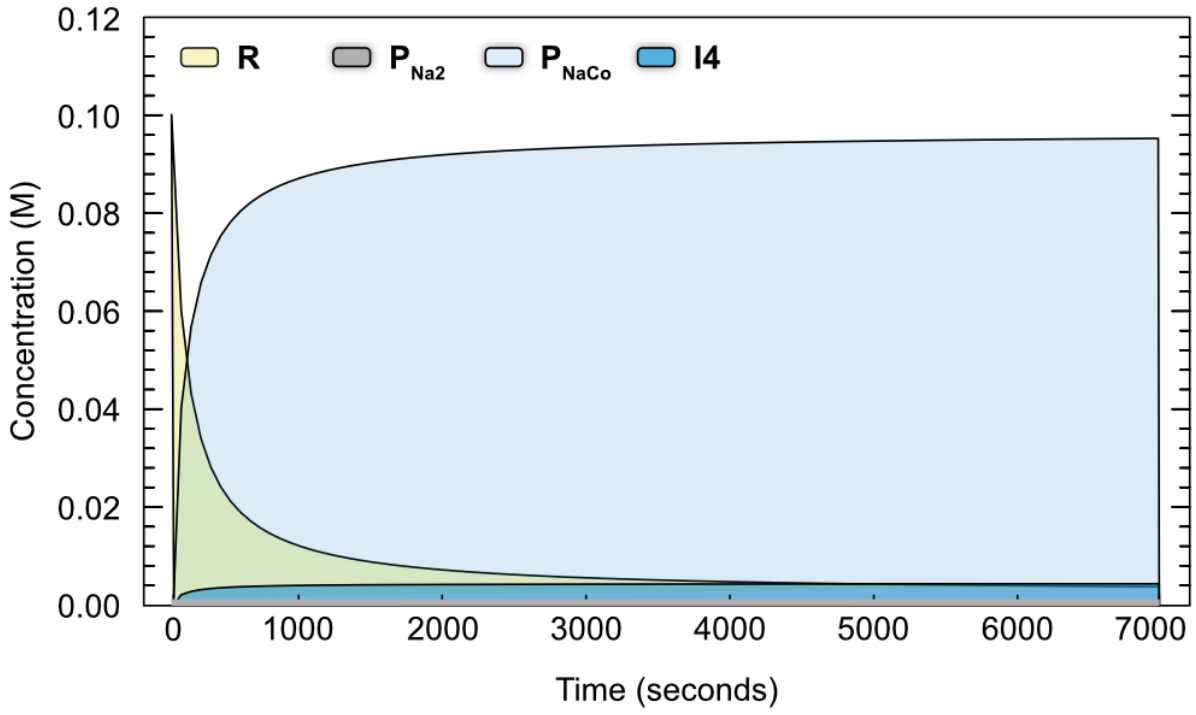

Figure 4.8. Concentration profiles obtained with COPASI using the DFT-calculated thermodynamic and kinetic data summarised in Scheme 4.2 and Table 4.1.

4.5 Ligand exchange mechanisms

The mechanism underlying the formation of the mono-aryl complex is now better understood. However, at room temperature, the reaction with Co, unlike that with Fe, continues beyond this intermediate, ultimately yielding the square planar complex [{Na(benzene)}$_2$Co(C_6F_5)$_4$].

4.5.1 Formation of square planar complexes

The rearrangement to form the square planar tetra-aryl complex from the mono-aryl complex at room temperature represents a distinctive feature of this novel metalation. To investigate this process with the optimal 2:1:4 ratio of Na:Co:C_6F_5H observed in experiments, a ligand scrambling reaction mechanism was posited. Different potential intermediates involved in a sequence of ligand exchanges were modelled to identify the lowest energy pathway leading to the tetra-aryl complex (Figure 4.9). The initial exchange of the aryl fragment between two mono-aryl complexes was considered, resulting in the formation of a bis-aryl species. Two isomers were examined: one featuring a bridging and a terminal aryl group [NaCo(μ-C_6F_5)(*t*-C_6F_5)(μ-HMDS)] with a Gibbs formation energy of +9.3 kcal mol^{-1}, and another with two bridging aryl groups [NaCo(μ-C_6F_5)$_2$(*t*-HMDS)] with a Gibbs formation energy of +19.5 kcal mol^{-1}.

To rule out the involvement of excess Na(HMDS) in this process, the aryl HMDS ligand exchange energy between the bimetallic mono-aryl and bis-aryl complexes with Na dimeric and trimeric species was calculated, all of which were found to be endergonic thus the deprotonated anionic aryl prefers to stay bonded to the Co than Na (Figure 4.10). However due to the low uphill energy of the sodiated species we cannot rule out these as potential intermediate species leading up to the bis-aryl complexes. It was also shown that the bimetallic bis-aryl complex is more favourable than the monometallic bis-aryl complex [Na_3(HMDS)(C_6F_5)$_2$] by +9.9 kcal/mol.

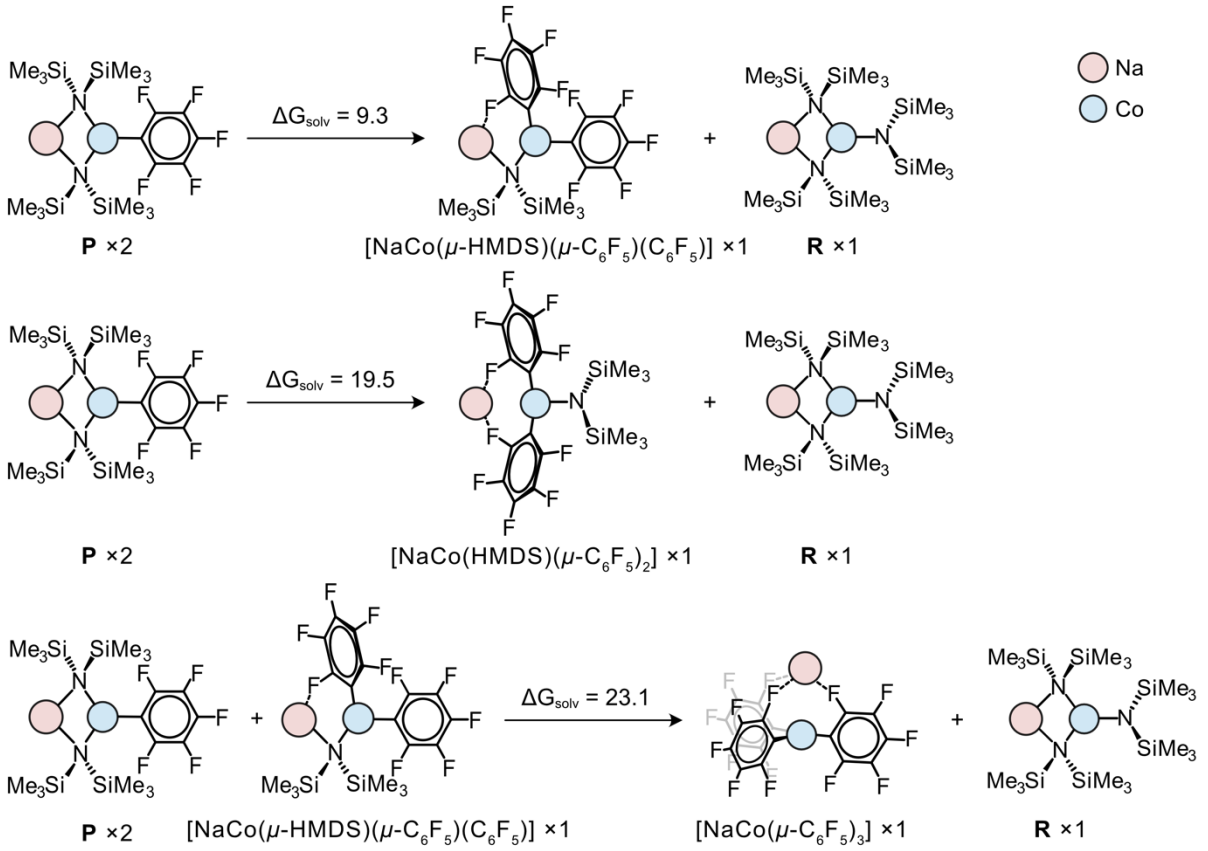

Figure 4.9. Alternative ligand rearrangements for the formation of sodium cobaltate intermediates.

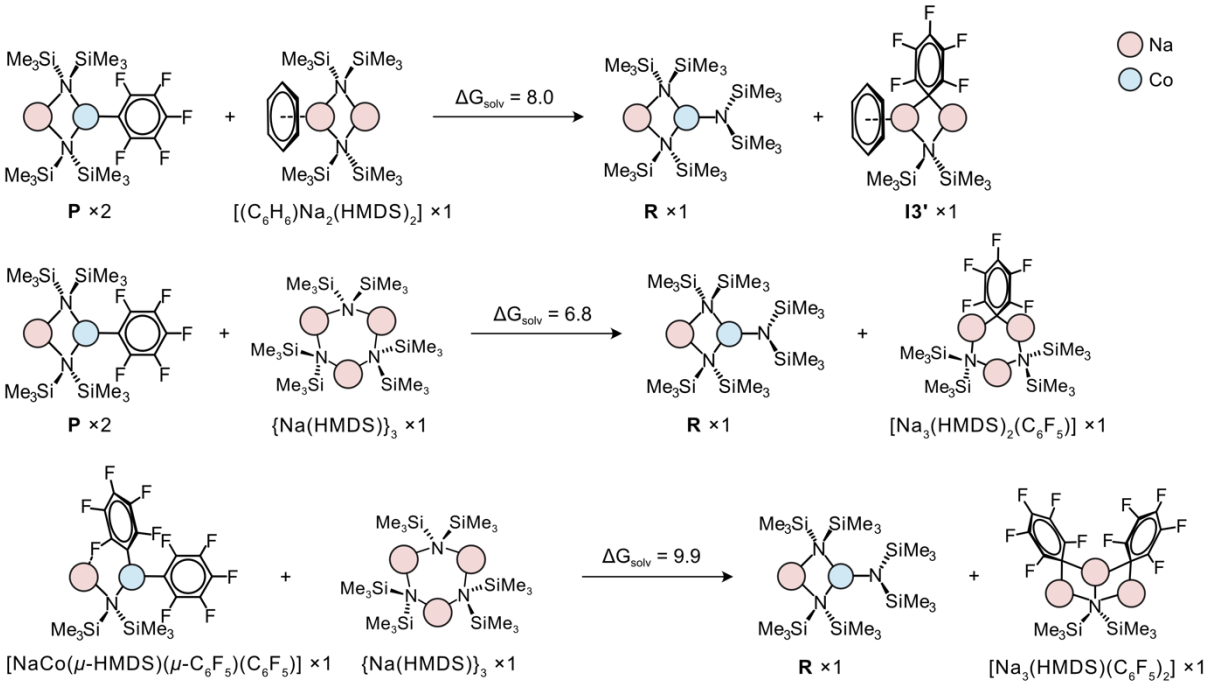

Figure 4.10. Alternative ligand rearrangement for the formation of sodium intermediates.

Subsequently, the more favourable isomer [NaCo(μ-C_6F_5)(t-C_6F_5)(μ-HMDS)] was considered for a further ligand exchange with a mono-aryl complex to form a tris-aryl complex [NaCo(μ-C_6F_5)$_3$] with a Gibbs energy of +23.1 kcal mol^{-1}. However, the formation of the tris-aryl complex was less favourable than the dimerisation of the bis-aryl intermediate to yield the more stable square planar complex, driving the overall reaction forward and expelling Co(HMDS)$_2$ (Figure 4.11). The expelled Co(HMDS)$_2$ subsequently co-complexes with the remaining Na(HMDS) to regenerate sodium cobaltate. Depending on the relative concentrations of Na(HMDS) and NaCo(HMDS)$_3$ present in solution, the reaction proceeds through one of the two pathways outlined in Figures 4.5 and 4.6 to metalate the excess substrate and regenerate the mono-aryl complex.

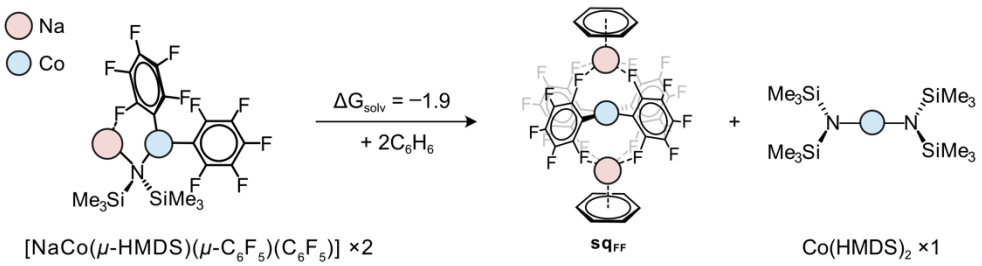

Figure 4.11. Dimerisation reaction of the bis-aryl intermediate [NaCo(μ-C_6F_5)(t-C_6F_5)(μ-HMDS)] to form the square planar complex [{Na(benzene)}$_2$Co(C_6F_5)$_4$] observed experimentally.

4.5.2 Substrate selectivity and ortho substituent effects

To rationalise the observations from Figure 4.1, the analogous bis-aryl intermediates for these arenes, as well as the hypothetical square planar analogues based on the structure of [{Na(benzene)}$_2$Co(C_6F_5)$_4$], were modelled computationally. The results indicate that the formation energies of both the bis-aryl and square planar complexes are endergonic relative to the corresponding mono-aryl complexes. Notably, the formation energies for the lowest energy square planar complexes follow the trend **sq$_{FH}$** > **sq$_{Cl}$** > **sq$_{Br}$** (+31.7 > +22.3 > +9.5 kcal mol^{-1}, respectively shown in Scheme 4.3), which explains why these species are not observed experimentally. The other isomers of the square planar complexes for sq$_{Br}$ and sq$_{FH}$ are slightly higher in energy ranging from +0.4 to +1.6 kcal/mol referenced from the lowest energy **sq$_{Br}$**, and from +1.5 to +4.2 kcal/mol referenced from the lowest energy **sq$_{FH}$** were also considered but found to be less stable (Scheme 4.4).

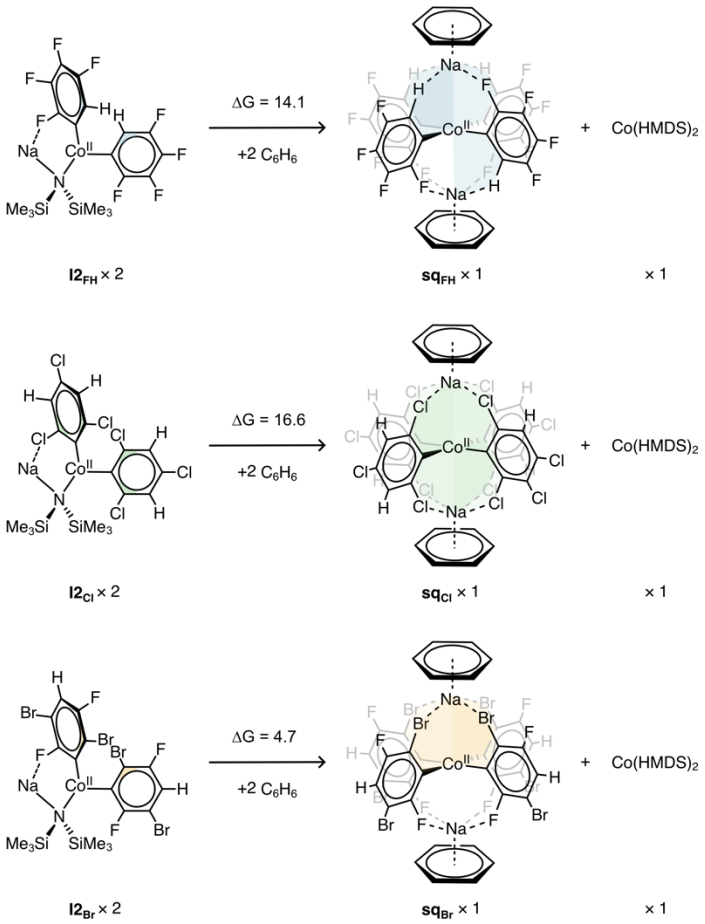

Scheme 4.3. Dimerisation of the bisaryl intermediates [NaCo(*μ*-HMDS)(*μ*-Ar)(*t*-Ar)] (**I2$_{FH}$**, **I2$_{Cl}$**, **I2$_{Br}$**) to form the hypothetical square planar complexes [{Na(C$_6$H$_6$)}$_2$Na$_2$Co(Ar)$_4$] (**sq$_{FH}$**, **sq$_{Cl}$**, **sq$_{Br}$**). The associated Gibbs reaction energies calculated in benzene at 298 K and 1 atm are reported in kcal mol^{-1}. Gibbs energies of the **I2** intermediates are referenced to **R**.

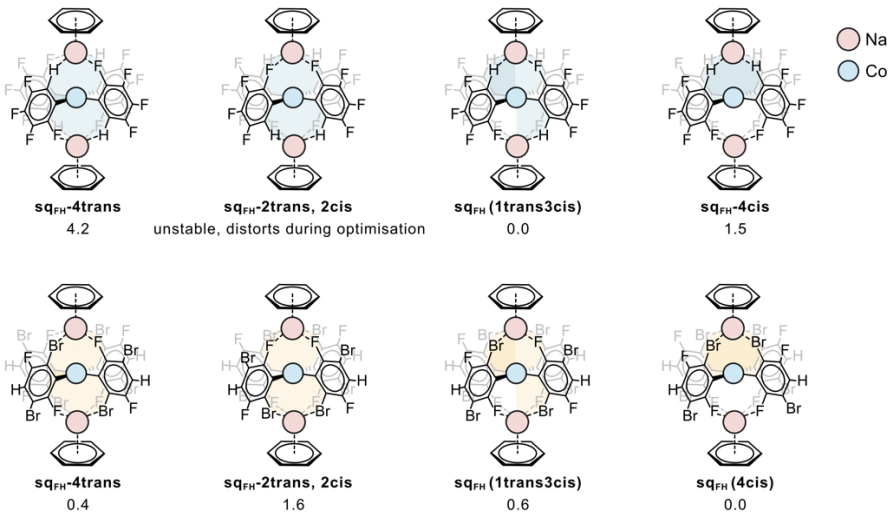

Scheme 4.4. Isomeric structures of **sq$_{FH}$** and **sq$_{Br}$**, the associated Gibbs reaction energies are reported in kcal mol^{-1} referenced to the lowest energy isomer of the **sq$_{FH}$** and **sq$_{Br}$**.

To further investigate the interactions between Na···X contacts (X = H, F, Cl, and Br), NCI analysis was performed on the DFT-computed square planar complexes (**sq$_{FF}$**, **sq$_{FH}$**, **sq$_{Cl}$**, **sq$_{Br}$**). The most relevant NCIs are depicted in the insets shown in Figure 4.12. For the model substrate pentafluorobenzene, the square planar complex **sq$_{FF}$** shown in Figure 4.12a was observed experimentally. NCI analysis indicates that van der Waals (vdW) interactions between the Co centre and the two peripheral Na atoms at ρ = 7.5×10^{-3} a.u. (Na···Co) are responsible for precluding the formation of a distorted z-out octahedral geometry. Additionally, two sets of four attractive Na···F interactions were identified, with an electron density of approximately 0.015 a.u. at the bond critical points (inset in Figure 4.12a), confirming their electrostatic nature.

For substrates with a single ortho F substituent, 1,2,3,4-tetrafluorobenzene was used as the model. The difference in pK_a between 1,2,3,4-tetrafluorobenzene and pentafluorobenzene (31.5 vs 30.6) was found to be insignificant, suggesting that while the initial cobaltation of these substrates occurs, the stabilisation of the square planar geometry is hindered. NCI analysis of the lowest energy conformer of the hypothetical square planar complex [{(benzene)Na}$_2$Co(C$_6$F$_4$H)$_4$], containing one *trans*- and three *cis*-positioned ortho F groups, revealed 5 less attractive electrostatic interactions compared to the tetrafluorobenzene analogue (Figure 4.12a). While stronger Na···F interactions were observed in this complex (indicated with higher ρ = 2.229 × 10^{-2} a.u. in **sq$_{FH}$** vs 1.52 × 10^{-2} a.u. in **sq$_{FF}$**), the total number of attractive interactions was significantly reduced by 5 Na···F contacts, and no major Na···H interactions were identified (Figure 4.12b).

Moving to heavier substituents such as Cl, **sq$_{Cl}$** exhibited weaker Na···Cl interactions (ρ = 1.33 vs 1.52 × 10^{-2} a.u. in sq$_{FF}$). This is attributed to the *'seesaw effect'*, where the ortho groups adjust to maximise Na···Cl contacts, elongating the Co−C (2.020 Å) and C−Cl (2.400 Å) bond lengths (inset, Figure 4.13). The larger **Ar$_{Cl}$** fragments further restrict the formation of strong interactions. This effect is more pronounced for substrates containing heavier Br substituents, as seen in **Ar$_{Br}$**, which also includes F atoms in ortho positions. The asymmetrical size of the ortho substituents causes the Br atoms to shift away from Na, while the F atoms attracted toward Na, resulting in stronger Na···F (1.85 × 10^{-2} a.u.) but weaker Na···Br (1.15 × 10^{-2} a.u.) interactions (Figure 4.12d).

ASA analysis was applied to further quantify the interaction strengths (ΔE_{int}) between the top and bottom $\{Na(benzene)\}^+$ and $\{Co_2(Ar)_4\}^{2-}$ fragments, revealing that Na···Br interactions in sq_{Br} are stronger than Na···F interactions in sq_{FF} by −3.6 kcal mol^{-1}. This apparent discrepancy with the behaviour observed in the NCI analysis was further investigated using NEDA analysis. Specifically, the ratio between charge transfer and polarisation (ΔE_{CT} : ΔE_{POL}) energy contributions to the interaction energy in the **sq** complexes were examined. The results summarised in Table 4.1 show an increase in ΔE_{CT} as we move down in the group 17: Na···F (13 : 87) > Na···Cl (26 : 74) > Na···Br (27 : 73). These values, calculated assuming that the Na···F charge transfer contribution matches that of sq_{FF}, correlates with the more diffuse *p*-orbitals in larger halides.

However, this trend underestimates ΔE_{CT}(Na···Br), as the seesaw effect strengthens Na···F interactions in sq_{Br}, altering the balance of ΔE_{CT} and ΔE_{POL} contributions. This finding highlights the role of orbital overlap in Na···Br interactions and explains the discrepancy between NCI and ASA analyses. NCI tends to underestimate Na···Br strength due to limitations in directly comparing interaction strengths (*e.g.*, Na···F vs Na···Br). ASA resolves this discrepancy, showing that Na···Br interactions are indeed stronger than Na···F by −3.6 kcal mol^{-1} (Table 4.1). Nevertheless, steric hindrance and repulsive Br···Br interactions offset the stabilisation provided by stronger Na···Br interactions, rendering $\mathbf{sq_{Br}}$ formation unfavourable (Scheme 4.5). Similar effects weaken $\mathbf{sq_{Cl}}$ and $\mathbf{sq_{FH}}$, with the general trend in formation energies being $\{Co(Ar_{Br})_4\}^{2-}$ (+48.8) > $\{Co(Ar_{Cl})_4\}^{2-}$ (+33.2) > $\{Co(Ar_{FH})_4\}^{2-}$ (+26.6). This leaves $\mathbf{sq_{FF}}$ as the only thermodynamically feasible complex, characterised by minimal repulsions and strong Na···F contacts, in line with experimental observations.

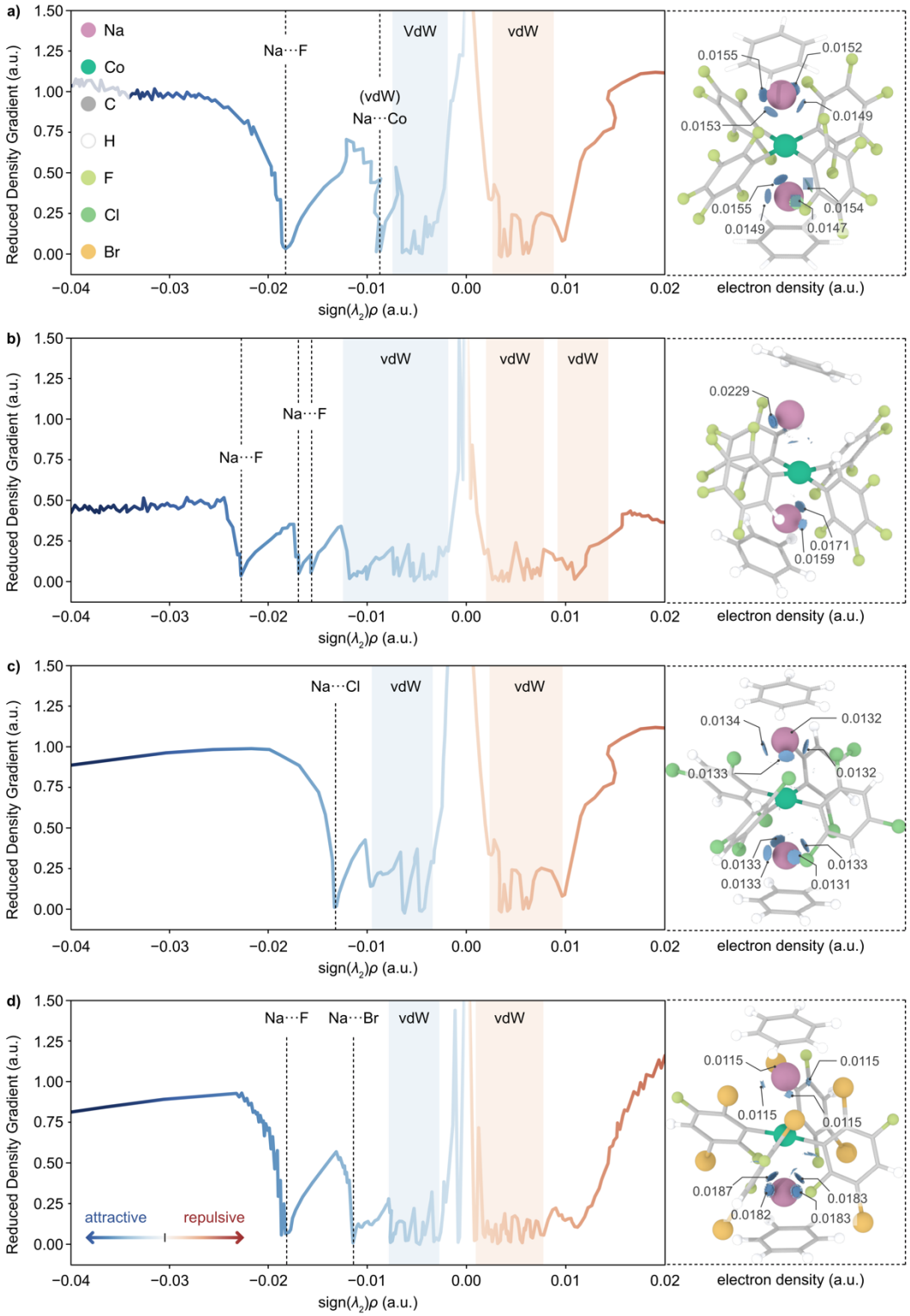

Figure 4.12. NCI analysis on complexes a) $\mathbf{sq_{FF}}$, b) $\mathbf{sq_{FH}}$, c) $\mathbf{sq_{Cl}}$, and c) $\mathbf{sq_{Br}}$ by plotting the reduced density gradient against the sign of the second eigenvalue of the Hessian matrix multiplied by the ρ, sign(λ_2)ρ. Left: NCI plots with attractive (repulsive) interactions denoted by blue (red) shades; the stronger (weaker) the interaction, the darker (lighter) the

shade. Right: Representation of the most relevant NCIs together with their associated ρ values (in a.u.).

4.5 Ligand exchange mechanisms

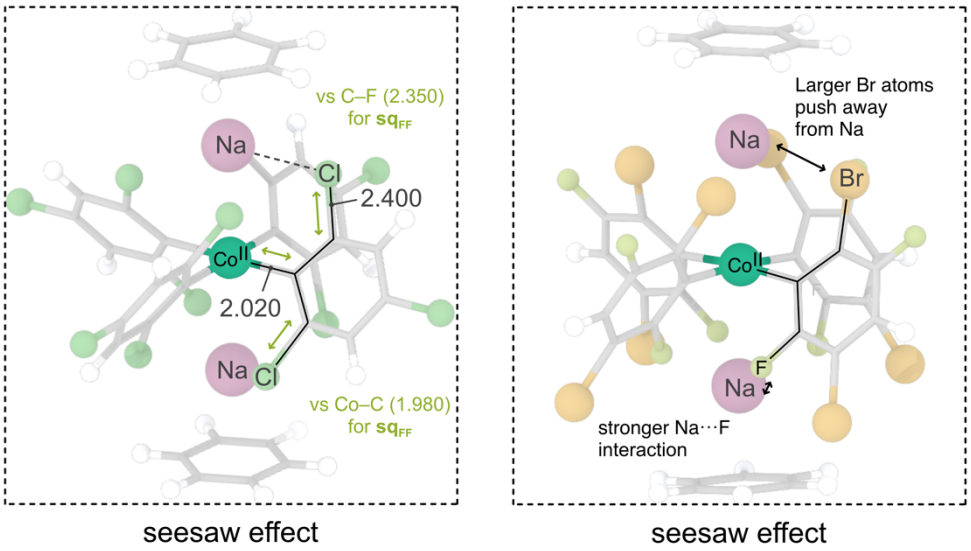

Figure 4.13. Optimised structures of $\mathbf{sq_{Cl}}$ and $\mathbf{sq_{Br}}$ to illustrate the *'seesaw effect'*. Relevant bond lengths are given in Å.

Table 4.1. Summary of the computed interaction (ΔE_{int}) and distortion (ΔE_{dist}) energies, and the ratio of charge transfer relative to the polarisation energy contribution (ΔE_{CT} : ΔE_{POL}) calculated via ASA and NEDA analyses, respectively. All the energies are given in kcal mol^{-1}. The number and type of contacts with the top and bottom $\{Na(C_6H_6)\}^+$ fragments, $Na_{top}\cdots(X)$ and $Na_{bot}\cdots(X)$, in each sq complex is also provided.

	ΔE_{int}[a]	ΔE_{int1}[b]	$Na_{top}\cdots(X)$	$\Delta E_{int1/Na\cdots X}$[c]	ΔE_{int2}[b]	$Na_{bot}\cdots(X)$	$\Delta E_{int2/Na\cdots X}$[c]	$\Delta E_{CT:POL}$[d]
$\mathbf{sq_{FF}}$	−274.0	0.0	4F	0.0	0.0	4F	0.0	13 : 87
$\mathbf{sq_{FH}}$	−264.4	+8.5	1F+3H	+2.8	+1.2	3F+1H	+1.2	9 : 91
$\mathbf{sq_{Cl}}$	−267.3	+3.4	4Cl	+0.8	+3.4	4Cl	+0.8	26 : 74
$\mathbf{sq_{Br}}$	−316.1	−14.5	4Br	−3.6	−27.5	4F	−6.8	27 : 73

[a] Total interaction energy between the three fragments considered. [b] Interaction energies between the top (ΔE_{int1}) and bottom (ΔE_{int2}) $\{Na(C_6H_6)\}+$ fragments and $\{Co(Ar)_4\}^{2-}$, relative to sq_{FF}. [c] ΔE_{int1} and ΔE_{int2} values divided by the number of Na···X contacts, referenced to sq_{FF}. [d] ΔE_{CT} : ΔE_{POL} values assuming that the charge transfer from the Na···F contacts in the hetero-substituted sq complexes is the same than in the homo-substituted sq_{FF} complex.

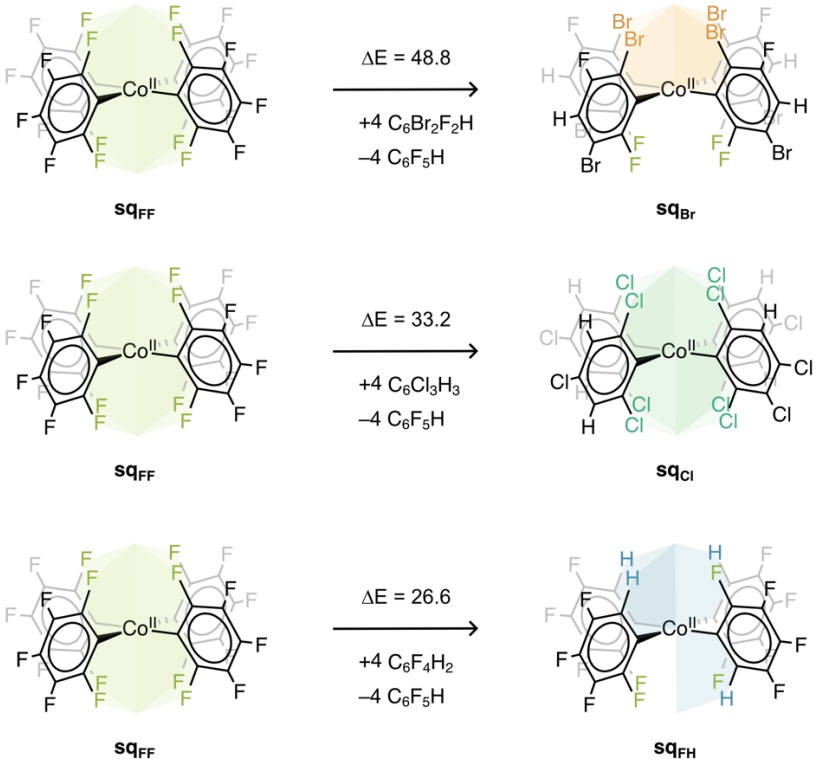

Scheme 4.5. Comparison of the relative stability of the different $\{Co(Ar)_4\}^{2-}$ fragments in the geometries adopted in their respective optimised **sq** complexes.

4.6 Conclusions

Overall, this chapter provides a detailed exploration of the C–H activation mechanisms facilitated by bimetallic Na/Co amide systems. By pairing Na(HMDS) with $Co(HMDS)_2$, the chemo- and regioselective cobaltation of fluoroarenes was demonstrated, yielding unique square planar tetra-aryl complexes. Notably, the formation of the square planar geometry was dependent on the presence of doubly ortho-fluorinated arenes, emphasising the critical role of steric and electronic effects in determining product selectivity. The computed reaction profiles for both inter- and intramolecular mechanisms revealed that cooperative interactions between sodium and cobalt are essential for stabilising intermediates and driving the reaction forward. Mechanistic investigations showed that the reaction follows distinct pathways depending on the Na:Co ratio. For a 2:1 ratio, intermolecular pathways dominate due to lower energy barriers, while 1:1 ratios favour bimetallic intramolecular pathways. These findings were further validated through MKM. Additionally, ligand exchange speciation studies uncovered the ligand-scrambling processes leading to the square planar complexes.

We also demonstrated that the fate of these complexes is determined by maintaining an optimal balance between the attractive intramolecular Na···X interactions and the repulsive X···X (X = H, F, Cl, Br) forces within their structures. Specifically, the interplay between the Na···X contacts, at the axial position, on the top and bottom of the complex influences the relative weakening or strengthening of these interactions, a phenomenon that we refer to as the *seesaw effect*. This behaviour accounts for the observed hierarchy of Na···X interaction strengths in the square planar complexes: H (**sq$_{FH}$**) < Cl (**sq$_{Cl}$**) < F (**sq$_{FF}$**) < Br (**sq$_{Br}$**). Moreover, the formation of these complexes is significantly influenced by the intramolecular X···X repulsions, which grow in magnitude with increasing substituent size. By factoring in both types of interactions, we predict the exclusive formation of the doubly F ortho-substituted aryl complex (**sq$_{FF}$**), aligning with experimental observations. These insights provide a foundation for designing stable Co complexes in a square planar geometry, which can support the development of more sustainable C−C coupling methodologies.

References

1. (a) P. Gandeepan, T. Müller, D. Zell, G. Cera, S. Warratz, L. Ackermann, *Chem. Rev.* **2019**, *119*, 2192–2452. (b) U. Dhawa, N. Kaplaneris, L. Ackermann, *Org. Chem. Front* **2021**, *8*, 4886-4913. (c) L. Woźniak, N. Cramer, *Trends in Chemistry*, **2019**, *1*, 471-484. (d) R. L. Carvalho, A. S. de Miranda, M. P. Nunes, R. S. Gomes, G. A. M. Jardim, E. N. da Silva Junior, *Beilstein J. Org. Chem.* **2021**, *17*, 1849–1938. (e) L. Ackermann, R. Vicente, A. R. Kapdi, *Angew. Chem. Int. Ed.* **2009**, *48*, 9792–9826.
2. (a) B. J. Fallon, E. Derat, M. Amatore, C. Aubert, F. Chemla, F. Ferreira, A. Perez-Luna, M. Pettit, J. *Am. Chem. Soc.* **2015**, *137*, 2448–2451. (b) J. Sanjosé-Orduna, D. Gallego, A. Garcia-Roca, E. Martin, J. Benet-Buchholz, M. H. Perez-Temprano, *Angew. Chem. Int. Ed.* **2017**, *56*, 12137-12141. (c) A. Reckziegel, C. Pietzonka, F. Kraus, C. G. Werncke, *Angew. Chem. Int. Ed.* **2020**, *59*, 8527–8531. (d) M. H. Li, X. J. Si, H. Zhang, D. Yang, J. L. Niu, M. P. Song, *Org. Lett.* **2021**, *23*, 914–919. (e) P. Gosh, R. Schoch, M. Bauer, A. J. Wangelin, *Angew. Chem. Int. Ed.* **2022**, *61*, e202110821.(f) M. Moselage, J. Li, L. Ackerman, *ACS Catal.* **2016**, *6*, 498-525.
3. (a) E. Clot, O. Eisenstein, N. Jasim, S. A. MacGregor, J. E. McGrady, R. N. Perutz, *Acc. Chem. Res.* **2011**, *44*, 333–348. (b) O. Eisenstein, J. Milani, R. N. Perutz, *Chem. Rev.* **2017**, *117*, 8710–8753
4. a) T. R. Dugan, X. Sun, E. V Rybakakimova, O. Olatunjiojo, T. R. Cundari, P. L. Holland, *J. Am. Chem. Soc.* **2011**, *133*, 12418–12421; b) T. R. Dugan, J. M. Goldberg, W. W. Brennessel, P. L. Holland, *Organometallics* **2012**, *31*, 1349–1360;
5. (a) T. P. Pabst, J. V. Obligacion, É. Rochette, I. Pappas, P. J. Chirik, *J. Am. Chem. Soc.* **2019**, *141*, 15378–15389. (b) J. V. Obligacion, M. J. Bezdek, P. J. Chirik, *J. Am. Chem. Soc.* **2017**, *139*, 2825–2832. (c) J. V. Obligacion, H. Zhong, P. J. Chirik, *Isr. J. Chem.* **2017**, *57*, 1032–1036.
6. NaFe
7. M. Pérez-Rodríguez, A. A. C. Braga, M. Garcia-Melchor, M. H. Pérez-Temprano, J. A. Casares, G. Ujaque, A. R. de Lera, R. Álvarez, F. Maseras, P. Espinet, *J. Am. Chem. Soc.* **2009**, *131*, 3650–3657.
8. C. P. Johnston, R. T. Smith, S. Allmendinger, D. W. C. MacMillan, *Nature,* **2016**, *536*, 322–325.
9. J. Choi, G. C. Fu, *Science,* **2017**, *356*, eaaf7230.
10. D. G. Barceloux, *J. Toxicol. Clin. Toxicol.* **1999**, *37*, 201–206.
11. L. S. Merz, C. K. Blasius, H. Wadepohl, L. H. Gade, *Inorg. Chem.* **2019**, *58*, 6102–6113.
12. Y. Gao, W.-T. Lee, V. Carta, C.-H. Chen, J. Telser, J. M. Smith, *EurJIC*. **2023**, *26*, e202200675.
13. S. A. Cantalupo, S. R. Fiedler, M. P. Shores, A. L. Rheingold, L. H. Doerrer, *Angew. Chem. Int. Ed.* **2012**, *51*, 1000–1005.
14. M. Cibian, S. Derossi, G. S. Hanan, *Dalton trans.* **2011**, *40*, 1038–1040.
15. Z. Mo, Y. Li, H. K. Lee, L. Deng, *Organometallics* **2011**, *30*, 4687–4694.
16. A. Logallo, M. Mu, M. García-Melchor, E. Hevia, *Angew. Chem. Int. Ed.* **2022**, e202213246.
17. M. Angeles García-Monforte, I. Ara, A. Martín, B. Menjón, M. Tomás, P. J. Alonso, A. B. Arauzo, J. I. Martínez, C. Rillo, *Inorg. Chem.* **2014**, *53*, 12384–12395.
18. H.-B. Choi, J.-S. Ryu, W.-J. Shin, N. Vigier, *Nat Commun.* **2019**, *10*, 5371.
19. J.-D. Chai, M. Head-Gordon, *Phys. Chm. Chem. Phys.* **2008**, *10*, 6615.

20. M. J. Frisch, G. W. Trucks, H. B. Schlegel, G. E. Scuseria, M. A. Robb, J. R. Cheeseman, G. Scalmani,V. Barone, G. A. Petersson, H. Nakatsuji, X. Li, M. Caricato, A. Marenich, J. Bloino, B. G. Janesko, R. Gomperts, B. Mennucci, H. P. Hratchian, J. V. Ortiz, A. F. Izmaylov, J. L. Sonnenberg, D. WilliamsYoung, F. Ding, F. Lipparini, F. Egidi, J. Goings, B. Peng, A. Petrone, T. Henderson, D. Ranasinghe,V. G. Zakrzewski, J. Gao, N. Rega, G. Zheng, W. Liang, M. Hada, M. Ehara, K. Toyota, R. Fukuda, J. Hasegawa, M. Ishida, T. Nakajima, Y. Honda, O. Kitao, H. Nakai, T. Vreven, K. Throssell, J. A. Montgomery, Jr., J. E. Peralta, F. Ogliaro, M. Bearpark, J. J. Heyd, E. Brothers, K. N. Kudin, V. N. Staroverov, T. Keith, R. Kobayashi, J. Normand, K. Raghavachari, A. Rendell, J. C. Burant, S. S. Iyengar, J. Tomasi, M. Cossi, J. M. Millam, M. Klene, C. Adamo, R. Cammi, J. W. Ochterski, R. L. Martin, K. Morokuma, O. Farkas, J. B. Foresman, and D. J. Fox, Gaussian 09, Revision E.01, Gaussian, Inc., Wallingford CT, **2016**.
21. a) A. W. Ehlers, M. Böhme, S. Dapprich, A. Gobbi, A. Höllwarth, V. Jonas, K. F. Köhler, R. Stegmann, A. Veldkamp, G. Frenking, *Chem. Phys. Lett.* **1993**, *208*, 111; b) A. Höllwarth, M. Böhme, S. Dapprich, A. W. Ehlers, A. Gobbi, V. Jonas, K. F. Köhler, R. Stegmann, A. Veldkamp, G. Frenking, *Chem. Phys. Lett.* **1993**, *208*, 273.
22. M. A. García-Monforte, I. Ara, A. Martín, B. Menjón, M. Tomás, P. J. Alonso, A. B. Arauzo, J. I. Martínez, C. Rillo, *Inorg. Chem.* **2014**, *53*, 12384.
23. S. N. König, D. Schneider, C. Maichle-Mössmer, B. M. Day, R. A. Layfield, R. Anwander, *Eur. J. Inorg. Chem.* **2014**, *2014*, 4302.
24. A. V. Marenich, C. J. Cramer, D. G. Truhlar, *J. Phys. Chem. B.* **2009**, *113*, 6378.
25. J. H. Jensen, *Phys. Chem. Chem. Phys.* **2015**, *17*, 12441.
26. A. Otero-de-la-Roza, E. R. Johnson, V. Luaña, *Comput. Phys. Commun.* **2014**, *185*, 1007.
27. A. Otero-de-la-Roza, M. A. Blanco, A. M. Pendás, V. Luaña, *Comput. Phys. Commun.* **2009**, *180*, 157.
28. R. F. W. Bader, *Chem. Rev.* **1991**, *5*, 893.
29. T. Lu, F. Chen, *J. Comput. Chem.* **2012**, *33*, 580.
30. E. D. Glendening, J, K. Badenhoop, A. E. Reed, J. E. Carpenter, J. A. Bohmann, C. M. Morales, P. Karafiloglou, C. R. Landis, and F. Weinhold, NBO 7.0., Theoretical Chemistry Institute, University of Wisconsin, Madison, **2018**.
31. a) C. L. McMullin, J. Jover, J. N. Harvey, N. Fey, *Dalt. Trans.* **2010**, *39*, 10833; b) C. L. McMullin, N. Fey, J. N. Harvey, *Dalt. Trans.* **2014**, *43*, 13545.

Chapter 5
Bimetallic K/Co amides in C–H metalation

The exception is more interesting than the rule. The rule proves nothing; the exception proves everything. In the exception the power of real-life breaks through the crust of a mechanism that has become torpid by repetition.

– Carl Schmitt

5.1 Introduction

Alkali metal-based bimetallic systems have gained significant prominence in synthetic chemistry due to their capacity to achieve challenging bond activations with high selectivity and functional group tolerance as seen in Chapter 4. Among them, alkali metal magnesiates and zincates have been extensively employed in organic synthesis, particularly for deprotonative metalation,[1–3] metal-halogen exchange,[4–6] and nucleophilic arylation or alkylation of unsaturated organic molecules.[7–10] These unique reactivities have often been ascribed to the cooperative interactions intrinsic to heterobimetallic frameworks, which allow for a fine balance between the nucleophilicity of the metal centres and their stabilising counterions. Notably, such cooperativity also enables the modulation of reactivity through the choice of alkali metal, the nature of the anionic ligands, and the inclusion or omission of Lewis

donors. These cooperative effects are exemplified in key studies involving lithium and sodium, which dominate the majority of heterobimetallic systems reported in the literature.[1]

Despite the rich chemistry observed with lithium and sodium-based systems, structurally defined potassium-containing bimetallic species remain comparatively underexplored, both in terms of synthetic development and application scope.[1] This is somewhat surprising given the potential of potassium to offer distinct electronic and steric properties due to its larger ionic radius and lower charge density. Nonetheless, several instructive cases have demonstrated the capacity of potassium to induce novel structural motifs and reactivity patterns. A prominent example is the deprotonation of naphthalene using the magnesiate [$KMg(TMP)_2Bu$] (TMP = 2,2,6,6-tetramethylpiperidide), leading to the formation of a 24-membered inverse crown structure with six selectively C2-magnesiated naphthalene units hosted within a $\{KNMgN\}_6$ macrocycle.[11] This striking assembly underscores the ability of potassium to support extended architectures that mediate site-specific transformations.

In addition to its role in magnesiates, potassium has shown promise in zincate chemistry, where its incorporation has facilitated the stabilisation of reactive intermediates such as vinyl anions arising from the deprotonation of ethene.[12] These advances have recently been extended into the realm of catalysis, demonstrating that potassium–zinc cooperativity can be harnessed not only in stoichiometric reactions but also in catalytic cycles.[13,14] Motivated by these precedents, recent studies have explored bimetallic systems involving sodium in combination with magnesium and zinc, supported by the bulky and rigid silyl(bis)amide ligand $\{Ph_2Si(NAr^*)_2\}_2$ (Ar* = 2,6-diisopropylphenyl).[15,16] This ligand has been shown to function as both a steric shield, stabilising radical anions[14,17] and low-coordinate species, and a potent Brønsted base, enabling selective deprotonation of N-heterocycles such as N-methyl benzimidazole,[18] ketones,[16] and even small molecules such as benzothiazole.[14] These findings collectively set the stage for the development of new heterobimetallic complexes involving potassium in combination with divalent, earth-abundant metals such as zinc, magnesium, or manganese.

In Chapter 4, the cooperativity between Na and Co was discussed. The key reaction mechanism revealed that the C–H activation transition state involves a pseudo-terminal sodium-amide species, suggesting that the observed reactivity might correlate with the basicity (pK_a) of the AM–amide (alkali metal amide) bases. Interestingly, for the potassium analogue K(HMDS), our experimental collaborators did not observe any reactivity when paired with $Co(HMDS)_2$.

This discrepancy highlights the fact that, despite predictive frameworks based on metal identity and basicity, subtle differences in the coordination environment and dynamics of complex formation can lead to significant deviations. These deviations necessitate a more nuanced and mechanistic understanding, particularly when attempting to rationalise unanticipated reactivity.

A compelling case study in this regard involves the reactivity of potassium and cobalt amides supported by monodentate HMDS ligands. The combination of K(HMDS) and $Co(HMDS)_2$ was originally anticipated, based on the trends discussed earlier, to exhibit limited reactivity in comparison to their lithium and sodium analogues. Yet, in practice, an unexpected and striking C–H activation event was observed by the group of Prof. Hevia. When K(HMDS) was added to neat toluene first, followed by the stepwise addition of $Co(HMDS)_2$ at room temperature, methyl C–H bond activation in toluene was observed, ultimately leading to the formation of a linear coordination polymer, $[\{KCo(HMDS)_2(CH_2Ph)\}_\infty]$. The structure of this product was unambiguously confirmed by XRD.

In stark contrast, when the same reagents were introduced simultaneously under identical conditions, the ion-pair complex $[(K)^+(Co(HMDS)_3)^-]$ was crystalised with no evidence of C–H activation. This clear divergence in reactivity as a function of reagent addition sequence underscores the sensitivity of these bimetallic systems to kinetic and thermodynamic factors, and the critical influence of intermediate formation pathways. Further probing revealed that this phenomenon is also highly substrate specific. In particular, when neat benzene was used in place of toluene, even under sequential addition conditions, no C–H activation was detected. Moreover, reversing the order of addition, by introducing $Co(HMDS)_2$ before K(HMDS), also failed to yield any C–H functionalisation, even in toluene. Additional experiments where benzene served as the solvent and toluene was present only in equimolar amounts similarly resulted in no activation. These results suggest that both the solvent environment and the exact sequence of metal addition play pivotal roles in enabling or suppressing reactivity.

To elucidate the mechanistic underpinnings of this unusual and selective behaviour, DFT calculations were undertaken. These computational studies aimed to identify key intermediates and transition states that could explain the C–H activation in neat toluene under specific reagent addition sequences. The results provide valuable insights into the mechanistic factors governing this reactivity, as well as the design of better reagent through understanding of alkali effect. Through these insights, this chapter provides a broader understanding of alkali effect

modulation and opens new avenues for the design of bimetallic systems tailored for selective C–H bond activation.

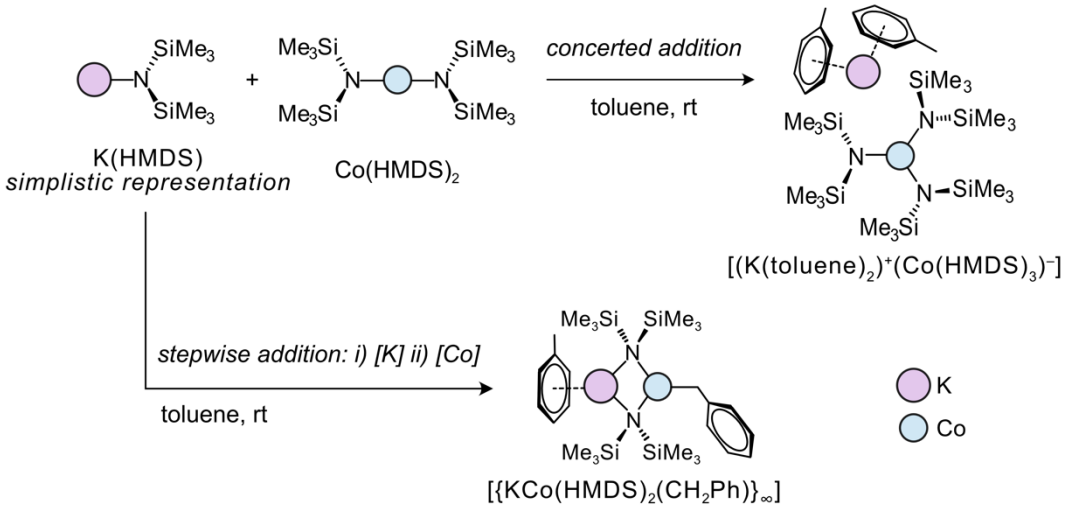

Figure 5.1. Experimental observations for the concerted and stepwise additions of K(HMDS) and $Co(HMDS)_2$ in toluene solution.

5.2 Computational details

The mechanisms for the C–H metalation of toluene were elucidated using DFT calculations, employing the dispersion-corrected hybrid exchange-correlation functional ωB97XD,[19] as implemented in the Gaussian16 software.[20] The Lanl2dz effective core potential and its associated double-zeta basis set, augmented with an *f*-polarisation function (exponent = 2.780), were used to describe Co atoms.[21] Meanwhile, K, Si, C, and H atoms were modelled using the double-zeta 6-31G(d,p) basis set. For the more electronegative N atoms, the 6-31+G(d) basis set, which includes diffuse functions, was applied.

Geometry optimisations were conducted in vacuum without imposing symmetry constraints, using unrestricted open-shell calculations. Co-based complexes were consistently modelled as Co(II) high-spin species, in accordance with experimental magnetic data.[22] The nature of the stationary points was confirmed via vibrational frequency analysis: energy minima exhibited only real frequencies, while transition states displayed a single imaginary frequency corresponding to the desired reaction coordinate. Relaxation of the optimised transition state structures along the reaction coordinate in both directions verified their connection to the expected energy minima.

To account for the solvent effects observed in experiments (toluene and benzene, with dielectric constants ε = 2.3741 and 2.2706, respectively),[23] single-point calculations were performed at the vacuum-optimised geometries using the SMD continuum solvation model. Standard state corrections were applied by adjusting the computed reaction Gibbs energies by ±1.90 kcal mol^{-1} for each additional or removed molecule relative to the products or reactants.[24] All Gibbs energies reported in this chapter were calculated in toluene or benzene at experimental conditions of 298 K and 1 atm and are expressed in units of kcal mol^{-1}. NCI analyses and corresponding plots were generated using the Critic2 software.[25,26] The electron density at critical points was calculated based on the QTAIM formalism via the Multiwfn software.[27] NBO analysis was performed using the converged wavefunctions and structures through the NBO 7.0 software.[28]

5.3 Speciation of K/Co amide complexes

To investigate the C–H activation mechanism of toluene with K(HMDS) and $Co(HMDS)_2$, we began by computing the speciation of the monometallic K(HMDS) and $Co(HMDS)_2$ reagents in toluene solution, as well as the speciation of the bimetallic KCo complexes formed after co-complexation. For the latter, we considered both the contacted and the interacting ion-pairs (IIP), as toluene's non-polar nature renders the formation of solvent-separated ion-pairs (SSIP) unlikely. These speciation analyses are discussed in detail in the following subsections, which outline the determination of the species most likely present in solution for both the concerted and stepwise addition of the K(HMDS) and $Co(HMDS)_2$ reagents.

5.3.1 Monometallic K(HMDS) species

We began by examining the speciation of the monometallic potassium reagents, which is critical for identifying both the potential active species in the stepwise addition and the bimetallic complex formation energy in the concerted addition. NMR experiments indicate that K(HMDS) exists in a monomer-dimer equilibrium in toluene solution, a finding corroborated by computational studies. The dimeric species, $[\{(toluene)K(HMDS)\}_2]$ (**a**), was identified as the most energetically favourable configuration, as depicted in Figure 5.2. The dissociation of one or two toluene molecules from the two potassium atoms (**d**, **e**) was calculated to be endergonic, with Gibbs energies of +5.1 and +10.4 kcal mol^{-1}, respectively.

Monomeric species were also investigated, with 0, 1, and 2 toluene ligands. Coordination of one toluene stabilised the K(HMDS) monomer (**g**) by –3.3 kcal mol^{-1}, while the second toluene (**b**) further stabilised it by –3.6 kcal mol^{-1}. Trimeric species, both with (**c**) and without two toluene ligands (**f**), were considered, following a similar trend where π-coordination with toluene stabilised the trimer by –8.1 kcal mol^{-1}. The formation of the most stable, two-toluene-coordinated monomer (**b**) and trimer (**c**) are also favourable by –6.7 kcal mol^{-1}. This gives rise to an energy difference of +3.7 kcal mol^{-1} between these species (**b**, **c**) and the most stable dimer (**a**). As a result, all three were considered as potential active species for the deprotonation of toluene in the mechanistic search discussed later in Section 5.4.1.

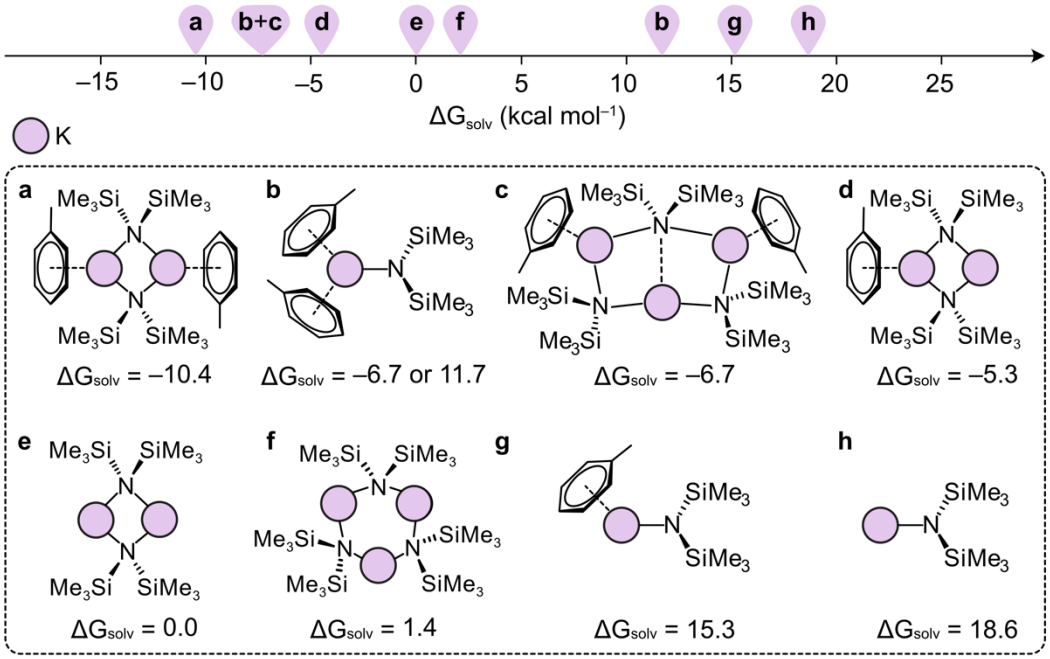

Figure 5.2. Speciation study of oligomeric structures of K(HMDS) in toluene solution, along with their relative Gibbs energies under experimental conditions, reported in kcal mol^{-1} referenced to the species [{K(HMDS)}$_2$] (**e**). The structures range from monomers to higher oligomers (**a-h**), with distinct coordination geometries and binding patterns are displayed ordered by their relative formation energies.

5.3.2 Monometallic Co(HMDS)$_2$ species

The preference for π-coordination in heavier alkali metals has been proposed in the literature and corroborated in the previous section using DFT calculations. This prompted us to explore

whether any π-coordination stabilisation could be observed between toluene and the $Co(HMDS)_2$ complex.

Initially, we investigated the interaction between toluene and the cobalt centre via the phenyl ring. However, this resulted in a weakly interacting toluene with a relative Gibbs energy of +4.5 kcal mol^{-1}. Alternatively, we examined the possibility of an agostic interaction between the methyl group of toluene and the cobalt centre. This interaction was disfavoured, as toluene dissociated during the geometry optimisation process. This outcome aligns with expectations, as the smaller covalent radii of first-row transition metals confer a more *hard acid* character, resulting in very weak binding affinities with soft π-coordinating donors like toluene and benzene. From this speciation study, we determined that the lowest energy cobalt species is $Co(HMDS)_2$. Subsequently, we investigated the formation energies of a series of bimetallic KCo complexes by referencing their energies to those of the corresponding lowest energy monometallic species.

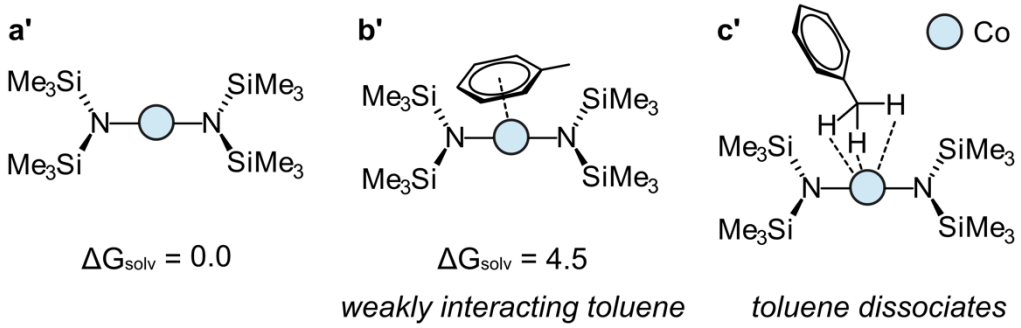

Figure 5.3. Speciation study for the binding of toluene to $Co(HMDS)_2$ in toluene solution, along with their relative Gibbs energies under experimental conditions, reported in kcal mol^{-1} referenced to the species $Co(HMDS)_2$ (**a'**).

5.3.3 Bimetallic $KCo(HMDS)_3$ species

We next considered the possible formation of potassium cobaltate complexes with 0, 1, and 2 molecules of toluene. Among these, coordination with one toluene molecule was the most favourable, resulting in a stabilisation of –6.1 kcal mol^{-1} compared to the bare $[KCo(HMDS)_3]$ (**b***, Figure 5.4). In contrast, coordination of a second toluene molecule, forming $[(toluene)_2KCo(HMDS)_3]$ (**c***), was disfavoured due to steric clashes between the toluene

groups and the methyl groups of the two bridging HMDS ligands. This led to an endergonic Gibbs energy of +0.8 kcal mol^{-1}, indicating that the association of the second toluene molecule is not favourable.

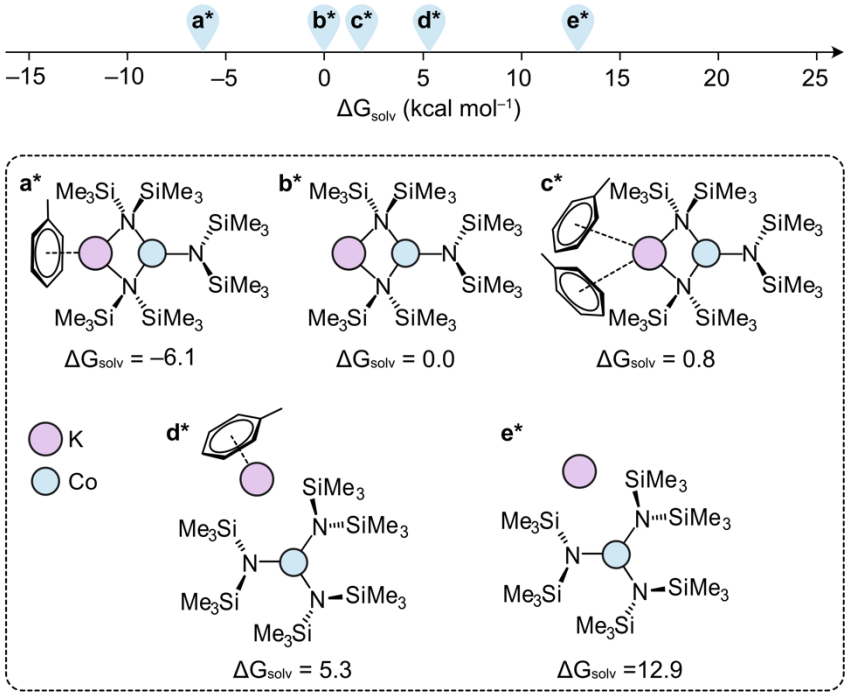

Figure 5.4. Speciation study for the oligomeric structures of [KCo(HMDS)$_3$] in toluene solution, along with their relative Gibbs energies under experimental conditions, reported in kcal mol^{-1} referenced to the species [KCo(HMDS)$_3$] (**b***). The structures (**a-h**) are displayed ordered by their relative formation energies.

In addition to the contacted ion-pairs in Figure 5.4, we examined interacting ion-pairs where the potassium ion behaves more like a cation and interacts weakly via NCIs with the methyl groups of one of the terminal HMDS ligands bound to the cobalt atom. For these interacting ion-pairs, we again evaluated the coordination of 0, 1, and 2 toluene molecules (**e***, **d*** and '**c***'). Coordination of one toluene molecule stabilised the interacting ion-pair by –7.6 kcal mol^{-1}. However, binding of a second toluene molecule proved unstable, with the optimised structure reverting to the same geometry as the contacted ion-pair analogue (**c***). Despite the stabilisation from toluene coordination, the interacting ion-pair (**d***) was less favourable than the contacted ion-pair by +11.4 kcal mol^{-1}. Interestingly, XRD experiments revealed that the isolated species corresponds to the lowest energy interacting ion-pair (**d***).

We hypothesise that this discrepancy arises from additional stabilisation provided by crystal packing of the ion-pairs. We also note that the crystalised structure is not necessarily the same present in solution, as it has been shown in many reports of organometallic reactions in the literature.[29] In summary, DFT predicts the contacted ion-pair with one toluene coordination (**a***) as the most stable bimetallic complex under the experimental conditions. Its formation from one equivalent of dimeric [{(toluene)K(HMDS)}$_2$] and two equivalents of Co(HMDS)$_2$ is thermodynamically favourable, with an overall stabilisation of –21.8 kcal mol^{-1}.

5.4 C–H activation mechanism

The speciation study provided a starting point for the mechanistic investigation, where we considered all the lowest energy intermediates as potential active species for C–H bond cleavage. Experimentally, the reaction was observed only when the reagents were added in a stepwise manner, beginning with K(HMDS) in a solution of toluene, followed by the subsequent addition of Co(HMDS)$_2$. We explored the possibility of the C–H activation step occurring either before or after the addition of Co(HMDS)$_2$. This required the consideration of different species as the most stable in solution for each scenario, which were explicitly analysed in detail.

5.4.1 Monometallic K(HMDS) pathways

First, we considered C–H activation to occur prior to the addition of Co(HMDS)$_2$, where the monometallic potassium complexes are the only possible active species, as no cobalt atoms have yet been introduced to the reaction medium.

Both dimeric and monomeric pathways were investigated, with the dimeric species [{(toluene)K(HMDS)}$_2$] taken as the most stable species and used as the energy reference point. In the monomeric pathway, two molecules of the dimer reaggregate to form one molecule each of the monomer, [(toluene)$_2$K(HMDS)], and the trimer, [(toluene)$_2${K(HMDS)}$_3$]. The alternative dissociation of the dimeric species into the two monomers is less favoured by +22.1 kcal mol^{-1}. The monomer, with two coordinated toluene molecules, undergoes a slight rotation of one toluene, orienting the hydrogen atom towards the N_{HMDS} lone pair, enabling deprotonation. This results in a C–H activation TS with a Gibbs energy of +21.7 kcal mol^{-1} (Figure 5.6), which is feasible for a reaction to occur at room temperature. Relaxation of this

TS along the reaction coordinate yields a high energy potassiation intermediate that lies at +20.0 kcal mol^{-1}.

Subsequently, the intermolecular transfer of the deprotonated toluene from potassium to cobalt requires dissociation of the protonated HMDS(H) ligand to create space for the association of Co(HMDS)$_2$. However, the dissociation of HMDS(H) produces an uphill species with a Gibbs energy of +26.8 kcal mol^{-1}. Considering diffusion-controlled ligand association/dissociation steps (approximately +5.0 kcal mol^{-1}),[31] this pathway results in a rate-limiting step with an overall energy barrier of approximately +31.8 kcal mol^{-1}. Such an energy barrier, exceeding 30 kcal mol^{-1}, renders this pathway unlikely to occur at room temperature.

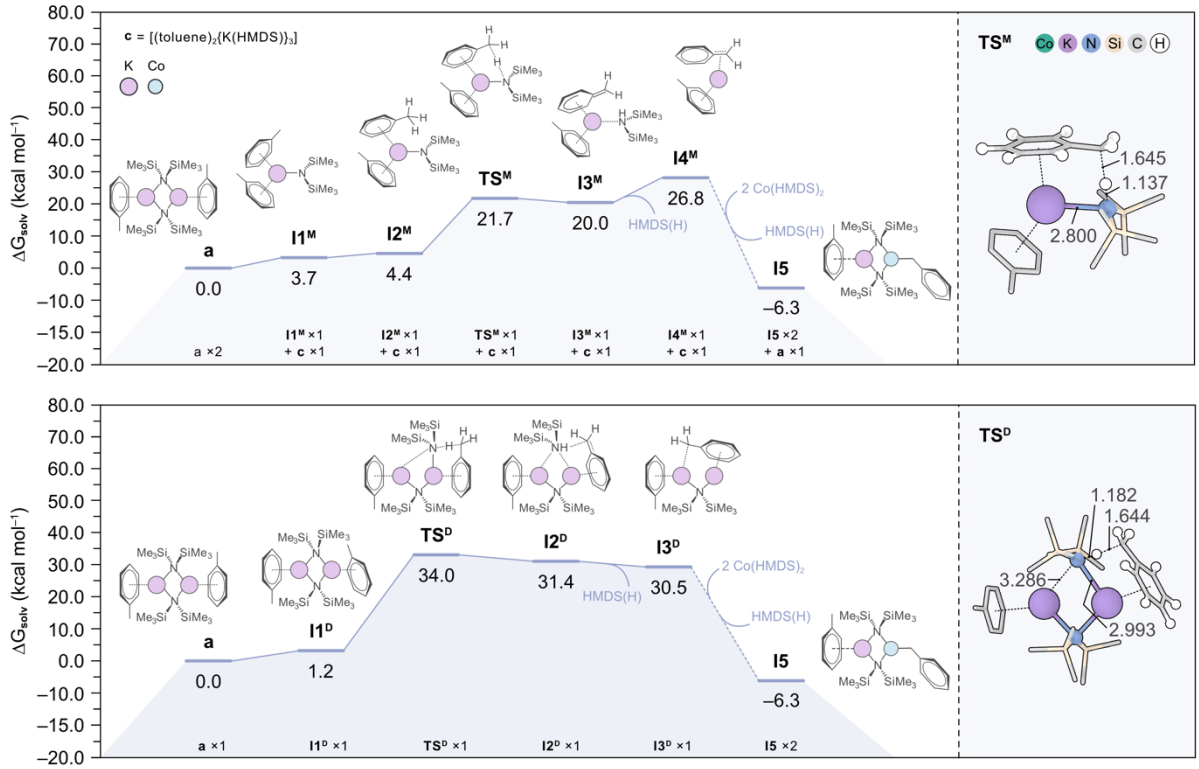

Figure 5.6. Gibbs energy profile calculated in toluene at 298 K and 1 atm for the C–H cobaltation of toluene by considering monomeric [(toluene)$_2$K(HMDS)] (top) and dimeric [{(toluene)K(HMDS)}$_2$] (bottom) as the active species. These are the two possible reaction pathways considered for the C–H activation to occur prior to the addition of Co(HMDS)$_2$ in the stepwise addition experiment. Optimised TS structures are shown as insets (right) with relevant bond distances given in Å.

The dimeric pathway, with [{(toluene)K(HMDS)}$_2$] as the active species, follows a mechanism similar to the monomeric pathway. However, in this case, one of the bridging HMDS ligands must partially dissociate from potassium to form a pseudo-terminally bound HMDS before C–H activation. This adjustment leads to a significantly higher TS compared to the monomeric pathway, with a Gibbs energy of +34.0 kcal mol^{-1}, making the dimeric pathway unfeasible at room temperature. In conclusion, the mechanistic investigation of the monometallic potassium complex as the active species indicates that C–H activation of toluene is unlikely to occur prior to the addition of Co(HMDS)$_2$. These computational results align with experiment observations that K(HMDS) alone cannot active toluene at RT.

5.4.2 Bimetallic KCo(HMDS)$_3$ pathways

As mentioned in Section 5.1, one significant experimental observation is that the reaction occurs only when performed in neat toluene. Toluene, widely recognised for its ability to act as a π-coordinating ligand to heavier alkali metals, including potassium, plays a critical role here. This is supported by our speciation studies, which show that coordination of two toluene molecules to [{K(HMDS)}$_2$] is stabilised by –10.4 kcal mol^{-1} (Figure 5.2). These findings suggest that, upon the addition of Co(HMDS)$_2$ to the solution, the dominant species in solution is the dimeric potassium complex. This species can interact with Co(HMDS)$_2$, leading to the formation of intermediate **I1** (Figure 5.7), where cobalt interacts with the hydrogen atoms of toluene, as highlighted by NCI analysis (ρ = –0.02 a.u., Figure 5.8), typifying weak electrostatic interactions.

It is important to note that co-complexation could potentially interfere with the C–H activation process during this stage. However, the rate of co-complexation remains uncertain. For co-complexation to occur, Co(HMDS)$_2$ must first interact with the potassium atom, necessitating the dissociation of at least one toluene molecule. This step requires +5.1 kcal mol^{-1}, along with an estimated diffusion-controlled barrier of approximately +10.1 kcal mol^{-1} (5.1+5.0=10.1). Additional rearrangements and the formation of the high-energy monomeric species [(toluene)K(HMDS)] (25.7 kcal mol^{-1}, Figure 5.2) further contribute to the energetic cost. Comparing the competition between co-complexation and the formation of **I1**, according to Le Chatelier's principle, the equilibrium between [(toluene){K(HMDS)}$_2$] and **I1** favours the latter, as it does not require toluene dissociation, which would otherwise impede the rate of co-complexation. It is not only governed by the Le Chatelier's principle as the monomeric

potassium species are much higher in energy, thus being the main driving force of **I1** formation instead of monomer Co and K amide co-complexation. While the exact rate of this competing process could not be precisely determined, we assume that the co-complexation process is slow and less favourable than the C–H activation step when reagents are added stepwise.

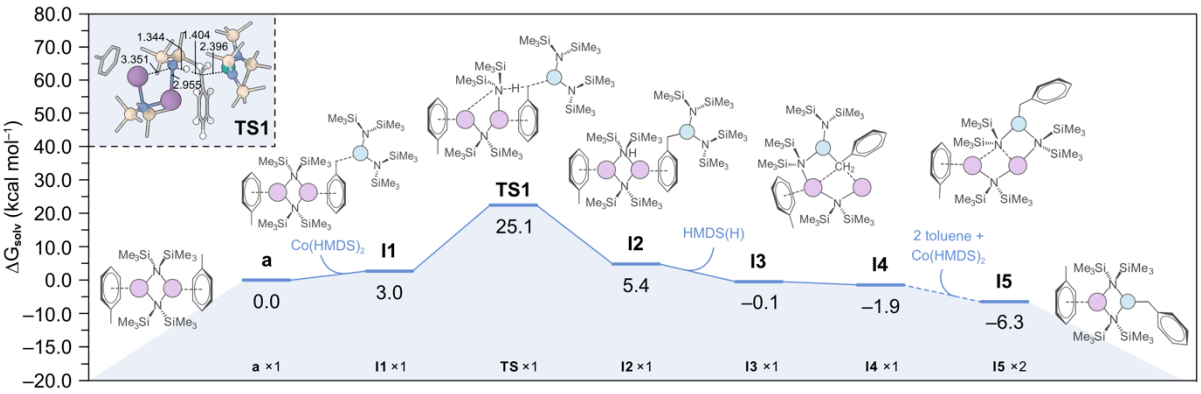

Figure 5.7. Gibbs energy profile calculated in toluene at 298 K and 1 atm for the C–H cobaltation of toluene by considering the dimeric [{(toluene)K(HMDS)}$_2$] as the active species interacting with Co(HMDS)$_2$, during the stepwise addition of Co(HMDS)$_2$. This is the possible reaction pathways considered for the C–H activation to occur prior to the addition of Co(HMDS)$_2$ in the stepwise addition experiment. Detailed structure of the C–H activation **TS1** is shown in the subsets, relevant bond distances are shown in Å.

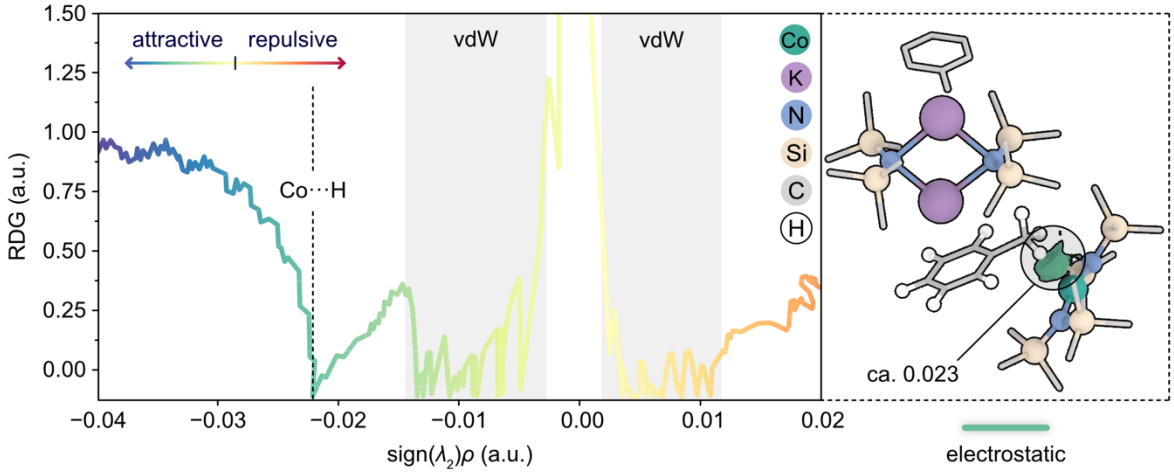

Figure 5.8. NCI analysis on **I1** by plotting the RDG against the sign of the second eigenvalue of the Hessian matrix multiplied by the ρ, sign(λ_2)ρ. The more attractive (repulsive) interactions are denoted by colder (warmer) shade. The most relevant NCIs are depicted in the inset as isosurfaces (isovalue = 0.6 a.u.).

Interaction of $Co(HMDS)_2$ with the sp^3 carbon of toluene results in the partial dissociation of one of the bridging HMDS ligands, allowing it to abstract the proton via a transition state (**TS1**) resembling an S_N2 mechanism. The relatively low barrier of **TS1** (+25.1 kcal mol^{-1}) is attributed to the optimal substrate fit. In this S_N2-like TS, the nearly collinear N–H–C–Co alignment facilitates the reaction, while the negative charge developing on the deprotonated carbon (Mulliken charge = –0.61 a.u.) is delocalised into the π-system (sum to –0.61 a.u.) and stabilised by coordination to the neighbouring potassium atom (with *r*(K–C) = 3.058 Å, 2.976 Å and 3.160 Å.

We also investigated the equivalent TS for the K(HMDS) monomer. This pathway exhibited a slightly higher barrier (+26.7 kcal mol^{-1}), likely due to the lack of flexibility and stabilisation provided by the spectating bridging HMDS ligand. Unlike previously reported mechanisms for NaCo and NaFe complexes, which involve the formation of a sodiation intermediate, the relaxation of **TS1** in this system led directly to the cobaltate intermediate **I2**. In **I2**, the negative charge is delocalised into the π-system, and stabilisation via coordination to the potassium atom is retained. Dissociation of the protonated HMDS(H) ligand gives rise to the trimetallic species **I3**. Subsequent ligand rotation leads to intermediate **I4**, which features a terminal benzyl group bound to cobalt. The reaction proceeds further via a similar mechanism involving another toluene molecule bound to the potassium atom in **I4**, assisted by the approach of a second $Co(HMDS)_2$ molecule. This overall mechanism ultimately results in the formation of two **I5** molecules, with an overall reaction energy of –6.3 kcal mol^{-1}.

Next, we investigated the reaction when the reagents K(HMDS) and $Co(HMDS)_2$ are introduced simultaneously into the toluene solution. Under these conditions, the prior formation of the toluene protected potassium dimer, $[\{(toluene)K(HMDS)\}_2]$, does not occur, leading instead to the direct formation of the potassium cobaltate complex. To confirm the favourability of this species in toluene solution, we compared its formation energy to the most energetically stable monometallic equivalents. Our calculations revealed that the formation of two equivalents of the cobaltate complex, $[(toluene)KCo(HMDS)_3]$, from one equivalent of dimeric $[\{(toluene)K(HMDS)\}_2]$ and two equivalents of $Co(HMDS)_2$ is exergonic by –21.8 kcal mol^{-1}. Assuming that the potassium cobaltate acts as the active species, we found an analogous mechanism to those previously reported for NaCo and NaFe systems.[32] This involves a bimetallic sodiation-like pathway followed by intramolecular transformations, with the key C–H activation TS depicted in Figure 5.9. However, this TS, which represents the rate-

limiting step, has an overall barrier of +44.3 kcal mol^{-1}, indicating that this pathway is not feasible at room temperature.

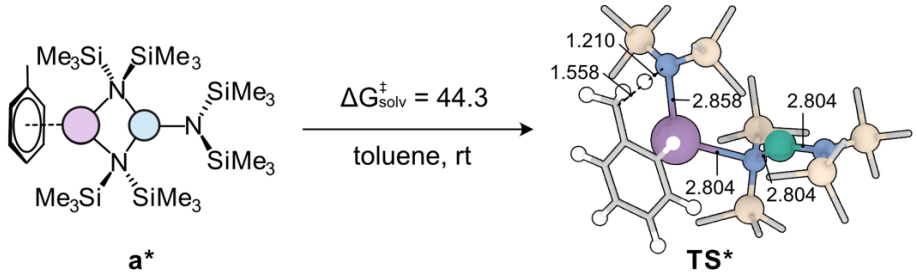

Figure 5.9. Detailed structure of the C–H activation TS considering the bimetallic potassium cobaltate as the active species, calculated at the experimental conditions. The computed activation Gibbs energy is given in kcal mol^{-1}, and relevant bond distances are shown in Å.

The endergonic nature of the product [(toluene)KCo(HMDS)$_2$(benzyl)] (**I5**), with a Gibbs energy of +8.8 kcal mol^{-1} relative to the potassium cobaltate, further confirms that C–H activation is unfavourable after the stable cobaltate [(toluene)KCo(HMDS)$_3$] is formed. The formation of the potassium cobaltate complex acts as a thermodynamic sink; once formed, no further C–H activation can occur. The formation of the cobaltate intermediate, which was experimentally isolated as the IIP form via XRD, provides additional evidence supporting this conclusion. This aligns with experimental observations, where the C–H metalation of toluene does not proceed when the reagents are added in a concerted manner.

5.4.3 C–H activation Substrate Selectivity

Motivated by the promising reactivity observed with the stepwise addition of reagents in a specific order, our collaborators attempted the C–H activation of a similar substrate, benzene, instead of toluene. However, no C–H reactivity was observed. To uncover the properties underlying this selective activation of toluene, we conducted further DFT calculations on benzene to better understand this intriguing reactivity (Figure 5.10). By elucidating the benzene analogue of the **TS1** structure (Figure 5.7), we identified a significantly higher transition state energy of +34.0 kcal mol^{-1}. Additionally, the geometry of this TS is highly distorted, failing to achieve the S_N2-like structure characteristic of a C(sp^2) bond. The strain in this TS arises from the H–C(sp^2) substrate and the rigidity imparted by the benzene ring. In contrast, the toluene substrate exhibits a near perfect *lock-and-key* mechanism, leading to a much more favourable TS energy barrier.

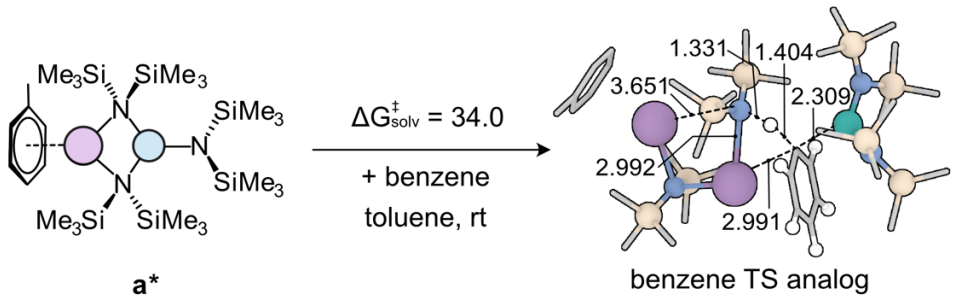

Figure 5.10. Detailed structure of the benzene analogue C–H activation TS considering the bimetallic potassium cobaltate as the active species, calculated at experimental condition with Gibbs energy reported in kcal mol^{-1}, relevant bond distances are shown in Å.

This interesting discovery prompted us to explore whether switching the alkali metal complex from K(HMDS) to Na(HMDS) or Li(HMDS) could further enhance reactivity, owing to their increasing basicity. The results of the effect of the alkali metals are described in detail in the following section.

5.4.4 Alkali metal effect

Utilising the knowledge gained from investigating the mechanism of the KCo system, we noted that TS barriers are generally high when considering the cobaltate as the active species. This is primarily attributed to the low basicity of K(HMDS) compared to Na(HMDS). Based on this, we hypothesised that Na(HMDS) would exhibit higher reactivity than K(HMDS) in a stepwise addition. However, no reaction was observed under identical reaction conditions when Na(HMDS) was used instead of K(HMDS).

As seen the previous sections the reactivity observed for K(HMDS) arises from the formation intermediate **I1** over co-complexation, which is mainly attributed to the favourable binding of toluene to K(HMDS). To investigate this further, we computed the relative binding energies of toluene to smaller alkali metal analogues, namely Li and Na. A. Mohajeri *et al*. provides a model for calculating general binding energies (BE) for alkali metal cation complexes, represented as $(M)^+$(toluene) (M = alkali metal), as illustrated in Figure 5.11. The general trends reported A. Mohajeri's model,[29] $E_{BE}(1a)$, were reproduced with our level of theory, $E_{BE}(1b)$. These trends indicate that binding energies decrease from Li to Na to K. However, this contradicts our experimental observations, where K was reactive for deprotonation while Li and Na were not.

Model by Mohajeri *et al.*

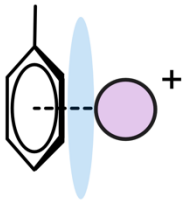

attractive interactions

M	E_{BE}(1a)	E_{BE}(1b)
K	–18.0	–21.4
Na	N/A	–30.8
Li	–38.5	–43.9

*E_{BE}(1): M^+ + toluene → M^+(toluene)

This work

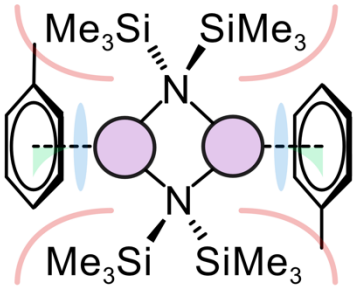

attractive interactions
steric repulsions
steric induced shift in coordination mode

M	E_{BE}(2a)	G_{BE}(2b)
K	–34.4	–10.4
Na	–38.5	–6.7
Li	–32.2	–0.6

*E_{BE}(2): $\{M(HMDS)\}_2$ + 2 toluene → $\{(toluene)M(HMDS)\}_2$

Figure 5.11. Comparative analysis of two models for the interactions of metal–HMDS with toluene. The Mohajeri model represents minimal interactions (left), while the improved HMDS model (right) incorporates attractive interactions (blue), steric repulsions (red), and steric-induced shifts in coordination mode (green). The electronic binding energies (E_{BE}) for different metal cations (K, Na, Li), and the relative Gibbs binding energies (G_{BE}) are shown for our model, all reported in kcal mol^{-1}. The values reflect the strength of interactions and steric effects under experimental conditions. Equations for $E_{BE}(1)$ and $E_{BE}(2)$ are also detailed.

We realised that this model provides a good description for other cationic systems but a poor representation of the steric and electronic contributions of the bridging HMDS ligands, which play a significant role in the relative binding strength of toluene. To address this, we proposed an alternative model in which the association of toluene molecules to the dimeric alkali metal HMDS complexes are calculated (Figure 5.11). This approach better reflects the toluene binding in alkali metal HMDS systems. Notably, if different ligands are used, the trends would vary, and the ligands would need to be included in the chemical model in future studies.

Applying this new model, we calculated the new E_{BE} values, $E_{BE(2a)}$, but they still failed to display the correct experimental trends. We then realised that the electronic energy alone is insufficient, as it neglects entropy contributions, which are important given the variation in toluene coordination modes after geometry optimisation. Instead, we used Gibbs energies, $G_{BE(2b)}$, to establish binding energy trends. This approach, which considers all relevant factors, revealed the correct trend: K (–10.4 kcal mol^{-1}) < Na (–6.7 kcal mol^{-1}) < Li (–0.6 kcal mol^{-1}). As the binding energies become less favourable (more positive) from K to Na to Li, the ability of Co(HMDS)$_2$ to interact with coordinated toluene diminishes (Na and Li), which is essential for promoting C–H metalation reactions (K). For Na and Li analogues, toluene dissociates more readily, facilitating Co(HMDS)$_2$ co-complexation and forming the corresponding metalates, thus a reaction dead end.

The effect of alkali metals on toluene binding affinity was further investigated through NBO analysis in Table 5.1, focusing on molecular orbital interactions within the complexes, particularly charge transfer. All filled donor, *i*, and empty acceptor, *j*, NBO interactions were included in the analysis, with special attention paid to π-interactions with alkali metal cations. These interactions are characterised by the donation of the filled π(C–C) orbital into the acceptor empty non-bonding orbital with antibonding character (*n**) of the cations. The relative stabilisation energy gained from these interactions, E_{SOPT}, was calculated using second-order perturbation theory and is reported in kcal mol^{-1}.

The analysis revealed minimal orbital interactions between the π-orbitals of toluene and the alkali metals in the [{(toluene)M(HMDS)}$_2$] complexes, as indicated by the low E_{SOPT} values shown in Table 5.1. Comparing the two models, the previous model (C_6H_6–M^+) exhibited larger magnitudes of interaction as well as different coordination modes, particularly for the Li complex. For the model reported in this work, no π(C–C) donor orbitals were identified for Li, instead, the σ(C–H) orbitals donate into the *n** orbital of the Li^+ cation. Nonetheless, the $E^{(2)}$ values displayed a trend opposite to that observed for the previously computed G_{BE}. This discrepancy is attributed to other energy contributions that outweigh the stabilisation arising solely from orbital interactions. The weak charge transfer nature of these interactions is further supported by the low charge transfer values (Q_{CT}) reported in Table 5.1, i.e. 0.002, 0.002, and 0.003 a.u. for K, Na, and Li complexes, respectively. These results clarify the non-covalent nature of the M–π interactions.

While NCI analysis could provide additional insight, its semi-quantitative nature makes QTAIM analysis more suitable, particularly for characterising changes in binding modes across alkali metals. QTAIM has been shown to identify π-coordination in borderline cases via a characteristic cage critical point (CCP), while other coordination modes are indicated by bond critical points (BCP), as summarised in Table 5.2. The QTAIM analysis revealed 2, 1, and 0 CCPs for the K, Na, and Li complexes, respectively. This indicates that in the K(HMDS) dimer, both toluene molecules are strongly π coordinated. In contrast, for Na and Li, the toluene molecules are partially dissociated, with no true π-coordination observed in the Li complex. These findings align with the computed G_{BE} trends.

Table 5.1. NBO analysis of Mohajeri literature sample (top three rows) and complete HMDS ligand model (bottom three rows), focusing on donor-acceptor orbital interactions for cation-π and toluene-metal complexes involving K^+, Na^+, and Li^+ ions. This table also contains the donor and acceptor orbitals, the energy gap between the orbitals ($\varepsilon_j - \varepsilon_i$) in a.u., the Fock matrix element ($F_{i,j}$) in a.u., E_{SOPT} in kcal mol^{-1}, and Q_{CT} in a.u. The values illustrate the nature and extent of orbital interactions and charge transfer in different complexes, with notable differences in interaction strength and charge transfer trends across metals.

Complex	Donor orbital	Acceptor orbital	$\varepsilon_j - \varepsilon_i$	$F_{i,j}$	E_{SOPT}	Q_{CT}
C_6H_6–K^+	π(C–C)	n*(K^+)	0.66	0.02	–0.91	0.002
C_6H_6–Na^+	π(C–C)	n*(Na^+)	0.54	0.03	–1.66	0.006
C_6H_6–Li^+	π(C–C)	n*(Li^+)	0.69	0.05	–4.52	0.010
[{(toluene)K(HMDS)}$_2$]	π(C–C)	n*(K^+)	0.50	0.02	–0.61	0.002
[{(toluene)Na(HMDS)}$_2$]	π(C–C)	n*(Na^+)	0.94	0.03	–1.10	0.002
[{(toluene)Li(HMDS)}$_2$]	σ(C–H)	n*(Li^+)	1.03	0.04	–2.07	0.002

Table 5.2. QTAIM analysis for π-system interactions in [{(toluene)M(HMDS)}$_2$] complexes. The table provides data on the nature of CPs, the ρ(r), $\nabla^2\rho$(r) both in a.u., distance between the metal and π-centroid ($R_{centroid}$) in Å, and the angle ($\angle$|C·centroid·M|) for cation interactions with toluene. [1,2] to distinguish the toluene at either side of the complexes, which are interchangeable.

π-system	cation	nature of CPs	ρ(r)	$\nabla^2\rho$(r)	$R_{centroid}$(Å)	$\angle\lvert C \cdot centroid \cdot M\rvert$
Toluene1	K^+	CCP, q(3,+3)	0.0055	0.026	2.972	90.1
Toluene2	K^+	CCP, q(3,+3)	0.0055	0.027	2.970	89.2
Toluene1	Na^+	CCP, q(3,+3)	0.0038	0.019	2.837	91.4
Toluene2	Na^+	BCP, q(3,–1)	0.0078	0.032	2.789	81.1
Toluene1	Li^+	BCP, q(3,–1)	0.0065	0.030	3.291	51.1
Toluene2	Li^+	BCP, q(3,–1)	0.0062	0.030	3.329	49.0

To improve the yield of toluene metalation and to activate less reactive C(sp^3)–H bonds, we propose replacing K with other M(HMDS) complexes. The aim is to establish stronger M^+–toluene (or other substrate) interactions to stabilise intermediate **I1** and the subsequent TS (Figure 5.7), thereby favouring the C–H activation pathway over the co-complexation pathway. Building upon our knowledge, we know that moving down Group 1 metals results in heavier analogues forming stronger bonds with toluene's π-system due to their increased size and decreasing electronegativity. The first candidate we considered was Rb(HMDS). However, Rb-based systems were experimentally found to be much less stable than their analogues and difficult to work with, consequently, we turned to Cs(HMDS) (Figure 5.12).

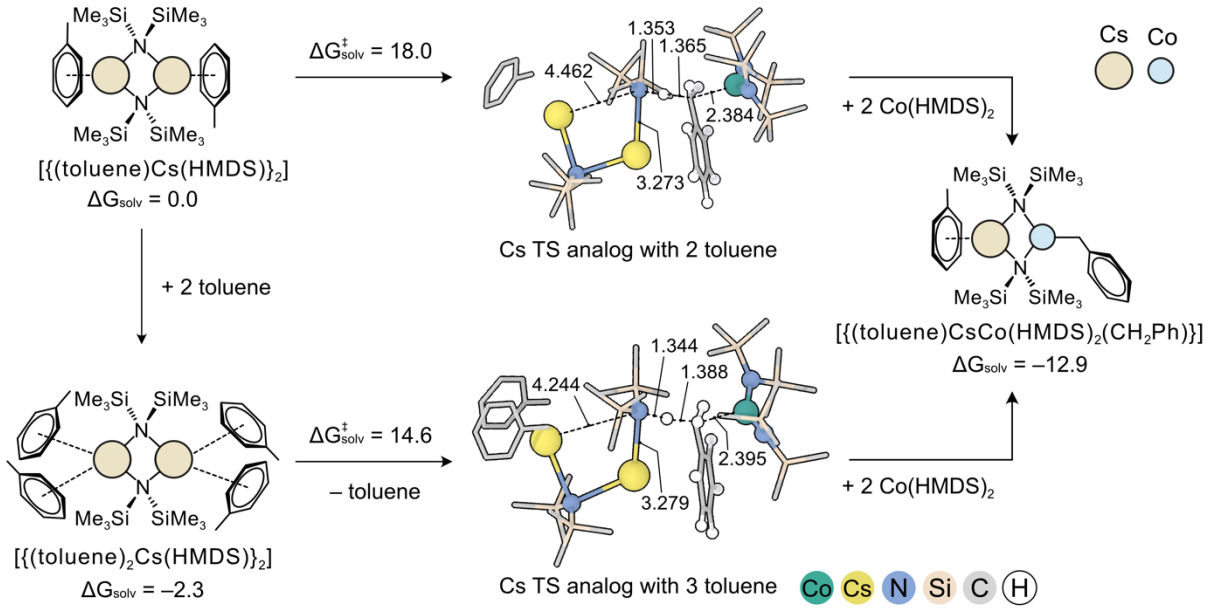

Figure 5.12. DFT-computed Gibbs energies at 298 K and 1 atm in kcal mol^{-1} for the Cs analogous C–H activation of toluene. The top pathway represents the formation of the Cs TS analogue with two toluene molecules, while the bottom pathway shows the analogue TS with three toluene molecules. The relevant bond distances of the TSs are shown in Å.

Initial speciation studies revealed that the dimeric {Cs(HMDS)}$_2$ complex prefers to coordinate with two toluene molecules per Cs atom (Figure 5.12), which results in a more stable [{(toluene)$_2$Cs(HMDS)}$_2$] than [{(toluene)Cs(HMDS)}$_2$] by –2.3 kcal mol^{-1}. The sequential TSs for the configurations involving three and two toluene molecules displayed the same trend, with energy barriers of 20.3 and 14.6 kcal mol^{-1}, respectively. This indicates that the lowest predicted barrier for the Cs system is 14.6 kcal mol^{-1}, significantly lower than the 25.1 kcal

mol^{-1} barrier observed for the K analogue. Thus, C–H activation reactivity is expected to be enhanced by replacing K with Cs.

Additionally, we modelled the analogous Cs product, [(toluene)CsCo(HMDS)$_2$(CH_2Ph)], which is predicted to form favourably in an overall exergonic process by –10.5 kcal mol^{-1} (2.3–12.9). This gives a backward reaction energy of +27.5 kcal mol^{-1} (14.6+12.9), which is slow to occur at room temperature, and the endergonic nature of the reaction will favour metalated product formation. These findings are very encouraging and that we hope our experimental collaborators can confirm this.

5.5 Conclusions

This chapter has explored the intricate reactivity and mechanistic pathways of bimetallic KCo amide systems in the C–H activation of toluene. By combining experimental and computational investigations, the study reveals how subtle changes in reaction conditions, reagent order, and substrate properties significantly influence the outcomes of these transformations.

The research highlights the unexpected reactivity observed with the combination of K(HMD) and Co(HMDS)$_2$ species, particularly the critical role of stepwise reagent addition in facilitating selective methyl C–H activation in toluene. The formation of the linear polymer [{KCo(HMDS)$_2$(CH_2Ph)}$_\infty$], as confirmed by X-ray diffraction, underscores the profound impact of reagent order on reaction pathways. Computational studies described in this chapter provide a detailed mechanistic understanding, including the substrate-specific nature of the reactivity, where benzene fails to undergo C–H activation under analogous conditions. This is attributed to differences in the geometric and electronic properties of the substrates, which influence TS energies. Additionally, the study demonstrates the fundamental role of potassium's ability to π-coordinate with toluene, stabilising intermediates and lowering energy barriers for C–H activation. In contrast, analogous Na and Li systems, despite their higher basicity, do not promote C–H activation due to their weaker toluene binding and higher tendency toward co-complexation.

The introduction of heavier alkali metals, such as Cs, is proposed as a potential avenue to further enhance reactivity. Preliminary computational studies suggest that Cs(HMDS) forms more stable complexes with toluene and exhibits significantly lower barriers for C–H activation

compared to the K analogue. These findings open new possibilities for designing alkali metal–transition metal systems as interacting monometallic reagents with tailored reactivity for substrates C–H bond selectivity.

In summary, this chapter underscores the nuanced interplay of metal speciation, reaction conditions, and substrate properties in governing the reactivity of bimetallic systems. The insights gained pave the way for the rational design of new catalytic systems, advancing our understanding of cooperative alkali metal–transition metal chemistry. Further experimental validation of these findings, particularly with Cs-based systems, is anticipated to deepen our understanding and expand the scope of C–H metalation processes.

References

1. S. D. Robertson, M. Uzelac, R. E. Mulvey, *Chem. Rev.* **2019**, *119*, 8332–8405.
2. A. Harrison-Marchand, F. Mongin, *Chem. Rev.* **2013**, *113*, 7470–7562
3. J. M. Gil-Negrete, E. Hevia, *Dalton Trans.* **2003**, *13*, 2718–2727.
4. D. Tilly, F. Chevallier, F. Mongin, P. C. Gros, *Chem. Rev.* **2014**, *114*, 1207–1257.
5. M. Balkenhohl, P. Knochel, *Chem. Eur. J.* **2020**, *26*, 3688–3697.
6. D. S. Ziegler, B. Wei, P. Knochel, *Chem. Eur. J.* **2019**, *25*, 2695– 2703.
7. M. Dell'Aera, F. M. Perna, P. Vitale, A. Altomare, A. Palmieri, L. C. H. Maddock, L. J. Bole, A. R. Kennedy, E. Hevia, V. Capriati, *Chem. Eur. J.* **2020**, *26*, 8742–8748.
8. M. Hatano, T. Matsumura, K. Ishihara, *Org. Lett.* **2005**, *7*, 573–576.
9. A. Hernán-Gómez, T. D. Bradley, A. R. Kennedy, Z. Livingstone, S. D. Robertson, E. Hevia, *Chem. Commun.* **2013**, *49*, 8659–8661.
10. M. De Tullio, A. Hernán-Gómez, Z. Livingstone, W. Clegg, A. R. Kennedy, R. W. Harrington, A. Antiñolo, A. Martínez, F. Carrillo-Hermosilla, E. Hevia, *Chem. Eur. J.* **2016**, *22*, 17646–17656.
11. A. J. Martínez-Martínez, A. R. Kennedy, R. E. Mulvey, C. T. O'Hara, *Science* **2014**, *346*, 834–837.
12. A. R. Kennedy, J. Klett, R. E. Mulvey, D. S. Wright, *Science* **2010**, *706*, 706–709.
13. W. Clegg, G. C. Forbes, A. R. Kennedy, R. E. Mulvey, S. T. Liddle, *Chem. Commun.* **2003**, *3*, 406–407.
14. Y.-F. Liu, D.-D. Zhai, X.-Y. Zhang, B.-T. Guan, *Angew. Chem. Int. Ed.* **2018**, *57*, 8245–8249.
15. V. L. Blair, W. Clegg, A. R. Kennedy, Z. Livingstone, L. Russo, E. Hevia, *Angew. Chem. Int. Ed.* **2011**, *50*, 9857–9860.
16. P. Mastropierro, Z. Livingstone, S. D. Robertson, A. R. Kennedy, E. Hevia, *Organometallics* **2020**, *39*, 4273–4281.
17. Z. Livingstone, A. Hernán-Gómez, S. E. Baillie, D. R. Armstrong, L. M. Carrella, W. Clegg, R. W. Harrington, A. R. Kennedy, E. Rentschler, E. Hevia, *Dalton Trans.* **2016**, *45*, 6175–6182.
18. D. R. Armstrong, W. Clegg, A. Hernán-Gómez, A. R. Kennedy, Z. Livingstone, S. D. Robertson, L. Russo, E. Hevia, *Dalton Trans.* **2014**, *43*, 4361.
19. J.-D. Chai, M. Head-Gordon, *Phys. Chm. Chem. Phys.* **2008**, *10*, 6615.
20. Gaussian 16, Revision E.01, M. J. Frisch, G. W. Trucks, H. B. Schlegel, G. E. Scuseria, M. A. Robb, J. R. Cheeseman, G. Scalmani, V. Barone, G. A. Petersson, H. Nakatsuji, X. Li, M. Caricato, A. V. Marenich, J. Bloino, B. G. Janesko, R. Gomperts, B. Mennucci, H. P. Hratchian, J. V. Ortiz, A. F. Izmaylov, J. L. Sonnenberg, D. Williams-Young, F. Ding, F. Lipparini, F. Egidi, J. Goings, B. Peng, A. Petrone, T. Henderson, D. Ranasinghe, V. G. Zakrzewski, J. Gao, N. Rega, G. Zheng, W. Liang, M. Hada, M. Ehara, K. Toyota, R. Fukuda, J. Hasegawa, M. Ishida, T. Nakajima, Y. Honda, O. Kitao, H. Nakai, T. Vreven, K. Throssell, J. A. Montgomery, Jr., J. E. Peralta, F. Ogliaro, M. J. Bearpark, J. J. Heyd, E. N. Brothers, K. N. Kudin, V. N. Staroverov, T. A. Keith, R. Kobayashi, J. Normand, K. Raghavachari, A. P. Rendell, J. C. Burant, S. S. Iyengar, J. Tomasi, M. Cossi, J. M. Millam, M. Klene, C. Adamo, R. Cammi, J. W. Ochterski, R. L. Martin, K. Morokuma, O. Farkas, J. B. Foresman, and D. J. Fox, Gaussian, Inc., Wallingford CT, 2016.
21. a) A. W. Ehlers, M. Böhme, S. Dapprich, A. Gobbi, A. Höllwarth, V. Jonas, K. F. Köhler, R. Stegmann, A. Veldkamp, G. Frenking, *Chem. Phys. Lett.* **1993**, *208*, 111; b) A. Höllwarth, M. Böhme, S. Dapprich, A. W. Ehlers, A. Gobbi, V. Jonas, K. F. Köhler, R. Stegmann, A. Veldkamp, G. Frenking, *Chem. Phys. Lett.* **1993**, *208*, 273.

22. S. N. König, D. Schneider, C. Maichle-Mössmer, B. M. Day, R. A. Layfield, R. Anwander, *Eur. J. Inorg. Chem.* **2014**, *2014*, 4302.
23. A. V. Marenich, C. J. Cramer, D. G. Truhlar, *J. Phys. Chem. B,* **2009**, *113*, 6378.
24. J. H. Jensen, *Phys. Chem. Chem. Phys.* **2015**, *17*, 12441.
25. A. Otero-de-la-Roza, E. R. Johnson, V. Luaña, *Comput. Phys. Commun.* **2014**, *185*, 1007.
26. A. Otero-de-la-Roza, M. A. Blanco, A. M. Pendás, V. Luaña, *Comput. Phys. Commun.* **2009**, *180*, 157.
27. a) R. F. W. Bader, *Chem. Rev.* **1991**, *5*, 893; b) T. Lu, F. Chen, *J. Comput. Chem.* **2012**, *33*, 580.
28. E. D. Glendening, J, K. Badenhoop, A. E. Reed, J. E. Carpenter, J. A. Bohmann, C. M. Morales, P. Karafiloglou, C. R. Landis, and F. Weinhold, NBO 7.0., Theoretical Chemistry Institute, University of Wisconsin, Madison, **2018**.
29. A. Mohajeri, E. Karimi, *J. Mol. Struct. THEOCHEM*, **2006**, *774*, 71.
30. M. D. Haynes, A. O'Reilly, A. J. M. Poole, A. F. Roper, S. Thum, L. J. Morris, M. P. Coles, J. R. Fulton, S. Harder, Z. R. Turner, D. O'Hare, *Dalton Trans*., **2025**, *54*, 4542.
31. a) C. L. McMullin, J. Jover, J. N. Harvey, N. Fey, Dalt. Trans. 2010, 39, 10833; b) C. L. McMullin, N. Fey, J. N. Harvey, Dalt. Trans. 2014, 43, 13545.
32. a) L. C. H. Maddock, M. Mu, A. R. Kennedy, M. García-Melchor, E. Hevia, Angew. Chem. Int. Ed. 2021, 60, 15296–15301; b) A. Logallo, M. Mu, M. García-Melchor, E. Hevia, Angew. Chem. Int. Ed. 2022, 61, e202213246.

Chapter 6
Monometallic Fe/Co amides in C–H metalation

Name the greatest of all inventors. Accident.
– Mark Twain

6.1 Introduction

Among s-block metal amides, TMP has earned a distinctive reputation due to its extensive utility in facilitating selective C–H bond deprotonation across a broad range of aromatic substrates.[1] Prototypes such as Li(TMP), and its more reactive congener (TMP)Mg(Cl)·Li(Cl) (a so-called Turbo-Hauser base), have showcased how the combination of strong basicity with minimal nucleophilicity can lead to highly controlled metalation processes.[2] TMP's cyclic scaffold, bearing two geminal dimethyl groups on each α-carbon, not only contributes to its basic strength but also imposes significant steric hindrance, characteristics that define its effectiveness in synthetic applications.[3]

Pioneering studies by Knochel, Mulvey, and Uchiyama have established the remarkable basicity of TMP in bimetallic frameworks, particularly those incorporating alkali-metal partners with zinc, magnesium, and aluminium.[4] These heterobimetallic platforms offer synergistic effects that boost both reactivity and site-selectivity, setting them apart from their monometallic analogues.[5] In many of these systems, TMP is not a passive spectator but a central actor; when replaced with alternative amides, a notable decline in reactivity is typically observed.[6]

Despite its prominence in main group chemistry, TMP's incorporation into transition metal complexes remains relatively underexplored. Only a few scattered reports suggest potential for TMP-supported iron or cobalt species to effect arene metalation. For instance, Knochel described a salt-metathesis approach wherein $Fe(Cl)_2{\cdot}Li(Cl)$ reacts with two equivalents of $(TMP)Mg(Cl){\cdot}Li(Cl)$ to afford an in situ $Fe(TMP)_2{\cdot}2(Mg(Cl)_2){\cdot}4(Li(Cl))$ mixture that can metalate electron-rich arenes, presumably forming $Fe(Ar)_2$ intermediates that participate in C–C bond formation.[7] However, the true identity of these iron species, as well as the role played by lithium and magnesium salts in stabilising or activating them, remains poorly resolved. Similarly, Mongin and co-workers generated $Co(TMP)_2$ by combining $Co(Br)_2$ with Li(TMP) in THF and used it in conjunction with excess Li(TMP) to deprotonate substituted anisoles,[8] though again, no structural or mechanistic characterisation was provided.

This gap in understanding is particularly striking when juxtaposed with the well-established literature on $M(HMDS)_2$ complexes (M = Fe, Co), which date back over sixty years.[9] These bis(silylamide) compounds have served as versatile precursors for accessing lower oxidation states, and have shown considerable utility in catalytic applications such as hydrosilylation and alkyne cyclotrimerisation.[10] Yet their ability to engage in deprotonative metalation is generally limited to highly acidic substrates like alcohols or secondary phosphines,[11] and they have proven unreactive towards the more inert C–H bonds of arenes. As discussed in Chapter 4, our research previously demonstrated that sodium amide NaHMDS, when paired with $M(HMDS)_2$ (M = Fe, Co), forms highly reactive bimetallic complexes capable of regioselective C–H activation in fluoroarenes.[12] Mechanistic insights revealed that initial arene metalation occurs via the sodium amide, with subsequent transmetalation to iron or cobalt, either intermolecularly or intramolecularly.[12a,c] Crucially, $M(HMDS)_2$ alone was found to be completely unreactive

with pentafluorobenzene under all tested conditions, reinforcing the critical cooperative role played by the alkali-metal component in enabling activation.

Motivated by these findings, and the general absence of well-defined TMP-transition metal complexes, we wanted to identify and suggest promising synthetic targets being new Fe(II) and Co(II) systems ligated by TMP. Our working hypothesis was that replacing HMDS with TMP in sodium amide complexes would enhance Lewis acidity and promote the formation of new reactive species. Specifically, we envisioned that reacting $Fe(HMDS)_2$ with Na(TMP) might yield a mixed-ligand species such as [Na(μ-TMP)$Fe(HMDS)_2$] which then performs C–H activation. However, previous DFT study pointed also to the formation of a tris(TMP) structure, [$NaFe(TMP)_3$], as the reactive species, a conclusion subsequently supported by X-ray diffraction.[12] Yet in attempts to isolate tris(TMP) complex directly, an unexpected outcome occurred: the crystallisation of a low-coordinate species, $Fe(TMP)_2$ (1^{Fe}), with formally Fe(II) oxidation state.[13] This di-coordinated iron complex proved particularly intriguing. While three- and six-coordinate Fe(II) and Co(II) species are widely known,[14–16] true di-coordinate analogues remain rare, especially outside of constrained ligand environments. In organometallic design, enhancing the reactivity of complexes is often approached by accessing high oxidation states or minimising coordination numbers to create open coordination sites.

The reactivity of $Fe(TMP)_2$ was explored experimentally using pentafluoroarene as a model substrate. When this reaction was performed in THF, both TMP ligands acted as bases, leading to the formation of [$(THF)_2Fe(C_6F_5)_2$], thereby demonstrating unexpected polybasic character (Figure 6.1). In contrast, performing the same transformation in benzene, a weak coordinating solvent, resulted in monobasic activation and the formation of the dimeric species [{Fe(μ-TMP)(C_6F_5)}$_2$] (2^{Fe}), confirmed by XRD analysis. These results underline the profound influence of solvent coordination on the expression of basicity and reactivity. To probe whether this behaviour extended to cobalt, the tri-coordinate complex [$(THF)Co(TMP)_2$] ($1^{Co–THF}$) was studied first. The $Co(TMP)_2$ (1^{Co}) was subsequently isolated and structurally characterised to be analogous to $Fe(TMP)_2$, despite being similar in geometry and stability to its iron counterpart, $Co(TMP)_2$ showed no polybasicity in either THF or benzene (Figure 6.1). These findings are notable on multiple fronts. First, they confirm that TMP is capable of stabilising highly unsaturated Fe(II) and Co(II) centres without requiring bulky or chelating ligands. Second, they reveal an exceptional, and unprecedented polybasic character in $Fe(TMP)_2$, not

observed in analogous alkali-metal amides or in related Fe-based ate complexes. The absence of such behaviour in $Co(TMP)_2$ highlights the importance of subtle electronic effects in shaping reactivity patterns.

To rationalise these observations, DFT calculations were employed to assess the electronic structure, coordination geometries, and relative basicity of different species. These studies illuminate the energetic landscapes governing reactivity and help explain why only the iron complex displays dual deprotonation reactivity under certain conditions. The insights gained here not only deepen our understanding of transition metal amide chemistry but also point toward new design strategies for alkali-free C–H activation using earth-abundant metals, which will be discussed in detail in the following sections.

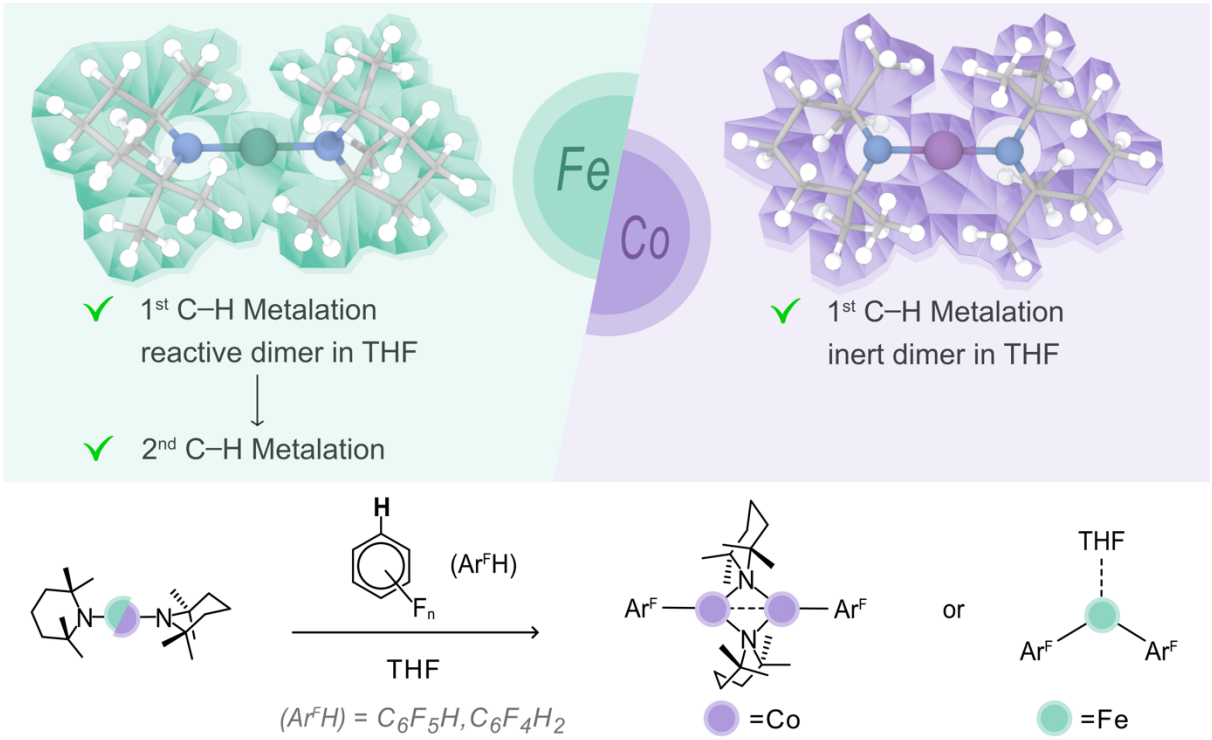

Figure 6.1. Summary of experimental findings for the C–H activation reactivity of $Fe(TMP)_2$ and $Co(TMP)_2$ with pentafluoroarene in THF.

6.2 Computational details

The reaction pathways discussed in the following sections were investigated using DFT calculations with the dispersion-corrected hybrid exchange-correlation functional ωB97XD,[17] as implemented in the Gaussian09 software.[18] The computational methodology outlined here was benchmarked against experimentally obtained XRD structures of Fe/Co(TMP)$_2$ and the corresponding dimer [{Fe/Co(μ-TMP)(C_6F_5)}$_2$]. The calculations reproduced the connectivity and key metal ligand bond distances observed experimentally, providing confidence in the chosen level of theory.

To balance computational cost and accuracy, Fe and Co atoms were described using the Lanl2dz effective core potential and its associated double-zeta basis set, augmented with an *f*-polarisation function (exponents = 2.780 and 2.462, respectively).[19] C and H atoms were modelled with the double zeta 6-31g(d,p) basis set, while the more electronegative nitrogen, oxygen, and fluorine atoms were treated with the 6-31+g(d,p) basis set. Geometry optimisations were conducted in vacuum without imposing any symmetry constraints. In all calculations, dimer and monomer, Fe and Co were modelled in the high-spin +2 oxidation state, consistent with experimental magnetic data.[13] For the dimeric complexes [{Fe/Co(μ-TMP)(C_6F_5)}$_2$], broken-symmetry DFT calculations were performed to account for antiferromagnetic coupling,[13] as suggested by experimental observations. These calculations yielded optimised structures with spin populations of +3.73/–3.73 for Fe, and +2.62/–2.61 for Co.

The nature of all stationary points was verified through vibrational frequency analysis. Energy minima were characterised by the absence of imaginary frequencies, while transition states displayed a single imaginary frequency corresponding to the desired reaction coordinate. Furthermore, optimised transition states were relaxed in both directions along the reaction coordinate to ensure they connected the expected energy minima. The NCI and IGM analysis and corresponding plots were obtained using the Critic2 software.[20,21] The electron density at the critical points was calculated by QTAIM[22] using the Multiwfn software.[23] NBO analysis was computed using the converged wavefunctions and structures through the NBO 7.0 software.[24]

6.3 Exploring solvent effects

The calculations were primarily performed in vacuum. To account for solvent effects, several methodologies were employed, broadly categorised into implicit and explicit models, as introduced in Chapter 2. For non-polar solvents, such as benzene and n-pentane, commonly used in this project, the implicit approach was adopted. Solvent effects were incorporated using the SMD continuum solvation model with dielectric constants of $\varepsilon = 2.2706$ for benzene, and $\varepsilon = 1.8371$ for n-pentane.[25] For more polar and coordinating solvents, such as THF ($\varepsilon = 7.4257$), the SMD solvation model was initially applied. However, it was noted that this model struggled to capture the strong coordinating ability of THF and tended to overestimate the translational entropy cost associated with THF binding. To address these limitations, various alternative approaches were benchmarked against experimentally measured THF binding constants. These included SMD, conductor-like polarizable continuum model (CPCM),[26] and a hybrid approach, which will be discussed in detail below.

6.3.1 A hybrid solvation method for THF binding energies

The investigation began by focusing on the deprotonation of two equivalents of pentafluoroarene by $Fe(TMP)_2$ in THF solvent. To understand how the reaction proceeds, identifying the most stable species in solution was a priority. Initial calculations employed the implicit SMD solvation model. The binding of THF to $Fe(TMP)_2$ to form the tri-coordinate species, $[(THF)Fe(TMP)_2]$, was considered, yielding a SMD computed Gibbs binding energy of +5.5 kcal mol^{-1}. Similarly, the binding energy of THF to $Co(TMP)_2$ was computed at +1.2 kcal mol^{-1}. These computational results were compared with experimentally measured THF binding constants derived from ^1H NMR titrations, $^{Fe}K_{eq} = 0.44\ M^{-1} \pm 0.47\ \%$ and $^{Co}K_{eq} = 113.61\ M^{-1} \pm 11.58\ \%$. The experimental data revealed significantly stronger binding of THF to $Co(TMP)_2$ than predicted, contradicting the computed endergonic binding energy of +1.2 kcal mol^{-1}. Moreover, significant formation of $[(THF)Fe(TMP)_2]$ in solution was observed in ^1H NMR experiments, indicating that $Fe(TMP)_2$ exists in equilibrium with its coordinated species. This suggests the actual binding energy for $Fe(TMP)_2$ is less endergonic than +5.5 kcal mol^{-1}. These discrepancies highlight limitations of the implicit solvation approach in accurately describing the binding of THF to Fe and Co complexes. This is attributable to THF's strong coordinating nature and its large excess in solution, where traditional implicit models fail to

account for the translational entropy penalty of THF molecules modelled as if coming from infinite distance. There are many different approaches that have been adopted to address this issue, some of which are summarised in the Computational methods section of my PhD thesis (p. 40, and refs. 128–137).

Prior to identifying the most suitable hybrid approach, other solvation models were explored. The first alternative considered was the conductor-like implicit solvation approach, specifically CPCM as implemented in Gaussian09. Given the higher polarity of THF compared to benzene, it was hypothesised that THF might be better represented as a conducting medium, allowing for improved modelling of electrostatic interactions in the surrounding solvent environment. While this approach slightly improved the Gibbs binding energies, yielding values of –2.0 kcal mol^{-1} and +3.6 kcal mol^{-1} for Fe and Co, respectively, it remained inconsistent with experimental observations. It became clear that a model accurately describing THF as individual molecules was needed to address the overestimation of translational entropy. Explicit solvation models or cluster solvation models were not pursued, as the bulk structure of THF has been less extensively studied compared to water. Furthermore, no readily available optimised bulk THF structures exist in the literature. Developing a reliable and representative bulk structure for THF would exceed the scope of this study.

Another model considered was COSMO-RS, which approximates each THF molecule as a three-dimensional shape with its surface representing the electrostatic potential mapped onto it.[27] This approach simulates the perception of viewing a “blurred” version of the molecule, focusing on its overall shape rather than the detailed interactions of individual electrons and atoms. Consequently, this method significantly accelerates optimisation while still accounting for critical electrostatic and hydrogen-bonding interactions. This model yielded satisfactory results comparable to those obtained using the hybrid solvation model approach, showing the correct trend with both THF binding to the Fe amide is in equilibrium, and binding to the Co amide is favourable in energy. However, as the data was generated using a trial version of COSMO-RS, license issue prevent its inclusion in this work. The similarity of the results provided further validation for the hybrid solvation model approach.

Ultimately, the hybrid model was employed throughout this study, balancing computational cost and accuracy. The limitations of this hybrid model will also be discussed in the following

sections. In this hybrid approach, explicit solvent molecules involved in association and dissociation processes with the active organometallic complexes were included in the same simulation. Unlike traditional approaches, where energy references are established with reactants and solvents in separate solute cavities, the hybrid method considers the zero of energy as the metal complex [Fe/Co(TMP)$_2$] and an uncoordinated THF molecule optimised together in vacuum. Gibbs solvation energies were then obtained using the implicit SMD method. This approach successfully eliminated the overestimated translational entropy penalty, providing more accurate Gibbs binding energies of −1.1 kcal mol^{-1} for Fe and −6.7 kcal mol^{-1} for Co, consistent with experimental data. These findings identified [(THF)Fe/Co(TMP)$_2$] as the resting state in solution.

Table 6.1. Summary of experimental and computed Gibbs binding energies (in kcal mol^{-1}).

	Experimental*	**SMD**	**Hybrid method**	**CPCM**
Fe(TMP)$_2$ + THF → [(THF)Fe(TMP)$_2$]	+0.48	+1.2	–1.1	–2.0
Co(TMP)$_2$ + THF → [(THF)Co(TMP)$_2$]	–2.8	+5.5	–6.7	+3.6

* The experimental values were obtained from titration experiments involving the gradual addition of a THF solution to a benzene solution of Co/Fe(TMP)$_2$. The relative concentrations of THF-bound and unbound species were determined by NMR spectroscopy between additions.

The placement of solvent molecules in explicit solvation models, including the hybrid approach, has often been debated. Despite the apparently arbitrary positioning, careful considerations were taken when building input structures: i) solvent molecule positions were kept consistent throughout the reaction profile; ii) donor molecules were positioned to avoid blocking reactive regions or interfering with substrate interactions; and iii) ligand dispositions maximised stabilising NCIs while minimising steric clashes, particularly with the methyl groups of the TMP ligand. Consequently, in this study, THF was consistently placed at the rear end of the spectator TMP ligand, which does not participate in the C–H activation step.

6.4 C–H metalation mechanism

6.4.1 1st C–H metalation mechanism in THF

We began investigating the reaction mechanism for the first deprotonation of pentafluoroarene with [(THF)Fe/Co(TMP)$_2$] in THF solvent. The reaction initiates with the dissociation of the THF molecule from the metal centers, resulting in the formation of a vacant site and di-coordinated Fe and Co(TMP)$_2$ species. This step is associated with a slightly uphill energy of 1.1 and 6.7 kcal mol^{-1}, respectively.

The relative stability of these di-coordinate species was unexpected as it is common for the Fe and Co to be in higher coordination numbers of 6 or 4. To gain further insight, we performed NBO analyses to examine the bonding interactions between the metal centers (Fe and Co) and the nitrogen atoms in the TMP ligand. For this analysis, an energy cut-off of 5.0 kcal mol^{-1} was applied, considering only orbital overlaps with ΔE_{SOPT} values exceeding this threshold as significant contributors to the complex's stability. The major donor-acceptor interactions identified are summarised in Figure 6.2 and Table 6.2, with ΔE_{SOPT} values of –35.88 and –36.36 kcal mol^{-1} for Fe and Co, respectively. These interactions involve the lone pair on the nitrogen atom of TMP donating into the anti-bonding orbital of the metal-nitrogen bond. The donating nitrogen lone pair exhibits sp^3 hybridisation, while the acceptor orbital, despite being an anti-bonding metal nitrogen orbital, primarily comprises the metal's *s* orbital, accounting for approximately 87% for both Fe and Co.

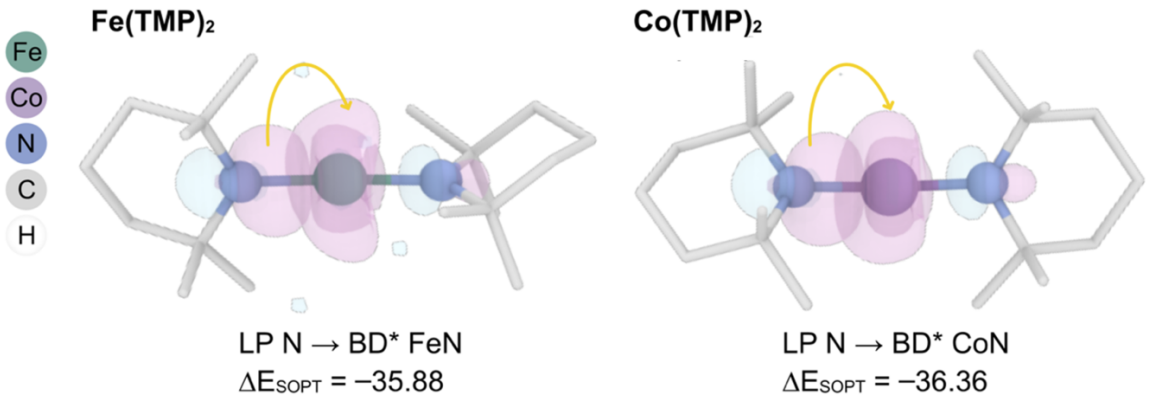

Figure 6.2. Representation of the isosurfaces (isovalue = 0.06 a.u) of strongest donor-acceptor NBO interactions for complexes Fe(TMP)$_2$ and Co(TMP)$_2$ (detailed in Table 6.2). The yellow arrows indicate the direction of electron donation (from the donor to the acceptor). All H atoms have been omitted for clarity. The computed ΔE_{SOPT} values are given in kcal mol^{-1}.

In addition to these dominant interactions, other significant donor-acceptor contributions were identified (Table 6.3). These primarily involve the donation of the N_{TMP} lone pair into the Rydberg orbitals of the metal and back-donation from the metal's *d*-orbital lone pair into the Rydberg orbitals of N_{TMP}. The total ΔE_{SOPT} values are –85.7 kcal mol^{-1} for Fe and –72.22 kcal mol^{-1} for Co, indicating a greater stabilisation of TMP with Fe. This difference explains the crystallisation of the low-valent $Fe(TMP)_2$ species, whereas for Co, the tri-coordinate species $[(THF)Co(TMP)_2]$ was observed and characterised through XRD analysis.

Table 6.2. Strongest NBO donor-acceptor interactions are shown in Figure 6.2, wherein the lone pair from the N_{TMP} acts as the donor. The antibonding orbital of M–N_{TMP} (M = Fe and Co) acts as the acceptor. ΔE_{SOPT} energies are reported in kcal mol^{-1}. The natural atom orbitals contributions are also given in percentage.

Complex	***Donor***	***Contribution***	***Acceptor***	***Contribution***	ΔE_{SOPT}
$Fe(TMP)_2$	LP (2) N2	*s* (28%) *p* (72%)	BD*(1) Fe1–N30	93% Fe *s* (95%) *d* (5%) 7% N *s* (30%) *p* (70%)	–35.88
$Co(TMP)_2$	LP (2) N29	*s* (27%) *p* (73%)	BD*(1) N1–Co57	92% Co *s* (95%) *d* (5%) 8% N *s* (30%) *d* (70%)	–36.36

Table 6.3. Detailed NBO analysis, including all the donor-acceptor interactions involved in the M–N_{TMP} bond with a cut-off of ΔE_{SOPT} = –5.0 kcal mol^{-1}, wherein donation and back donation between M and N_{TMP} are involved. LP, BD, BD*, RY denote lone pairs, bonding, antibonding and Rydberg orbitals, respectively. ΔE_{SOPT} energies are given in kcal/mol. The natural atom orbitals contributions are also given in percentage.

Complex	***Donor***	***Contribution***	***Acceptor***	***Contribution***	ΔE_{SOPT}
$Fe(TMP)_2$	LP (2) N2	*s* (28%) *p* (72%)	RY(6) Fe1	*s* (23%) *p* (60%)	–6.75
$Fe(TMP)_2$	LP (2) N2	*s* (28%) *p* (72%)	RY(8) Fe1	*s* (24%) *p* (61%) *d* (15%)	–6.09
$Fe(TMP)_2$	LP (2) N2	*s* (28%) *p* (72%)	RY(12) Fe1	*s* (24%) *d* (75%)	–6.38
$Fe(TMP)_2$	LP (2) Fe1	*s* (5%) *d* (95%)	BD*(1) Fe1–N30	93% Fe *s* (95%) *d* (5%) 7% N *s* (30%) *p* (70%)	–5.30
$Fe(TMP)_2$	LP (2) Fe1	*s* (5%) *d* (95%)	RY(2) N30	*s* (17%) *p* (81%)	–12.34
$Fe(TMP)_2$	LP (2) Fe1	*s* (5%) *d* (95%)	RY(2) N2	*s* (17%) *p* (81%)	–12.33
$Co(TMP)_2$	LP (2) N29	*s* (27%) *p* (73%)	RY(5) Co57	*s* (53%) *p* (27%) *d* (20%)	–6.46
$Co(TMP)_2$	LP (2) N29	*s* (27%) *p* (73%)	RY(7) Co57	*s* (24%) *p* (67%) *d* (9%)	–5.39

$Co(TMP)_2$	LP (2) N29	*s* (27%) *p* (73%)	RY(12) Co57	*s* (16%) *p* (2%) *d* (82%)	–5.78
$Co(TMP)_2$	LP (5) Co57	*s* (4%) *d* (96%)	RY(2) N1	*s* (10%) *p* (88%) *d* (1%)	–9.12
$Co(TMP)_2$	LP (5) Co57	*s* (4%) *d* (96%)	RY(2) N29	*s* (11%) *p* (88%) *d* (1%)	–9.11

From the orbital analysis, we determined that the donor-acceptor interactions between Fe and N_{TMP} are stronger (85.07 kcal mol^{-1}) than those between Co and N_{TMP} (72.22 kcal mol^{-1}). This prompted us to consider whether NCIs might also contribute to the stability of these complexes, focusing specifically on H···H Van der Waals interactions, as recently reviewed by David J. Liptrot and Philip P. Power.[28] Their work highlights that these often-overlooked weak attractive forces, frequently arising from C–H moieties, can significantly influence the stability of both organic molecules and organometallic complexes. To explore the potential role of such weak NCIs, we conducted an IGM analysis. With this method, we evaluated the interactions between the hydrogen atoms of the TMP ligand bound to the metal centers, particularly those arising from adjacent C–H moieties. The IGM approach quantifies the relative interaction energies (ΔE_{int}) of defined fragments based on electron density, isolating only weak NCIs. It also provides a three-dimensional visualisation of the contacts between fragments through isosurfaces mapping, which represents changes in electron density in 3D space. In addition to the 3D visualisation, the IGM analysis generates a two-dimensional plot of electron density against the electron density gradient. This plot is instrumental in identifying individual NCIs and their nature, with the resulting peaks and patterns distinguishing different types of interactions.

We were particularly interested in capturing the H···H interactions across the two TMP ligands. However, this posed a challenge, as the analysis did not allow us to specify the type of NCI to investigate; instead, all NCIs were captured simultaneously. To address this limitation, we divided the $M(TMP)_2$ complex into $[M(TMP_a)]^+$ and TMP_b^- units, allowing us to compute the IGM ΔE_{int}, which included both the desired H···H interactions and the M···H interactions. Subsequently, the $[M(TMP_a)]^+$ fragment was further separated into M^{2+} and TMP_a^- units to isolate only the M···H interactions. By subtracting the M···H interactions from the total, we determined the IGM ΔE_{int} values for the H···H interactions to be –2.2 kcal mol^{-1} for Fe and –6.7 kcal mol^{-1} for Co (Table 6.4). Interestingly, unlike the NBO results, the IGM analysis revealed greater NCI stabilisation for Co compared to Fe, with a difference of –4.5 kcal mol^{-1}. Using the same subtraction method, we generated 2D and 3D plots to visualise these

interactions. After removing the M···H interactions (represented in white), the remaining peaks and surfaces corresponded to the H···H interactions, shown in green for Fe (Figures 6.3) and purple for Co (Figure 6.4). These plots revealed a more pronounced twist in the plane formed by the methyl groups of the TMP ligand in the Fe complex compared to the Co complex. This structural difference facilitated better and more extensive H···H contacts for Co than for Fe.

Table 6.4. Summary of the interaction energies estimated by the IGM-δginter approach with promolecular energy density, as implemented in the IGMPlot software. The difference in ΔE_{int} accounts for the van der Waals interactions, which are displayed in Figures 6.3 and 6.4 for Fe and Co, respectively.

Fe Fragments	ΔE_{int} **(kcal mol^{-1})**
[Fe(TMP$_a$)] + TMP$_b$	–19.4
Fe + TMP$_b$	–17.2
Difference = ΔE_{int} (vdW)	–2.2

Co Fragments	ΔE_{int} **(kcal mol^{-1})**
[Co(TMP$_a$)] + TMP$_b$	–24.1
Co + TMP$_b$	–17.4
Difference = ΔE_{int} (vdW)	–6.7

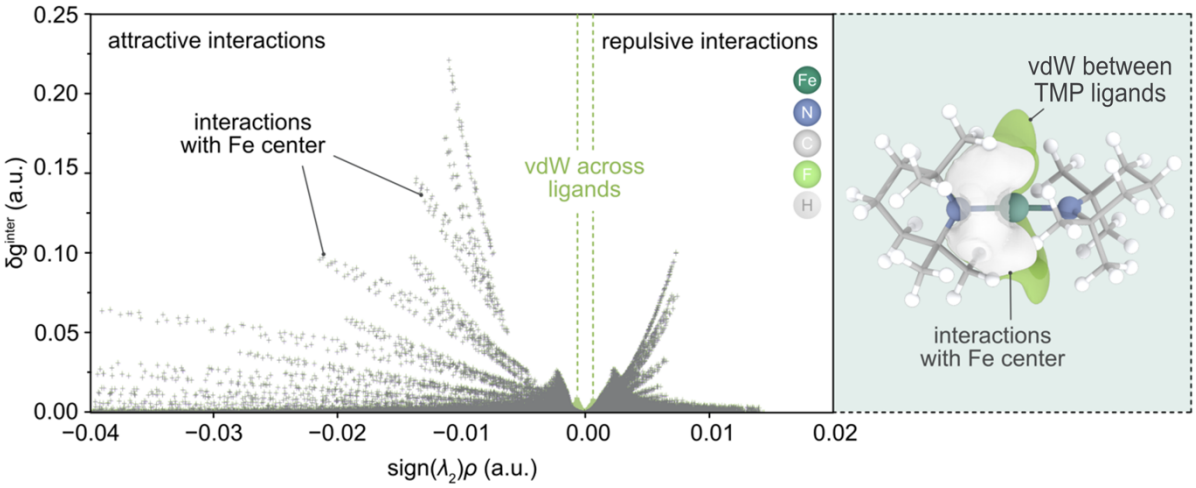

Figure 6.3. IGM analysis performed on the Fe(TMP)$_2$ complex by plotting the parameter derived from IGM against the sign of the second eigenvalue of the Hessian matrix multiplied by the ρ, sign(λ_2)ρ. The interactions arising from H atoms from one of the TMP ligands with the Fe center (grey) and the van der Waals interaction between the H atoms from two TMP ligands (green) are both displayed in the IGM plot. The detailed IGM peaks are displayed as isosurfaces (isovalue = 0.1 a.u.) in the inset.

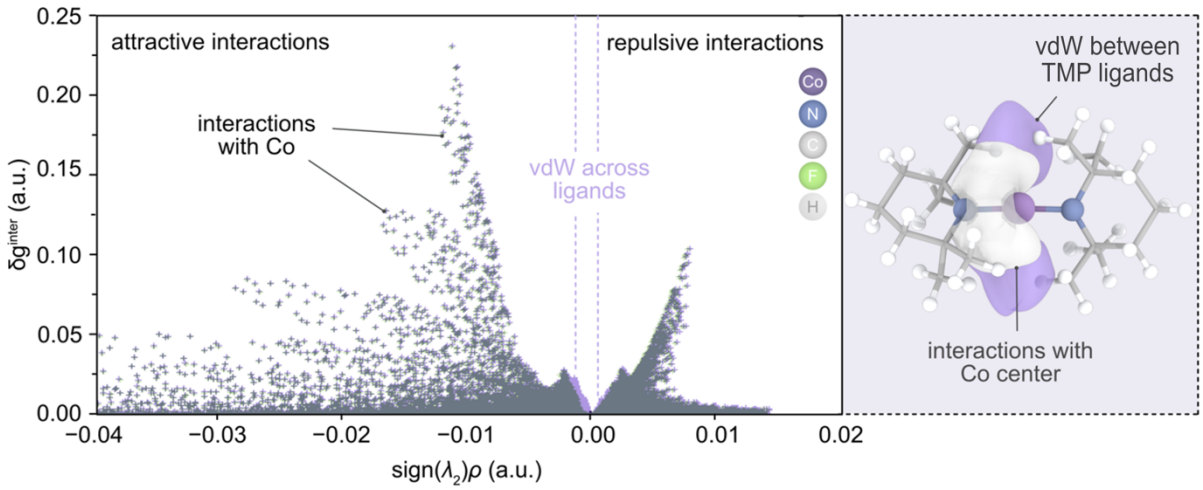

Figure 6.4. IGM analysis performed on the $Co(TMP)_2$ complex by plotting the parameter derived from IGM against the sign of the second eigenvalue of the Hessian matrix multiplied by the ρ, sign(λ_2)ρ. The interactions arising from H atoms from one of the TMP ligands with the Co center (grey) and the van der Waals interaction between the H atoms from two TMP ligands (purple) are both displayed in the IGM plot. The detailed IGM peaks are displayed as isosurfaces (isovalue = 0.1 a.u.) in the inset.

Conformers for both Fe and Co complexes were computed by setting the dihedral angle to 90° and 180°. The present structure, analysed and discussed here, corresponds to the lowest energy conformer. These findings prompted the consideration that while results from both NBO and IGM analyses indicate that overall, $Fe(TMP)_2$ is less stable than $Co(TMP)_2$, the difference in stability is substantial. This led to the hypothesis that the low-valent Co complex could also be crystallised, which have been crystalised by our Collaborators.

To investigate the energy contributions to THF binding and understand why it binds more strongly to Co than to Fe (6.7 versus 1.1 kcal mol^{-1}), ASA was performed. This analysis decomposes the electronic binding energy of THF to $M(TMP)_2$ into two contributions: the ΔE_{int} and the ΔE_{dist}. ΔE_{int} represents the energy gain from interactions between the fragments in their fixed geometries adopted from the geometries of the complex [(THF)$M(TMP)_2$], while ΔE_{dist} accounts for the energy cost of distorting the relaxed fragments of the isolated fragments. The results of this analysis are summarised in Table 6.5. The ΔE_{dist} is +6.0 kcal mol^{-1} for Fe and +2.6 kcal mol^{-1} for Co. Additionally, Co exhibits a higher ΔE_{int} gain (–24.3 kcal mol^{-1}) compared to Fe (–22.4 kcal mol^{-1}), resulting in the overall stronger THF binding observed for Co. The energy contributions highlight that the difference in THF binding energy is primarily

driven by the distortion of [M(TMP)$_2$] from its relaxed state to the frozen geometry, which creates the necessary space for THF coordination.

Table 6.5. Summary of the ΔE_{int} and ΔE_{dist} contributions obtained by means of ASA and are reported in kcal mol^{-1} between the fragments [M(TMP)$_2$] and THF.

Fe Fragments	**Energies (kcal mol^{-1})**
ΔE_{int} [(THF)Fe(TMP)$_2$]	–22.4
ΔE_{dist} [Fe(TMP)$_2$]	+6.0
ΔE_{dist} THF	+0.4

Co Fragments	**Energies (kcal mol^{-1})**
ΔE_{int} [(THF)Co(TMP)$_2$]	–24.3
ΔE_{dist} [Co(TMP)$_2$]	+2.6
ΔE_{dist} THF	+0.4

The labile THF molecule can dissociate from the metal centers, as shown in Figure 6.5, creating a vacant site (**1^{M}**) that enables the fluoroarene to approach and interact weakly via π-coordination. This interaction leads to a higher-energy intermediate (**I1^{M}**) with relative energies of 6.2 and 10.3 kcal mol^{-1} for Fe and Co, respectively. In the intermediate structure, the hydrogen atom of the arene is oriented towards the lone pair of the TMP nitrogen. Subsequently, the nitrogen deprotonates the hydrogen atom and proceeds to a transition state featuring M···F coordination. This step involves energy barriers of 21.1 and 22.4 kcal mol^{-1} for Fe and Co, respectively. These barriers indicate that the reaction is feasible at room temperature, as they are well below the threshold of 30 kcal mol^{-1}, consistent with experimental observations of the C–H metalation of the first pentafluoroarene at room temperature. MKM later refined these barriers, yielding transition state energies of 19.1 and 20.4 kcal mol^{-1} for Fe and Co (**TS1^{M}**), respectively, as shown in Figure 6.5. These adjustments are due to sensitivity of the reaction rate to the height of the barriers. A more detailed discussion of the MKM can be found in Section 6.3.3.

An alternative transition state (**TS1'^{Fe}**), where THF remains bound to the metal centers while establishing Fe···F coordination, was also considered. However, due to steric hindrance from the bulky TMP ligand, this transition state was found to be less favourable by 3.1 kcal mol^{-1} compared to the one without bound THF, as shown in the inset of Figure 6.5. These findings strongly suggest that THF dissociation is necessary for the first metalation step. This hypothesis was experimentally confirmed by replacing THF with a non-labile ligand, such as the carbene I*t*Bu (1,3-di-tert-butylimidazol-2-ylidene). The resulting complex, [(I*t*Bu)Co(TMP)$_2$], was prepared in situ and found to be unreactive towards pentafluoroarene, even when heated to 65 °C for extended reaction times of up to 16 hours. This lack of reactivity is attributed to the

strong binding of the carbene ligand, which prevents the formation of the active linear complex [Fe/Co(TMP)$_2$] required for interaction with the fluoroarene (Figure 6.5).

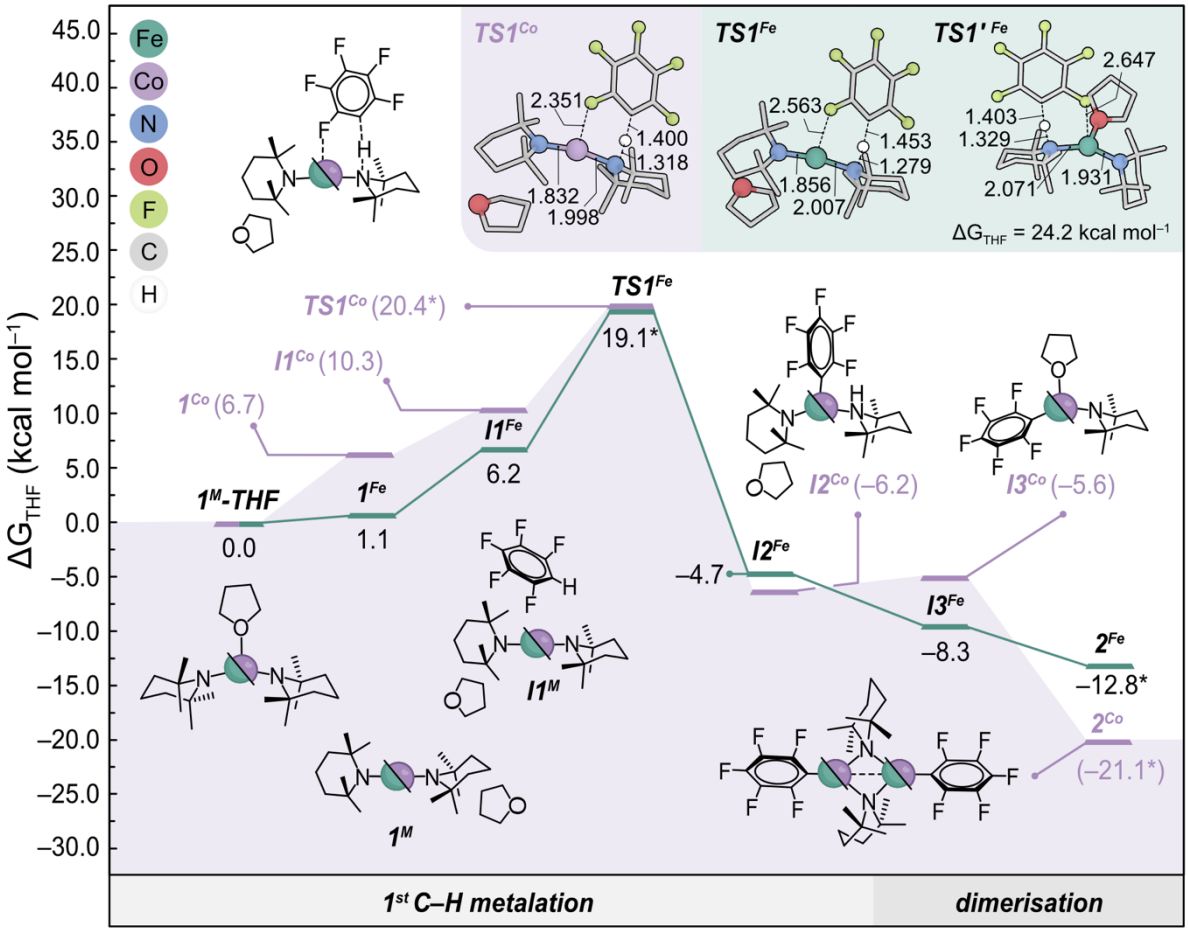

Figure 6.5. Gibbs energy profile calculated in THF at 298 K and 1 atm for the C−H metalation of the first C_6F_5H from the **1^{M}-THF** complexes (M = Fe, Co, in green and purple, respectively) using a hybrid solvation model. Energies refined with MKM are labelled with an asterisk. Relevant bond lengths (in Å) are shown for **TS1^{Co}**, **TS1^{Fe}**, and the alternative transition structure **TS1'^{Fe}** for the first C–H metalation of pentafluorobenzene with a coordinated THF.

NCI analysis was performed on the lowest-energy transition states of Fe (**TS1^{Fe}**) and Co (**TS1^{Co}**), as shown in Figure 6.6. The analysis revealed distinct electrostatic interactions between the M···F atoms for Fe and Co, with ρ values of 0.023 and 0.024 a.u., respectively. These findings highlight the role of fluorine as an ortho-directing group in the C–H metalation processes. In addition to M···F interactions, the 2D and 3D NCI plots revealed a network of interactions involving the two ortho-fluorine atoms, the carbon undergoing deprotonation, and the hydrogen atoms of the TMP ligand. While each interaction within this network is

individually weak, their cumulative effect contributes significantly to docking the substrate in place, stabilising the transition states for both Fe and Co. Notably, the contributions and disruptions of NCIs in the transition states of both metals are similar based on the computed electron density profiles. To gain deeper insight into the electronic structure of the M···F contact, NBO analysis was performed. The absence of significant donor-acceptor interactions supports the non-covalent character of this contact, which is best described as primarily electrostatic in nature.

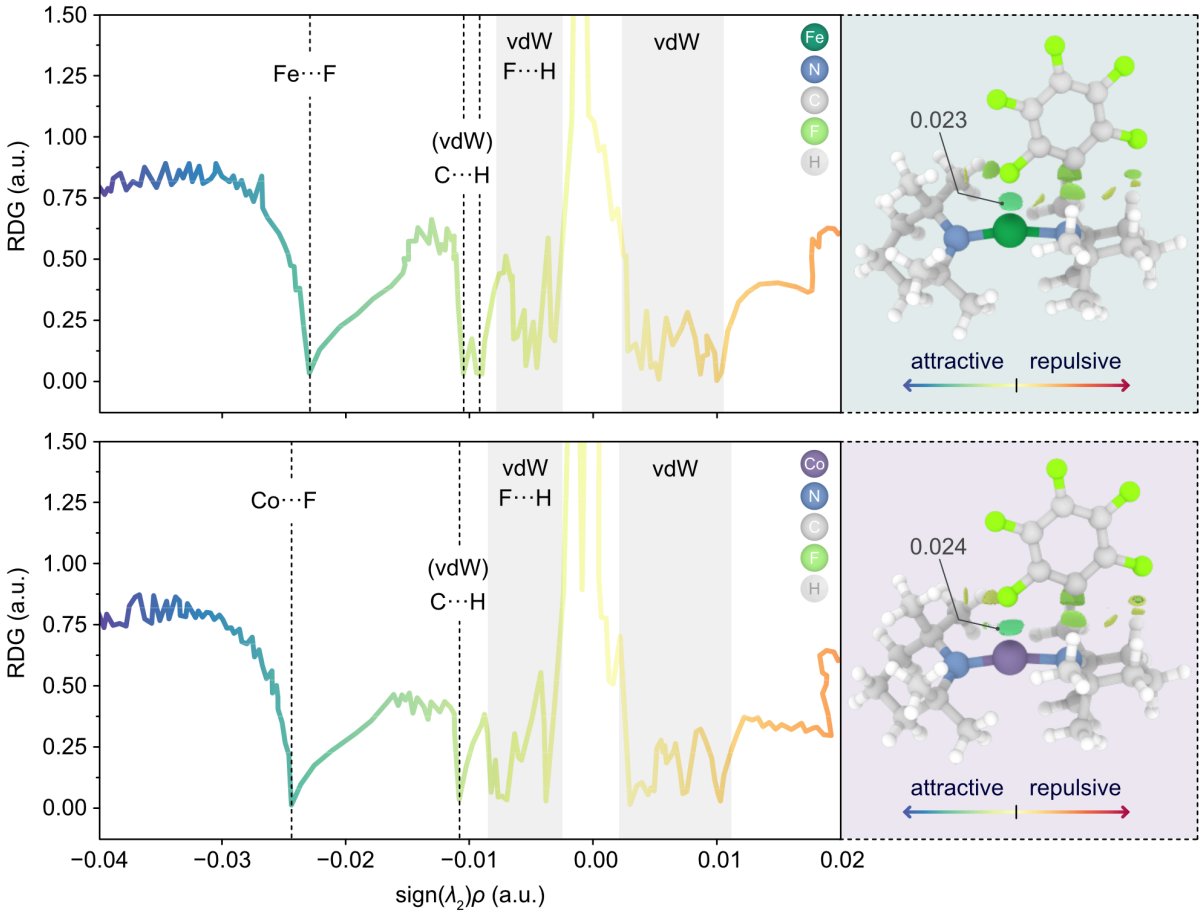

Figure 6.6. NCI analysis on **TS1^{Fe}** (top) and **TS1^{Co}** (bottom) by plotting the RDG against the sign of the second eigenvalue of the Hessian matrix multiplied by the ρ, sign(λ_2)ρ. In the NCI plot, attractive (repulsive) interactions are denoted by cold (warm) colours. The most relevant NCIs are displayed as isosurfaces (isovalue = 0.5 a.u.) in the inset along with their associated ρ values (in a.u.).

Post-deprotonation, the geometry relaxation of **TS1^{M}** leads to the metalated intermediate with the formation of the covalent M–C_6F_5 bond, and the protonated TMP(H) remains coordinated to the metal center too, forming a temporary tricoordinate metal species in an exergonic process by –4.7 and –6.2 kcal mol^{-1} for Fe and Co, respectively. The protonated TMP(H) is then replaced by a solvent THF molecule to yield [(THF)M(C_6F_5)(TMP)] (**I3^{M}**) in a slightly endergonic step for Co (+0.6 kcal mol^{-1}), while for Fe this process is exergonic by –3.6 kcal mol^{-1} . This species then undergoes dimerisation with concomitant dissociation of THF to form the experimentally observed and isolated dimer (**2^{M}**) for both Fe and Co.

The Fe dimer, **2^{Fe}**, was initially modelled as a high-spin Fe(II) ferromagnetic species, with a total S = 4 and S_{loc} = 2 for each Fe center. However, this resulted in a highly endergonic formation energy for the dimer (+16.9 kcal mol^{-1} in SMD benzene), contradicting experimental observations of its isolation in benzene or THF. This discrepancy prompted a re-evaluation of the computational model and the chemical structure. To benchmark the computational results, the optimised structure was compared to experimental XRD data. The Fe–Fe distance of 2.513 Å observed in the XRD structure was shorter than the sum of their covalent radii (2.64 Å). This suggested the possibility of antiferromagnetic coupling or Fe–Fe bond formation. Previous experimental evidence indicated that Fe(II) in these amide complexes typically exists in a high-spin state. However, if coupling or M–M bond formation occurred, alternative multiplicities beyond S = 4 needed consideration. Further insight was gained by re-examining the experimental ^{1}H NMR spectrum, which exhibited sharp signals indicative of short spin relaxation times, supporting the possibility of spin-coupling or M–M bonds. To test this hypothesis, various multiplicities were explored, ranging from S = 4 to S = 0. Energy calculations revealed that S = 2, 3, 4 were unfavourable, with formation energies of +19.6, +31.5, and +41.0 kcal mol^{-1}, respectively. The structure with S = 1 results in the dimerisation energy of –3.2 kcal mol^{-1}, but it remained unfavourable compared to the antiferromagnetic coupling singlet case M_s = 0, S_{loc} = 2, with a formation energy of –12.8 kcal mol^{-1}.

To model the antiferromagnetically coupled Fe dimer, broken-symmetry DFT was employed. The correct initial wavefunction was generated by flipping the spin of the four unpaired *d*-electrons on one of the Fe centers. The dimer was segmented into four fragments: {Fe_1(*t*-C_6F_5)}, {Fe_2(*t*-C_6F_5)}, {μ-TMP_1}, and {μ-TMP_2}. Charges and multiplicities were manually assigned for each fragment in the input file, with Fe spins specified as +4 and –4 for the two Fe-

containing fragments (the signs are arbitrary and only indicate opposite spins). Geometry optimisation of this antiferromagnetic dimer yielded Mulliken spin populations of +3.73/–3.73 a.u. and an Fe–Fe distance of 2.556 Å, consistent with the XRD structure (2.513 Å). The relative energy of the antiferromagnetic Fe dimer was calculated as –16.6 kcal mol^{-1} in benzene. Later, experimental determination of the dimer's magnetic moment (μ_{eff} = 0.34 B.M.) confirmed antiferromagnetic coupling.

The formation of Fe and Co dimers in THF was also modelled using both the SMD solvation model and a hybrid solvation model, as shown in Figures 6.7 and 6.8 for Fe and Co, respectively. The hybrid model demonstrated a limitation, that is the dissociation of multiple solvent molecules simultaneously led to the overestimation of dissociation energies, making dimers appear more stable than they are. Nevertheless, the two approaches provided upper and lower bounds for the dimerisation energies (–20.8 to –7.3 kcal mol^{-1} for Fe and –30.7 to –9.0 kcal mol^{-1} for Co). These estimates were further refined using experimental kinetic data and DFT-computed energies as input for the COPASI software. To complete the kinetic profile of the reaction, further investigation of the second C–H activation pathway was required, which is discussed in the next section.

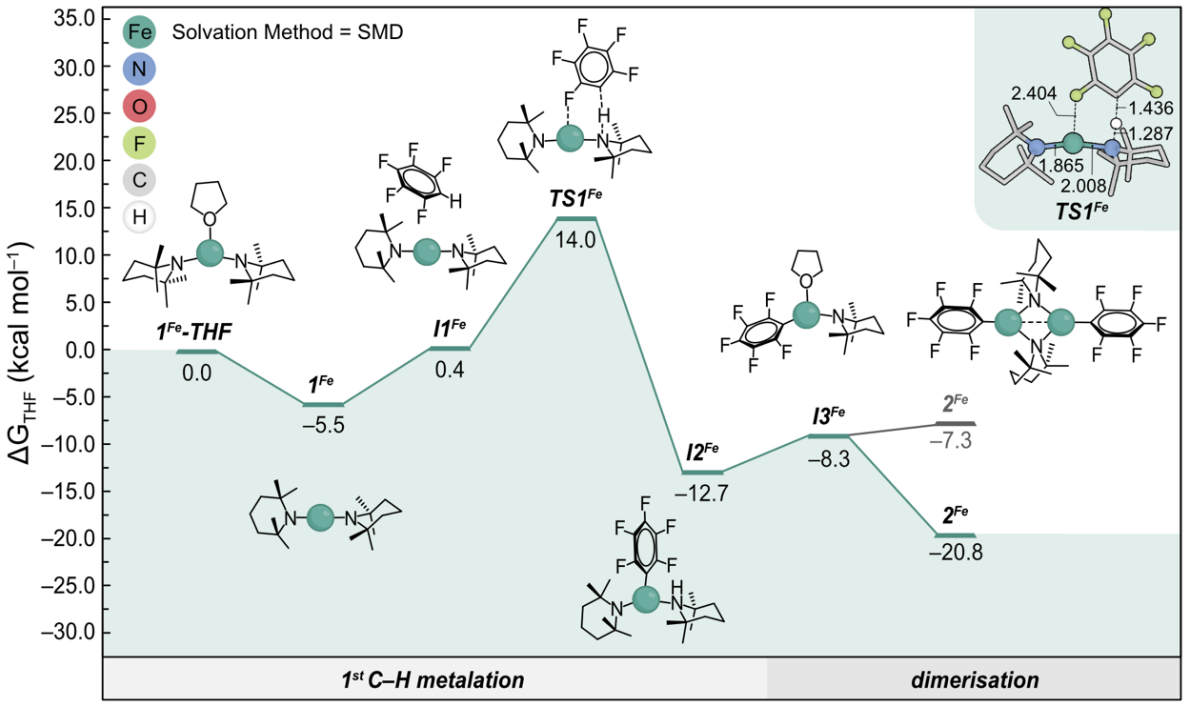

Figure 6.7. Gibbs energy profile calculated in THF at 298 K and 1 atm for the C–H metalation of the first equivalent of C_6F_5H with [Fe(TMP)$_2$] (**1^{Fe}**) using the implicit SMD model through

single-point calculations on gas phase optimised geometries. Here we show that without explicit THF the stabilities of **1**^{Fe}, **I1**^{Fe}, **TS1**^{Fe}, **I2**^{Fe}, and **2**^{Fe} are overestimated with respect to the energies shown in Figure 6.5. The energy of the dimer, obtained through hybrid (grey) and implicit (green) solvation models are compared. Relevant bond distances (in Å) are also shown for **TS1**^{Fe}.

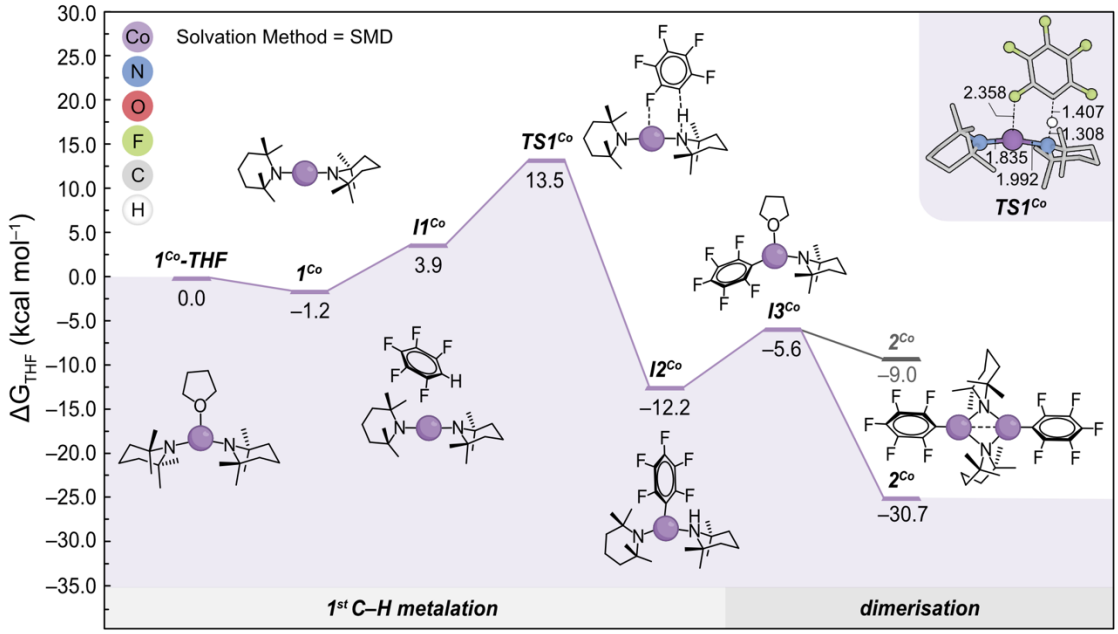

Figure 6.8. Gibbs energy profile calculated in THF at 298 K and 1 atm for the C–H metalation of C_6F_5H with [(THF)Co(TMP)$_2$] using the implicit SMD model through single-point calculations on gas phase optimised geometries. Here we show that without explicit THF the stabilities of **1**^{Co}, **I1**^{Co}, **TS1**^{Co}, **I2**^{Co}, and **2**^{Co} are overestimated with respect to the energies shown in Figure 6.5. The energy of the dimer, obtained through hybrid (grey) and implicit (purple lines) approaches are compared. Relevant bond distances (in Å) are also shown for **TS1**^{Co}.

6.4.2 2nd C–H metalation mechanism in THF

The tricoordinate complex [(THF)Fe(C_6F_5)(TMP)] can undergo dimerisation or form a less stable tetracoordinate Fe complex (**I4**^{Fe}, +3.2 kcal mol^{-1}) through the coordination of a second pentafluoroarene molecule, establishing Fe···F contacts as shown in Figure 6.9. Despite the endergonic formation of this intermediate, it proceeds to deprotonate the second arene molecule, with its hydrogen atom readily oriented towards the lone pairs of the nitrogen in the TMP ligand. The resulting transition state (**TS2**^{Fe}) has a Gibbs energy of 12.2 kcal mol^{-1}, while the

analogous transition state for Co (**TS2^{Co}**) lies slightly higher in energy at 14.8 kcal mol^{-1}. However, when considering only the TS barrier, these results do not explain the experimentally observed lack of reactivity for the Co dimer. To address this, the energy of the dimer must be estimated, necessitating continuation of the mechanistic study. In addition to this tetracoordinate transition state, an alternative transition state analogous to **TS1^{Fe}**, but without THF coordination to Fe, was also considered. This alternative was found to be higher in energy by +6.5 kcal mol^{-1}. The difference in coordination, without and with binding of THF to the Fe, between **TS1^{Fe}** and **TS2^{Fe}** can be attributed to the stronger donation from the spectator TMP ligand present in **TS1^{Fe}** (Fe–N = 1.832 Å), which electronically compensates for the absence of interaction with THF. Additionally, the replacement of one TMP ligand with a less bulky $\{C_6F_5\}^-$ moiety reduces steric hindrance, further stabilising **TS2^{Fe}** compared to **TS1^{Fe}**.

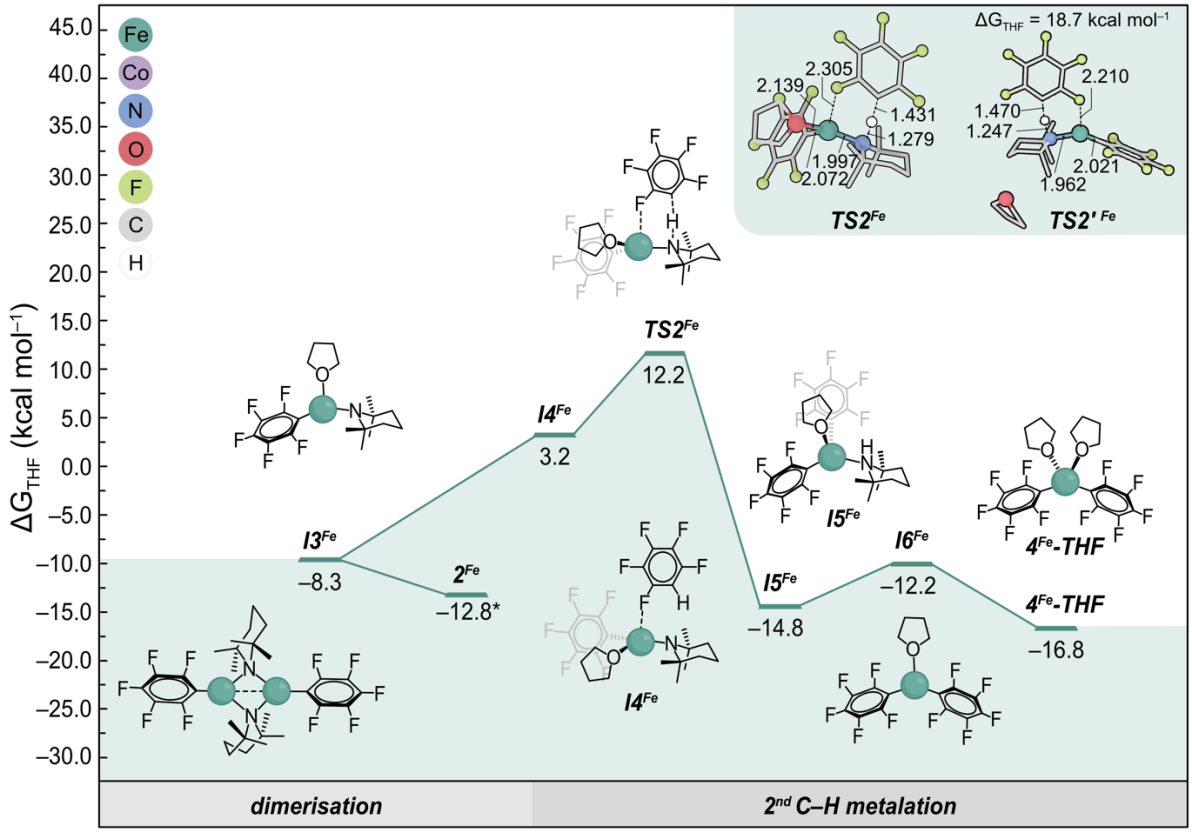

Figure 6.9. Gibbs energy profile calculated in THF at 298 K and 1 atm for the C−H metalation of the second C_6F_5H from the **I3^{Fe}** complexes using a hybrid solvation model. Energies refined with MKM are labelled with an asterisk. Relevant bond lengths (in Å) are shown for **TS2^{Fe}**, and the alternative TS structure **TS2'^{Fe}** with a dissociated THF, which was found to be *ca.* 6.5 kcal mol^{-1} higher in energy. Gibbs energies were calculated relative to **1^{Fe}-THF** + C_6F_5H.

Relaxation of **TS2^{Fe}** leads to the formation of the second ferration of pentafluoroarene (**I5^{Fe}**), with a Gibbs energy of –14.8 kcal mol^{-1}. Subsequently, the protonated TMP(H) ligand dissociates, and another THF molecule coordinates to Fe, yielding the final experimentally observed product, [(THF)$_2$Fe(C$_6$F$_5$)$_2$] (4^{Fe}-THF). The overall formation of this product is exergonic, with a Gibbs energy of –16.8 kcal mol^{-1} relative to the most stable reactant complex **1^{Fe}-THF**, consistent with experimental observations. The analogous mechanism for the C–H cobaltation of a second pentafluoroarene was also modelled, yielding similar reaction energies, as shown in Figure 6.10. These two modelled pathways, along with the corresponding reaction and transition state energies, will be utilised as inputs for the MKM simulations, which are described in detail in the next section.

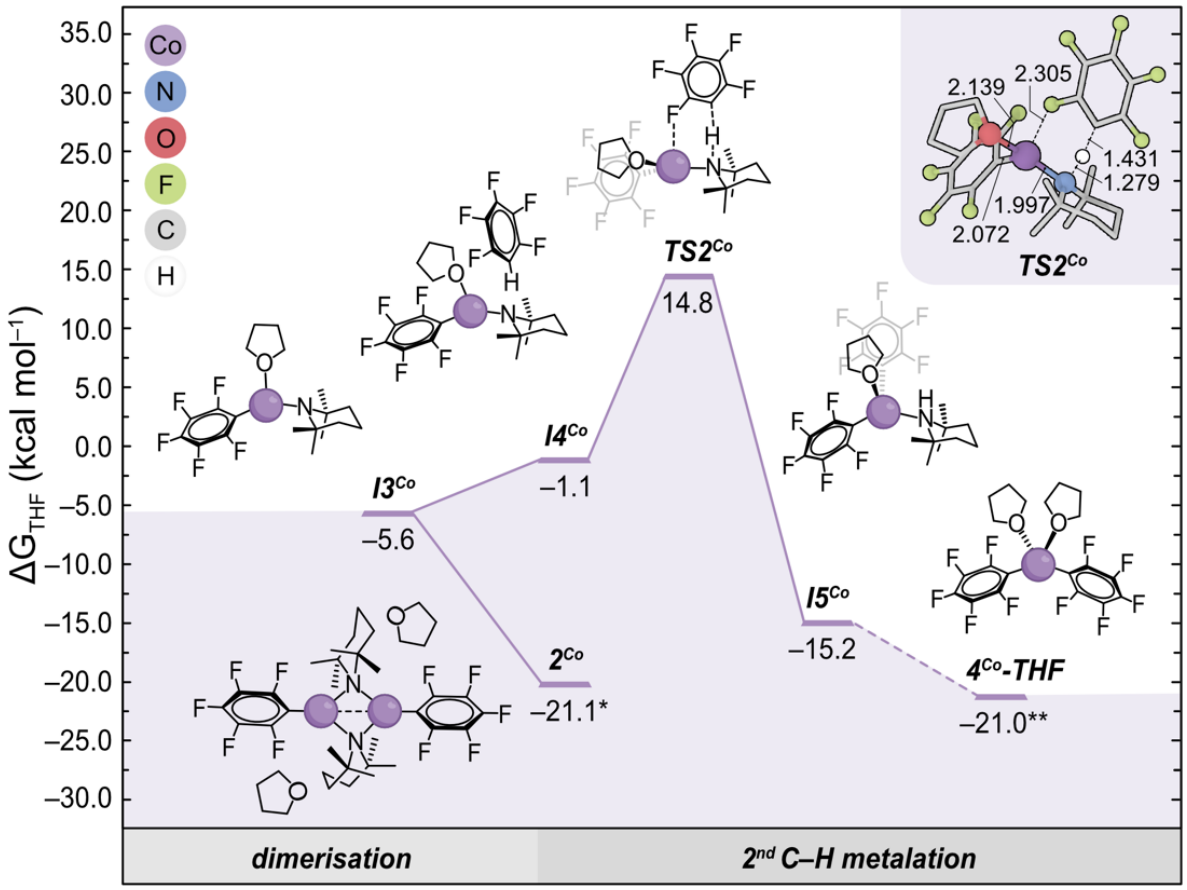

Figure 6.10. Gibbs energy profile calculated in THF at 298 K and 1 atm for the undetected C–H metalation of a second equivalent of C$_6$F$_5$H with [(THF)Co(TMP)(C$_6$F$_5$)] (**I3$_{Co}$**), using a hybrid solvation model with MKM refined energies labelled with and asterisk. **Energy referenced to the reactant **1^{Co}-THF** (Figure 6.5) with an additional explicit THF. Relevant bond distances (in Å) are also shown for **TS2^{Co}**. The high overall barrier of +35.9 kcal mol^{-1} supports the unfeasibility of the second metalation, in agreement with experiments.

6.4.3 Microkinetic modelling

MKM was employed to gain deeper insights into the thermodynamics and kinetics of the dimerisation step, which involves the dissociation of two THF molecules. This approach utilises DFT calculated reaction energies and barriers for each elementary step to derive forward and reverse rate constants using the Arrhenius and Eyring equations. Elementary steps involving ligand association or dissociation, known to be fast and often diffusion controlled, present challenges in locating the associated transition states. To address this, experimentally measured kinetic data for typical association/dissociation processes were adopted, with an estimated barrier of approximately 5.0 kcal mol^{-1}.[29] The goal of this MKM was to estimate the reaction energy and barrier of the dimerisation step, which introduces two unknown variables. Since MKM can be represented as a system of linear equations, at least two outputs are required to solve for both unknowns. These outputs correspond to intermediate or product concentrations at specific reaction times, which can be obtained from experiments.

Our collaborators conducted experiments with various THF concentrations using $Fe(TMP)_2$ and $Co(TMP)_2$. Three key observations were made: (i) the dimeric $[\{Co(\mu\text{-}TMP)(C_6F_5)\}_2]$ species was predominantly formed within one hour in THF solution at room temperature, with no bisaryl cobalt complex $[(THF)_2Co(C_6F_5)_2]$ observed, even after extended reaction times; (ii) the bisaryl iron complex $[(THF)_2Fe(C_6F_5)_2]$ (Figure 6.9) was detected after one day at room temperature when the reaction was conducted in benzene with one equivalent of THF; (iii) the bisaryl iron complex $[(THF)_2Fe(C_6F_5)_2]$ (**4^{Fe}-THF**, Figure 6.9) was detected within one hour when the reaction was performed in THF. These experimental observations provided the necessary data to estimate the dimerisation energy and associated barrier through manual fitting of the Gibbs energy.

A kinetic model was first constructed for the $Co(TMP)_2$ reaction under condition (i) (see Scheme 6.1). However, no dimer or bisaryl Co complex was formed, and no significant consumption of the starting material $Co(TMP)_2$ was observed. This is likely due to the high sensitivity of the COPASI software to reaction barriers, as it is primarily designed for experimental kinetic data. Although the DFT-calculated barrier falls within the range expected for room-temperature reactions, it was too high for the reaction to proceed in the kinetic model. The **$TS1^{Co}$** Gibbs energy was manually adjusted in 0.5 kcal mol^{-1} increments until the reaction

matched experimental results at a corrected energy of 20.4 kcal mol^{-1}. This corresponds to a 2.0 kcal mol^{-1} lowering of the DFT barrier calculated using the hybrid solvation model, a correction consistent with typical DFT error margins. The same correction was applied to the iron analogue, **TS1^{Fe}**.

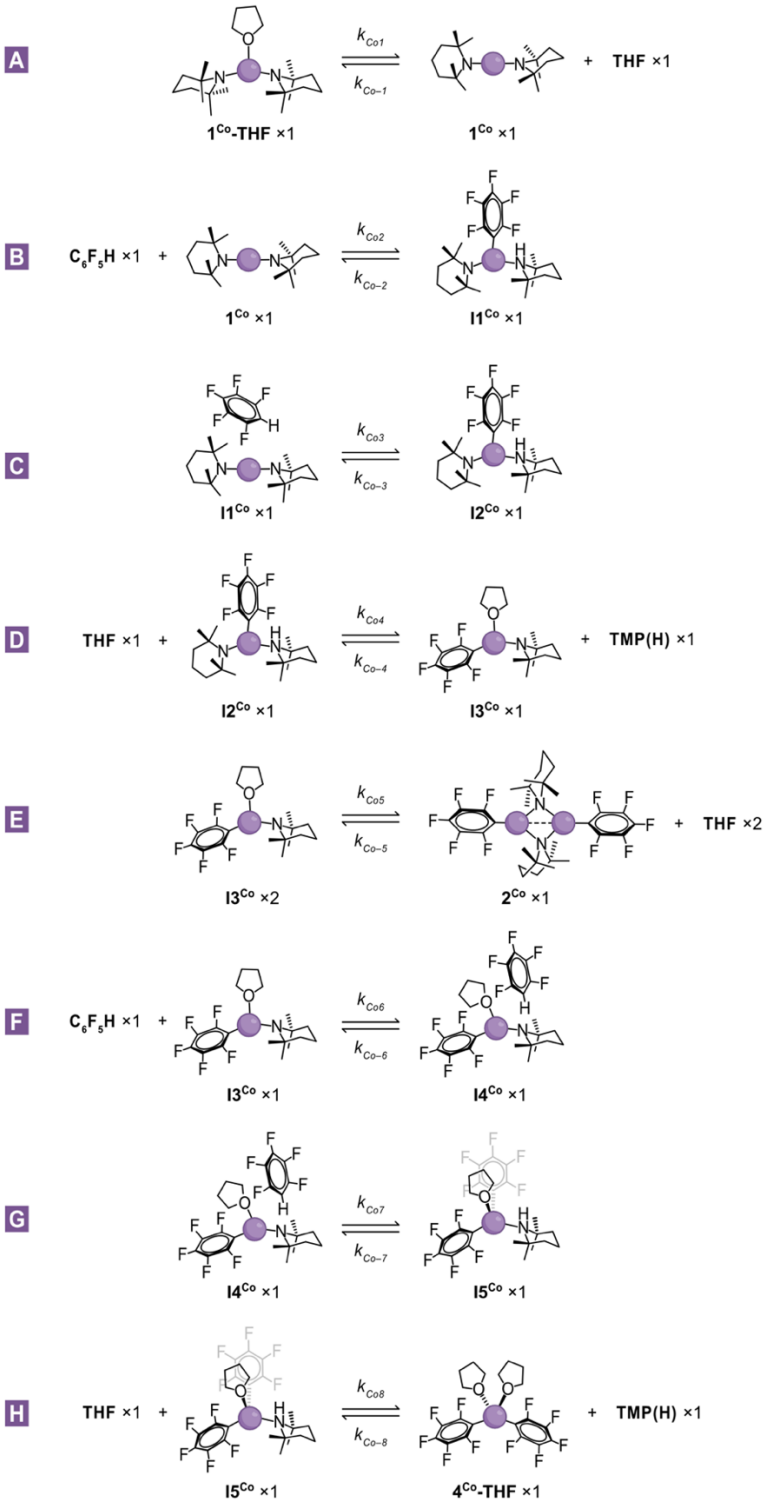

Scheme 6.1. Kinetic model considered for the C–H metalation of C_6F_5H with [(THF)Co(TMP)$_2$] (**1^{Co}-THF**) in THF.

Estimating the barrier for the dimerisation step presented challenges, as DFT cannot reliably calculate both the barrier and reaction energy for this step. With two unknowns and one experimental reaction rate, it becomes more complicated when THF is present in excess as a solvent. However, in a weakly or non-coordinating solvent such as benzene, intermediate energies can be more accurately computed.

For condition (ii), the Gibbs energy profile for the reaction of [Fe(TMP)$_2$] with two equivalents of C_6F_5H and one equivalent of THF in benzene was calculated via DFT. These energies (Figure 6.11) were used to generate input data for elementary reaction rates, enabling an estimation of the energy of the dimeric species. Scanning different relative dimerisation barriers from **I3^{M}** to **2^{M}** (values ranging from 8 to 20 kcal mol^{-1}) revealed that 8 kcal mol^{-1} allowed rapid reaction progression, while 20 kcal mol^{-1} was too high for any reaction. Subsequent refinement with ±1 kcal mol^{-1} adjustments showed that at 13 kcal mol^{-1} (6.6 + 6.4), the reaction proceeded slowly to the bis-aryl [(THF)$_2$Fe(C_6F_5)$_2$] within the experimental timeframe of one day. This value (13.0 kcal mol^{-1}) was identified as the optimal barrier (dashed line in Figure 6.11), for consistency, this dimerisation barrier was also applied to cobalt.

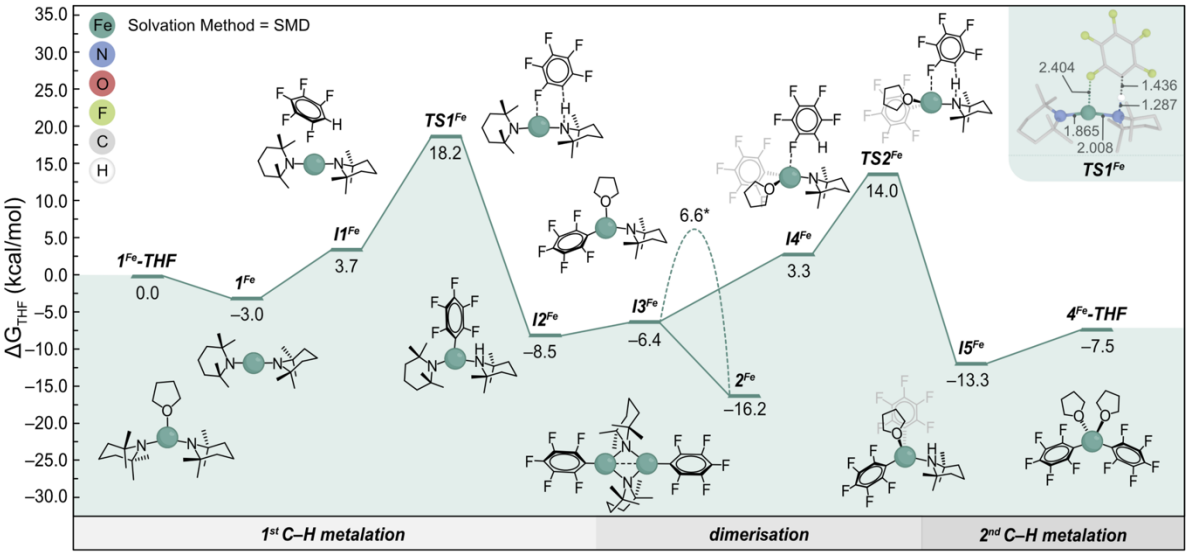

Figure 6.11. Gibbs energy profile calculated in benzene at 298 K and 1 atm for the C–H metalation of C_6F_5H with Fe(TMP)$_2$, 1^{Fe}, in the presence of 1 equivalent of THF. The optimised structure of TS1^{Fe} is shown as inset with relevant bond distances given in Å.

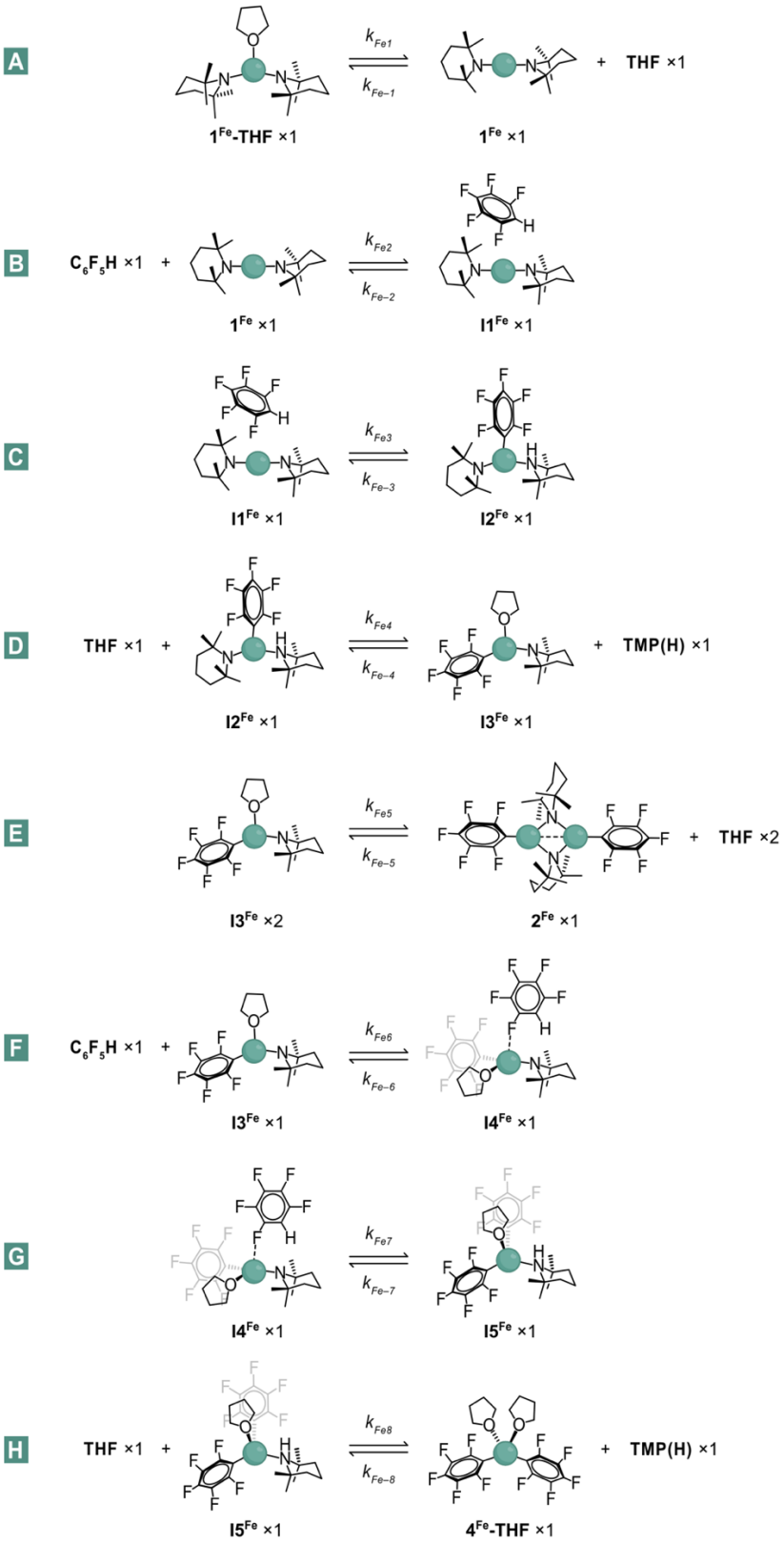

Scheme 6.2. Kinetic model considered for C–H metalation of C_6F_5H with $Fe(TMP)_2$ (**1^{Fe}**) in THF.

With the dimerisation barrier estimated, the remaining unknown variable was the actual formation energy of the dimer. Using experimental results from reacting $M(TMP)_2$ with two equivalents of fluoroarene in THF at room temperature (iii), Gibbs energies for the dimers $\mathbf{2^{Fe}}$ and $\mathbf{2^{Co}}$ were refined. For Fe, the energy was adjusted until $\mathbf{4^{Fe}}$**-THF** became the predominant product within an hour, while for Co, the corresponding $\mathbf{4^{Co}}$**-THF** was not formed even after prolonged reaction times, with $\mathbf{2^{Co}}$ remaining as the final product. This approach yielded refined dimer energies of –12.8 and –21.1 kcal mol^{-1} for $\mathbf{2^{Fe}}$ and $\mathbf{2^{Co}}$, respectively. These values fall within the bounds defined by implicit and hybrid solvation models (–20.8 to –7.3 kcal mol^{-1} for Fe and –30.7 to –9.0 kcal mol^{-1} for Co). The resulting time concentration plots are shown in Figures 6.12 and 6.13, and detailed kinetic constants are summarised in Table 6.6.

Table 6.6. Kinetic constants (see notation in Scheme 6.1 and Scheme 6.2 for Fe and Co, respectively) derived from DFT calculations using a hybrid solvation approach and the refinements described above. Reaction conditions: T = 298.15 K, $[\mathbf{1^M}]_0$ = 0.2 M , $[C_6F_5H]_0$ = 0.4 M, [THF] = 12.31 M (excess). The units are s^{-1} and L mol^{-1} s^{-1} for 1st and 2nd reaction kinetics, respectively.

k_{Fe1}	$2.09\times10^{+8}$	k_{Co1}	$1.64\times10^{+4}$
k_{Fe-1}	$1.34\times10^{+9}$	k_{Co-1}	$1.34\times10^{+9}$
k_{Fe2}	$2.45\times10^{+5}$	k_{Co2}	$3.08\times10^{+6}$
k_{Fe-2}	$1.34\times10^{+9}$	k_{Co-2}	$1.34\times10^{+9}$
k_{Fe3}	$2.17\times10^{+3}$	k_{Co3}	$2.45\times10^{+5}$
k_{Fe-3}	2.22×10^{-5}	k_{Co-3}	1.97×10^{-7}
k_{Fe4}	$1.34\times10^{+9}$	k_{Co4}	$4.87\times10^{+8}$
k_{Fe-4}	$3.08\times10^{+6}$	k_{Co-4}	$1.34\times10^{+9}$
k_{Fe5}	$1.84\times10^{+3}$	k_{Co5}	$1.84\times10^{+3}$
k_{Fe-5}	9.22×10^{-1}	k_{Co-5}	7.97×10^{-9}
k_{Fe6}	$4.99\times10^{+0}$	k_{Co6}	$6.75\times10^{+5}$
k_{Fe-6}	$1.34\times10^{+9}$	k_{Co-6}	$1.34\times10^{+9}$
k_{Fe7}	$1.57\times10^{+6}$	k_{Co7}	$1.37\times10^{+1}$
k_{Fe-7}	1.00×10^{-7}	k_{Co-7}	6.34×10^{-10}
k_{Fe8}	$1.34\times10^{+9}$	k_{Co8}	$1.34\times10^{+9}$
k_{Fe-8}	$3.93\times10^{+10}$	k_{Co-8}	$7.52\times10^{+4}$

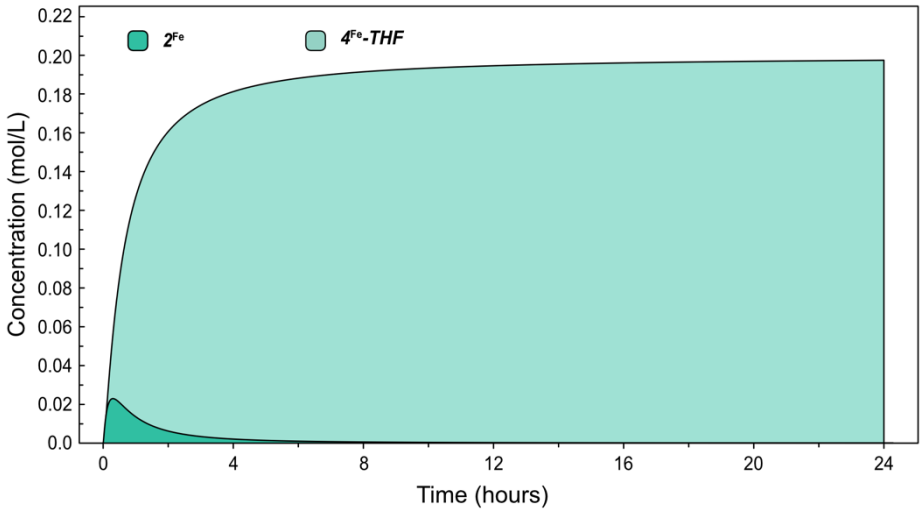

Figure 6.12. Concentration profile for the Fe system obtained with COPASI using the kinetic constants reported in Table 6.6 and the kinetic model shown in Scheme 6.2. The simulated profile clearly shows the quantitative formation of the bisaryl complex $[(THF)_2Fe(C_6F_5)_2]$ (**4^{Fe}-THF**).

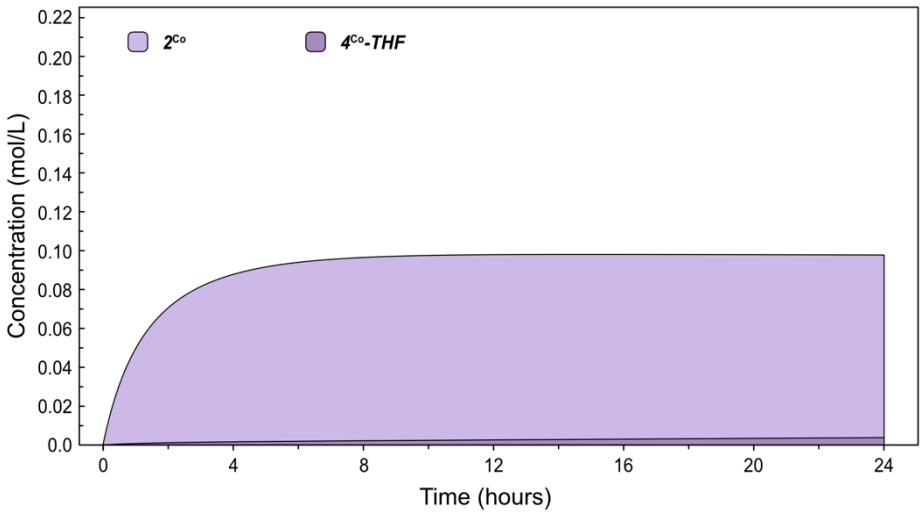

Figure 6.13. Concentration profile for the Co system obtained with COPASI using the kinetic constants reported in Table 6.6 and the kinetic model shown in Scheme 6.1. The simulated profile clearly shows the formation of the dimer **2^{Co}** as major product with traces of the experimentally undetected bisaryl complex **4^{Co}-THF**.

An alternative mechanism was also considered, involving the formation of the dimeric species **2^{M}**. Instead of undergoing a second C–H activation, the dimer could proceed via ligand scrambling to produce one bis-amide and one bis-aryl metal complex, as outlined in Figure 6.14 (steps **I7^{Fe}** to **I8^{Fe}** + **1^{Fe}**), with **1^{Fe}** eventually evolves to **1^{Fe}-THF** with the coordination of THF. Subsequently, the bis-amide metal complex undergoes C–H activation of another pentafluoroarene, regenerating **2^{Fe}**. This cycle continues, gradually converting the bis-amide complex into the bis-aryl complex until the concentration of the bis-amide species becomes too low to sustain further reaction. Assume the dimerisation barrier is as estimated above via MKM to be 13.0 kcal mol^{-1}. The overall barrier for this ligand scrambling process was calculated to be 25.5 kcal mol^{-1}, making it a slightly less favourable pathway compared to the second C–H activation (25.0 kcal mol^{-1}). However, it remains kinetically feasible at room temperature, as supported by experimental evidence. This pathway was detected experimentally when **2^{Fe}** was dissolved in THF in the absence of fluoroarene, leading to the formation of both **4^{Fe}-THF** and **1^{Fe}-THF**.

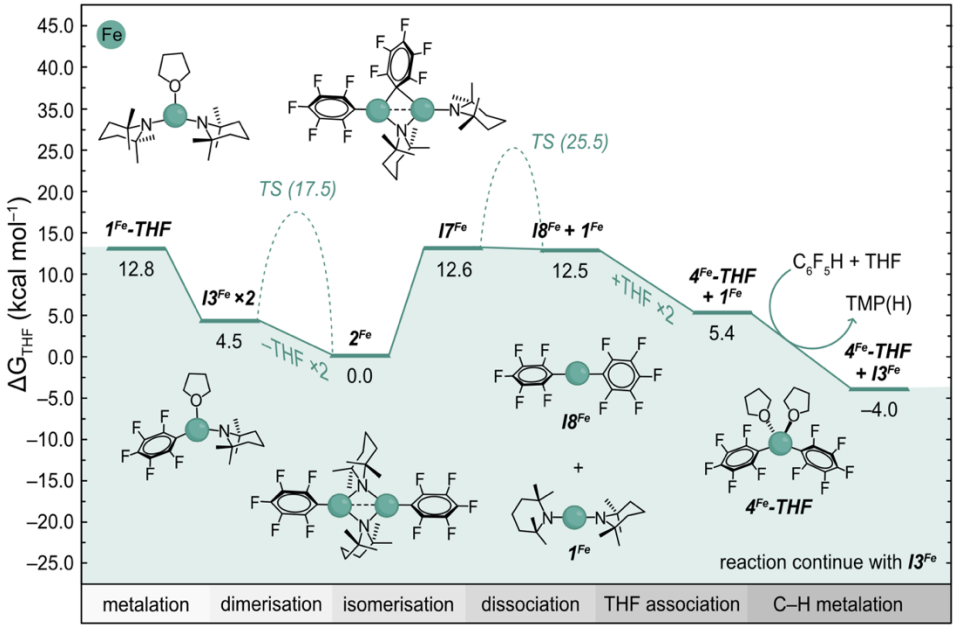

Figure 6.14. Rearrangement pathway calculated in THF at 298 K and 1 atm for the formation of **4^{Fe}-THF** and **I3^{Fe}** from **2^{Fe}**. The overall barrier of 25.5 kcal mol^{-1}, which can be overcome at room temperature, is referenced to **2^{Fe}** assuming that the co-complexation of **I8^{Fe}** with **I1^{Fe}** has a comparable barrier to the dimerisation step from **I3^{Fe}** (*i.e.,* 13.0 kcal mol^{-1}, see above).

For **2**^{Co}, a similar ligand rearrangement pathway was computed, mirroring the mechanism observed for Fe (Figure 6.15). However, the overall reaction barrier for Co was significantly higher, at +34.3 kcal mol^{-1}. This aligns with the experimental observation that no bis-aryl product (**4**^{Co}**-THF**) was formed for Co, even after prolonged reaction times.

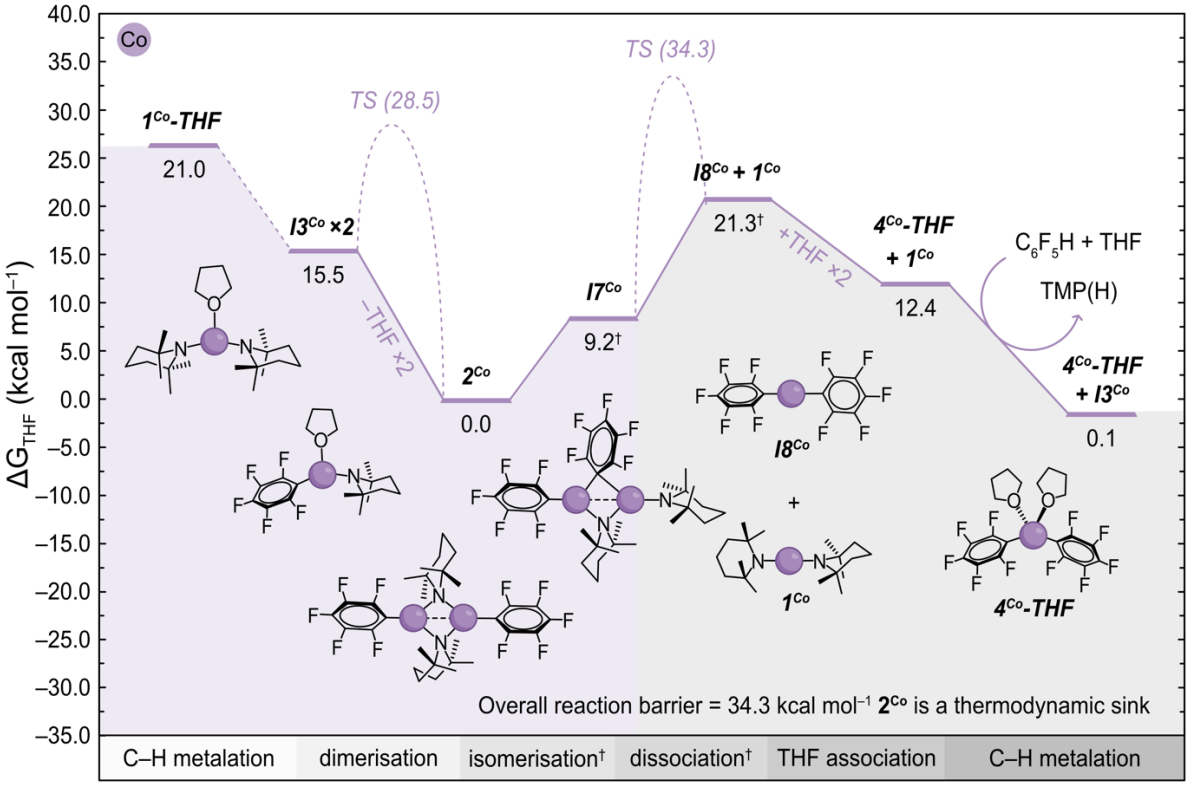

Figure 6.15. Rearrangement pathway calculated in THF at 298 K and 1 atm for the formation of **4**^{Co}**-THF** and **I3**^{Co} from **2**^{Co}. The overall barrier of 34.3 kcal mol^{-1}, which cannot be overcome at room temperature, is referenced to **2**^{Co} assuming that the co-complexation of **I8**^{Co} with **I1**^{Co} has a comparable barrier to the dimerisation step from **I3**^{Co} (*i.e.,* 13.0 kcal mol^{-1}).

Focusing on the major pathway being the 2nd C–H activation as described in the reaction profiles shown in Figure 6.5 and Figure 6.9, we see that the C–H metalation of the second pentafluorobenzene requires the formation of the active species **I3**^{M} from **2**^{M}. Thus, the relative stabilities of **I3**^{M} and **2**^{M} are important for understanding the divergent experimental behaviours observed for iron and cobalt regarding the C–H metalation of the second equivalent of pentafluorobenzene. For the cobalt complexes, the stability of **I3**^{Co} is low and the formation of dimer **2**^{Co} is very favourable compared to the iron analogues, which in turn reduces the

concentration of $\mathbf{I3^{Co}}$ in solution to be less than the kinetically efficient concentrations. On the contrary, for the Fe complexes, the reversible $\mathbf{2^{Fe}} \rightleftharpoons \mathbf{I3^{Fe}}$ equilibrium ensures there is an effective concentration of $\mathbf{I3^{Fe}}$ present in solution for the second C–H activation. This species $\mathbf{I3^{Fe}}$ allows the binding of the second equivalent of C_6F_5H ($\mathbf{I4^{Fe}}$) to the Fe center by establishing an Fe···F contact, docking the substrate in place for C–H activation, which could not be achieved with the dimeric $\mathbf{2^{Fe}}$.

6.4.4 C–H ferration mechanism in benzene

For completeness, the mechanism of the reaction between [Fe(TMP)$_2$] and two equivalents of pentafluoroarene in benzene was modelled. The first C–H activation step (Figure 6.16) mirrors the mechanism observed for the reaction carried out in THF (Figure 6.5, 6.9 and 6.10). For the second C–H ferration step, both monomeric and dimeric pathways were evaluated. The monomeric pathway is analogous to the one identified in THF, but with no THF included in the calculations. This resulted in a tricoordinate Fe transition state ($TS2_b$) with a Gibbs energy barrier of +37.6 kcal mol^{-1}, rendering the reaction unfeasible at room temperature. This finding aligns with experimental observations of the monobasic behaviour of $\mathbf{1^{Fe}}$ in benzene, which leads exclusively to the quantitative formation of the dimeric complex $\mathbf{2^{Fe}}$.

Given the high stability of the dimer $\mathbf{2^{Fe}}$, its potential role as an active species was also investigated, and the dimeric pathway originating from it was computed (Figure 6.16). All intermediates and transition states along this pathway, involving two Fe centers, were modelled as high-spin Fe(II) with antiferromagnetic coupling (S_{loc} = 2 for each Fe center, total M_s = 0). A key feature of this pathway is the partial dissociation of one bridging TMP ligand in the transition state ($\mathbf{TS3_b}$), which becomes terminally bound to a single Fe center and deprotonates the pentafluoroarene.

Attempts were made to model $\mathbf{TS3_b}$ with ferromagnetic spin coupling (S_{loc} = 2 for each Fe center, total S = 4), but this configuration resulted in a transition state that was +0.3 kcal mol^{-1} higher in energy compared to the antiferromagnetic configuration. Despite this, the antiferromagnetic $\mathbf{TS3_b}$ was still less favourable than the monomeric transition state.

The speciation of the product resulting from the second deprotonation was also examined. Two potential products were identified: the monomeric bis-aryl complex **I5$_b$** (–10.5 kcal mol^{-1}) and the dimeric tris-aryl complex **I8$_b$** (–13.5 kcal mol^{-1}). However, both products were found to be higher in energy than the dimeric starting material, **2^{Fe}** (–16.6 kcal mol^{-1}), and are therefore thermodynamically disfavoured.

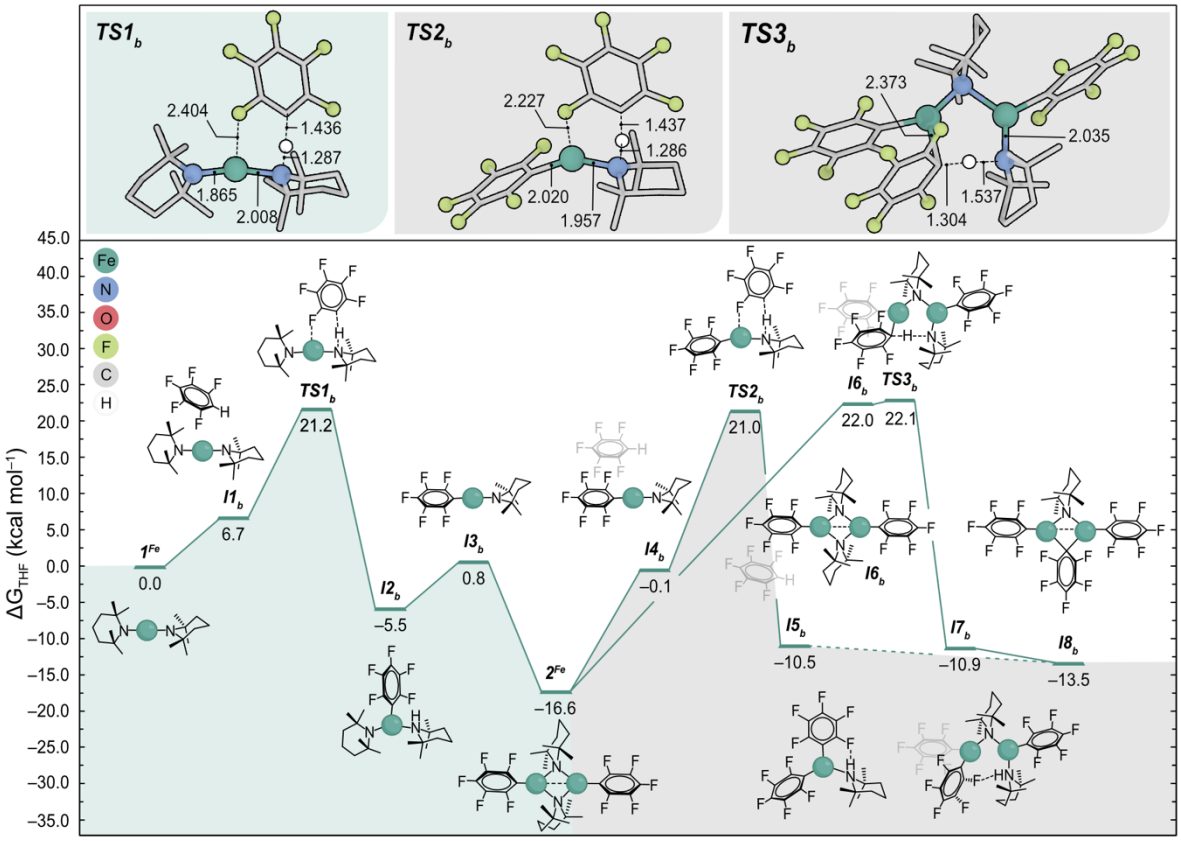

Figure 6.16. Gibbs energy profile calculated in benzene (using the SMD solvation model) at 298 K and 1 atm for the C–H metalation of C_6F_5H with **1^{Fe}**. The optimised structures for **TS1$_b$**, **TS2$_b$**, and **TS3$_b$** are shown as insets, with relevant bond distances given in Å. The overall barriers for **TS2$_b$** and **TS3$_b$** (referenced to **2^{Fe}**) are +37.6 and +38.7 kcal mol^{-1}, respectively, confirming the unfeasibility of the second C–H metalation in benzene. These results, highlighted in grey, agree with the formation of the dimer **2^{Fe}** as the sole product of the reaction, even in the presence of an excess of C_6F_5H.

6.5 Conclusions

DFT calculations presented in this chapter reveal that the second C–H activation step is both kinetically and thermodynamically unfavourable in benzene, primarily due to the high stability of the Fe dimer (**2^{Fe}**) in the absence of a coordinating donor such as THF. In benzene, the dimeric species remains dominant, and the transition state for the second C–H ferration step exhibits a prohibitively high Gibbs energy barrier, rendering the reaction unfeasible at room temperature. This observation aligns with experimental results, where monomeric bis-aryl species are not formed under these conditions.

The presence of THF in solution introduces a critical factor that facilitates the reaction. THF reversibly binds to Fe, stabilising the monomeric active species **I3^{Fe}**, and providing access to the second C–H activation step. This stabilisation enables the **2^{Fe}** dimer to dissociate partially, thereby creating a reactive pathway for the metalation of pentafluorobenzene. As a result, the second C–H activation becomes feasible in the presence of THF, leading to the experimentally observed bis-aryl iron complex $[(THF)_2Fe(C_6F_5)_2]$ (**4^{Fe}-THF**). These findings underscore the significant role of solvent coordination in dictating reaction pathways and influencing the accessibility of intermediates.

In contrast, for cobalt, even with THF as the solvent, the high stability of the dimeric species **2^{Co}** prevents the second C–H cobaltation of pentafluoroarene. The strong binding of the TMP ligands in **2^{Co}** inhibits the formation of the analogous monomeric intermediate **I3^{Fe}**, effectively blocking the pathway for the second C–H activation. Our computational results also reveal a significantly higher Gibbs energy barrier for the ligand rearrangement and C–H activation pathways in Co, corroborating experimental observations where no bis-aryl cobalt product (**4^{Co}-THF**) is detected, even after prolonged reaction times.

These results provide critical insights into the contrasting reactivity of iron and cobalt systems in C–H activation. They highlight the interplay between metal-ligand bonding, solvent effects, and reaction kinetics, demonstrating how subtle changes in the coordination environment and metal-ligand stability can drastically alter the feasibility of multistep reaction mechanisms. The findings also suggest that further tuning of the ligand framework or solvent environment might be required for cobalt systems to achieve comparable reactivity to iron.

References

1. a) A. S. Michael Lappert, Andrey Protchenko, Philip P. Power, Metal Amide Chemistry, Wiley, **2008**; b) R. E. Mulvey, S. D. Robertson, *Angew. Chem. Int. Ed*. **2013**, 52, 11470–11487.
2. a) J. F. Remenar, B. L. Lucht, D. Kruglyak, F. E. Romesberg, J. H. Gilchirst, D. B. Collum, *J. Org. Chem.* **1997**, 62, 5748–5754; b) E. Hevia, A. R. Kennedy, R. E. Mulvey, D. L. Ramsay, S. D. Robertson, *Chem. Eur. J.* **2013**, 19, 14069–14075; c) M. F. Lappert, M. J. Slade, A. Singh, J. L. Atwood, R. D. Rogers, R. Shakir, *J. Am. Chem. Soc.* **1983**, 105, 302–304; d) P. García-Álvarez, D. V. Graham, E. Hevia, A. R. Kennedy, J. Klett, R. E. Mulvey, C. T. O'Hara, S. Weatherstone, *Angew. Chem. Int. Ed.* **2008**, 47, 8079–8081; e) W. Lin, O. Baron, P. Knochel, *Org. Lett*. **2006**, 8, 5673–5676.
3. R. E. Mulvey, F. Mongin, M. Uchiyama, Y. Kondo, *Angew. Chem. Int. Ed*. **2007**, 46, 3802–382; (b) E. Nagaradja, F. Chevallier, T. Roisnel, V. Jouikov, F. Mongin, *Tetrahedron* **2012**, 68, 3063–3073.
4. a) Y. Kondo, M. Shilai, M. Uchiyama, T. Sakamoto, *J. Am. Chem. Soc.* **1999,** 3539–3540; b) M. Uchiyama, Y. Matsumoto, D. Nobuto, T. Furuyama, K. Yamaguchi, K. Morokuma, *J. Am. Chem. Soc.* **2006**, 128, 8748–8750; c) W. Clegg, S. H. Dale, E. Hevia, G. W. Honeyman, R. E. Mulvey, *Angew. Chem. Int. Ed.* **2006**, 45, 2370–2374; d) E. Hevia, D. J. Gallagher, A. R. Kennedy, R. E. Mulvey, C. T. O'Hara, C. Talmard, *Chem. Commun.* **2004**, 21, 2422–2423; e) P. C. Andrikopoulos, D. R. Armstrong, D. V. Graham, E. Hevia, A. R. Kennedy, R. E. Mulvey, C. T. O'Hara, C. Talmard, *Angew. Chem. Int. Ed.* **2005**, 44, 3459–3462; f) D. R. Armstrong, A. R. Kennedy, R. E. Mulvey, R. B. Rowlings, *Angew. Chem. Int. Ed.* **1999**, 38, 131–133; g) M. Uchiyama, H. Naka, Y. Matsumoto, T. Ohwada, *J. Am. Chem. Soc.* **2004**, *126*, 10526–10527.
5. S. D. Robertson, M. Uzelac, R. E. Mulvey, *Chem. Rev.* **2019**, 119, 8332–8405.
6. D. R. Armstrong, J. A. Garden, A. R. Kennedy, S. M. Leenhouts, R. E. Mulvey, P. O'Keefe, C. T. O'Hara, A. Steven, *Chem. Eur. J.* **2013**, *19*, 13492–13503.
7. S. H. Wunderlich, P. Knochel, *Angew. Chem. Int. Ed*. **2009**, 48, 9717–9720.
8. G. Dayaker, F. Chevallier, P. C. Gros, F. Mongin, *Tetrahedron* **2010**, 66, 8904–8910.
9. a) H. Bürger, U. Wannagat, *Monatshefte für Chemie und verwandte Teile anderer Wissenschaften* **1963**, 94, 1007–1012; b) R. A. Andersen, K. Faegri, J. C. Green, A. Haaland, M. F. Lappert, W. P. Leung, K. Rypdal, *Inorg. Chem*. **1988**, 27, 1782–1786.
10. a) A. Panda, M. Stender, M. M. Olmstead, P. Klavins, P. P. Power, *Polyhedron* **2003**, *22*, 67–73; b) W. Alexander Merrill, T. A. Stich, M. Brynda, G. J. Yeagle, J. C. Fettinger, R. De Hont, W. M. Reiff, C. E. Schulz, R. D. Britt, P. P. Power, *J. Am. Chem. Soc.* **2009**, *131*, 12693–12702; c) W. Stroek, M. Keilwerth, D. M. Pividori, K. Meyer, M. Albrecht, *J. Am. Chem. Soc.* **2021**, *143*, 20157–20165; d) M. A. Putzer, B. Neumüller, K. Dehnicke, J. Magull, *Chem. Ber.* **1996**, *129*, 715–719; e) H. Hope, M. M. Olmstead, B. D. Murray, P. P. Power, *J. Am. Chem. Soc.* **1985**, *40*, 712–713; f) A. M. Bryan, G. J. Long, F. Grandjean, P. P. Power, *Inorg. Chem.* **2013**, *52*, 12152–12160; g) R. A. Layfield, J. J. W. McDouall, M. Scheer, C. Schwarzmaier, F. Tuna, *Chem. Commun.* **2011**, *47*, 10623–10625; j) B. M. Day, T. Pugh, D. Hendriks, C. F. Guerra, D. J. Evans, F. M. Bickelhaupt, R. A. Layfield, *J. Am. Chem. Soc.* **2013**, *135*, 13338–13341; k) L. C. H. Maddock, T. Cadenbach, A. R. Kennedy, I. Borilovic, G. Aromí, E. Hevia, *Inorg. Chem.* **2015**, *54*, 9201–9210; l) A. Massard, P. Braunstein, A. A. Danopoulos, S. Choua, P. Rabu, *Organometallics* **2015**, *34*, 2429–2438; m) R. Araake, K. Sakadani, M. Tada, Y. Sakai, Y. Ohki, *J. Am. Chem. Soc.* **2017**, *139*, 5596–5606; n) T. N. Gieshoff, U. Chakraborty, M.

Villa, A. Jacobi von Wangelin, *Angew. Chem. Int. Ed.* **2017**, *56*, 3585–3589; o) C. Y. Lin, J. C. Fettinger, F. Grandjean, G. J. Long, P. P. Power, *Inorg. Chem.* **2014**, *53*, 9400–9406.
11. a) B. A. Frazier, P. T. Wolczanski, E. B. Lobkovsky, T. R. Cundari, *J. Am. Chem. Soc.* **2009**, *131*, 3428–3429; b) R. A. Bartlett, J. J. Ellison, P. P. Power, S. C. Shoner, *Inorg. Chem.* **1991**, *30*, 2888–2894; c) H. Chen, M. M. Olmstead, D. C. Pestana, P. P. Power, *Inorg. Chem.* **1991**, *30*, 1783–1787; d) Y. Ohki, Y. Ikagawa, K. Tatsumi, *J. Am. Chem. Soc.* **2007**, *129*, 10457–10465.
12. a) L. C. H. Maddock, T. Nixon, A. R. Kennedy, M. R. Probert, W. Clegg, E. Hevia, *Angew. Chem. Int. Ed.* **2018**, 57, 187–191; b) L. C. H. Maddock, M. Mu, A. R. Kennedy, M. García-Melchor, E. Hevia, *Angew. Chem. Int. Ed.* **2021,** 60, 15296–15301; c) A. Logallo, M. Mu, M. García-Melchor, E. Hevia, *Angew. Chem. Int. Ed.* **2022**, 61, e202213246; d) A. Logallo, E. Hevia, *Chem. Commun*. **2023**, 59, 5383–5386.
13. A. Logallo, L. C. H. Maddock, M. Mu, L. Gravogl, N. Jin, M. N. Peñas-Defrutos, K. Meyer, M. García-Melchor, E. Hevia, *Angew. Chem. Int. Ed.* **2024**, *63*, e202402907.
14. A. Hauser, *Coord. Chem. Rev.* **1991**, *111*, 275.
15. J. Bonin, A. Maurin, M. Robert, *Coord. Chem. Rev*. **2017**, *334*, 184.
16. M. B. Davies, *Coord. Chem. Rev.* **1996**, *152*, 1.
17. J.-D. Chai, M. Head-Gordon, *Phys. Chem. Chem. Phys.* **2008**, *10*, 6615.
18. M. J. Frisch, G. W. Trucks, H. B. Schlegel, G. E. Scuseria, M. A. Robb, J. R. Cheeseman, G. Scalmani,V. Barone, G. A. Petersson, H. Nakatsuji, X. Li, M. Caricato, A. Marenich, J. Bloino, B. G. Janesko, R. Gomperts, B. Mennucci, H. P. Hratchian, J. V. Ortiz, A. F. Izmaylov, J. L. Sonnenberg, D. WilliamsYoung, F. Ding, F. Lipparini, F. Egidi, J. Goings, B. Peng, A. Petrone, T. Henderson, D. Ranasinghe,V. G. Zakrzewski, J. Gao, N. Rega, G. Zheng, W. Liang, M. Hada, M. Ehara, K. Toyota, R. Fukuda, J. Hasegawa, M. Ishida, T. Nakajima, Y. Honda, O. Kitao, H. Nakai, T. Vreven, K. Throssell, J. A. Montgomery, Jr., J. E. Peralta, F. Ogliaro, M. Bearpark, J. J. Heyd, E. Brothers, K. N. Kudin, V. N. Staroverov, T. Keith, R. Kobayashi, J. Normand, K. Raghavachari, A. Rendell, J. C. Burant, S. S. Iyengar, J. Tomasi, M. Cossi, J. M. Millam, M. Klene, C. Adamo, R. Cammi, J. W. Ochterski, R. L. Martin, K. Morokuma, O. Farkas, J. B. Foresman, and D. J. Fox, Gaussian 09, Revision E.01, Gaussian, Inc., Wallingford CT, **2016**.
19. a) A. W. Ehlers, M. Böhme, S. Dapprich, A. Gobbi, A. Höllwarth, V. Jonas, K. F. Köhler, R. Stegmann, A. Veldkamp, G. Frenking, *Chem. Phys. Lett.* **1993**, *208*, 111; b) A. Höllwarth, M. Böhme, S. Dapprich, A. W. Ehlers, A. Gobbi, V. Jonas, K. F. Köhler, R. Stegmann, A. Veldkamp, G. Frenking, *Chem. Phys. Lett.* **1993**, *208*, 273.
20. A. Otero-de-la-Roza, M. A. Blanco, A. M. Pendás, V. Luaña, *Comput. Phys. Commun.* **2009**, *180*, 157.
21. a) C. Lefebvre, G. Rubez, H. Khartabil, J. C. Boisson, J. Contreras-García, E. Hénon, *Phys. Chem. Chem. Phys.* **2017**, *19*, 17928; b) M. Ponce-Vargas, C. Lefebvre, J. C. Boisson, E. Hénon, *J. Chem. Inf. Model.* **2020**, *60*, 268.
22. R. F. W. Bader, *Chem. Rev.* **1991**, *5*, 893.
23. T. Lu, F. Chen, *J. Comput. Chem.* **2012**, *33*, 580.
24. E. D. Glendening, J, K. Badenhoop, A. E. Reed, J. E. Carpenter, J. A. Bohmann, C. M. Morales, P. Karafiloglou, C. R. Landis, and F. Weinhold, NBO 7.0, Theoretical Chemistry Institute, University of Wisconsin, Madison, **2018**.
25. J. H. Jensen, *Phys. Chem. Chem. Phys.* **2015**, *17*, 12441.
26. A. Klamt, F. Eckert, *Fluid Ph. Equilib.* **2000**, *172*, 43.
27. M. Stahn, S. Ehlert, S. Grimme, *J. Phys. Chem. A*, **2023**, *127*, 703
28. D. Liptrot, P. Power, *Nat Rev Chem,* **2017**, *1*, 4.
29. a) C. L. McMullin, J. Jover, J. N. Harvey, N. Fey, Dalt. Trans. 2010, 39, 10833; b) C. L. McMullin, N. Fey, J. N. Harvey, Dalt. Trans. 2014, 43, 13545.

Chapter 7 General conclusions and future work

7.1 General conclusion

This thesis set out to dissect and rationalise the factors that control reactivity and selectivity in C–H activation reactions mediated by metal amide complexes. Emphasis was placed on understanding how alkali metals, transition metals, and ligands cooperate to enable selective transformations, especially in the context of bimetallic and monometallic systems. Combining experimental characterisation with computational analysis, we explored how subtle variations in reaction conditions and metal identity can dramatically shift the course of metalation reactions.

In Chapter 4, we developed a conceptual model for a Na/Co bimetallic amide system that describes the balance between mono- and bimetallic reactivity via a "seesaw effect," governed by Na···X (X = F, Cl, Br, H) NCIs. DFT and MKM simulations confirmed that these interactions shift the thermodynamic stability of different intermediates and enable a predictive framework for selective arene metalation. Importantly, these findings underscore the value of incorporating alkali metal π-interactions into mechanistic models to refine regioselectivity and understand reactivity trends.

Chapter 5 describes the unexpected reactivity dependence in K/Co systems based on reagent addition order. Stepwise addition (K first, Co second) yielded transient K(HMDS) dimers that activate toluene via an S_N2-like transition state, while the one-pot reaction resulted in an unreactive potassium cobaltate that precluded C–H activation. These findings were interpreted through detailed DFT-based speciation analysis and solvent modelling, revealing that reactivity is suppressed or enabled by the presence of toluene coordination and the energetic accessibility of reactive intermediates.

Chapter 6 focuses on the reactivity of monometallic systems, particularly $Fe(TMP)_2$ and $Co(TMP)_2$ in the C–H metalation of fluoroarenes. Despite structural similarities, only $Fe(TMP)_2$ showed polybasic behaviour, activating two equivalents of substrate. This divergence was attributed to stronger donor-acceptor interactions between Fe and TMP, captured through NBO and IGM analysis. Solvent-dependent speciation and THF binding

energies were quantified using a hybrid solvation model, showing that $Fe(TMP)_2$ exists in dynamic equilibrium between the reactive monomer and the dimeric resting states, whereas $Co(TMP)_2$ dimerisation is irreversible. MKM simulations reproduced experimental kinetics, offering quantitative insight into the interplay of speciation, solvent, and ligand effects on C–H metalation.

Together, these studies demonstrate that the choice of alkali metal, ligand identity, coordination geometry, solvent and even the order of reagent addition can act as powerful levers to control C–H activation reactivity. The work lays the foundation for the predictive design of cooperative organometallic reagents using earth-abundant metals.

7.2 Future work

While this thesis addressed speciation in selected cases such as the K(HMDS) and Na(TMP) systems, the broader question of how s-block amides oligomerise and coordinate with solvents remains underexplored. Future work should also consider the formation of oligomeric Li-, Na-, and K-amide species in coordinating and non-coordinating solvents using a combination of DFT, and advanced chemical space sampling techniques similar to the design of conformer search packages. The role of π-arene interactions and alkali metal aggregation tendencies (e.g., contact vs separated ion pairs) could be more fully explored with quantitative QTAIM and NBO descriptors. This understanding is essential for tuning the C–H activation selectivity and for designing amides that resist unwanted aggregation.

The design principles uncovered for NaFe, NaCo, and KCo systems suggest that other bimetallic combinations, such as CsFe, MnCo, and NaZn, could exhibit distinct reactivity patterns worth investigating. In particular, Cs-based systems are predicted to offer lower C–H activation barriers based on enhanced π-coordination with arenes. However, their instability and tendency to form poorly soluble oligomers necessitate new synthetic and ligand designs. Exploring chelating amides, bulky pincer ligands, or crown-ether stabilised s-block species could help achieve this. Further integration of kinetic isotope effects, in situ IR, and rapid-quench techniques could provide real-time speciation snapshots provided these intermediate species are relatively low in energy.

Taken together, future work should aim to extend the scope of cooperative amide-mediated activation chemistry by integrating structural speciation, solvent modelling, and data-driven reactivity prediction. These tools offer a promising path to the design of more selective, tunable, and sustainable catalytic systems.

End of thesis